An integrated diamond nanophotonics platform for quantum optics

A dissertation presented
by
Ruffin Eley Evans
to
The Department of Physics

in partial fulfillment of the requirements
for the degree of
Doctor of Philosophy
in the subject of
Physics

Harvard University
Cambridge, Massachusetts
April 2018

Thesis advisor: Professor Mikhail D. Lukin Ruffin Eley Evans

An integrated diamond nanophotonics platform for quantum optics

Abstract

Efficient interfaces between optical photons and quantum bits are fundamental building blocks for quantum networks and large-scale quantum computers. We demonstrate an integrated platform for scalable quantum optics based on color centers coupled to diamond nanodevices. First, we incorporate nitrogen-vacancy (NV) centers in diamond into hybrid nanophotonic crystal cavities. Despite our progress towards coupling the NV to cavity photons, we find that the NV-cavity interface is limited by the imperfections of the color center's properties and its local environment. We approach this challenge first by characterizing and modifying the diamond surface to reduce the environmental noise affecting the NV optical transition. Subsequently, we develop a new approach that makes use of a quantum emitter with intrinsic protection from this noise: the silicon-vacancy (SiV) center in diamond. We demonstrate that SiVs introduced through ion implantation feature highly coherent optical transitions, even inside nanostructures. By placing SiV centers inside all-diamond photonic crystal cavities, we achieve strong SiV-photon coupling with a cooperativity of $C > 20$. Using this platform, we realize a quantum-optical switch controlled by the spin degree

of freedom of a single SiV. By measuring intensity correlations of indistinguishable Raman photons emitted into a single waveguide, we observe a quantum interference effect resulting from the superradiant emission of two probabilistically entangled SiV centers. Finally, we demonstrate controllable photon-mediated interactions between the spin degrees of freedom of two cavity-coupled SiV centers. When the optical transitions of the two SiV centers are tuned into resonance, the coupling of each SiV to the common cavity mode results in a coherent interaction between the two SiVs, leading to the observation of super- and sub-radiant two-SiV states.

Contents

To Natalie

Acknowledgments

First, I thank my advisor Misha Lukin for his support and encouragement throughout graduate school. Misha's combination of creativity and physical intuition is truly unique, and I am lucky to have had a chance to learn so much from him over the years. I am especially grateful for his faith in me and the rest of our team when we started exploring the silicon-vacancy color center in diamond. I also thank Hongkun Park for sharing his wide-ranging expertise in the science of nanoscale systems. His original proposals for quantum optics with color centers in nanophotonic and plasmonic devices are an important basis for the work described in this thesis, and I have greatly benefited from his long-term advice and support in these areas. Markus Greiner also generously contributed his more traditional optics and atomic physics knowledge over the years. I have learned a lot by considering the physics of my work using this perspective. His curiosity and genuine interest in diverse fields of physics are inspiring.

In addition to support from my committee, several close collaborations made my work possible. First, Marko Lončar contributed his tremendous knowledge and experience in nanophotonics and diamond nanofabrication. The most exciting work presented in this thesis was performed using nanoscale diamond devices that were

made by members of the Lončar group. In particular, Mike Burek took an early lead in developing general techniques for the design and fabrication of diamond nanophotonic devices and provided us with many high-quality devices that enabled our research. Even more importantly, Mike provided high-level leadership and coordination for the diamond photonics efforts in the Lončar and Lukin groups that lead to extremely rapid development of new device designs and fabrication techniques. Bart Machielse has recently mastered these techniques and has already made substantial contributions in these areas. I am confident that Bart will pioneer new and exciting ideas in quantum nanophotonics and diamond nanofabrication that will be essential for the next generation of experiments. In the early years of my research, I also had the pleasure of working with Birgit Hausmann, who helped train me both in the cleanroom and in the lab. Her quality as a scientist is matched only by her kindness and optimism; in this regard, she served as an important model for mentorship. I was also lucky to work briefly with Haig Atikian on several projects. Moreover, my work benefited greatly from his creative development of ion-beam milling techniques and focused-ion-beam implantation, both of which were essential to the success of my work. Finally, over the years I have benefited from many productive conversations with Srujan Meesala. Even though we have rarely worked together directly, his advice and friendship have been invaluable.

The second crucial collaboration is with the group of Fedor Jelezko at Ulm University. Fedor is almost singlehandedly responsible for making us aware of the silicon-

vacancy color center (as well as, later, the germanium-vacancy center). His generosity in sharing his discoveries is as remarkable as his curiosity and deep understanding of the physics of these systems. Over the years, we have explored the fundamental physics and applications of these systems with Fedor and several of his students and postdocs, most notably Kay Jahnke and Lachlan Rogers. I look forward to hearing from Fedor about new color centers with intriguing applications in quantum optics.

More recently, we have also begun to work with Dirk Englund's group at MIT. Dirk and his group have made remarkable progress on some of the engineering challenges required to make large-scale quantum devices practical. Although the plans for a Cambridge-area quantum network remain nascent, I am confident that our collaboration will continue to bear fruit.

Throughout my graduate career, I have also worked with a number of students and postdocs in the Lukin group. I am especially grateful to Nathalie de Leon, Kristiaan De Greve, Yiwen Chu and Brendan Shields for working with me in my formative years in the lab. When I was starting out, Brendan and Nathalie helped me learn and understand key aspects of quantum optics and diverse techniques in experimental physics. Brendan in particular helped me learn the practical elements of working in an atomic physics lab. The more I mature as a scientist, the more I appreciate the practicality and wisdom of his advice. Nathalie also made huge contributions to my understanding in these areas, but was most important in contributing to my understanding of nanophotonics and nanofabrication. These fields are often overlooked

within the quantum optics and atomic physics communities, but spending a significant fraction of several years in the Harvard cleanroom gave me an appreciation both for their importance and challenge. Yiwen joined the NV project in its denouement and contributed her vast experience with cryogenic NV spectroscopy and the underlying physics of NV centers. Her results-driven attitude helped drive the project forward and helped me learn how to effectively manage a project. Finally, Kristiaan shared with me an indescribable wealth of experience in all areas of physics. I learned so much from him in the relatively short time during which we worked together. I regret that we did not continue working together throughout my PhD, and I hope we have the opportunity to collaborate in the future. Finally, Nathalie and Kristiaan were the key players in the diamond surface science described in chapter 3. Although the statistical analyses described in that chapter were mine, the surface treatment procedures and data generation were done as part of this team.

After my work with the NV center, I worked with a number of remarkable scientists on experiments using the SiV center. Most notably, Alp Sipahigil brought the SiV to Harvard and made seminal contributions in understanding both the fundamental properties of the SiV and its possibilities for applications in quantum optics. It was a truly incredible experience to work with Alp on the SiV nanophotonics efforts from the very beginning. I will never forget a fateful discussion where we agreed to pool our different skills to build a platform for quantum optics using the SiV. Shortly after Alp and I started this project, Denis Sukachev joined the effort. I have contin-

ued to work with Denis throughout my PhD, and I have been constantly impressed by his wisdom, broad perspective and diverse set of skills. I would also like to thank Johannes Borregaard, who provided us with key theoretical support and insights over the past several years. His patience and kindness have been remarkable, and I hope that we can implement another one of his theoretical schemes soon. More recently, I have been lucky to work with a number of younger students: Christian Nguyen, Mihir Bhaskar, Bart Machielse and Grace Zhang. I am constantly impressed by their dedication and burgeoning skill as physicists, and I look forward to seeing the exciting work that they will produce in the coming years.

I'm also grateful to a number of other scientists who contributed to my intellectual development even though we did not work together directly. Jeff Thompson shared his profound understanding of nanophotonics and the physics of cavity QED. For a very brief period, Mike Goldman joined the NV nanophotonics effort. Even in that short time, he taught me a lot and impressed me with his rigorous and considerate approach to problem solving. Shimon Kolkowitz made crucial contributions to my understanding of how to do physics in an abstract sense, helping me learn what problems are worth focusing on and why. Alexey Akimov was an occasional contributor to the NV project, and, along with Sasha Zibrov, gave me a deeper appreciation of old-school techniques in experimental physics, especially laser physics. Both Sasha and Alexey made key experimental contributions to our work, with Sasha in particular designing and building several external-cavity diode lasers that we continue to use in

our experiments.

Over the years, I also had valuable discussions and received experimental help from many colleagues: Arthur Safira, Igor Lovchinsky, Alex High, János Perczel, Emma Rosenfeld, Marc Warner, Alex Keesling, Tamara Šumarac, Tamara Djordjevic, Joonhee Choi, Renate Landig, Soonwon Choi, Norman Yao, Peter Maurer, Quirin Unterreithmeier, Alex Sushkov, Javier Sanchez-Yamagishi, Hannes Bernien, Harry Levine, Bo Dwyer, Jan Gieseler, Hannes Pichler, David Levonian, Peter Komar, Michael Gullans, Alexei Bylinskii, Kristine Rezai, Polnop Samutpraphoot, Crystal Senko and Leo Zhou. I am also grateful to the patient and hard-working staff in the department, including Sam, Clare, Karl, Joan, Lisa, Jacob, Adam and Stan.

I am also lucky to have had a number of close friends in graduate school, several of whom deserve particular mention. Anders Andreassen has been a constant presence throughout my time at Harvard, starting from our early days working on problem sets together and continuing over the past six years as roommates. Elana Urbach has in recent years shared both in physics-related commiseration and non-physics-related fun. I am grateful to Dom for his fascinating and wide-ranging discussions on subjects ranging from the quotidian (quantum optics) to the sublime (sphero-immunology). Ian, Alex, Brooke and Eric have been wonderful friends and roommates. I am glad that I have always had a welcoming apartment to come home to. Finally, Ana, Anne and Anj(u) have become steadfast friends whom, in different ways, have helped me grow as a person even as we have had many good times together.

Most importantly, I am grateful to my family for their love, support and patience. I am especially grateful to my wife, Natalie Dawley. It has been a very long seven years living apart while we have both pursued our PhDs. Her determination to make our relationship flourish despite the long distance and our separate struggles still amazes me. This thesis is dedicated to her.

Citations to previously published work

Parts of this dissertation cover research reported in the following articles:

Elements of section 2.2 have been published as

> "Coherent Optical Transitions in Implanted Nitrogen Vacancy Centers", Y. Chu, N. P. de Leon, B. J. Shields, B. Hausmann, R. Evans, E. Togan, M. J. Burek, M. Markham, A. Stacey, A. S. Zibrov, A. Yacoby, D. J. Twitchen, M. Loncar, H. Park, P. Maletinsky, M. D. Lukin, *Nano Letters*, 14(4):1982–1986 (2012).

Chapter 4, in its entirety, has been published as

> "Narrow-Linewidth Homogeneous Optical Emitters in Diamond Nanostructures via Silicon Ion Implantation", R. E. Evans, A. Sipahigil, D. D. Sukachev, A. S. Zibrov, M. D. Lukin, *Phys. Rev. Appl.*, 5(4):044010 (2016).

Chapter 5, in its entirety, has been published as

> "An integrated diamond nanophotonics platform for quantum-optical networks", A. Sipahigil, R. E. Evans, D. D. Sukachev, M. J. Burek, J. Borregaard, M. K. Bhaskar, C. T. Nguyen, J. L. Pacheco, H. A. Atikian, C. Meuwly, R. M. Camacho, F. Jelezko, E. Bielejec, H. Park, M. Lončar, M. D. Lukin, *Science*, 354(6314):847–850, (2016).

1

Introduction

1.1 Background

The development of quantum mechanics in the 20^{th} century revolutionized physics and led to sweeping technological advances. Modern computing and information technology, for example, is based on the development of the transistor, which relies on a quantum-mechanical description of semiconductor systems[1]. Medical technologies, such as magnetic resonance imaging (MRI), require understanding of the quantum-mechanical dynamics of biological systems. Finally, quantum mechanics has led to an increased understanding of chemical bonding and reactivity[2] essential for modern organic chemistry and biochemistry and their many applications.

The evolution of quantum technologies in the 21^{st} century has required the development of complete control of complex quantum systems. For example, the fields of

quantum metrology and sensing use coherent control of atom-like systems to achieve goals impossible for classical systems, including the production of atomic clocks[3] with relative uncertainties of one part in 10^{18} [4] and the extension of MRI to single molecules[5, 6]. Quantum information processing (QIP), a related field, can lead to significant improvements in key tasks in information technology: Quantum cryptography can allow two parties to exchange information with absolute privacy guaranteed by the laws of physics[7]. Quantum computing[8], probably the most active subfield of QIP, has been shown in theory to provide possibly exponential speed-ups in classically relevant tasks, such as factoring [9] and quantum chemistry[10, 11].

Despite the promise of quantum computing, no quantum computer can yet outperform the best classical computer at even a single task.[1] Nevertheless, there has been tremendous progress in the last decade realizing small-scale quantum processors which are currently at the scale of tens of individually-controllable quantum bits (qubits)[14, 15]. Quantum computing platforms based on superconducting qubits[16] in particular have been used to demonstrate high-fidelity individual and multi-qubit operations at the threshold for fault-tolerant computing[15], where operations on individual qubits are sufficiently high-fidelity such that errors can be identified and corrected (rather than compounded) by local operations. Quantum computing platforms based on trapped atomic ions [17] have demonstrated control over similar numbers of qubits[18]. Trapped ions typically have a different set [19] of advantages (high qubit

[1] This benchmark is known as "Quantum Supremacy"[12, 13].

connectivity, long absolute coherence times) and disadvantages (difficulty of scaling, relatively slow operation speeds) relative to superconducting systems and represent a promising alternative approach towards quantum computing. Other systems, such as arrays of trapped neutral atoms[20, 21], have been instrumental in quantum simulation[22, 23, 24, 25], where the properties of an important but difficult-to-explore quantum system are reproduced in a controllable way. Recently-demonstrated single-site control over such arrays could extend these systems to general purpose large-scale quantum computers[26, 27].

An important general goal for scaling up QIP systems is to build long-distance links between quantum subsystems[28]. Generally, the scale over which local operations can be performed is limited; in this case, "long" distance links can act as a quantum bus linking local quantum registers, allowing for the scalable creation of large quantum computers[29]. Even if it becomes possible to engineer arbitrarily large quantum processors, there is an independent motivation to send quantum information over long distances. This is, in fact, a fundamental ingredient in quantum cryptography[7]. The ability to send quantum information over long distances also has applications to distributed quantum computing schemes, such as blind quantum computing, where a remote quantum server performs calculations on encrypted quantum data provided by a client while remaining "blind" to the contents of the data[30, 31].

To achieve these goals, it is necessary to build a quantum network of local nodes connected together over long distances via photons[32, 33]. The local quantum nodes

must have three generic properties[34, 35]. First, interactions between a stationary qubit in a local node and an optical photon (the "flying qubit") should be nearly deterministic. In other words, it should be efficient to convert information stored locally into an photon and vice versa. These photons are ideally at standard telecommunications wavelengths where attenuation is minimized[2] and commercially-available optical fiber can be used. Second, the node should have a long-lived quantum memory. At minimum, the memory time of the node should be at least as long as the transit time $t = L/c$ required to send the photon over distance L in a medium with a speed of light c.[3] Third, the node should have multiple quantum bits and the ability to perform gates between them, so that error correction and other local protocols can be performed[36]. Given these ingredients, it is possible to realize schemes for distributed quantum computing[29] as well as quantum repeaters[37, 36, 38] that can be used to efficiently send quantum information over arbitrarily long distances.

Meeting these requirements for a quantum node has many of the same challenges as building a small quantum computer. However, the additional emphasis in quantum networking on coupling to optical photons suggests that a different set of physical systems may be more appropriate than those used for qubits in a quantum computer. For example, although superconducting systems are perhaps the leading candidate for

[2] Around 0.5 dB/km at wavelengths of 1550 nm or 1310 nm.

[3] For example, sending a signal from Boston to San Francisco requires a coherence time of at least 25 ms.

realization of a quantum computer, high-fidelity transduction of a single microwave photon (at the natural energy scale for superconducting qubits) to the optical domain has not yet been realized[39]. It is therefore natural to search for quantum systems that have both spin and optical degrees of freedom that can be used for storing, manipulating and sending quantum information stored in photons.

There has been impressive progress towards realizing these goals using trapped atoms and ions[40, 41, 42]. More recently-developed solid-state systems have the advantage of scalability and higher operation speeds enabled by larger dipole moments and sub-diffraction-limit confinement of light. However, solid-state systems such as self-assembled quantum dots[43, 44], rare earth ions in solids[45, 46] and small molecules[47, 48, 49] typically suffer from inhomogeneity (which is a barrier to engineering interactions; see section 5.3) and both spin and electronic noise introduced by their solid-state environment. Experience with these systems provides a strong motivation for using intrinsically-identical, atom-like systems in an environment with as little noise as possible.

Color centers in diamond can meet these criteria. Diamond is a wide-bandgap semiconductor able to host defects with a wide range of optical transitions[50]. Moreover, diamond is one of the few materials that can be synthesized to be free of nuclear spins, thereby preventing a major source of magnetic field noise.[4] Even in diamond

[4]For example, the electronic spin coherence time of InGaAs quantum dots is limited to several microseconds by the high density of nuclear spins in the crystal[51, 52, 53]. Coherence times of several milliseconds have been reported with NV centers in isotopically purified dia-

with a natural isotopic abundance, only 1.1% of carbon nuclei (the ^{13}C isotope) have spin. Finally, the diamond structure has high symmetry. This symmetry is important because the symmetry of the crystal limits the symmetry of any system within the crystal. As we will see later when we compare the optical properties of the nitrogen-vacancy (NV) and silicon-vacancy (SiV) color centers in diamond, having a defect with inversion symmetry is crucial for avoiding the effects of electronic noise. It is not possible to have a defect with inversion symmetry in, for example, silicon carbide, another wide-bandgap semiconductor with color centers that have been studied for quantum optics[56, 57].

Over the past several decades, development of the nitrogen-vacancy color center in diamond as an optically-addressible spin qubit has led to promising applications in metrology and sensing[58, 5, 59, 60] that are enabled by the long room-temperature coherence time of the NV[54]. The NV has also been developed as a platform for quantum information science, with significant work dedicated to producing entanglement first with a single photon[61] and then, by interfering such photons from separate NVs[62], entanglement between two spatially-separated NVs[63]. Despite the success of this work, long-distance entanglement generation rates remain slow[64], generally significantly less than 1 Hz. The main limitation of these experiments is that the NV-photon interaction is weak, leading to slow rates of NV-photon entanglement

mond[54]. Coherence times of greater than one second can be acheived using a nuclear spin close to the NV as a ancillary qubit[55].

and hence even slower rates of NV-NV entanglement. Moreover, to constitute a fully-featured quantum node for more general applications, interactions between multiple local NV centers must be engineered. Although room-temperature NV-NV entanglement based on direct dipolar coupling has been demonstrated[65], scaling these techniques to systems of more than two NV centers in a controllable, high-fidelity fashion is an ongoing challenge.

1.2 Overview of this thesis

This thesis focuses on addressing the challenges of realizing a quantum node using color centers in diamond. First, in chapter 2, we present techniques for creating a prototype for a quantum node by coupling the NV center to a nanoscale photonic crystal cavity.[5] We construct this system by first engineering NV centers with coherent optical transitions in bulk diamond (section 2.2). Then, we provide a brief overview of the physics of atom-photon coupling through cavity quantum electrodynamics (cavity QED) in section 2.3. In particular, we define the *cooperativity* of such a system as the key figure-of-merit for coherent atom-photon coupling and discuss some key factors limiting the cooperativity in solid-state systems. With this theoretical background in mind, we present an experimental demonstration of Purcell enhancement from an NV

[5]We will not review the properties of the NV or SiV here. Doherty has an excellent review of the NV center[66]. Hepp reviews the properties of the SiV center[67]. Since that work, the understanding of the effect of strain on the SiV has evolved slightly[68].

center coupled to a hybrid photonic crystal cavity (section 2.4). Although the NV center is a promising spin qubit, its optical transitions are sensitive to electric-field noise in the environment. Creating NV centers with coherent optical transitions in nanostructured diamond is therefore the primary difficulty in creating a high-cooperativity interface between an NV and a nanoscale cavity.

We attempt to address this issue in chapter 3 by understanding the electronic properties of the diamond surface. This chapter begins with an overview of the electronic properties of the surface that are relevant to the optical properties of color centers (section 3.1). We then give a brief review of the previous literature on diamond surface science (section 3.2), focusing on experimentally observed and theoretically predicted reconstructions of the diamond surface. Next, we turn to two complimentary techniques for characterizing the diamond surface. The first, reflection high-energy electron diffraction (RHEED), is presented in section 3.3. RHEED allows us to characterize the spatial ordering of the diamond surface. Although the spatial ordering does not directly tell us about the electronic properties of the surface, we compare our observed spatial ordering to that predicted for various proposed surface terminations, allowing us to support or rule out various such proposals. The second surface characterization technique we use is x-ray photoelectron spectroscopy (XPS). This technique, presented in section 3.4, allows us to determine the chemical composition of the diamond surface. Most simply, XPS tells us which atoms are at the surface. A careful analysis of the XPS data can also provide important clues about the chemical bond-

ing at the surface. The large number of samples (N = 99) we analyze with XPS allows us to make generalizations about the effects of different surface processing techniques that are designed to improve the optical properties of near-surface NVs. Again, XPS does not give us direct information about the relevant electronic properties of the diamond surface, but allows us to compare the observed chemical composition of the surface with various proposed surface terminations.

Despite progress understanding the structural and chemical properties of the diamond surface, it remains a challenge to translate this understanding into a process for improving the optical properties of NV centers in nanostructured diamond. Fortunately, it is possible to circumvent most of the negative effects of the environment by working with a system that is intrinsically less sensitive to electric field noise. The silicon-vacancy (SiV) center in diamond is such a system and has superior optical properties arising from its inversion symmetry, which makes it insensitive to first-order Stark shifts. The rest of this thesis focuses on developing a platform for solid state quantum optics using the SiV center in diamond.

In chapter 4, we present a procedure for producing SiV centers via ion implantation. This procedure is very similar to the procedure presented in section 2.2 for the creation of NV centers. The procedure used for SiV centers is in fact considerably simpler, with fewer processing steps. Despite this, the SiV centers created using ion implantation have significantly narrower optical linewidths (relative to their lifetime limit) than NV centers. Moreover, the inhomogeneous distribution of optical transi-

tion frequencies for implanted SiV centers is low. Most remarkably, these desirable optical properties persist even in SiV centers that are incorporated into nanoscale diamond devices.

We then present an integrated diamond nanophotonics platform for solid-state quantum optics based on the SiV (chapter 5). In this work, we describe the incorporation of the SiV center into all-diamond nanoscale photonic crystal cavities. We achieve SiV-cavity cooperativities of order unity and harness the SiV orbital degree of freedom to realize a quantum-optical switch controlled by a single SiV center. Raman transitions are used to realize a single-photon source with a tunable frequency and bandwidth in a diamond waveguide. By measuring intensity correlations of indistinguishable Raman photons emitted into a single waveguide, we observe a quantum interference effect resulting from the superradiant emission of two SiV centers. This effect arises from probabilistic generation of an entangled state of the two SiVs.

In chapter 6, we extend this work to a system of two SiV centers which are both strongly coupled to a single mode of a diamond nanocavity. By improving the cavity quality factor and mode volume and by improving our ability to localize the SiV centers within the diamond nanocavity, we achieve cooperativities of $C \gtrsim 20$. We use this platform to engineer photon-mediated interactions between pairs of cavity-coupled SiV centers. When the optical transitions of the two SiV centers are tuned into resonance, the coupling of each SiV to the common cavity mode results in a coherent interaction between the two SiVs, leading to the deterministic formation of

super- and sub-radiant two-SiV states. We use the electronic spin degrees of freedom of the two SiVs to create a controllable optically-mediated spin-dependent interaction. The photon-mediated interactions between emitters demonstrated in this chapter are essential for scalable quantum information processing and can be used to implement deterministic cavity-mediated quantum gates between SiV spin qubits.

Finally, we conclude in chapter 7 with a summary of the work in this thesis and an outlook for future work. In particular, I highlight some of the key opportunities and challenges for our system and describe how these challenges might be met.

2

Towards a solid-state quantum optics platform with the nitrogen-vacancy center

2.1 Introduction

In section 1.1, we provided a general motivation for building a quantum network and highlighted the promise of color centers in diamond as a building block for a quantum node. We also described some of the considerable advantages of the nitrogen-vacancy center, in particular its long room-temperature coherence time[54] and spin-dependent optical transitions[66]. These properties have enabled a number of impressive proof-

of-principle experiments in quantum networking using the NV[61, 62, 63, 64]. For these schemes to be technologically useful[38], the operation rates must be improved considerably[63]. These operation rates are often limited by the rate of generation of indistinguishable photons from the NV. To improve the indistinguishable photon generation rate, NVs can be incorporated into optical cavities[69, 42, 70] where the NV-cavity interaction strength can be increased due to the enhanced optical density of states in the cavity. This can allow for significant increases in the emission rate of indistinguishable photons, improving the speed and efficiency of these schemes[38]. Previous work with the NV center has focused on both nanophotonic[71, 72, 73] and microscopic Fabry-Pérot-style [74, 75, 76, 77, 78] optical cavities Finally, achieving strong coupling[1] between quantum emitters and photons can enable fundamentally different protocols in quantum information processing, including gates between atoms and photons[80] and cavity-assisted entanglement generation between local qubits[81]. These protocols can enable new architectures for quantum networks with faster operation rates and more favorable scalings with distance and local errors[36].

In this chapter, we discuss progress towards realizing an efficient interface between optical photons and NV centers. Section 2.2 presents the creation of NV centers in bulk diamond via implantation of nitrogen ions. We discuss a procedure for improv-

[1] In this work, the strong-coupling regime will be defined as the case where the cooperativity $C > 1$, not the more typical definition where $g > \kappa$ and $g > \gamma$. We use this definition because most protocols only require a large cooperativity rather than the stricter condition above. Compare Ref. [79] to Ref. [80].

ing the optical coherence properties of implanted NV centers through a combination of high-temperature annealing and surface processing, and then give a summary of the optical properties of the resulting NV centers. This section begins with a brief overview of cavity quantum electrodynamics (cavity QED), which is the theoretical framework underlying the enhanced atom-photon interactions present in an optical cavity (section 2.3). Section 2.4 describes integrating these implanted NV centers into a hybrid platform for acheiving strong light-matter interactions. We then turn to a characterization of the properties of the NV center in a hybrid nanophotonic crystal cavity. Finally, we conclude in section 2.5 with a discussion of these results and the prospects for future work with the NV and other color centers.

2.2 Creation of narrow-linewidth optical emitters in bulk diamond via nitrogen ion implantation

2.2.1 Background

The negatively charged nitrogen vacancy (NV) center combines excellent spin coherence with atomic-like optical transitions at cryogenic temperatures[66]. Like many solid-state systems, however, the NV is sensitive to noise arising from its environment,

leading to decoherence. Most studies have focused on the coherence properties of the NV spin, both in bulk diamond [82] and near the diamond surface [83, 84, 85]. The coherence properties of the NV optical transition are also important for engineering coherent spin-photon interactions. Because the electronic states of the NV center are first-order sensitive to electric fields through the linear Stark effect[66, 86], the optical transition frequencies of the NV fluctuate in response to changes in its local environment. This phenomenon is known as spectral diffusion and is present in many solid-state systems[87, 49]. Spectral diffusion results in an effective broadening of the NV optical transition. This leads, for example, to a mismatch in wavelengths in experiments relying on identical, Fourier-limited photons[88] and also decreases the effective figure-of-merit (the cooperativity) that characterizes emitter-photon interactions (discussed in section 2.3 below).

Spectral diffusion can have several timescales. Fast electric field noise results in spectral diffusion that corresponds to an extra source of decoherence for the optical excited state of the NV. If the timescale for spectral diffusion is longer than the timescale of an individual run of a particular experiment, it is often possible to circumvent spectral diffusion by pre-selecting for instances of the experiment where the emitter is in a desirable spectral position[89]. In this regime, the NV optical transition frequency can also be actively stabilized[90, 88]. The timescales for spectral diffusion can also change as a function of the wavelength and power of any applied laser driving: in general, higher power leads to more spectral diffusion. In fact, we have not

observed spectral diffusion to occur in the absence of laser illumination.

Extremely narrow linewidths have been measured over short timescales for NV centers. For example, a lifetime-limited linewidth of 13 MHz has been reported for an NV in a bulk diamond sample [90], and a nearly lifetime-limited linewidth of 16 MHz was reported for an NV in a diamond nanocrystal[91]. However, the linewidths measured in these studies over long times are much broader. One particular problem arises from the fact that the NV center will ionize from the NV^-charge state into the NV^0 charge state after being excited on-resonance[92]. In order to bring the NV back into the correct NV^- charge state, a high-power off-resonant laser (usually at 532 nm) is typically applied. This high-power pulse also ionizes other defects within the diamond, changing the local electric field environment and contributing to spectral diffusion[93, 94]. Hence, the typical procedure of reionizing the NV^0 to NV^- introduces spectral diffusion. This example demonstrates an important general point: the linewidth of the NV in the presence of spectral diffusion is not an intrinsic property of the emitter and its environment but rather a complicated function of experimental conditions.

The problem of spectral diffusion is rendered even more difficult by the requirements that NV centers are isolated into a single device layer in the diamond and that, for many applications, it is desirable to fabricate nanostructures out of the diamond surrounding the NV. The first requirement can be met by creating NV centers during diamond growth by careful doping with nitrogen gas[95]. However, growth of high-quality diamond is notoriously difficult, making this technique impractical for

many researchers. A layer of NV centers can also be introduced via implantation of nitrogen ions[96]. This technique offers straightforward control of the concentration (through the number of input ions) and depth (through the energy of the ions) of the resulting NV layer. Unfortunately, this implantation process also forms other defects in the diamond lattice, leading to additional sources of electronic noise and hence spectral diffusion. Similarly, the requirement that the diamond should undergo fabrication leads to damage of the diamond surface near the NV, again leading to noise and spectral diffusion[71].

In this section, we focus on the creation of NV centers with relatively narrow optical linewidths via ion implantation. First, we describe the implantation technique. We then develop a procedure based on high-temperature annealing and surface processing that improves the optical linewidths of the implanted NV centers. We characterize the optical properties of the resulting NV centers, and finally apply a technique[92] that allows us to avoid spectral diffusion by using a resonant low-power laser to reionize the NV from the NV^0 to the NV^- charge state.

2.2.2 Creation of NV centers via implantation and annealing

To create NV centers with the highest quality spin and optical properties, it is important to begin with a diamond substrate that is as free of defects as possible. We use

a commercially-available polished CVD diamond (Element Six Inc., $[N]_S^0 < 5\,\text{ppb}$, {100} oriented top face). Previous work suggests that mechanical polishing produces a strained and damaged layer close to the surface that results in reduced mechanical stability of nanofabricated structures[97]. We also observe that damage introduced by mechanical polishing leads to greater spectral diffusion and reduced photostability. We reduce this damage by removing 5 μm of diamond through reactive ion etching, producing a smooth (under 1 nm RMS roughness) surface. More details on this technique can be found in Fig. 2.2 and elsewhere[97].

NV centers are then created via implantation of nitrogen ions. We then implant $^{15}N^+$ ions at an energy of 85 keV, corresponding to a resulting depth of around 100 nm (Fig. 2.1) as calculated using the Stopping Range of Ions in Matter (SRIM) package[98]. The predicted variation in implantation depth (*i.e.* straggle) is around 20 nm, although channeling effects can produce a significantly higher variation[99]. To minimize these effects, we implant at a small angle of generally 1-7°. We implant at four different nitrogen doses: $10^N/\text{cm}^2$ for $N \in \{9, 10, 11, 12\}$ to study the effect of concentration on the NV properties. Implantation is performed by a commercial foundry.

We then anneal the samples at high vacuum ($P < 10^{-6}$ Torr). The annealing procedure consists of a four-hour step at 400 °C followed by a two-hour step at 800 °C and a two-hour step at 1200 °C. Each temperature is reached in a one-hour ramp. The physical justification for this annealing process is as follows: The 400 °C step has two purposes. First, it acts as a bake-out step that helps to maintain low pressures in our

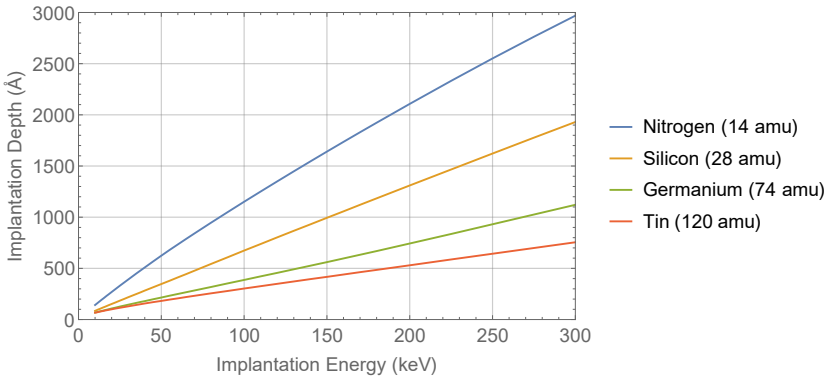

Figure 2.1: Implantation depth as a function of implantation energy for several species that lead to creation of color centers in diamond. The SiV center will be discussed in later chapters. The GeV center is discussed in Refs. [100, 101, 102]. The SnV center is discussed in Ref. [103].

furnace. Second, at these temperatures it is believed that vacancies and interstitial nitrogen atoms (both of which are introduced during implantation) recombine to form substitutional nitrogen defects [104]. At 800 °C, vacancies are mobile[105, 106, 50] leading to the formation of defect-vacancy complexes, including the NV. Diffusion of substitutional nitrogen in diamond is not believed to occur (except at very high temperatures and pressures) without assistance from a nearby vacancy[106], so the diffusion of vacancies is the dominant process by which NV centers are formed. The anneal at 1200 °C is designed to remove additional damage to the crystal lattice. For example, at this temperature, divacancies and other defects can also anneal out[107, 108, 109, 110, 111]. Previous work has also demonstrated that annealing at these temperatures can improve the coherence time of NV centers, indicating that some of the

defects removed by annealing are paramagnetic[112]. NV centers themselves will generally be stable up to around 1700°C[106, 113]. Because NV formation relies on the presence of nearby vacancies, the conversion yield from N^+ to NV is limited by the local vacancy concentration. This vacancy concentration can be boosted by irradiating the diamond with high-energy electrons, which can result in a near-unity conversion yield and a high concentration of NV centers[107].

After annealing, we remove any surface impurities and graphitic carbon in an oxidative acid clean (approximately 1 h in boiling 1 : 1 : 1 perchloric : nitric : sulfuric acid)[114]. Finally, we anneal the sample in a low-temperature (465°C) oxygen environment in three 48-minute steps[115]. At the time of this work, it was believed that this process removed sp^2 hybridized carbon at the surface of the diamond and also produced a surface of higher quality than that produced after acid cleaning alone. A detailed characterization of the surface of the diamond after acid cleaning compared to low-temperature oxygen annealing will be discussed in chapter 3. After this work was performed, later work by other groups also explored the effect of low-temperature oxygen annealing[116]. Our complete processing procedure is given in Fig. 2.2.

2.2.3 Optical properties of implanted NV centers

We characterize the optical properties of the implanted NV centers by using scanning confocal microscopy. At room temperature, the zero-phonon line (ZPL) optical tran-

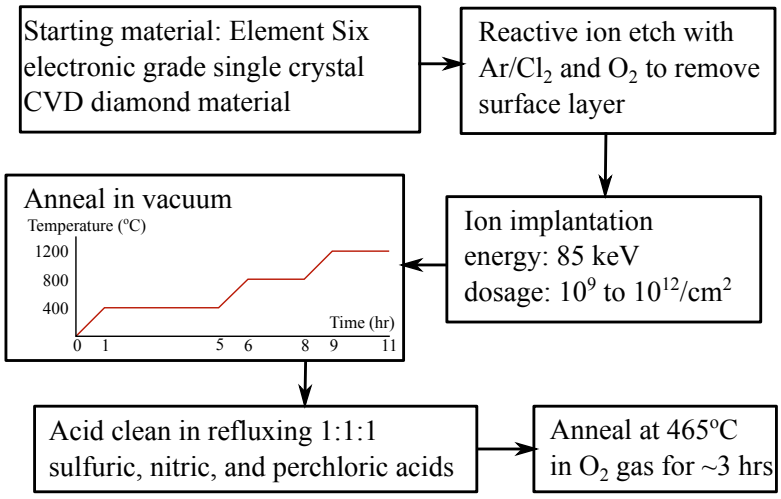

Figure 2.2: Procedure for creating NV centers through ion implantation, annealing and surface treatment. The Ar/Cl_2 (O_2) etch was done using an ICP power of 400 W (700 W), a RF power of 250 W (100 W), a DC bias of 423 V (170 V), a chamber pressure of 8 mTorr (10 mTorr) and a gas flow rate of 25/40 sccm (30 sccm). The sample temperature was set to 17°C.

sition of the NV is broadened by phonon processes[66]. Hence, we work at temperatures less than 10 K by placing the sample in a continuous-flow liquid helium cryostat (Janis Cryogenics model ST-500) where the ZPL linewidth is limited only by the lifetime (Fourier) limit plus spectral diffusion. We first characterize the density of the implanted NV centers at the four implantation doses using off-resonant excitation. In this technique, we excite at 532 nm with approximately 1 mW of power and perform a spatial scan over the sample, collecting fluorescence in the NV phonon side-band (PSB). As expected, the concentration of NV centers increases with increasing implantation dose (Fig. 2.3a). At a dose of $10^{10}/cm^2$, we observe isolated single NV centers with a density of approximately $1/cm^2$, implying a conversion efficiency of around 1%.

The conversion efficiency as a function of various implantation parameters was later studied elsewhere[117]. The sample at $10^{10}/\text{cm}^2$ implantation dose has a moderate density of optically-resolvable NV centers. Samples at higher density had too many NV centers to easily resolve single NVs, and the sample at $10^{9}/\text{cm}^2$ had a very low density of NVs, making characterization difficult.

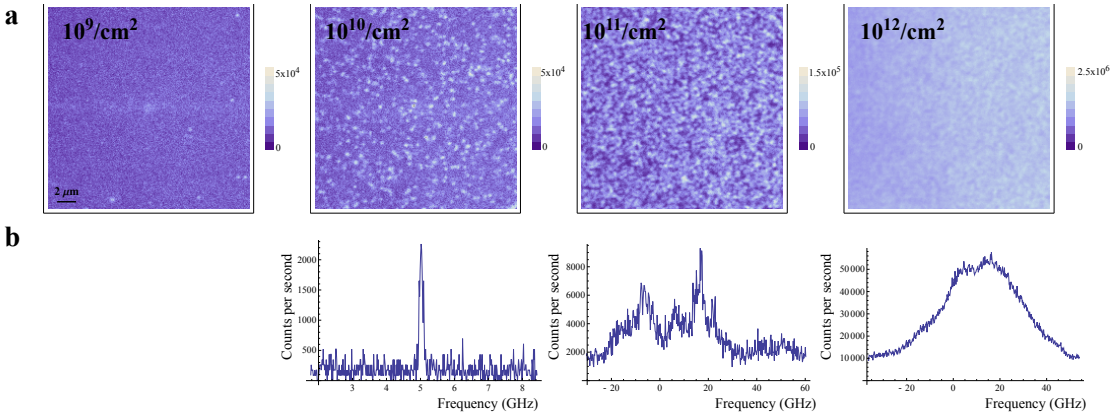

Figure 2.3: (a) Confocal images of the implanted layer of NV centers for four different nitrogen ion doses. (b) Corresponding PLE spectra for the three highest doses.

We characterize the linewidths of the implanted NV centers as a function of implantation dose by using photoluminescence excitation (PLE) spectroscopy (Fig. 2.3b). In this technique, we scan a resonant laser (New Focus Velocity external-cavity diode laser) across the NV ZPL at around 637.2 nm and collect fluorescence in the NV PSB. Because the resonant excitation can ionize the NV^- into the NV^0 charge state, we also apply an off-resonant pulse at 532 nm to re-ionize the NV^0 into the NV^-state. These off-resonant pulses are applied at roughly 10% duty cycle at every frequency,

not just at the beginning or end of the PLE scan. As explained above, this reionization procedure also leads to spectral diffusion. The data shown in Fig. 2.3b are also scans averaged over several minutes. Hence, these linewidths are a faithful representation of the linewidth of the NV averaged over the different photoionization-induced configurations of the local environment.

To more thoroughly determine the distribution of NV optical properties, we focus on samples at an implantation density of $10^{10}/\mathrm{cm}^2$ where NVs are resolvable and the optical linewidths are relatively narrow compared to linewdiths in samples at higher densities (Fig. 2.3b). We measure the linewidths of 50 NVs in four such samples (Fig. 2.4a). The dimensionless figure-of-merit that can be compared across emitters is the measured linewidth Γ_b relative to the lifetime-limited linewidth in bulk γ_b =13 MHz.[2] A majority of NV centers in our study have linewidths less than 500 MHz, which is a significant improvement over NV centers created via ion implantation without using our processing technique where the measured linewidths are typically many GHz. This gives us a ratio $\Gamma_b/\gamma \lesssim 40$. The linewidths we measure approach those measured for naturally-occuring NV centers deep within high-quality bulk diamond, where a ratio $\Gamma_b/\gamma \sim 10$ is typically observed[88, 89, 95].

[2] We use the subscript b here in Γ_b for linewidths observed in bulk diamond, anticipating work in section 2.4 and in chapter 4 with nanostructured diamond where the linewidth Γ_n for NV centers in nanostructures can be significantly broader. Note that the lifetime-limited linewidth in bulk γ_b is different than the lifetime-limited linewidth in nanostructures γ_n since the local dielectric environment and hence the optical density of states is different. The SiV is believed to be dominated by non-radiative decay which is insensitive to the local optical density of states; in fact, we observe $\gamma_b = \gamma_n$ for the SiV.

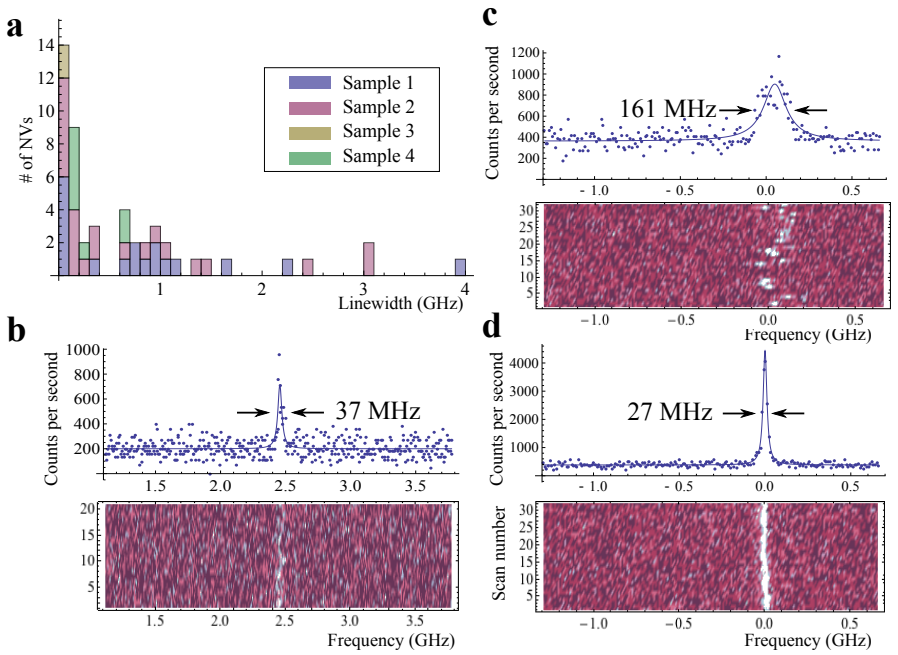

Figure 2.4: (a) Histogram of linewidths for NV centers in four samples implanted with a dose of $10^{10}/\text{cm}^2$ using 532 nm excitation to repump the NV into the NV^- charge state. (b) Spectrum showing the narrowest linewidth from (a) (top) obtained by averaging twenty-one successive PLE scans (bottom). Each scan takes around 2 seconds. (c) Spectrum of another NV taken using the 532 nm reionization laser (top). Corresponding single PLE scans illustrating spectral jumps due to repumping (bottom). (d) Spectrum of the same NV as in (c), taken using 575 nm resonant excitation of the NV^0 state to reionize the NV back into NV^-.

Finally, we present a technique for mitigating the effects of photoionization of the NV center while simultaneously avoiding spectral diffusion. Recall that the 532 nm laser used here is necessary to ionize the NV from the NV^0 to the NV^- charge state after resonant excitation at 637 nm ionizes the NV^-. The absorption cross section of the NV^0 at 532 nm is not large, requiring a relatively large amount of power (of or-

der 1 mW) to convert the NV^0 to the NV^-. Instead of using this laser, we use a tunable narrowband laser at 575 nm (home-built external-cavity diode laser at 1150 nm, frequency-doubled) that is resonant with the ZPL of the NV^0 where the NV^0 absorption cross-section is much higher. By scanning the laser at 575 nm across the NV^0 resonance in between PLE scans with the 637 nm laser, we can efficiently reionize the NV at significantly lower powers than when we use the 532 nm off-resonant reionization scheme. This technique was first developed in Ref. [92]. Using this technique, we measure NV^- optical transition linewidths as narrow as 27 MHz (Fig. 2.4d).

2.3 An introduction to cavity QED and considerations for solid-state systems

As described in Sec. 2.1, integrating the NV center into an optical cavity can result in strong NV-photon coupling. Historically, a primary motivation for this goal with NV centers was to increase the rate of indistinguishable photons from the NV center, which is a key technical parameter for previously-demonstrated quantum networking schemes with the NV[61, 62, 63, 64]. However, engineering coherent interactions between NV centers and the mode of an optical cavity has applications in quantum information that extend far beyond simply increasing the rate of indistinguishable photons[38, 80, 81, 36]. Some examples of this physics will be given in chapters 5 and

6. There are many excellent resources covering the theoretical and experimental background behind cavity QED.[3] Here, we will give a very basic overview and point out some of the key considerations for building a cavity QED system with imperfect optical emitters.

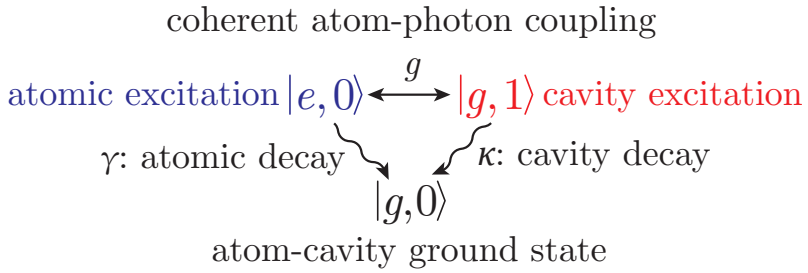

Figure 2.5: Diagram of relevant atomic and cavity states and rates in the single-excitation regime of cavity QED. The atomic $|e, 0\rangle$ and cavity $|g, 1\rangle$ excited states exchange an excitation at the single-photon Rabi frequency g. Spontaneous emission at rate γ from $|e, 0\rangle$ or cavity decay at rate κ from $|g, 1\rangle$ can bring the system into the ground state $|g, 0\rangle$. Note that this picture neglects decoherence of the atomic excitation arising from, for example, spectral diffusion. To lowest order, this decoherence can be modeled as an increase in γ.

Consider the system of a two-level atom (or any other quantum emitter) coupled to a single mode of an optical cavity. An atom in its excited state can emit a photon into the empty cavity or, symmetrically, an atom in its ground state can absorb a

[3] Haroche gives a good general overview of the field as of 2013[118]. Some relevant theory, including a good overview of the input-output formalism, is presented in a textbook by Walls and Milburn[119]. The fact that the strong coupling regime in the traditional sense is not required for most applications was first pointed out by Waks and Vučković[79]. A highly underappreciated fact in the field is that most of the effects in cavity "quantum" electrodynamics (particularly in the linear regime) can be understood as the physics of two coupled oscillators[120].

single photon from the cavity mode and transition to its excited state. This is the fundamental process for atom-photon coupling in cavity QED and occurs at a rate given by the single-photon Rabi frequency

$$g = \vec{E} \cdot \vec{\mu}/\hbar \tag{2.3.1}$$

$$\leq \mu\sqrt{\frac{\omega}{\epsilon_0 \hbar V}} \tag{2.3.2}$$

where $\vec{E}$ is the electric field in the cavity due to a single photon and μ is the transition dipole moment of the atom. In the second line, we have assumed perfect overlap between the atomic transition dipole $\vec{mu}$ and the single-photon electric field $\vec{E}$ (which accounts for the inequality) and written g in terms of the mode-volume of the cavity

$$V = \frac{\int |\vec{E}(\vec{x})|^2 dV}{|\vec{E}_{max}|^2} \tag{2.3.3}$$

which expresses the degree to which the cavity can concentrate the electric field.

Rabi oscillations between the atom and the cavity are damped by two loss mechanisms. First, the cavity has some intrinsic loss rate given by $\kappa = \frac{Q}{\omega}$ where Q is the cavity quality factor and ω is the resonance frequency of the cavity.[4] Second, the atom can undergo spontaneous emission at rate $\gamma = \frac{\omega^3 \mu_{total}^2}{3\pi\epsilon_0 \hbar c^3}$ where ω is the resonance frequency of the atom and μ_{total} is the total transition dipole moment out of the opti-

[4]This equation can be taken as a definition of Q.

cal excited state. To good approximation,[5] any optical decoherence for the atom will also contribute to γ and damp out the Rabi oscillations between the atom and the cavity. The relevant states and their corresponding rates are described in Fig. 2.5.

To quantitatively determine the evolution of this system, we write the general wavefunction in the one-excitation manifold:

$$|\psi\rangle = c_{g,1}\,|g,1\rangle + c_{e,0}\,|e,0\rangle \tag{2.3.4}$$

we apply the stochastic wavefunction approach [121] and consider the evolution of $|\psi\rangle$ under the effective Hamiltonian [122]

$$\hat{H}_{eff}/\hbar = -i\gamma\hat{\sigma}^\dagger\hat{\sigma} + (\delta - i\kappa)\hat{a}^\dagger\hat{a} + g\hat{a}^\dagger\hat{\sigma} + g^*\hat{a}\hat{\sigma}^\dagger \tag{2.3.5}$$

where $\hat{a}$ and $\hat{\sigma}$ are the annihilation operators for the cavity and atomic excitations, respectively, and we have included the effects of loss as non-Hermitian terms. The atom-cavity detuning is given by δ. Applying $\hat{H}_{eff}$ to $|\psi\rangle$ yields the equations of motion:

[5] Markovian decoherence should properly be modeled in a full master-equation approach. Examples of such an approach are given in section C.5 in the appendix. However, the stochastic wavefunction formalism described here generally produces good agreement with experiment in the parameter regimes explored in this thesis.

$$\dot{c}_{g,1} = -\left(\frac{\kappa}{2} - i\delta\right) c_{g,1} + igc_{e,0} \tag{2.3.6}$$

$$\dot{c}_{e,0} = igc_{g,1} - \frac{\gamma}{2} c_{e,0} \tag{2.3.7}$$

In this work, we use nanophotonic cavities instead of macroscopic Fabry-Pérot-style optical resonators. These nanophotonic cavities have the advantage that they can concentrate the light very tightly into a small mode volume around the quantum emitter, increasing the electric-field intensity and increasing g (*cf.* Eqn. 2.3.2). However, these nanophotonic cavities have the disadvantage that their loss rate κ is generally larger than for a macroscopic cavity. This means that we work in the "fast-cavity limit"[6], where $\kappa > g > \gamma$. In this regime, we can adiabatically eliminate the cavity mode, setting $\dot{c}_{g,1} = 0$ to solve for the evolution of the atomic degree of freedom. We obtain:

$$\dot{c}_{e,0} = -\left(\frac{\gamma}{2} + \frac{2g^2/\kappa}{1 + (2\delta/\kappa)^2}\right) c_{e,0} + i\frac{4g^2\delta/\kappa^2}{1 + (2\delta/\kappa)^2} c_{e,0} \tag{2.3.8}$$

The first term is the atomic decay rate and has two components. The first component $\frac{\gamma}{2}$ is the atomic decay rate from spontaneous emission, while the second, proportional to g^2/κ, arises from coherent emission of the atom into the cavity. In other words, we have an enhanced spontaneous emission rate (taking the resonant cavity

[6]Sometimes called the "bad-cavity limit".

case $\delta = 0$):

$$\gamma_{\text{Purcell}} = \gamma_{\text{spont.}} + \frac{4g^2}{\kappa} \tag{2.3.9}$$

The enhancement of the spontaneous emission rate $\gamma_{\text{spont.}}$ of a dipolar system in a resonator was first discovered by Purcell, and is therefore known as the Purcell Effect[123].

A simple justification for the Purcell effect can be given based on the enhanced density-of-states present in the cavity. Recall that, according to Fermi's Golden Rule, the spontaneous emission rate is proportional to the density of states. In free space, the density of states is proportional to ω^2/c^3 as usual. For a cavity, there is only a single mode with a spectral density (bandwidth) of Q/ω in a spatial volume V, giving a cavity density of states of $Q/V\omega$. Hence, the expected enhancement of the spontaneous emission rate in a cavity relative to the free-space value is:

$$\frac{Q}{\omega V} \Big/ \frac{\omega^2}{c^3} = \frac{Q}{V/\lambda^3} \tag{2.3.10}$$

By substituting the definitions for g, κ and γ given on page 28 into Eqn. 2.3.9, we can confirm that the enhancement $\gamma_{Purcell}/\gamma - 1 = \frac{4g^2}{\kappa\gamma_{\text{spont.}}}$ is in fact equal to $\frac{Q}{V/\lambda^3}$ up to a constant of proportionality. This dimensionless quantity is known as the *coopera-*

tivity and characterizes the strength of the atom-photon coupling:

$$C \equiv \frac{4g^2}{\kappa\gamma} \leq \frac{3}{4\pi^2}\frac{Q}{V/\lambda_n^3} \tag{2.3.11}$$

where λ_n is the effective wavelength λ/n_{eff} in the cavity.[7] It is also convenient to define a dimensionless mode volume $\bar{V} \equiv V/\lambda_n^3$. Typical nanophotonic cavities can achieve $\bar{V} \sim 1$, although some exotic designs can achieve significantly smaller mode volumes[125, 126]. The field of plasmonics also promises strong matter-photon interactions in part by the tight confinement of light possible in plasmonic structures[127, 128].

This equation for the cooperativity gives us a seemingly straightforward recipe for achieving strong atom-photon coupling: create a cavity with a high quality factor and a small mode volume. There are two important subtleties worth noting here. First, in suggesting that the Purcell factor was equal to the cooperativity, we have elided a key distinction between the spontaneous emission rate of an ideal two-level system and the total optical decoherence rate of a multi-level atom or quantum emitter. Arriving at the equality in Eqn. 2.3.11 requires expanding the definitions of g and γ in terms of the atomic dipole operator μ. However, μ in g (Eqn. 2.3.1) is only the dipole matrix element that coherently couples to the cavity mode, whereas μ_{total} in γ includes

[7] In general, the effective refractive index n_{eff} is not the same as the bulk index of the material out of which the cavity is fabricated and must be calculated based on a full consideration of the geometry of the cavity around the emitter[124].

the total dipole matrix element for all transitions out of the excited state, including non-radiative transitions or non-cavity coupled radiative transitions. In other words, $\mu_{cavity} \leq \mu_{total}$. Moreover, recall that γ can also include sources of decoherence, such as spectral diffusion, that do not affect the ratio of spontaneous emission rates in the definition of the Purcell factor but do limit the coherent exchange of excitations between the atom and the cavity as expressed by the cooperativity. In other words, $\gamma_{\text{spont.}} \leq \gamma$.

The second subtlety concerns the placement and orientation of the atom. Even in the case of a perfect two-level atom, the atomic transition dipole has a particular orientation that must match the polarization of the cavity mode. This is the physical meaning of the dot product in the definition of g (Eqn. 2.3.1). Moreover, the cavity mode has a particular location in space where the amplitude of the electric field is maximized. If the atom is not placed at precisely this position (which varies on the scale of the optical wavelength), g will be reduced. Both of these effects result in the inequality in the second line of Eqn. 2.3.1.

These subtleties are crucially important for solid-state systems. We will see in the next section that for a modest cavity of $Q/\bar{V} \sim 1200$, we achieve a cooperativity of significantly less than unity due to imperfections in the optical properties of the NV. In particular, the NV has a branching ratio into the ZPL (*i.e.* Debye-Waller factor) of only 3-5% [66], and also has a linewidth broadened by spectral diffusion by a factor of several hundred. Another example of the impact of these imperfections is described in

detail in section C.5.5 for the SiV center.

2.4 Purcell-enhancement of NVs in hybrid nanophotonic devices

There are two general techniques for coupling an NV center to an optical cavity. First, a diamond membrane containing NV centers could be inserted into a macroscopic Fabry-Pérot cavity, or similarly, the diamond itself could be used as one side of a such a cavity. The latter approach in particular has been pursued by a number of groups with the primary goal of achieving moderate enhancement of the rate of generation of indistinguishable photons from NV centers[74, 75, 76, 77, 78]. Second, the NV center could be incorporated into a nanoscale photonic crystal cavity. This approach has been pursued extensively with other solid-state emitters including self-assembled quantum dots[44, 70, 129], and is especially attractive given the high refractive index of diamond and the promise of scalability inherent in a nanoscale solid-state platform. We pursue this approach. The design of photonic crystal cavities is a complex and mature field and will not be discussed here.[8] In this section, we discuss the properties of NV centers incorporated into hybrid nanoscale photonic crystal cavities and present a

[8]The textbook by Joannopoulos is essential reading[130]. Methodologies of one-dimensional photonic crystal cavity design can be found in the thesis of J. Chan[131]. Some relevant details are also given in section C.2.1.

measurement of Purcell enhancement of the NV emission.

Because there is currently no technique for heteroepitaxial growth of high-quality single-crystal diamond thin films, traditional methods of fabricating photonic structures are not easy to adapt to diamond.[9] Moreover, the alignment of the optical cavity relative to the NV is important to achieve the highest possible value for the single-photon Rabi frequency g as noted above. Because NV centers are introduced via ion implantation, we have no control over the spatial position of the NV centers.[10] To circumvent these issues, we use a hybrid approach where we first fabricate diamond waveguides, locate the NV centers in these waveguides and then use a second material to define cavities around the NV centers.

The outline of our fabrication process is as follows (Fig. 2.6): First, we use an angled-etching technique to create free-standing one-dimensional waveguides out of bulk diamond[97] (Fig. C.3). We use a home-built scanning confocal microscope with a motorized sample stage to automatically characterize an entire chip (thousands of devices) at room temperature to locate NVs near the centers of the diamond waveg-

[9]Thin films of diamond can be fabricated by extensive polishing and etching, although this technique has a number of disadvantages[73, 132]. Recently, a technique has been developed to create two-dimensional photonic structures directly from bulk diamond[133].

[10]It is possible to deterministically position NV centers using implantation through a fabricated mask[134, 135] or other small aperture[136]. For ions that can be produced through a liquid-metal ion source, such as silicon and germanium, it is also possible to use a focused-ion beam for implantation[137]. This technique has even been demonstrated with nitrogen ions created using a particle accelerator[96]. This technique will be used in chapters 5 and 6 and enables more sophisticated all-diamond cavities[138, 139]. Most recently, we have adopted a masked-implantation technique[134] because it is relatively simple to perform and troubleshoot.

uides (Fig. 2.6B). We also select NVs that are bright and photostable at room temperature, since these NVs also tend to be photostable at lower temperatures. After a number of candidate NVs are located, we use Poly(methyl methacrylate) (PMMA), a common electron-beam lithography resist, to fabricate a cavity in every waveguide that contains a suitable NV (Fig. 2.6C). These cavities consist of periodic arrays of planar slabs of PMMA that are oriented normal to the axis of the waveguide (Fig. 2.6D-F, see also Fig. 2.7a). The effective refractive index of the waveguide mode is therefore periodically modulated by the change in the refractive index of the surrounding material. By properly designing this periodic modulation, we can engineer photonic crystal cavities with experimentally measured quality factors of $Q \lesssim$ 1-3$\times 10^3$ and simulated mode volumes $\bar{V} \sim 0.5$. These cavities can be made anywhere along the waveguide and are precisely positioned around each NV to maximize the NV-cavity coupling.

To measure the coupling between the NV center and the cavity, the resonance of the NV must spectrally overlap with the cavity resonance. This can be seen in equation 2.3.8, where there is no effect from the cavity onto the NV if the NV cavity detuning δ is much greater than the cavity linewidth κ. In general, variations in fabrication result in cavity detunings $\delta \gg \kappa$. We have two techniques to adjust δ, both of which are described in Ref. [73]. First, we can use an oxygen plasma etcher (Technics, Model 220) to remove PMMA from the cavity. This etching process tunes the cavity resonance to higher energies (lower wavelengths) because after etching, more of

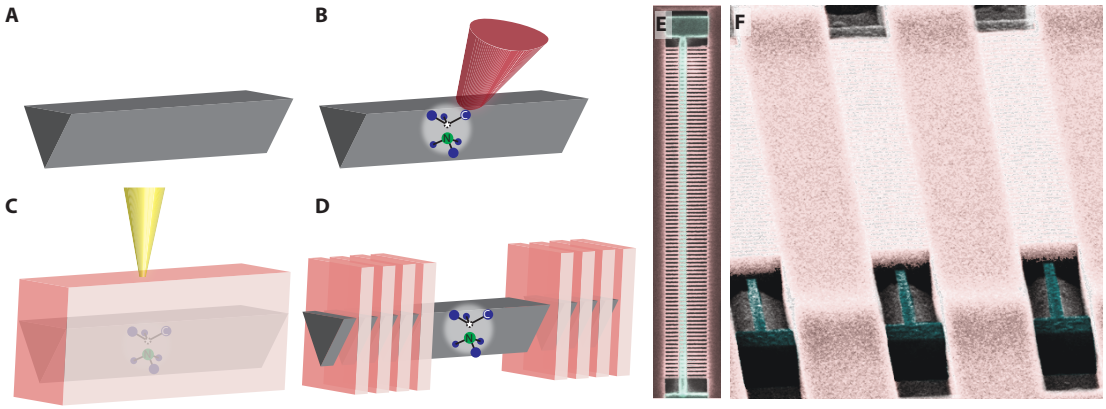

Figure 2.6: Fabrication process for hybrid diamond-PMMA photonic crystal cavities containing NV centers. **A.** We create free-standing diamond waveguides using angled etching [97]. **B.** Confocal microscopy is used to identify NV centers in the waveguides. **C.** PMMA is deposited and electron-beam lithography is used to define cavities. **D.** These cavities are optimally positioned around the NV centers found previously. **E.** False-color scanning electron micrograph (top view) of a diamond waveguide (blue) surrounded by slabs of PMMA (pink). **F.** Micrograph of a set of three devices taken at an angle to the surface. The surface shown underneath the structures in parts E. and F. is also diamond but is not colored blue to provide visual contrast to the waveguides.

the cavity field resides in air (which has a lower refractive index than PMMA). This technique results in permanent tuning of δ by up to around 15 nm without significant reduction in the cavity Q. We can also reversibly tune the cavity resonance *in situ* during our cryogenic experiments by depositing solid neon on the structure [140]. Details on this technique are described in sections C.2.3 and D.1.4. Although we have demonstrated gas tuning ranges of more than 20 nm with no reduction in the cavity quality factor[73], this technique is less effective for these PMMA structures, due to their high aspect ratio which prevents most of the gas from reaching the diamond waveguide where the cavity field is maximized. Hence, we have only achieved tuning ranges of the cavity resonance of at most $\sim$6 nm. The tuning range is even less in typical experiments. However, our tuning range and control is sufficient to achieve $\delta \ll \kappa$ (Fig. 2.7b, c).

We measure the lifetime of the NV center in the cavity by exciting the NV with a pulsed off-resonant laser (NKT photonics SuperK EXTREME, filtered to a narrow band around 532 nm). We record the arrival times of photons in the NV PSB using fast acquisition electronics (PicoQuant PicoHarp 300) and construct a histogram of these arrival times. By fitting a decaying exponential to this data, we determine the lifetime of the NV in the cavity (Fig. 2.7d). First, we measure the lifetime of the NV in the cavity-detuned regime ($\delta \gtrsim 2\kappa$, blue curves in Fig. 2.7c and d). We measure a lifetime of 18.5 ns. By tuning the cavity onto resonance with the NV $\delta < \kappa$, we measure a reduced lifetime of 11.7 ns (yellow curves in Fig. 2.7). For an intermediate

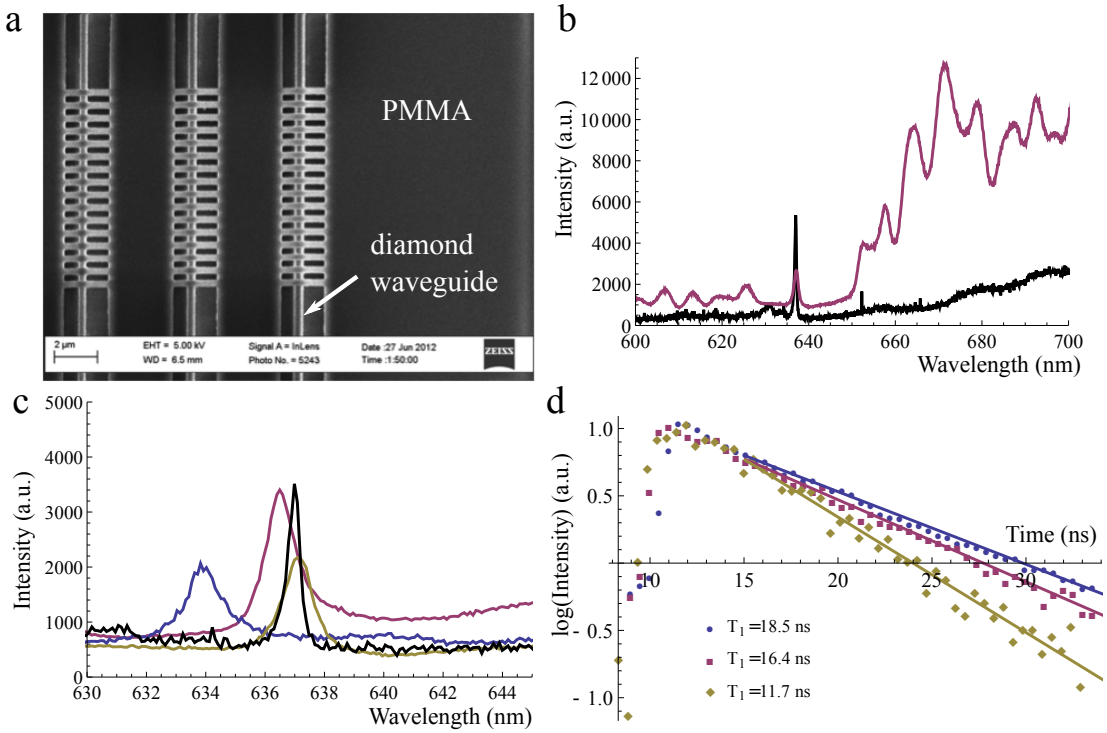

Figure 2.7: Purcell enhancement of the NV center ZPL emission. **a.** Scanning electron micrograph of hybrid diamond-PMMA cavities. Visible are the top surface of the suspended triangular beams, the top of the the PMMA layer and slabs, along with the exposed diamond surface underneath. **b.** Transmission spectrum of the cavity (magenta) and emission spectrum of NV center (black). The vertical axis is arbitrary and different for each of the two curves. **c.** Spectra showing ZPL of NV center (black) and cavity resonance tuned to three different frequencies (blue, magenta, and yellow). Note the reduced scale on the wavelength (horizontal) axis relative to part b. **d.** Measurement of the NV center lifetime at the cavity detunings shown in c. There is a 37% reduction in the lifetime of the NV when the cavity is on resonance (yellow curve) compared to far off-resonance (blue curve).

detuning, we measure an intermediate lifetime (purple curves in Fig. 2.7). The cavity quality factor is approximately $Q \sim 600$ in this device.

This lifetime reduction corresponds to a Purcell factor of $P = 0.59$. Because the Debye-Waller factor is only 3-5% for the NV, this means that the emission into the ZPL is enhanced by a factor of almost 20. The cooperativity in this system is much lower than the Purcell factor due to the spectral diffusion of the NV: The linewidth of the NV in this device is around 3 GHz, giving $\Gamma_n/\gamma \sim 200$.[2] The cooperativity in this system is then $C \sim \frac{P}{200} \sim 3 \times 10^{-3}$.

2.5 Conclusion and outlook

In this chapter, we first introduced a technique to create NV centers in bulk diamond via ion implantation in annealing (section 2.2). This procedure, coupled with improved schemes for reionizing the NV into the NV^- charge state, allowed us to measure optical transition linewidths for the NV that were within an order-of-magnitude of the lifetime limit. After giving a broad overview of cavity QED in section 2.3, we presented a process for incorporating such implanted NV centers into hybrid nanophotonic crystal cavities with modest quality factors $Q \sim 600$ and measured a Purcell enhancement for NV emission in these devices (section 2.4).

There are several sources limiting the cooperativity of the NV-cavity system. Although improving the cavity figure of merit Q/V is almost always desirable, most of

the limitations on the cooperativity arise from the NV center itself. In other words, our measured cooperativity $C \sim 3 \times 10^{-3}$ is much lower than $C = \frac{4g^2}{\kappa\gamma} = \frac{3}{4\pi^2}\frac{Q}{V}\left(\frac{\lambda}{n}\right)^3 \sim 90$ in the ideal case of a perfect emitter coupled optimally to our cavity with measured quality factor $Q \sim 600$ and $\bar{V} \sim 0.5$. The Debye-Waller factor is an intrinsic property of the NV center and offers no obvious route towards improvement. However, the optical coherence properties of the NV vary considerably from sample to sample, and we have some experience improving these properties in bulk with improved sample processing (section 2.2.2).

These considerations suggest two paths forward. First, we can attempt to understand the sources of noise in the solid-state environment that are leading to spectral diffusion of the NV. We have already observed that the linewidths of NV centers in nanofabricated structures are significantly broader than those in bulk diamond, suggesting the the fabrication process causes damage at or close to the diamond surface that plays a role in spectral diffusion. Understanding the properties of the diamond surface and attempting to develop sample processing techniques to mitigate these issues is the most obvious approach, and is presented in the following chapter (chapter 3). Another approach is to work with a system with intrinsically more favorable optical properties, including a higher Debye-Waller factor and intrinsic resistance to the electric field noise that causes spectral diffusion. This approach is first explored in chapter 4 and makes up the remainder of this thesis.

3

Diamond surface characterization for enhanced emitter properties

The goal of this chapter is to develop a detailed understanding of the surface properties of the diamond that are relevant to our technological applications. In particular, we described a technique in section 2.2 to improve the optical properties of implanted NV centers. In a related work, a similar procedure was used to improve the coherence time of near-surface NVs for sensing applications[5]. These procedures work in part by modifying the physical and chemical properties of the diamond surface. However, understanding the precise modifications that the various processing steps make to the surface, and, in turn, how these modifications to the surface lead to superior emitter optical and spin properties, is in general poorly understood.

First, in section 3.1, I will give a brief summary of some of the key properties of the diamond surface and the ways in which they can impact emitter properties. Section 3.2 then gives a review of the diamond surface, focusing in particular on the possible surface reconstructions and their accompanying electronic properties. The next two sections discuss characterization of our samples. We focus in particular on samples that have been treated using one of two techniques: either annealed at high temperature and then "acid cleaned" in the tri-acid mixture described in section 2.2.2 or "surface terminated" by annealing and acid cleaning followed by cleaning in a piranha solution,[1] annealing in an oxygen environment at around 460°C (similar to the procedure presented in section 2.2.2) and then again piranha cleaning. Although we are most interested in the properties of the diamond surface after our complete nanofabrication process, the small sampling volume of our nanostructures makes this extremely difficult. As a first step, we focus on the surface of unstructured bulk diamond.

We answer two questions about the diamond surface after these processing steps: where are the atoms on the surface, and what are their chemical properties (which atoms and in what bonding configuration)? We explore the first question using electron diffraction in section 3.3, where we find that the diamond surface is most likely in an ordered 1×1 reconstruction. The second question is addressed using x-ray pho-

[1] A mixture of around 3:1 concentrated sulfuric acid and 30% hydrogen peroxide that removes organic contamination and acts as a strong oxidizing agent. Because the mixture is a strong oxidizing agent, it will remove most organic matter, and it will also add hydroxyl (OH) groups to many surfaces.

toelectron spectroscopy (XPS) in section 3.4, where we find a mixture of oxygen functional groups that changes as a function of processing technique. These techniques may be unfamiliar to scientists working within the quantum optics or quantum sensing communities; for this reason, each section begins with an introduction to the technique as well as an overview of previous studies in diamond. Some background material about using infrared spectroscopy as a complimentary technique to characterize the diamond surface can be found in section A.3. We conclude with a brief summary of the results and outlook for future work.

3.1 Background and motivation

There are three key properties of the diamond surface that are especially relevant for applications with color centers. The first is the position of the Fermi level near the diamond surface. The Fermi level relative to the color-center charge transition point determines the equilibrium charge-state stability of the color centers, determining for example whether an NV center is in the NV^- or the NV^0 charge state (Fig. 3.1). The properties of the surface have an important local effect on the Fermi level. In general, the surface atoms can have either a higher or lower electron affinity than bulk diamond, leading to band bending as either electrons or holes are drawn to the surface[1]. See, for example, Fig. 3.3, which contrasts the electron affinity for a hydrogen and an oxygen diamond surface termination. One important note is that a bulk Fermi level

in extremely pure diamond (as is the case for our experiments) is not necessarily well-defined: because of the extremely long screening length in diamond, the Fermi "level" depends dramatically on the local environment; the presence of a single nearby defect can be dominant[141]. This same observation can be extended to the presence of the diamond surface, which in essence means that the surface properties are relevant microns into the bulk and play a crucial role in setting the Fermi level throughout our nanostructures.

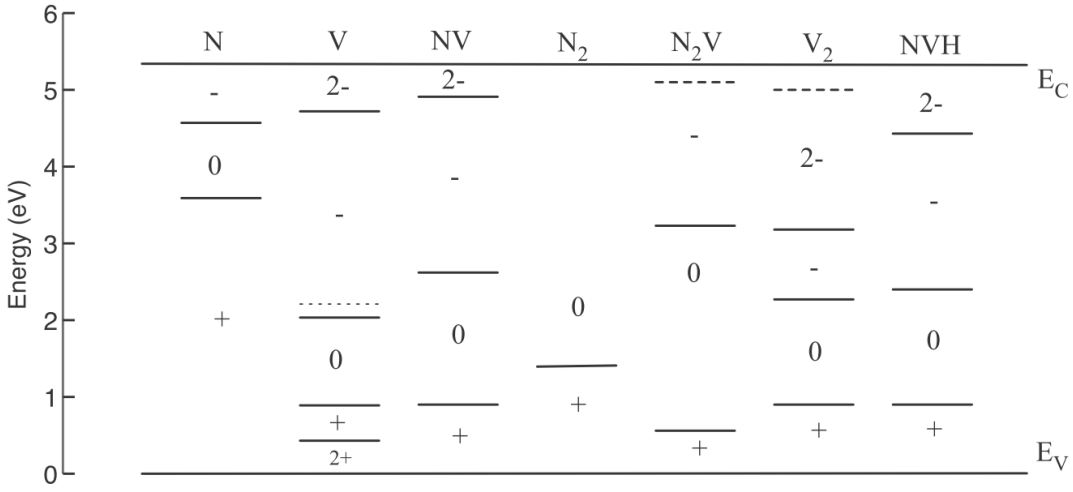

Figure 3.1: Charge transition levels of various point defects in diamond[106]. It is not precisely known where the silicon vacancy lies. One theoretical study from Maze and Gali[142] predicts a very narrow range of stability for the SiV^- that would be surprising given the reasonable stability of this charge state under various experimental conditions, including in undoped diamond where it is predicted to be unstable. Reprinted figure with permission from Ref. [106]. Copyright 2014 by the American Physical Society.

The second key property is the surface-induced density of states, especially within

the diamond bandgap.[2] The presence of midgap states is theorized to play an important role in the photoionization dynamics of color centers. The putative mechanism[92] for photoionization of the NV center, for example, relies on multiphoton processes since there are, by assumption, no available states in the bandgap. The presence of a non-negligible local density of states in the gap around a color center could change these processes to single-photon processes, dramatically changing the ionization dynamics. Although local bulk-like defects can also produce mid-gap states, we have observed a clear difference in the ionization dynamics of both NV and SiV centers in bulk compared to in fabricated nanostructures where the primary difference is the presence of more and different surfaces. This observation suggests that the presence of midgap states introduced by the surface is worth exploring.

Finally, the coherence time of the spin degree of freedom of color centers can be reduced by the presence of magnetic field noise at the surface. Previous work has in fact used near-surface NV centers in a scanning configuration to sense the presence of optically-inactive ("dark") near-surface spins that were found to have a density of about one unpaired electron spin for every 60 surface atoms[143]. The dynamics of these dark spins has been probed in two more-recent complementary efforts using the NV spin population (T_1) and coherence (T_2) decay times for near-surface NV centers[144, 145]. Despite these and other efforts, the nature of these surface dark spins

[2] A significant change in the density of states either above or below the bandgap mainly influences the Fermi level.

remains unclear. Because in many cases these spins limit the coherence times of near-surface NV centers[145, 5], identifying and finding mechanisms to eliminate them is important for sensing and other applications[5].

Fortunately, there has been considerable theoretical interest in the electronic, and, to a lesser extent, spin, structure of various surface terminations in diamond, some of which will be reviewed in the next section. These terminations are defined by particular spatial and chemical arrangements of atoms on the surface. In sections 3.3 and 3.4, we probe these arrangements and use this information to support or rule out various options for the diamond surface termination in our experiments.

3.2 Properties of the diamond surface

Three different inequivalent diamond surfaces are possible: the (100), the (111), and the (110) surfaces.[3] Of these, the (100) and (111) surfaces are the most technologically important. These are the slowest growing surfaces in CVD and therefore the ones that remain after synthesis[146, 147]. However, the ⟨110⟩ planes are the "easy" directions for cleavage, so many of the edges of our samples are these surfaces; see section 3.3.3 below. In general, previous studies have focused on the reconstruction of

[3]Here, we use the following conventions, although the distinctions are not so important for the diamond lattice:
(hkl) is a direction in reciprocal space,
{hkl} is all equivalent directions in reciprocal space,
[hkl] is a direction in real (direct) space and
⟨hkl⟩ is all equivalent directions in real space

(111)[148, 149, 150, 151, 152] and (100)[153, 147] surfaces. Although the (100) surface is perhaps more relevant to our samples, there has been a larger focus in the literature on understanding (111) surfaces, so I will focus on these first. Very few studies have focused on the C(110) surface; at least some of those studies observe no reconstruction[154].

Before focusing on the (111) and (100) surfaces in turn, there are a few general studies that discuss several surface orientations. These are particularly helpful in translating results from various surface characterization techniques from one surface to another. Frauenheim has studied both (111) and (100) surfaces with STM[155]. Baumann and Nemanich examine the effect of hydrogen plasma and annealing on the electronic properties of all three possible surface orientations using UPS[156].[4] Finally, we note that reconstructions for diamond are somewhat similar to reconstructions for silicon and (to a lesser extent) germanium, which at moderate temperatures have a monohydride (2×1) termination and at higher temperatures a hydrogen-free (2×1) reconstruction[5] as well as contributions from other higher-order reconstructions.[6]

[4]Ultraviolet Photoelectron Spectroscopy, a technique to measure the energy of valence-level molecular orbitals by measuring the kinetic energy of photoelectrons emitted upon absorption of a UV photon with a wavelength typically less than 100 nm. Because it measures the properties of the molecular orbitals rather than the elemental chemical composition of the analyte, it is in some ways a complimentary technique to XPS.

[5]It is unclear if Germanium has a (1×1) phase. Also, the hydrogen-free(2×1) reconstruction is thought not to involve π-bonding, which is normally weak for silicon.

[6]These higher-order reconstructions are not observed for C(100) diamond, though there is one report[157] of a (4×1) reconstruction.

The (111) orientation, if truncated, has one dangling bond[7] per surface carbon atom[153]. Above around 700 K, these surfaces develop sharp (1×1) LEED[8] patterns that correspond to the dangling bonds terminated by hydrogen atoms[159, 152, 154]. Thermodynamic arguments suggest that these highly hydrogenated states are the most stable, but can proceed through (2×1) and $(\sqrt{3} \times \sqrt{3})$ states at lower hydrogen coverage[151]. Heating above 1275 K desorbs hydrogen and produces a hydrogen-free π-bonded (2×1) zig-zag surface chain reconstruction with both empty and occupied surface states in the bulk band gap[159, 153]. This hydrogen-free state is believe theoretically to be stable up to about 2500 K[148]. These observed reconstructions, as well as those for C(100) surfaces, are sometimes reproducibly not present in apparently identically prepared samples[154, 153]; Lurie and Wilson believe that atomically smooth surfaces are more difficult to reconstruct and that this explains the sample-to-sample variation also seen by Lander and Morrison[160].

The electronic properties of these hydrogen-based (111) reconstructions is a subject of debate. Some work suggests that the (1×1) reconstruction produces no states in the band gap[153], whereas other authors claim that this reconstruction should produce a large density of surface states that are half-filled and lie within the band-

[7] If cut along the bonds itself, there are three dangling bonds. However, the stable state under hydrogen exposure is identical to the picture with a single dangling bond[157, 151].

[8] Low-energy electron diffraction, a technique similar to RHEED. See section 3.3 below. Vickerman[158] also has a brief introduction.

gap[148].[9] Himpsel *et al.* used ARPES[10] to study diamonds that were cleaved in a hydrogen atmosphere and then heated to 900°C to remove the adsorbed hydrogen and induce the surface reconstruction [161]. They find that the reconstructed surface has $(2 \times 1)/(2 \times 2)$ symmetry with energy levels lying just below the valence band. These surface states have only weak overlap with the bulk. Other work using ARPES examines the Fermi level of hydrogen plasma terminated (111) diamond and claims that the Fermi energy is 0.7 eV deep in the valence band[162]; if there are surface states, then, they should be unfilled.

Unlike the (111) surface, the truncated (100) orientation leaves two dangling bonds per surface carbon atom[153]. Under vacuum, the two dangling bonds can significantly lower their energy to form a carbon-carbon double bond, giving a symmetric (2×1) reconstruction[157]. These double bonds introduce occupied π and unoccupied π^* states within the bulk bandgap[146, 163]. Under most circumstances, however, these dangling bonds are at least partially satisfied by hydrogen.[11] In analogy to their earlier work[152], Hamza[153] reports a transition from C(100)-(1×1) to a C(100)-(2×1) reconstructed surface beginning at around 1030°C and characterized by LEED. This (2×1) : H termination is generally agreed to be the most stable

[9] See also the first five references in reference [161].

[10] Angle Resolved Photoelectron Spectroscopy, also covered in Ref. [158].

[11] This hydrogen termination has been achieved in an H_2 plasma by flowing 400 sccm of H_2 in a CVD reactor at 60 Torr with a 700 W plasma for three minutes[164]. High-temperature hydrogen plasmas can introduce hydrogen diffusion into the bulk up to many tens of microns. This bulk hydrogen can passivate NV and create NVH centers[165].

termination under a variety of circumstances[146]. The authors also use UPS to find that the C(100)-(1 × 1) surface has no occupied states between the top of the valence band and the Fermi level, wheras the C(100)-(2 × 1) surface does. The authors also note that hydrogen remains on the surface up to 1260 K and present convincing evidence that as-polished surfaces can have a large amount of hydrogen *ab*sorbed into the diamond lattice itself. This deep hydrogen diffusion has also been seen after exposure to a hydrogen plasma[165]. The authors posit that the (2 × 1) surface is made up of symmetric dimers with monohydride termination at each hydrogen atom of the dimer pair (Figs. 3.2 and 3.9). Later work by Nimmrich *et al.*[166] was able to visualize the surface reconstruction directly using AFM. The (1 × 1) reconstruction can be restored after exposure to hydrogen according to Lander and Morrison[160]. Lurie and Wilson claim that this is only true for more disordered surfaces: smooth surfaces are harder to reconstruct and also have a higher barrier for hydrogen desorption[154]. Fürthmuller also has a more modern discussion of higher hydrogen exposure (several monolayers) resulting in a 1 × 1 reconstructed surface[167]. Although a variety of exotic hydrogen terminations have been proposed, few have been realized experimentally[157].

These results for the (100) surface agree for the most part with theory. Early theoretical work by Fürthmuller also identifies the 2 × 1 clean and monohydride surfaces as the most stable under different circumstances[168] but claims that the 2 × 1 : H state has no states in the bulk bandgap. This observation contrasts with (even earlier)

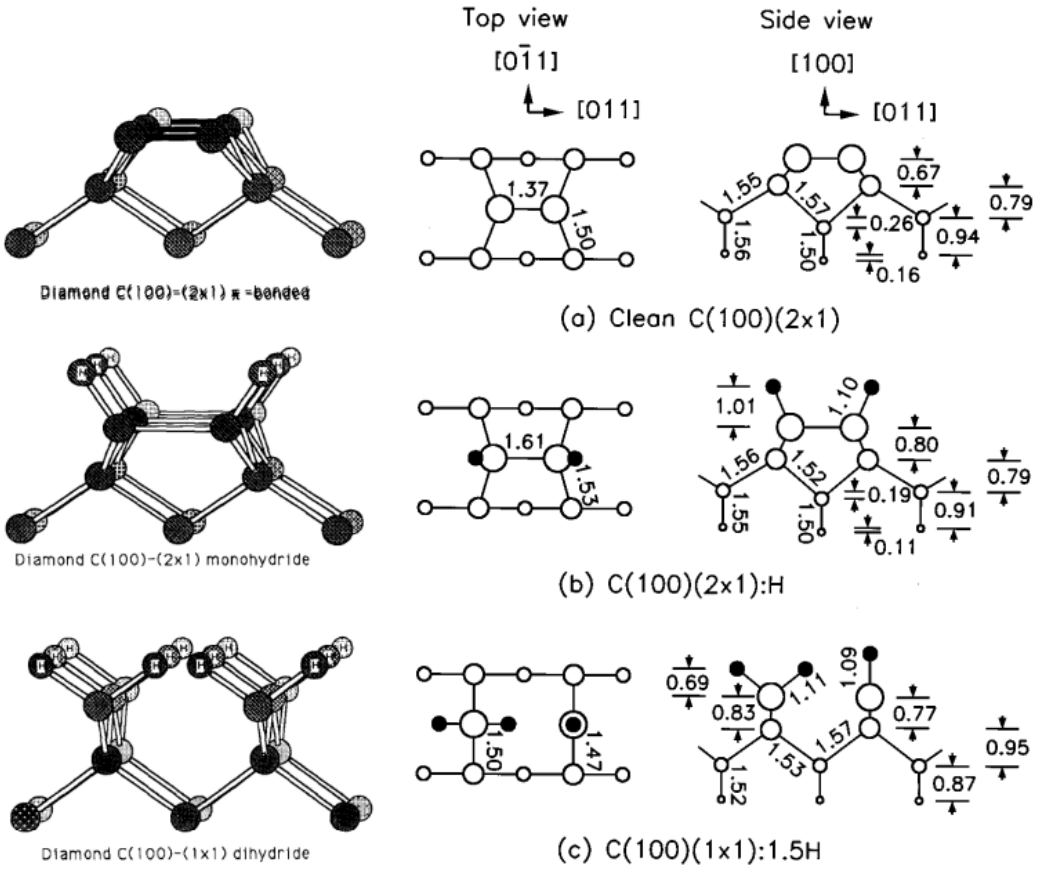

Figure 3.2: Schematic of three different hydrogen surface terminations for the diamond C(100) surface. The first two rows show 3D and 2D drawings of the clean (2×1) and (2×1) : H surfaces. The bottom row shows a (1×1) dihydride reconstruction (3D) and a (2×1) : 1.5H reconstruction (2D). The most saturated surface is favored below around 900-1000°C. Above that temperature, hydrogen begins to desorb from the surface (and bulk), producing the (2×1) : H surface. At even higher temperatures, the clean, π-bonded 2×1 surface emerges. See also Fig. 3.9. To the best of my knowledge, the 2×1 : 1.5H surface has only been proposed in Ref. [168]. The left (3D) figures are reprinted from Ref. [153] with permission from Elsevier. The right (2D) figures are reprinted with permission from Ref. [168], copyright 1996 by the American Physical Society.

experimental work[153] which suggests that the π-bonded (2×1) reconstructed surface has no electronic surface states within the bulk bandgap, while the (2×1) : H surface does.[12]

The contemporary position is summed up in two excellent review articles by Ristein[169, 163]. The first summarizes the structural and electronic properties of diamond surfaces especially as they relate to electron emission. Ristein also notes that graphitic carbon on the surface pins the Fermi level to 1.4 eV above the VBM[169]. In his later work[163], Ristein updates these results and includes some discussion of oxygen terminated surfaces.[13] See Table 3.1 for a summary of reconstructions and related electronic states of various diamond surfaces. In particular, Ristein cites later work by Kern[150, 151] as definitive. These results are consistent with simulations from the Gali group[170].

In addition to the hydrogen terminations described above, there has been some more recent work on various oxygen terminations. An oxygen surface termination can be created through thermal methods[171] similar to those discussed in Section 2.2.2. More exotic methods involve oxygenation with UV light[172, 173] or by thermally-excited oxygen molecules at standard[174] and elevated[175] temperatures. A general overview of the properties of oxygen-terminated diamond surfaces is given in

[12]Fürthmuller suggests that this confusion is from misidentification of the valence band maximum (VBM) in Ref. [153]. See also references 31, 32, and 63 in Ref. [168].

[13]The two reviews are similar: the later review is more complete, but the first has a focus on electron emission that is useful for understanding electron affinity and band bending from different surface terminations.

Table 3.1: Summary of reconstructions and electronic states of clean, hydrogen-, and oxygen-terminated diamond surfaces. Energies are referenced to the valence band maximum (VBM). Here, the monohydride surfaces are labeled $2 \times 1 : 2H$ instead of $2 \times 1 : H$ because with the 2×1 reconstruction, there are two carbon atoms per unit cell, and hence two hydrogen atoms as well. Table reprinted with permission from Springer, from Ref. [163], copyright 2006.

Surface	(100)	(111)	(110)	
Reconstruction	2×1	2×1	1×1	Clean surfaces
occupied s.s. from experiment	-1.9 to -0.2 eV[a]	-1.3 to 0.4 eV[a]	-0.6 to 0 eV[d]	
from theory	-2.0 to 0 eV[b]	-1.0 to $+1.0$ eV[c]	-1.0 to $+1.0$ eV[e]	
unoccupied s.s. from theory	$+1.3$ to $+2.4$ eV[b]	$+1.0$ to $+4.8$ eV[c]	$+1.0$ to $+4.0$ eV[e]	
Reconstruction	2×1:2H	1×1:H	1×1:2H	Hydrogen-terminated surfaces
occupied s.s. from experiment	None	None	None	
from theory	< -2 eV[b]	< -4 eV[c]	< -2.5 eV[e]	
unoccupied s.s. from theory	$+3.3$ to $+6.0$ eV[b]	$+3.6$ to $+6.0$ eV[c]	$+2$ eV to $+7$ eV[e]	
Reconstruction	1×1:O	2×1:O	–	Oxygen-terminated surfaces
occupied s.s. from experiment	≈ -2 eV[f]	≈ -8.4 eV; ≈ -4.2 eV[g]	–	
from theory	≈ -2 eV[f]	–	–	
unoccupied s.s. from theory	None[f]	–	–	

[a] R. Graupner, M. Hollering, A. Ziegler, J. Ristein, L. Ley, A. Stampfl, Phys. Rev. B **55**, 10841 (1997)
[b] G. Kern, J. Hafner, J. Furthmüller, G. Kresse, Surf. Sci. **352–354**, 745 (1996)
[c] G. Kern, J. Hafner, G. Kresse, Surf. Sci. **366**, 445 (1996); unfortunately Figs. 5 and 7 are erroneously exchanged in this publication
[d] F. Maier, R. Graupner, M. Hollering, L. Hammer, J. Ristein, L. Ley, Surf. Sci. **443**, 177 (1999)
[e] G. Kern, J. Hafner, Phys. Rev. B **56**, 4203 (1997)
[f] J.C. Zheng, X.N. Xie, A.T.S. Wee, K.P. Loh, Diamond Relat. Mater. **10**, 500 (2001)
[g] K.P. Loh, X.N. Xie, S.W. Yang, J.S. Pan, P. Wu, Diamond Relat. Mater. **11**, 1379 (2002)

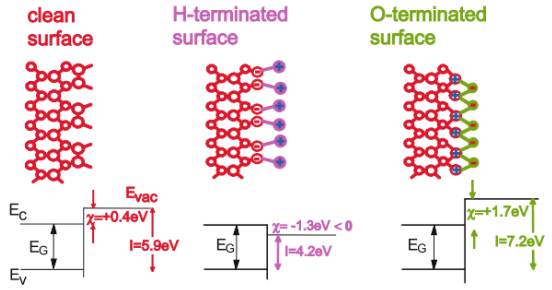

Figure 3.3: Schematic of electron affinities for different surface terminations displaying also the ionization energies. Figure reprinted with permission from Springer, from Ref. [163], copyright 2006.

Ref. [163].

Two additional theoretical studies are particularly worth noting[146, 170]. Sque[146] studies many different termination options, including hydrogen, oxygen, and mixed terminations. The authors determine the eletronic states present from the various surface terminations (Figs. 3.4 and 3.6). The authors also calculate the electron affinities of the surface and conclude that all of the hydrogen terminations produce band bending (assuming that nitrogen is the majority dopant); the oxygen terminations do not, or produce very little. This work also studies a mixture of hydrogen and oxygen terminations that have the lowest density of states in the bulk bandgap (Fig. 3.5). A later study from the Gali group studies a similar combination of terminations[170]. This work also proposes a very similar 2×2 : H/O/OH reconstruction (Fig. 3.7) that has no states in the band gap and the proper electron affinity to support stable NV centers near the surface. To the best of my knowledge, this particular oxygen termination has never been observed experimentally. In general, the various proposed oxygen surface terminations have significantly more desirable electronic properties than those arising from the various hydrogen terminations. This is one of the key motivations for our oxygen surface termination process.

Finally, Sque *et al.* study the relative stability of carboxyl versus ether carbon-oxygen bonds at the surface and conclude that the carboxyl state is unstable and has practically no barrier to formation of ether bonds.[14] These ether bonds give some

[14]However, see the section on XPS below where there are many reports of carboxyl groups

states in the bandgap. The authors also study a (2×1) OH termination in both an aligned ("para") and anti-aligned ("anti") configuration. The "anti" configuration is slightly more stable because the distance between hydrogen atoms is greater. In practice, a mixture of configurations with various amounts of hydrogen bonding would likely be observed. The authors also note that the -OH (hydroxy) terminated surface is more thermodynamically stable than the ether surface plus isolated hydrogen molecules, but they do not study the reaction barrier.

So far, we have focused only on hydrogen and oxygen terminations of the diamond surface since these are the most common and also the most technologically relevant. Given the rich chemical reactivity of carbon, however, there are many other possibilities. One such possibility is a fluorine terminated surface. Work by Cui reports a fluorinated layer (on a (100) sample) after low-energy CF_4 plasma exposure[164]. This layer is relatively thick (a few nanometers), so it is not clear whether the diamond itself is becoming heavily fluorinated or if the plasma is depositing fluorinated hydrocarbons onto the diamond surface. Regardless, this treatment appears to increase the average concentration of NV^- relative to NV^0 at least as well as an oxygen termination studied in the same work, and appears to be more photostable in air over the timescale of weeks. Theoretical work from the Gali group suggests that the fluorine terminated (100) surface produces thermodynamically stable NVs, but some localized states just below the conduction band minimum[170]. Similar work on nanometer-

on the diamond surface.

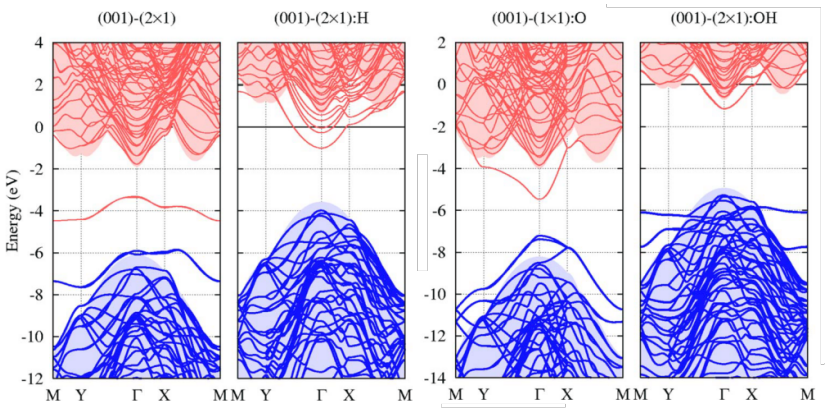

Figure 3.4: Electronic states of different surface terminations. The oxygen configuration is the stable ether bonding. The hydroxy (OH) termination is in the "anti" configuration, but the "para" configuration is smilar. Energies are referenced to the vacuum potential. Reprinted figure with permission from Ref. [146]. Copyright 2006 by the American Physical Society.

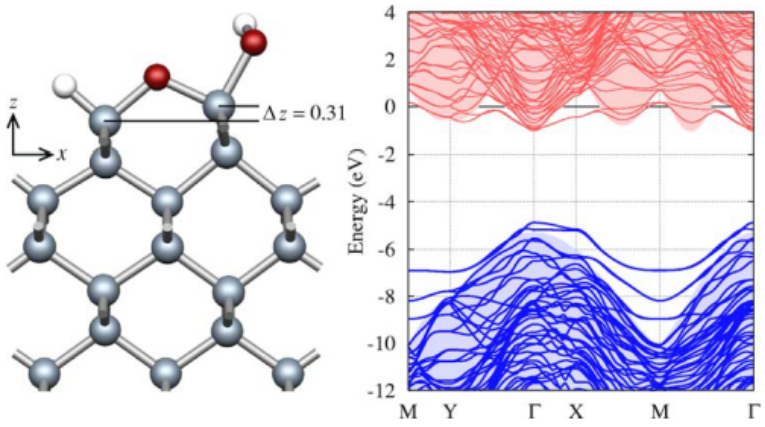

Figure 3.5: Molecular structure and electronic states of a particular "HOOH" surface termination with no mid-gap states. Energies are referenced to the vacuum potential. Reprinted figure with permission from Ref. [146]. Copyright 2006 by the American Physical Society.

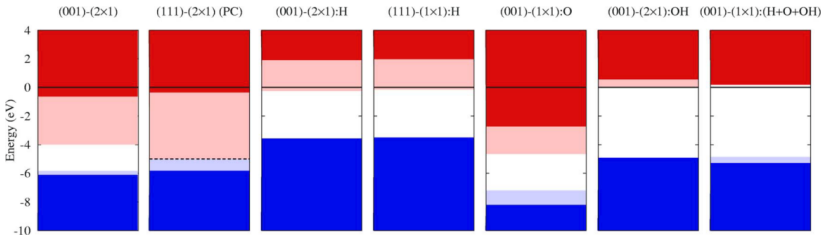

Figure 3.6: Simplified diagram of electronic states of different surface terminations. The oxygen configuration is the stable ether bonding. The OH termination is in the "anti" configuration, but the "para" configuration is similar. Energies are referenced to the vacuum potential. Reprinted figure with permission from Ref. [146]. Copyright 2006 by the American Physical Society.

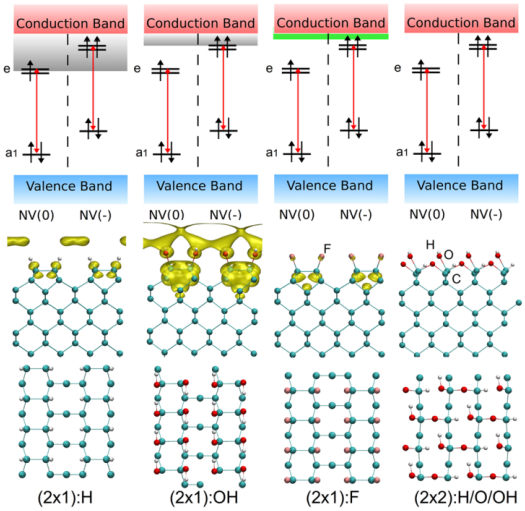

Figure 3.7: Diagram of location of delocalized image states (gray) and localized acceptor states (green) for four different surface terminations. The positions of the NV^0 and NV^- states are superimposed to emphasize the relative stability of these defects under different surface terminations. Figure reprinted with permission from Ref. [170], copyright 2014 American Chemical Society. See Fig. S2 in the supporting information of this reference for detailed plots of the surface states arising from these terminations.

scale diamondoids also discusses fluorine terminations, but with few applications to NVs[176].

Finally, there has been some work on more exotic surface terminations. Lurie and Wilson[154] also study the deposition of various metals on different surface orientations. Aluminum will form epitaxial aluminum carbide on C(111) surfaces but not on C(100) surfaces. Nickel is also studied; the results are more subtle. Lander and Morrison[160] report in a (very early) LEED study that there is no ordering on the C(111) surface after exposing it to iodine, bromine, oxygen, water, magnesium, copper, indium or lead in vacuum at medium to high temperatures.

Given this background on the possibilities for the diamond surface termination, we discuss characterizing the properties of the diamond surface using two complimentary techniques. First, we will use Reflection High-Energy Electron Diffraction to determine the spatial ordering of the diamond surface. This technique will provide information about the periodicity of the surface reconstruction, telling us if our surface has an ordered $m \times n$ reconstruction and, if so, the values of m and n. This information is crucial to determine or rule out various theoretical proposals for our surface termination. Second, we will use X-ray photoelectron spectroscopy to determine which elements are at the diamond surface and in what concentration. This will allow us to straightforwardly determine whether we have a hydrogen or oxygen termination, for example, by examining the concentration of oxygen atoms at the surface. More careful analysis will allow us to extract some information about the functional groups

present at the surface, again helping us to discriminate between the different surface terminations proposed above.

3.3 Characterization of surface ordering with Reflection High-Energy Electron Diffraction

3.3.1 Details of the technique

Reflection High-Energy Electron Diffraction (RHEED) is a technique where electrons are elastically scattered off of a surface to determine its periodicity.[15] The electrons' wavelength must be short relative to the scale of the features on the surface; typically electrons on the order of 10 keV ($\lambda = 0.12\,\text{Å}$) are used to probe the surface on the atomic scale. RHEED then gives a Fourier-space image of the surface that can be used to determine the degree of crystallinity, the orientation of the surface and the surface reconstruction (by comparing the observed periodicity with the periodicity of the underlying lattice). Like many diffraction techniques, it is fairly easy to perform,

[15] Ichimiya and Cohen have written a self-contained and thorough textbook on RHEED[177]. Page 39 presents a particularly useful example of calculating RHEED patterns, and Chapter 7 has a good overview of Kikuchi lines. Braun also has a concise textbook with applications to MBE[178]. Chapters 2 and 4 give an introduction to RHEED and kinematical scattering analysis. Chapter 5 focuses on the interpretation of Kikuchi lines. Li *et al.* also have a review with some illustrative figures[179].

though complete understanding the data it produces can be difficult.

The instrumentation required for RHEED is relatively simple. Electrons are produced by thermionic emission and are focused onto the sample. The sample can be rotated in the azimuthal plane (the plane of the sample) to select different crystallographic orientations relative to the incoming electron beam. The electrons are detected via a phosphor screen which is imaged with a camera. The signal is generally quite large: it is easy to produce a large flux of electrons, and electrons have a large scattering cross section. More sophisticated RHEED systems sometimes have the ability to filter the incoming or detected electrons by their energy.

RHEED is performed at a glancing angle (typically less than 10°) to minimize noise from inelastically scattered electrons. Using a glancing angle also means that the component of the wavevector in the out-of-plane direction is very small, so the electrons lack the momentum to penetrate deep into the crystal. As a result, RHEED only measures the top few atomic layers.[16] Because only the surface is sampled, the diffraction pattern is mainly produced by the lattice of the surface rather than the full lattice of the bulk.

[16]This extreme surface selectivity is one of the primary reasons it is most commonly used in Molecular Beam Epitaxy (MBE), where deposition is monitored monolayer-by-monolayer.

3.3.2 Understanding RHEED patterns

Diffraction patterns produced by RHEED, like diffraction patterns from many other techniques, are best understood through the Ewald Sphere formalism. The Ewald Sphere is a geometric construction expressing two facts about the diffracted electrons: total momentum is conserved, and momentum transfer can occur only with wavevectors of the reciprocal lattice. To construct an Ewald sphere, draw the reciprocal lattice and put the tip of the incoming wavevector at the origin of the reciprocal lattice. Then, draw a sphere around the origin of the incoming wavevector with radius given by the magnitude of that wavevector. Diffraction will occur where the sphere intersects the reciprocal lattice. The sphere (technically a shell) enforces the energy conservation condition, since all points on the sphere that intersect points on the reciprocal lattice are separated from the origin of the lattice by a reciprocal lattice vector.[17]

The standard Ewald Sphere construction works well for diffraction from a three-dimensional lattice. In RHEED, however, only the surface is sampled because the out-of-plane wavevector is very small. Because the momentum in the out-of-plane direction is low, there is little penetration. As a result, the three-dimensional reciprocal lattice is reduced to a two-dimensional reciprocal net from the surface and is continuous in the third dimension, forming a series of one-dimensional rods. Diffraction oc-

[17]The point at the origin of the reciprocal lattice, for example, corresponds to the trivial reciprocal lattice vector indicating no scattering. In RHEED, this spot corresponds to specular reflection.

curs when these rods intersect the Ewald sphere [180].

Each of these rods intersects the Ewald sphere in exactly two points. One of the points lies below the "shadow" plane of the sample and is not seen on the diffraction image. Hence the intersection of each rod with the Ewald Sphere produces one reflection in the diffraction pattern. Multiple rods corresponding to diffraction by wavevectors of the same magnitude will intersect the Ewald sphere in the same plane, thus defining a circle of points where the rod intersects the sphere. These circles are known as Laue[18] circles. The width of the reciprocal rods increases with disorder, blurring the RHEED image from points into streaks. Because the electron wavelength is very small, the surface only needs to be locally ordered to give a diffraction pattern. In particular, a polycrystalline material with small grain sizes will give a diffraction pattern that is a sum of the intensities of the different patterns from each orientation.

This formalism describes coherent, elastic scattering: energy is conserved and the direction of the incident wavevector plays a crucial role in determining the diffraction pattern. Both of these assumptions can fail. The most important example is a two-step scattering process that produces distinctive "Kikuchi lines" in diffraction patterns[178]. In this process, the incident electrons interact with the surface and scatter diffusely. Typically, this collision is nearly elastic. When these electrons are emitted from the surface, they are emitted over a wide range of angles. These scattered electrons can then undergo diffraction the same way as an incident electron, but because

[18] *Low*-eh, where the first syllable rhymes with "cow" and the second with "bay".

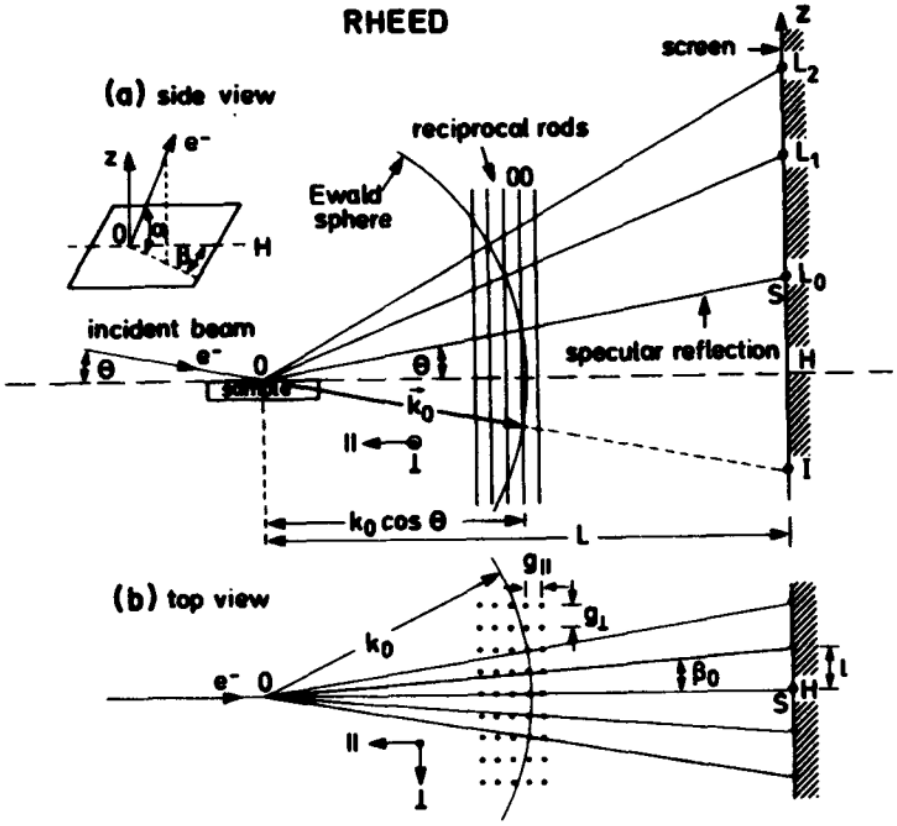

Figure 3.8: A graphical representation of the Ewald Sphere technique used for RHEED. Reprinted figure with permission from Ref. [180]. Copyright 1983 by the American Physical Society.

they have a range of directions, the diffraction condition is poorly represented by the Ewald sphere picture where the initial wavevector is emphasized. The intensity of Kikuchi lines depends strongly on the surface quality because they are broadened by terraces and steps on the surface[177].

For some applications, including the identification of Kikuchi lines, it is important to know how much the electron wave diffracts when it enters the crystal. Typically, an electron penetrating into the bulk is able to lower its energy by a quantity known as the inner potential. This potential plays an effect analogous to the index of refraction in photon optics and can produce bending of Kikuchi lines at low emission angles and even total internal reflection for certain lines.[19] For diamond, the inner potential is estimated to be between 15 eV[181] and 18 eV[182].

The small-angle Kikuchi line pattern in produced for scattering off of a given reciprocal lattice vector can be calculated.[20] Lines in θ and ϕ are given by:

$$h|\boldsymbol{a}_1^*|\phi + l|\boldsymbol{a}_3^*|\left(\theta + \frac{eV}{E}\right)^{1/2} = \frac{G^2}{2K} \tag{3.3.1}$$

Here, h and l are the indices of the surface reciprocal lattice. G^2 is the magnitude of the corresponding reciprocal lattice vector. $\boldsymbol{a}_1^*$ and $\boldsymbol{a}_3^*$ are the primitive reciprocal lattice vectors in the direction of the beam and in the out-of-plane direction.[21] E is

[19] See chapter 7 and especially equation 7.4 of Ichimiya[177].

[20] See example 7.1.1 in [177].

[21] See section 5.3 of Ichimiya. The authors sometimes also define lattice matrices $\boldsymbol{B}$ and

the energy of the incoming electron and eV is the energy of an electron in the inner potential. Free software is available to calculate the expected Kikuchi lines from a given crystal surface[183].

The above equation often predicts many more Kikuchi lines than are typically seen in a sample. This formalism can be extended to incorporate surface wave resonant conditions that describe which lines are favored by resonance as well as the widths of these lines. Also, both constructive and destructive interference are possible: distinctive "dark" bands (sometimes called "defect" lines) are also Kikuchi lines.

3.3.3 Applying RHEED to diamond

The bulk diamond structure is a face-centered cubic (FCC) with a two-atom basis (two interpenetrating FCC lattices) with lattice constant $a = 3.56\,\text{Å}$. The (100) surface is therefore a square lattice with periodicity $a/\sqrt{2} = 2.52\,\text{Å}$ that is rotated 45° relative to the underlying diamond lattice—in other words, the surface lattice is in the [110] direction of the underlying diamond lattice with half the periodicity of the bulk lattice [110] direction. See Fig. 3.9. The "easy" diamond cleavage planes are along the $\langle 110 \rangle$ directions, so the edges of our samples are in the [110] and $[1\bar{1}0]$ directions. Hence, the [100] direction of the diamond is oriented 45° from from the edges of the sample. However, because the surface lattice is also rotated by 45°, the square sur-

---

$\boldsymbol{A}$ where the lattice vectors $\boldsymbol{a}$ make up the rows of $\boldsymbol{A}$ and the lattice vectors $\boldsymbol{a}^*$ make up the rows of $\boldsymbol{B}$; then the relationship between the direct and reciprocal lattice is given by $\boldsymbol{A} \cdot \boldsymbol{B} = 2\pi\mathbf{1}$.

face lattice is aligned with the axes of the sample. If we are probing the pattern of the surface directly, we expect to see the $a/\sqrt{2} = 2.52\,\text{Å}$ periodicity depending on the surface reconstruction. Contributions from the bulk are modulated by the bulk structure factor[22] which describes which reciprocal lattice vectors produce constructive or destructive interference. In fact, most lattice vectors are forbidden and only a few points from the bulk can be seen in RHEED patterns of diamond[185].

3.3.4 Previous work on diamond surfaces with RHEED

There have been relatively few systematic studies of the diamond surface using electron diffraction. Nishitani-Gamo and coworkers have several studies using RHEED to probe the hydrogen-terminated diamond surface. These studies generally find a C(100)-$2\times1/1\times2$: H surface[185, 186].[23] Complimentary work has focused on oxygen-terminated surfaces where RHEED is used in conjunction with UPS[187] and suggests a 1×1 reconstruction. The diamond surface has also been studied with LEED[154], where C(100)-1×1 and C(100)-2×1 reconstructed surfaces have been found for hydrogen-terminated diamonds[153]. The surface lattice dimensions observed experimentally can be used to test theoretical predictions[168]. Because silicon (and germanium) have the same bulk crystal structure and have been studied more extensively

[22] Wikipedia has an excellent article on this topic which treats the diamond lattice specifically[184].

[23] The last study[186] also characterizes their surface with AFM. Later work by other authors[166] was able to visualize the surface reconstruction directly using AFM.

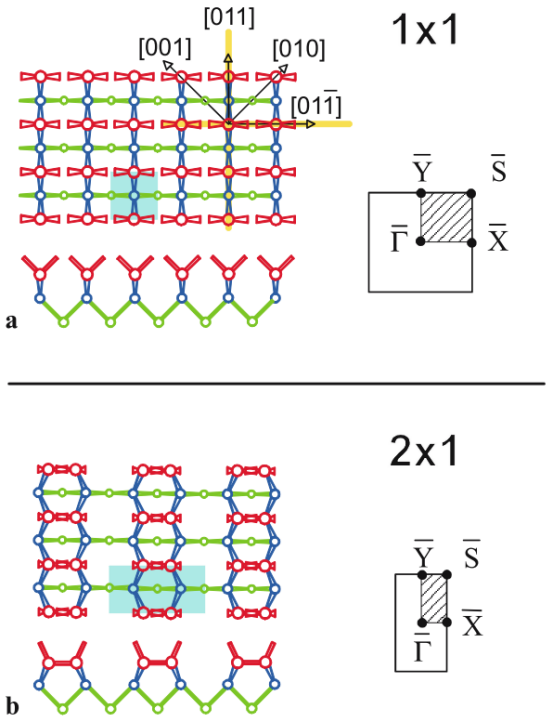

Figure 3.9: Two reconstructions of diamond surfaces in top and side view: 1 × 1 (a) and 2 × 1 (b). The crystallographic orientations are indicated; note again that the direction of shortest periodicity is rotated 45° relative to the bulk. Different layers of atoms are shown in different colors. The distinction between different layers will become important in section 3.3.5. Figure reprinted with permission from Springer, from Ref. [163], copyright 2006.

given their technological importance, studies of these surfaces can also be a useful guide to interpreting RHEED results with diamond.

3.3.5 Our results

Our goal is to determine the structure of the diamond surface after the two surface processing options described at the beginning of this chapter: high-temperature annealing followed by acid cleaning, or that procedure followed by an additional low-temperature anneal in an oxygen environment at around 460°C preceded and followed by a piranha clean. For convenience, we denote these two processes "acid cleaning" and "surface termination". We analyzed four samples: 10098, 10100, 10101, and 10102. Samples 10098 and 10100 were acid cleaned. Samples 10101 and 10102 were given the complete surface termination. No additional cleaning or baking was done before the start of these experiments.

First, calibration was performed to accurately determine the distances observed in the RHEED pattern (section A.1). Two different known compounds were examined at two orientations each. All four calibrations agreed to within 2%. We then measured the samples both as a function of temperature to see if the surface reconstruction would change at higher temperatures, and as a function of angle (at low temperatures), to more completely understand the structure of the surface.

3.3.5.1 RHEED at different temperatures

For the first experiment, we analyzed both 10101 and 10102 at variable temperatures and a fixed substrate angle. We began with the samples at low temperatures of around 130°C and monitored the signal continuously as the samples were heated to around 860°C.[24] The error on these temperature measurements is on the order of 10°C.

There was no observable change in the RHEED pattern for any sample as the temperature increased. Once the maximum temperature was reached, we realigned the electron gun to correct for thermal drift during the heating process and monitored the sample for an additional 10 minutes. We then cooled down the sample. We did not record the RHEED patterns during this cooling step. The low and high temperature limits for each sample are noted in Fig. 3.10 below.

Because there was no observable change in either sample during the heating process, we conclude that there was no dramatic change in the surface reconstruction as a function of temperature. We would also expect to observe any change in the surface from the desorption of gas or adventitious carbon, even if the symmetry of the first *ordered* layer remained unchanged. (Recall that RHEED samples the top one to (at most) two or three monolayers of the surface [178, 177].) Removing a significant fraction of disordered material from the surface would therefore drastically increase

[24]Sample 10102 was also examined at temperatures at or less than than 56°C, where it again looked the same as at all of the other temperatures.

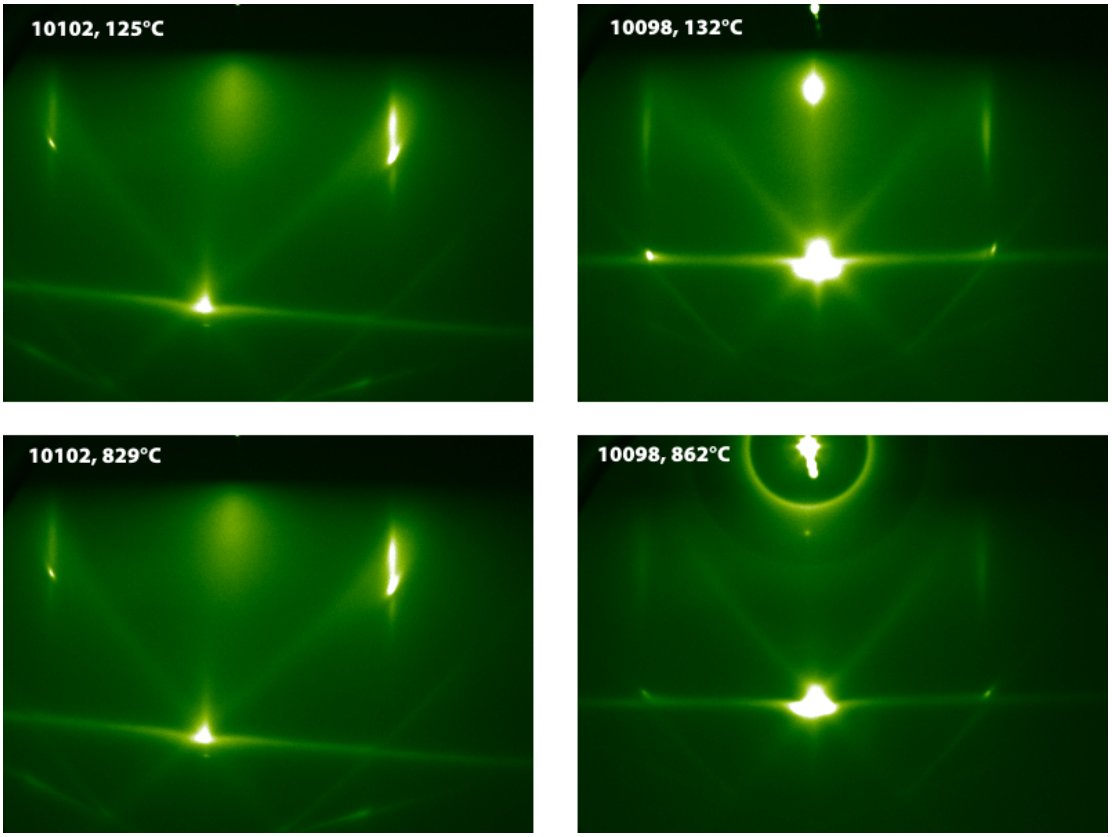

Figure 3.10: RHEED patterns from samples 10098 (acid cleaned) or 10102 (terminated) as a function of temperature. There is no significant change in the pattern for either sample as the temperature is increased over a 700°C range. The two patterns, both taken in the [100] direction, have an identical set of Kikuchi lines. The first allowed out-of-plane scattering occurs at (004). The diffraction spots above the specular spot, corresponding to scattering by (022) and $(0\bar{2}2)$, are more pronounced in 10102. The diffraction spots at the same vertical position as the specular spot, corresponding to scattering by (024) and $(0\bar{2}4)$, are more pronounced for 10098. These peaks give a separation of 1.79 Å which is $a/2$. These assignments agree with those given in Ref. [185]. In this and following figures, the top of the image corresponds to small glancing angles and the bottom of the image corresponds to large glancing angles. Our convention is upside-down compared to some other authors[185, 186].

the signal from the ordered crystal beneath. Furthermore, some work[188] suggests that any adventitious carbon would desorb at much lower temperatures (200-450°C). The most logical explanation is that the surface was clean before we measured the RHEED patterns. One possibility is that adventitious carbon was present at the surface before beginning our RHEED study, but that in analogy with electron stimulated desorption,[25] inelastic electron scattering at the surface removed any adventitious carbon.[26]

Figure 3.10 gives a direct comparison of sample 10102 (terminated) and sample 10098 (acid cleaned) at both low and high temperatures. The periodicity is consistent with a 1×1 surface ordering. This will be explored in the following section. The presence and persistence of Kikuchi lines also suggests that the surface is very well ordered over a long length scale. No unusual rise in pressure was noted during the heating process. A residual gas analysis (RGA) spectrum did not detect a significant carbon monoxide peak at high temperatures. These observations all suggest that there was no etching or graphitization during the heating process. It is interesting to note that Himpsel *et al.* claim that high intensity electron beams in a hydrogen environment, even at the low energies used by LEED, can graphitize the surface[161].

The pattern of Kikuchi lines for 10102 and 10098 is very similar, as we would ex-

[25]This technique is performed with much lower energy electrons than we are using with RHEED[189].

[26]The issue of adventitious carbon in particular and signal from the surface vs. bulk is explored in greater depth below. See page 75.

pect if the underlying lattices are the same. This confirms that we are looking at the same orientation for both samples. However, the pattern and visibility of the diffraction spots in these two samples is somewhat different: 10102 has clear spots above the specular spot, and 10098 has clearer spots in the same vertical position as the specular spot. Both of these peaks correspond to scattering from the bulk, so the difference here is probably primarily due to alignment. These sets of spots have the same horizontal positions and thus correspond to a separation of 1.79 Å which matches $a/2 = 1.78$ Å; this observation will be discussed in detail later. So far, we conclude that our surface termination procedure does not improve the crystallinity of the surface.Furthermore, neither the surface quality pattern nor quality changes from 50-850°C in UHV ($P = 10^{-10} - 10^{-8}$ Torr) over the timescale of tens of minutes, suggesting that there is no degradation of or desorption from the surface.

3.3.5.2 RHEED at different azimuthal angles

We also examined the RHEED patterns of two additional samples at different azimuthal angles over the full 360° range (Fig. 3.11). Again, one of the samples (10100) was acid cleaned, and the other (10101) was terminated. In this configuration, the samples could not be heated and so remained at temperatures of less than 100°C. A second electron gun, oriented 45° from the first, was used to record additional diffrac-

tion patterns for angles with a clear diffraction pattern for the first gun. [27]

First, we note that all RHEED patterns are invariant under 90° rotation of the sample. We therefore give all angles modulo 90°. This 90° periodicity is a clear indication that the surface has square symmetry, ruling out any $n \times m$ reconstruction for $n \neq m$, except in the case where the surface is an essentially equal mixture of large domains with rectangular symmetry.[28] In addition, the bilateral symmetry of the RHEED spots and Kikuchi lines in each individual pattern also suggests that we have a square reconstruction. Finally, the 2×1 reconstruction produces clear lines when the sample is oriented along the [110] direction[185]. We see no evidence of these lines. For all of these reasons, we can rule out the common $2 \times 1 : \mathrm{H}$ reconstruction.

Finally, we can extract the real-space distance from these images. The periodicity at 0° is 1.77 Å and at 45° is 2.48 Å. These distances are $a/2$ and $a/\sqrt{2}$ respectively and correspond to scattering by (024) and $(\bar{1}13)$ from the central (004) spot[185]. The two samples have matching patterns of prominent Kikuchi lines, again suggesting that the surface is well-ordered over many lattice constants. The pattern of diffraction spots between the two samples is also the same, although the spots are more prominent in the acid cleaned sample 10100. Although it is difficult to draw conclusions

[27] Because the geometry of this second gun is different than that of the first, the distances measured have a different (and unknown) calibration factor.

[28] See, for example, the discussion in Ref. [185]. Any $n \times m$ reconstruction would also result in a strong diffraction pattern at $tan^{-1}(m/n)$, which we do not observe. In any case, the symmetry of the sample under azimuthal rotation puts strong constraints on the possible surface geometries.

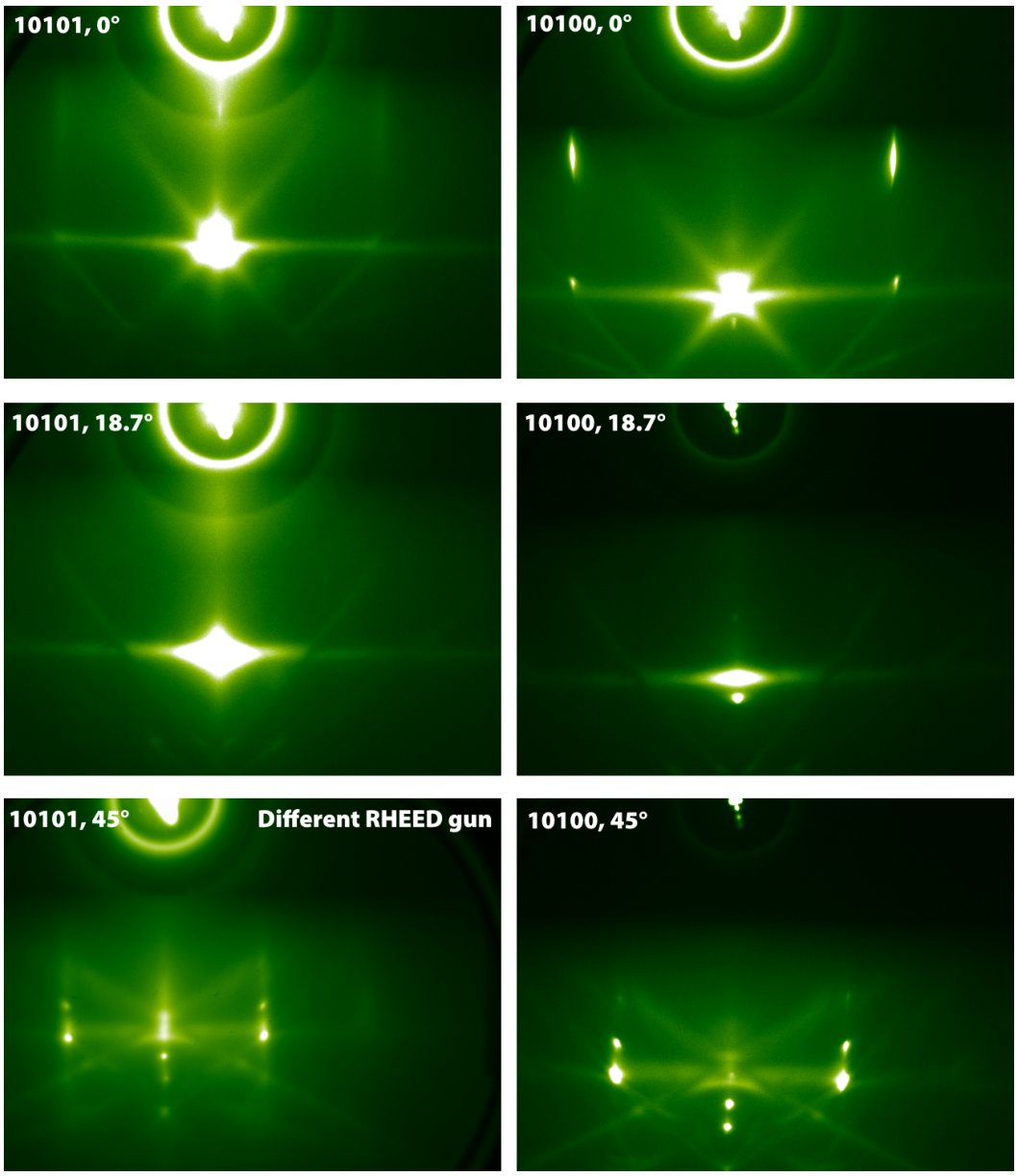

Figure 3.11: RHEED patterns from samples 10101 (terminated) and 10100 (acid cleaned) as a function of angle modulo 90°. The 0° direction corresponds to the [100] orientation[185]. The diffraction patterns are the same for each sample, though 10100 has more pronounced peaks. The image of 10101 at 45° is from a different RHEED gun.[27] The peak around 18.5° corresponds to scattering in the (130) direction, since $tan^{-1}(1/3) = 18.4$.

from such qualitative observations, the fact that we observe this trend across many RHEED patterns with different angles and alignment indicates that the acid-cleaned 10100 probably has a slightly higher-quality (and certainly not lower-quality) surface than the terminated 10101.

3.3.5.3 The role of disorder at the surface

We want to make clear claims about the ordering of the diamond *surface*. It is therefore important to determine how much of the measured signal is actually coming from the surface compared to the bulk. As mentioned before, only the top one to (at most) two or three monolayers of the surface are sampled because the scattering cross section is so high and the out-of-plane component of momentum is relatively low[178, 177]. If there were more than a few monolayers of amorphous or disordered material on top of our samples, we would not expect to see a clear RHEED signal. Moreover, it is only possible for the bulk-like signal to dominate if the surface itself is not ordered: if the top plane of atoms has some periodicity, it will contribute significantly to the diffraction pattern.[29]

If this disorder exists, what could be its source? Typically, adventitious carbon ad-

[29]Of course, the surface could have the same structure as the diamond lattice itself (*i.e.* the structure of the truncated lattice), but we are interested here in the cases where we cannot make any claims about the diamond surface whatsoever. *A priori*, we expect RHEED to give us information about primarily the top surface layer. If we rule out all of the likely confounding factors and it appears that the surface has the same structure as diamond, we will conclude that that structure is the correct one.

sorbs onto all or almost all surfaces exposed to an ambient atmosphere. Although it is difficult to estimate exactly how much adventitious carbon will adsorb onto a surface, XPS studies[190, 191, 192] usually see a small but significant carbon peak, implying that the carbon signal is around 1-5% of the overall XPS signal. Assuming that the XPS samples on the order of ten lattice constants, the total carbon coverage on the surface should be between 10-50% of a monolayer and certainly not more than one or two monolayers. This concentration is enough to have an impact on our RHEED signal, but depending on the concentration, may or may not be enough to obscure it completely. Furthermore, even if our signal had a large adventitious carbon contribution, we would still expect our RHEED signal to come from the first ordered layer, which would be the diamond surface if the surface is ordered. In other words, regardless of the presence of surface contamination, either the diamond surface is ordered (and contributes to the RHEED pattern), or it is disordered.

Finally, the length scale over which the surface must be disordered to not provide a clear diffraction pattern is given by the electron wavelength $\lambda = 0.12\,\text{Å}$. In other words, the sample must be amorphous. If the surface is polycrystalline with more than a few possibilities for domain orientation, polycrystalline rings will show up in the diffraction pattern even if there are a large number of domains. We observe no such rings.

3.3.5.4 Conclusions from our RHEED study

From our studies of the diamond surface using RHEED, we can draw the following conclusions:

1. None of the four samples has the common 2×1 : H surface reconstruction or any other reconstruction higher than 1×1. In particular, we do not see the 2×2 reconstruction proposed in, for example, Ref. [170].
2. The surface is either highly ordered or completely amorphous, but not polycrystalline.
3. The bulk immediately under the surface is highly crystalline. The acid cleaned samples appear to have slightly higher bulk quality than the terminated samples.
4. None of these conclusions changes upon heating to above 800°C in UHV.

Although this experiment studied only four representative samples, it still sheds some light on the physical ordering of atoms at the diamond surface. In the following section, we will explore the elemental composition and chemical properties of the diamond surface using X-ray photoelectron spectroscopy.

3.4 Characterization of surface chemical properties with X-ray Photoelectron Spectroscopy

3.4.1 Details of the technique

X-ray Photoelectron Spectroscopy (XPS), also known as Electron Spectroscopy for Chemical Analysis (ESCA), is a technique that measures the energy of electrons ejected from a surface by incident X-rays [158]. More specifically, high-energy X-rays (around 1500 eV for the commonly-used aluminum $K\alpha$ line) excite core-level electrons at the sample which are then directly ejected from the surface. The XPS spectrum is a measurement of the number of electrons ejected as a function of the ejection energy. This binding energy (typically measured in eV) is related to the chemical environment of the sample, and the number of detected electrons is a measurement of the concentration of the emitting species.

This concentration measurement is typically fairly sensitive: all elements other than hydrogen and helium[30] can be detected as long as the concentration is above about 0.1%. These concentration measurements are semiquantitative (typically with uncertainty of around or less than 10%) and can be made quantitative with careful calibration against known standards and corrections based on the instrument transfer func-

[30]Hydrogen and helium have no core electrons, and it is difficult to distinguish their valence electrons from the valence electrons of other elements[193]. Their absorption cross sections are also low. In principle, some information can be gleaned from the ejected low-energy valence electrons, but this is a challenging technique[194, 195].

tion, the symmetries of the underlying orbitals, and the energies of the emitted photoelectrons. The electron escape depth is typically only a few nanometers (depending on the analyte), which makes XPS a surface-selective technique.[31] For diamond, the sampling depth for aluminum Kα lines is around 6.6 nm.[32] However, typical XPS instruments are also often paired with in-situ ion milling beams so that a depth profile of the sample can be generated. XPS can be made more surface selective by tilting the sample, which increases the depth the electrons must travel to reach the detector by the cosine of the tilt angle and therefore decreases the sampling depth. It is then possible to deconvolve the chemical composition as a function of depth[197].

3.4.2 Chemical state determination with XPS

When an electron is ejected from a solid, its final kinetic energy is the difference between the (known) energy of the excitation source and the binding energy of the electron in the solid. This binding energy depends primarily on the orbital of the electron before ionization and the number of protons in the nucleus binding the core electron. For example, electrons ejected from a carbon $1s$ orbital have binding energies around $E_{C(1s)} = 285\,\text{eV}$ whereas electrons ejected from an oxygen $1s$ orbital have binding energies around $E_{O(1s)} = 532\,\text{eV}$. It is therefore generally simple to use XPS to distin-

[31] See section 3.4 of Vickerman[158] for more information on estimating the sampling depth.

[32] The sampling depth is three times the inelastic mean-free-path λ by definition. λ is 22-25 Å[196].

guish between and measure the relative concentration of different elements present at the surface.

There are a few corrections to this simple picture. The most important contribution comes from the electron density around the atom of interest. As the atom becomes more positively charged (increasing formal oxidation state), the remaining electron density is held more tightly to the atom and the XPS binding energy increases. For example, the C($1s$) peak increases in binding energy as its bonding with oxygen increases in the order C-C, C-O, C=O, O-C=O, O-(C=O)-O from 286.5 eV to 290.3 eV for small molecules. Likewise, the O($1s$) peak shifts by about +0.5 eV from carbonyl oxygens (high electron density, low binding energy) to alcohols (lower electron density, higher binding energy), and another +1 eV from alcohols to esters.[33] In this way, some chemical state information can be extracted from an XPS spectrum. If the analysis is done carefully, the results can be quantitative[199].[34] Siegbahn, a pioneer in this field, earned the Nobel prize for his work on ESCA. His Nobel lecture is a good introduction and overview of this field[200].

In order for these binding energies to be accurately determined, the electron spectrometer must first be accurately calibrated. This is typically done by referencing binding energies in clean gold and copper to fix the linearity of the instrument and determine any instrumental contributions to the measured binding energies via the work

[33] See tables 3.2 and 3.3 of Vickerman[158] as well as López[198].

[34] This chemical selectivity is why some researchers prefer the term ESCA.

function. Another important subtlety is that the sample must be properly grounded to the stage. For conductive samples, this is straightforward. For insulating samples, it may be impossible, in which case the sample can be "flooded" with low-energy electrons to compensate for the positive charge created by continuous x-ray photoionization. Still, determining the absolute energy of the emitted photoelectrons is practically impossible, so typically the energy offset is fixed by setting the energy of a well-defined peak to a certain value. Adventitious carbon is almost always present and is typically set to 284.8 eV, though this varies from study to study[190]. If the sample to be analyzed is itself carbon (*e.g.* diamond), performing this simple correction is insufficient. Alternatively, a small amount of silver or gold can be deposited or painted onto the insulating sample and used as an absolute reference.

In the case of either an insulating or a conducting sample, the most essential point is to have the entire sample at a well defined potential throughout the experiment. It is therefore essential to avoid situations where the sample is partially or locally grounded; so called "differential charging" can distort peak shapes.

Even when chemical shifts can be reliably observed in XPS, it is often not possible to gain complete chemical state information. For example, alcohol and ether bonds both appear in the same location in C($1s$) spectra. In some cases, it is possible to functionalize the surface of the sample with other groups or elements that bond only to particular functional groups. There are also various control experiments to make sure that the desired chemical group is actually being targeted. For example, hy-

droxyl groups can react with trifluoroacetic anhydride to produce a trifluoromethyl ester, wheras carbonyl groups can react with hydrazine to produce a hydrazone.[35]

3.4.3 Previous work on diamond surfaces with XPS

A number of efforts have focused on understanding the composition of the diamond surface using XPS. The two most important elements are carbon and oxygen. Hydrogen is present in most diamond surface terminations, but it is not visible in XPS.[30] Here, we will review a few of the most relevant studies. Summaries of the XPS peak assignments for the carbon and oxygen peaks from the literature are given in tables 3.2 and 3.3.

John *et al.*[171] performed oxidative annealing studies up to 800°C including an XPS study that focused on the relative concentration the oxygen peak without studying the chemical properties. The authors note a decrease in the oxygen concentration from 9% to 7% after in-situ annealing to 250°C and a complete disappearance of the oxygen peak at 800°C. They also note a complete lack of angular dependence, concluding that the oxygen is dispersed isotropically in the top surface 120 Å.

Kumaragurubaran *et al.*[201] grow a thin layer of heavily phosphorus doped MPCVD diamond on top of a (111) substrate. They compare a nitric and sulfuric acid cleaned ("O-terminated" in their parlance) surface to a hydrogen plasma exposed ("H-terminated")

[35] See section 3.11 of Vickerman[158] for some references.

surface. Both surfaces were annealed for 10 minutes at several points in the temperature range 750-1150°C. The authors' main observation is that the C(1s) peak shifts to higher binding energy (up to 1.0 eV for the hydrogen terminated surface and 0.5 eV for the oxygen terminated surface) after annealing up to about 950°C. From 950°C to 1150°C, the main peak shifts back to lower binding energy and a second peak at -1 eV appears, growing in intensity until it matches the main peak in intensity. This second peak is interpreted as the formation of graphitic carbon, which is consistent both with our experience and with other studies[202]. The authors provide a mechanistic interpretations of their results. For the hydrogen termination, they cite a previous RHEED study showing hydrogen desorption at around 850°C (again consistent with other results[203, 166]) accompanied by a reconstruction of the unsaturated surface from (1×1) to (2×1). The interpretation for the oxygen termination is less clear. There are some studies in the literature suggesting that oxygen desorption occurs in a broad temperature range around 600°C.[36] The authors do not perform any chemical state interpretation of their spectra beyond identifying the graphitic carbon peak.

In a recent study, Baldwin *et al.*[202] use XPS to study the surface termination of two-photon laser ablated diamond surfaces. This two-photon ablation technique can slowly remove diamond in an ambient environment. The mechanism requires oxygen, but is otherwise poorly understood. In this study, charging is a significant problem

[36]Compare to the work of Ando[204] discussed below in section A.3.3, which suggests that oxygenation occurs up to about 500°C.

even with charge compensation (this has also been our experience). Only the relative separation between peaks is extracted.[37] Their piranha-treated (100) samples before etching have about 6% C-O and 6% C=O on the surface; this is consistent with their O(1s) XPS results. Laser ablation may lower the total oxygen concentration slightly and clearly decreases the contribution of C=O bonds.

The peak positions discussed in these and a few other references are summarized in tables 3.2 and 3.3. In general, there are few results discussing the O(1s) peak for diamond. However, the carbon and oxygen peaks for various oxygen-containing polymers have been thoroughly studied[198]. These results could be useful as a baseline for understanding oxygen-containing functional groups at the diamond surface, so they have been included in table 3.3.

3.4.4 Our results

Our main objective is to determine the impact of our surface termination procedure. We are therefore most interested in comparing samples that have been acid cleaned to samples with our full surface termination procedure. For completeness, we also include results for samples that have undergone the etching process described in the previous chapter (see Fig. 2.2). Here, we present a survey of 280 different datasets taken across over 99 different samples and around 30 substantially different process

[37]The authors also see silicon contamination, which we also frequently observe, and attribute it to the glass beaker used to contain the sample.

Table 3.2: Literature values for chemical shifts of the C(1s) peak at 285 eV in XPS[190, 198]. Because the position of the central sp^3 carbon peak can vary from study to study, I have normalized the binding energy shifts to this quantity. Bonds not indicated in the second column below are assumed to be to carbon.

Peak shift, eV	Assignment	Notes
-1.8 ± 0.5	Unknown	Makes up 10% of (100) surface.[202]
-1.9 ± 0.2	Unknown	(100). This work.
-0.9 ± 0.2	C=C (graphite)	(100). This work.
-0.9 ± 0.1	C=C (graphite)	(111)[201], (100), (110)[202] diamond.
-0.9	C=C ((2×1) dimers)	In-situ annealed above 1050°C.[157]
0.7 ± 0.1	C β to COOH	Average of several polymers.[198]
0.7	Hydrocarbons	Hydrogen terminated Ib diamonds.[157]
1.0 ± 0.2	C-O	(100). This work.
1.16 ± 0.09	C-O-C	(100) diamond[171]. Possibly -OH.
1.2 ± 0.1	C-O	(100) diamond[202]. 1.1 eV for (110).
1.5	C-O	Plasma oxidized polypropylene[199]
1.6 ± 0.2	C-O	Average of several polymers.[198]
1.87 ± 0.05	C=O	(100) diamond[171]
2.3 ± 0.1	C=O	(100) diamond[202]. 2.2 eV for (110).
2.4 ± 0.2	C=O	(100). This work.
2.7	C=O	Plasma oxidized polypropylene[199]
2.7 ± 0.2	C=O	Average of several polymers.[198]
3.9 ± 0.2	O-C=O	Average of several polymers.[198]
4.3	O-C=O	Plasma oxidized polypropylene[199]

Table 3.3: Literature values for chemical shifts of the O(1s) peak at around 532.5 eV in XPS. I have normalized the positions to the C-O-C or C-O-H oxygen peak (which are at the same chemical shift[198]). For diamond, there is some debate about the interpretation of the O(1s) peak[202].

Peak shift, eV	Assignment	Notes
-1.2 ± 0.2	C=O	(100). -1.7 eV for (110). Small shift, broad peak.[202]
-1.1 ± 0.2	C=O	(100), this work.
-0.6 ± 0.1	C-C=O and COOH	Average of several polymers.[198]
0.9 ± 0.2	O=C-O-C	Average of several polymers.[198]

histories. For an overview of the methodology we have used to analyze the data, see chapter A.2 in the appendix.

To analyze the surface termination of the samples, we analyze the C(1s) and O(1s) peaks. Although the C(1s) peak is in principle a rich source of chemical state information, in practice it is dominated by the sp^3 signal from the bulk diamond carbon. Careful analysis and high contrast is required to extract meaningful chemical state information from this peak. The oxygen peak is therefore potentially more useful as a chemical state probe since all of the signal from the oxygen peak is necessarily from oxygen-containing functional groups at or near the surface. The signal-to-noise for chemical state information from the oxygen peak is therefore significantly higher than that from the carbon peak, which contains significant bulk contributions based on the sampling depth of 6.5 lattice constants (see footnote 32 and accompanying text). However, the oxygen peak is less well studied in the literature[202].

We use two techniques to aid these analyses. First, we rely on statistical methods to find small differences between processing steps that might not be obvious with a small number of samples. This is enabled by the large number of samples in our dataset (see Fig. 3.12). Our work differs substantially in this regard from much of the previous literature where usually only one or two (and almost always less than ten) samples of each type are analyzed. Second, we examine correlations between the carbon subpeak intensities and oxygen subpeak intensities since some of these signals come from the same chemical groups.

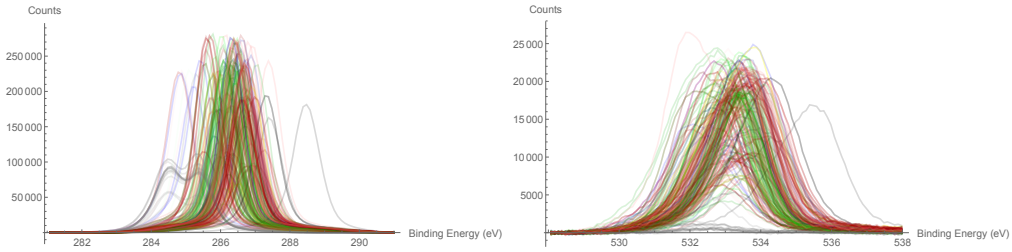

(a) Carbon Peaks (b) Oxygen Peaks

Figure 3.12: All of the XPS Peaks for our data. Different colors correspond to different processing histories. (See Fig. 3.13 for the color scheme). A Shirley background subtraction has been applied, but the peak positions have not been corrected.

We will first focus on the relative oxygen concentration at the surface since this quantity is the simplest to measure. The total oxygen concentration is a simple probe of the surface termination: different chemical groups contain different concentrations of oxygen, and different surface reconstructions can have different concentrations of chemical groups. We compute the total weight of the oxygen peak on the sample and normalize it to the sum of the carbon and oxygen peaks.[38] See Fig. 3.13 and table 3.4 for the results. Acid cleaned samples that have never been terminated have a significantly[39] higher concentration of oxygen ($7.5 \pm 0.6\%$) than samples that have been terminated ($5.4 \pm 0.8\%$). This lower oxygen concentration persists even after the terminated samples are acid cleaned again ($5.2 \pm 0.7\%$).

[38] I first perform background subtraction as described in section A.2 in the appendix.

[39] Here, we distinguish between different distributions using the Komolgorov-Smirnov test. Statements about the means are based on a Kruskal–Wallis one-way analysis of variance, although strictly speaking this method tests stochastic dominance. Statistical methods are described in section A.2. Statements of significance are made at the 95% level.

Here, I have included only data from samples that have been both acid cleaned and later terminated. The results are essentially the same if the data from all samples are included (in which case the sample sizes are much larger), or if only runs with no contaminants are included.

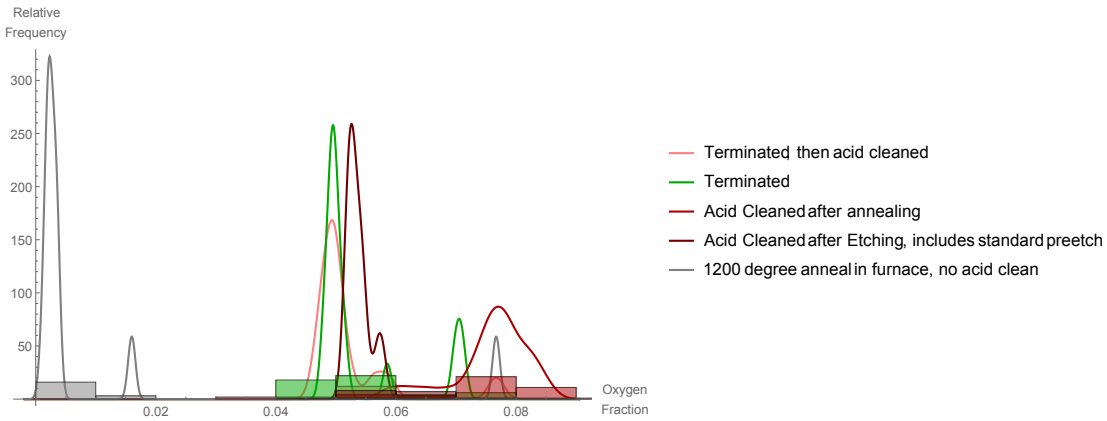

Figure 3.13: Histogram and smoothed histogram (kernel density estimation) of oxygen fraction for five different process histories. The terminated samples have no significant change even after acid cleaning. Both of these distributions are significantly different from the acid cleaned after annealing. The samples that are acid cleaned after etching are similar to the terminated samples. All differ from the annealed samples which show practically no surface oxygen. See Fig. A.7 in the appendix for more detailed statistics.

To compare these results to the theoretical possibilities for the surface termination, it's important to estimate what these oxygen fractions correspond to in terms of total surface coverage. In order to do this, we first make the canonical assumption that the electron escape probability falls off exponentially as a function of depth beginning at the surface. We also assume that the surface layer has the same geometry and inelastic mean-free-path (IMFP) as the bulk, or rather that the effective scattering

Table 3.4: Mean oxygen concentrations for various process histories. N is the sample size. The O(1s) fraction is expressed as a percentage. Samples that are acid cleaned after annealing have a significantly higher oxygen concentration than terminated samples or samples that have been acid cleaned after etching. Samples that have been annealed have graphitic carbon and very little oxygen. Samples that are acid cleaned after termination are not statistically different from samples that have just been terminated; otherwise, all of the processes are statistically different. See Fig. A.7 in the appendix for more detailed statistics.

Process	O(1s) %	N	Notes
Acid cleaned after etching	5.4 ± 0.1	7	Standard beam etch or pre-etch
Acid cleaned after annealing	7.5 ± 0.6	26	1200°C anneal, before any termination
Terminated	5.4 ± 0.8	33	
Acid cleaned after termination	5.2 ± 0.7	15	
Annealed	1.0 ± 2.2	11	Before acid cleaning

per atom is the same. The geometry can be referenced to simulation[153, 167, 170], but the effect on the IMFP is hard to calclate. Assuming the simple Z^2 scaling of Rutherford scattering (which may not be accurate at these low energies) gives a 77% scattering enhancement for oxygen over carbon.

Under these assumptions, the calculated coverage of oxygen atoms (in terms of planes of atoms packing in a 1×1 configuration) is between 25% and 70%. Because other scattering mechanisms that depend on electron density contribute for these relatively low-energy electrons, the Z^2 scaling is probably an overestimate, so the scaling is in between Z^1 and Z^2. Hence, the effective IMFP for the surface is almost certainly not more than that of carbon, and not less than 77% less. In this case, the surface oxygen coverage is probably between 30% and 50%. This estimate of approximately 50% oxygen coverage for a 7% total oxygen fraction is important to keep in mind

when estimating the density of various oxygen-containing groups on the surface.

One possible objection is that the oxygen on the surface of the sample is coming from adsorbed water or organics rather than a true diamond surface termination. While it can be difficult to differentiate between these two cases, there is little evidence in the literature for adventitious adsorption of oxygen-containing compounds[190]. In our experiments, samples that have been annealed at high temperature contain a large proportion of graphitic carbon and typically have a small or non-existent oxygen peak, which excludes an omnipresent source of oxygen contamination. Furthermore, we have been able to hydrogen terminate diamond surfaces, resulting in a single narrow carbon peak and very small (under 0.2%) concentrations of oxygen. NEXAFS evidence also suggests that while the carbon edge changes after *in situ* annealing in vacuum, the oxygen edge remains unchanged[188]. It is therefore unlikely that our oxygen peak contains significant contributions from adsorbed water.

Now, we turn to a chemical analysis of the diamond surface. The goal is to determine what functional groups exist on the surface by carefully analyzing the sub-peaks contributing to the total signal for each element. The methodology is given in section A.2 of the appendix. In addition to having a higher absolute oxygen concentration, the samples that are acid cleaned after annealing have almost a factor of four higher carbonyl concentration relative to the total oxygen peak intensity (Fig. 3.14 and table 3.5). This supports the hypothesis that the acid cleaning gives a mixture of surface oxygen groups of higher oxidation state rather than primarily ether and

alcohol groups. There is no evidence of ester groups in these samples: including an ester group in the model does not improve the fit. These data are consistent with studies reporting an increase in the carboxyl peak intensity after annealing in a dry oxygen environment at 500°C or above[205]. Note, however, that previous theoretical work[146] indicates that carbonyl groups should be unstable to spontaneous formation of bridging ether groups; this prediction stands in clear contrast to these and our experimental results. This decreased carbonyl concentration present in samples that have been terminated could lead to enhanced NV stability. According to theoretical work from the Gali group[170], the unoccupied π^*-like LUMO of a carbonyl group on an otherwise OH-terminated surface gives an empty localized surface state 0.4 eV below the excited state of the NV^-. For an NV close to the surface, this state can accept electrons from an excited NV^-.

We now turn to an analysis of the surface chemical structure based on an interpretation of the carbon peak. This interpretation is, as expected, less straightforward thank for the oxygen peaks. The data are summarized in Fig. 3.15 and table 3.6, as well as Fig. A.9 in the appendix. First, there are no statistically significant differences between the C-O, C=O, or sp^2 relative peak weights for the different processing steps.[40] The only exception is that the samples that are acid cleaned after etching have a lower C-O concentration than the samples that are acid cleaned after anneal-

[40]Here, I restrict myself to only the processing steps described below. Of course, the annealed samples have a huge graphitic carbon concentration that can exceed 50% of the total carbon contribution.

ing. This is consistent with the oxygen fitting results; see table 3.4. Terminated samples and samples that have been acid cleaned after etching have a fourfold smaller fraction of the unassigned peak at -1.8 eV compared to samples that have been acid cleaned after annealing or even samples that have been acid cleaned after previous termination. The peak at -1.8 eV is a significant mystery both in our work and in the literature. Because the peak occurs at a lower binding energy than the central peak, it represents an electron-rich species.[41] This energy corresponds roughly to the chemical shift expected for *sp* hybridized carbon[202].

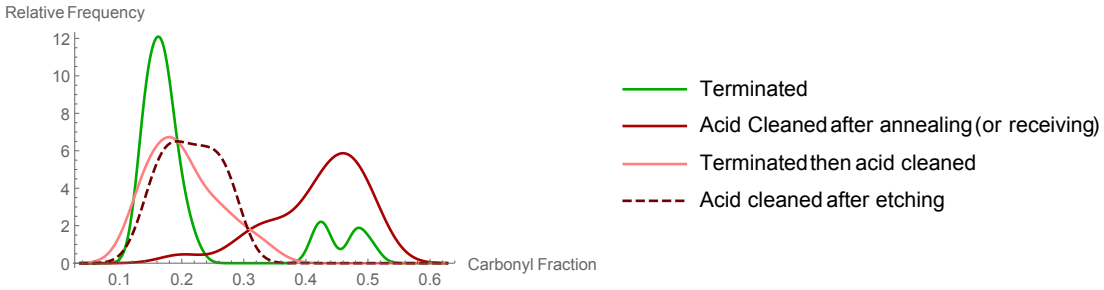

Figure 3.14: Smoothed histogram of carbonyl fraction fitted from the $O(1s)$ peak for different process histories. The terminated samples have on average almost a factor of four lower carbonyl coverage than the acid cleaned samples. There is significant hysteresis in this process: the carboynl fraction remains low even after the terminated samples are acid cleaned again. The etched samples have a broader distribution, but are more similar to the terminated samples than the acid cleaned samples. See chapter A.2 and especially Fig. A.5 for more information on the fitting methodology. Figure A.8 has more detailed statistics on this data.

[41] Recall section 3.4.2 above.

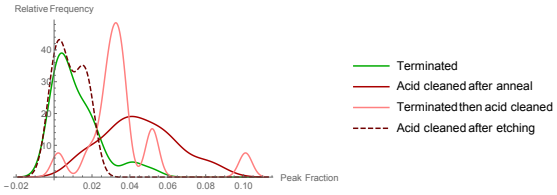

(a) Peak at -1.8 ± 0.2 eV with unknown assignment. Terminated samples have a fourfold smaller fraction of this peak.

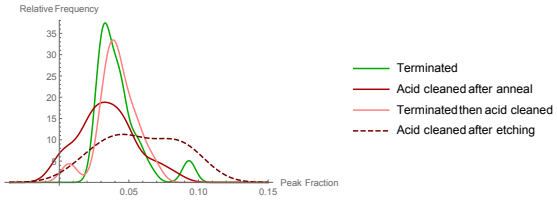

(b) C=C (graphite) peak at -0.9 ± 0.1 eV. There is no statistical difference between these samples.

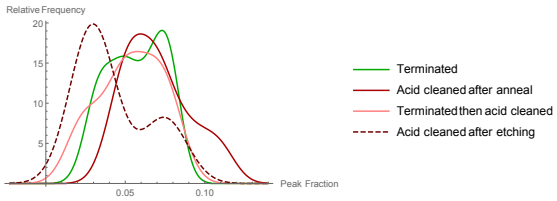

(c) C-O peak at 1.0 ± 0.2 eV. Samples that are acid cleaned after etching have a lower C-O concentration than the samples that are acid cleaned after annealing

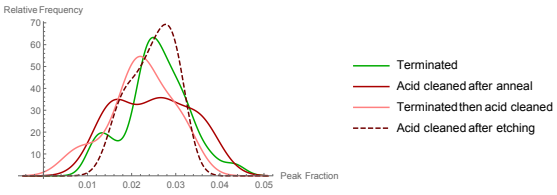

(d) C=O peak at 2.4 ± 0.2 eV. There is no statistical difference between these samples.

Figure 3.15: Smoothed histogram of carbon fraction for different process histories. All samples have similar oxygen subpeak concentrations of around 10%, consistent with our oxygen data above.

Table 3.5: Mean carbonyl concentrations from the $O(1s)$ peak for various process histories. N is the sample size. The relative carbonyl fraction is expressed as a percentage. The mean peak position is at -1.1 ± 0.2eV relative to the central C-O peak. These data come from the same spectra as before, so the sample sizes are the same as in *e.g.* table 3.4. The samples that have only been annealed have negligible surface oxygen content so are not included in this table. Note that the fractions here are the fractions of the total oxygen peak and are not renormalized based on relative magnitude of the oxygen peak compared to all other peaks. See also Fig. A.8 in the appendix for more detailed statistics.

Process	Carbonyl %	N	Notes
Acid cleaned after etching	21.4 ± 21.5	7	Standard beam etch or pre-etch
Acid cleaned after annealing	42.0 ± 7.7	26	1200°C anneal, before any termination
Terminated	21.8 ± 11.7	33	
Acid cleaned after termination	20.4 ± 5.7	15	

Table 3.6: Mean carbon subpeak concentrations for various process histories. Samples that are acid cleaned after annealing have more than four times as much of the unknown peak relative to terminated samples. All of the samples have comparable amounts of graphitic carbon. Sample sizes and descriptions are the same as in the other tables. See also Fig. A.9 in the appendix for more detailed statistics.

Process	Unknown (-1.8 eV) %	C=C %	C-O %	C=O %
Acid cleaned after etching	0.8 ± 0.8	5.8 ± 2.8	4.3 ± 2.3	2.5 ± 0.5
Acid cleaned after annealing	4.5 ± 1.9	3.5 ± 2.1	7.0 ± 2.0	2.5 ± 0.8
Terminated	1.1 ± 1.2	4.3 ± 1.6	5.7 ± 1.7	2.6 ± 0.7
Acid cleaned after termination	3.6 ± 2.1	4.1 ± 1.4	5.3 ± 2.0	2.2 ± 0.7

3.5 Conclusion

The goal of this section was to build and understanding of the structure and properties of the diamond surface and then use this understanding to analyze the results of surface processing and their implications for emitter properties. In particular, we wanted to understand how two different processes—the tri-acid clean and the more complex surface termination—affect the surface and the emitter properties. By ana-

lyzing the spatial order of the structure using RHEED in section 3.3, we determined that the surface likely had a 1×1 reconstruction that was stable over a range of temperatures and did not depend on processing technique, although it is also possible that the surface itself is completely disordered. By analyzing the elemental and chemical composition of the surface using XPS in section 3.4, we discovered some statistically significant differences in the chemical composition of the diamond surface upon different processing steps. However, these differences did not allow us to confirm or rule out various options for the surface termination that have been proposed theoretically, especially given the results from our RHEED study. Although this work remains somewhat inconclusive, these results and techniques should be a valuable starting point for researchers continuing to answer these and similar questions about the diamond surface.

4

Narrow-linewidth homogeneous optical emitters in diamond nanostructures via silicon ion implantation

4.1 Introduction

Coherent emitters of indistinguishable single photons are a basic ingredient in many quantum information systems[206]. Atom-like emitters in the solid state are a particularly appealing platform for practical quantum information because they can be scalably integrated into nanophotonic devices. However, no single solid-state system has yet combined high brightness of narrowband emission and a low inhomogeneous

distribution of photon frequencies from separate emitters (indistinguishability) with ease of incorporation into nanophotonic structures on demand. For example, optically active semiconductor quantum dots can be bright and integrable into nanostructures, but have a large inhomogeneous distribution[44]. Nitrogen-vacancy (NV) centers in bulk diamond[207] are bright and photostable, with a moderate inhomogeneous distribution that allows straightforward tuning of multiple NV centers into resonance. These properties allow proof-of-principle demonstrations of quantum information protocols such as remote spin-spin entanglement generation[63, 64] and quantum teleportation[208]. Further progress towards developing NV based quantum devices has been hindered by low indistinguishable photon generation rates associated with the weak NV zero-phonon line, a challenge that could be addressed by integrating NV centers into nanophotonic structures. However, the optical transition frequencies of NV centers are very sensitive to their local environment[90, 92], making integration of spectrally stable emitters into nanophotonic structures a major challenge[71].

The negatively charged silicon-vacancy color center in diamond (SiV) has shown promise in fulfilling the key criteria of high brightness[209], lifetime-limited optical linewidths[210], and a narrow inhomogeneous distribution of optical transition frequencies[211]. The SiV (Fig. 4.1) has electronic states with strong dipole transitions where 70% of the emission is in the zero-phonon line (ZPL) at 737 nm[209]. The inversion symmetry of the SiV prevents first-order Stark shifts, suppressing spectral diffusion[210] and allowing indistinguishable photons to be generated from separate

emitters without the need for tuning or extensive pre-selection of emitters[212]. When combined with a spin degree of freedom[213], the SiV center's bright narrowband transition, narrow inhomogeneous distribution, and spectral stability make it a promising candidate for applications in quantum optics and quantum information science.

Silicon-vacancy centers occur only rarely in natural diamond[215], and are typically introduced during CVD growth via deliberate doping with silane[216, 217] or via silicon contamination[210, 218, 219, 211, 220]. While these techniques typically result in a narrow inhomogeneous distribution of SiV fluorescence wavelengths, these samples have a number of disadvantages. For example, the concentration of SiV centers can be difficult to control and localization of SiV centers in three dimensions is impossible.

Ion implantation offers a promising solution to these problems. By controlling the energy, quantity, and isotopic purity of the source ions, the depth, concentration, and isotope of the resulting implanted ions can be controlled. Ion implantation is widely commercially available. Targeted ion implantation using a focused silicon ion beam is also possible, allowing for placement of silicon defects in all three dimensions with precision on the scale of tens of nanometers[137]. Despite the advantages of ion implantation, there have been conflicting results[221, 137, 214] on the brightness and creation yield of SiV centers produced using this method and no systematic studies of the inhomogeneous distribution of SiV fluorescence wavelengths. Although there has been a single report of an implanted SiV with a linewidth roughly 10 times the life-

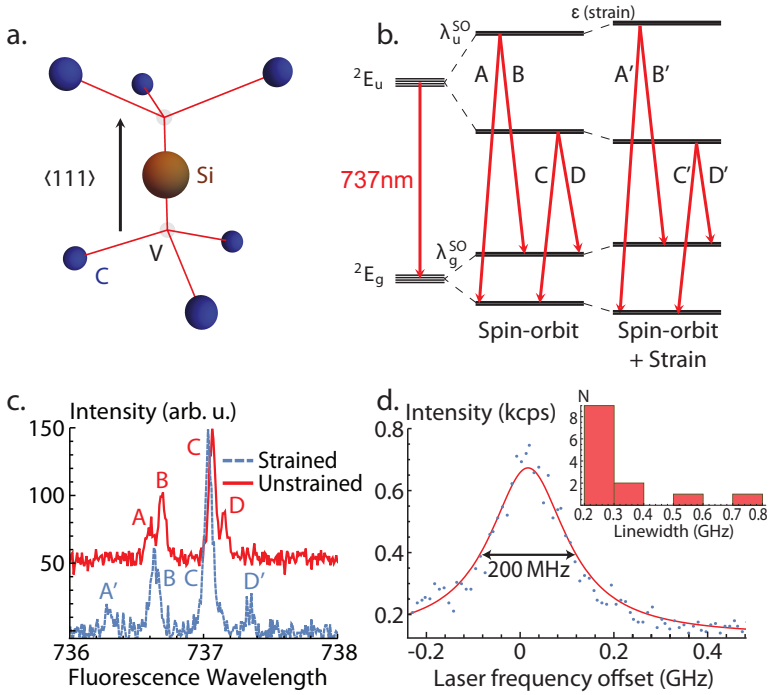

Figure 4.1: Properties of the SiV center. **a.** Atomic structure of the SiV center. The V-Si-V axis lies along the ⟨111⟩ lattice direction. The SiV has D_{3d} symmetry. **b.** Level structure of the SiV center. The SiV is a single-hole system with double orbital and spin degeneracy. This degeneracy is partially lifted by spin-orbit coupling ($\lambda_g^{SO} = 47\,\text{GHz}$ and $\lambda_u^{SO} = 260\,\text{GHz}$[214, 210]). Lattice strain increases the splitting between these spin-orbit levels, shifting the transition frequencies. **c.** Fluorescence spectra of the ZPLs of single SiV centers in high-strain (blue, dashed) and low-strain (red) environments at 9–15 K. Transitions B and C are less sensitive to strain compared with transitions A and D because the ground and excited states shift in the same (opposite) directions for transitions B and C (A and D)[211]. Unstrained spectrum offset and scaled vertically for clarity. **d.** Linewidth (FWHM) of representative implanted SiV in bulk (unstructured) diamond measured by PLE spectroscopy (blue points: data; red line: Lorentzian fit). Inset: histogram of emitter linewidths in bulk diamond. Almost all emitters have a linewidth within a factor of three of the lifetime limit (94 MHz).

time limit[222], to the best of our knowledge there has been up to now no consistent method for producing SiV centers with bright, narrow-linewidth emission using ion implantation. These two criteria of a low inhomogeneous distribution relative to the single-emitter linewidth and narrow single-emitter linewidth relative to the lifetime limit are essential for quantum optics applications[206, 223].

In this chapter, we report the creation of SiV centers in diamond using ion implantation. Implantation is followed by high-temperature high-vacuum annealing to facilitate SiV formation and repair implantation-induced damage to the lattice. The resulting emitters have narrow optical transitions within a factor of four of the lifetime limited linewidth and a narrow inhomogeneous distribution such that the half of the emitters have transitions that lie in a 15 GHz window. Finally, we incorporate these SiV centers into nanostructures and demonstrate that their favorable optical properties are maintained even after fabrication.

The silicon-vacancy color center is a point defect in diamond wherein a silicon atom occupies an interstitial position between two vacancies (Fig. 4.1a)[224]. The SiV is a spin-$\frac{1}{2}$ system with ground ($^2\mathrm{E}_g$) and excited ($^2\mathrm{E}_u$) states localized to the diamond bandgap[225, 224, 142]. Both states have double spin and orbital degeneracies partially lifted by the spin-orbit interaction (Fig. 4.1b) which splits each quartet into two degenerate doublets. The spin-orbit splittings for the ground and excited states are 0.19 and 1.08 meV (47 and 260 GHz), respectively (Fig. 4.1c)[225, 214]. All transitions between the ground and excited states are dipole-allowed with a ZPL energy

of 1.68 eV ($\lambda = 737$ nm) and an excited state lifetime of under 1.7 ns[226]. These optical transitions can have linewidths (Fig. 4.1d) comparable to the lifetime limit of 94 MHz[210].

The SiV is sensitive to strain, which can both shift the average energy (for axial strain) and increase the splitting (for transverse strain) in the ground and excited state manifolds (Fig. 4.1b, last column)[213, 214]. Transitions B and C within the ZPL are relatively insensitive to transverse strain because their ground and excited states shift in the same direction: both upward for transition B and both downward for transition C (Fig. 4.1c)[211]. Transition C is between the lowest energy ground and excited states which are also isolated from the phonon bath at low temperatures[226]. This transition is therefore the most suitable for applications in quantum information science.

4.2 Creating SiV centers with ion implantation

We create SiV centers using the following procedure: As in section 2.2.2, we begin with a polished CVD diamond (Element Six Inc., $[N]_S^0 < 5$ ppb, {100} oriented top face). Recall that mechanical polishing produces a strained and damaged layer close to the surface that results in reduced mechanical stability of nanofabricated structures[97]. This strain can also lead to a larger inhomogeneous distribution of SiV wavelengths. We again reduce the damage from polishing by removing 5 μm of dia-

mond through reactive ion etching, producing a smooth (under 1 nm RMS roughness) surface. An otherwise identical control sample was also put through the same implantation procedure but without this pre-etching step. We then implant $^{29}Si^{+}$ ions (Innovion Corporation) at a dose of 10^{10} ions/cm^2 and an energy of 150 keV resulting in an estimated depth of 100 ± 20 nm[227]. See also Fig. 2.1 on page 18.

After implantation, we clean the samples using an an acid clean and then perform two high-temperature high-vacuum ($\lesssim 10^{-6}$ Torr) anneals. The procedure here is very similar to that used for creation of NV centers described in section 2.2.2. The first anneal is at 800 °C for eight hours after a four-hour bake-out step at 400 °C. At 800 °C, vacancies are mobile[105, 106, 50] leading to the formation of SiV centers. The second anneal is the same as the first, but with an additional step at 1100 °C with a two-hour dwell time to anneal out other defects. For all annealing steps, we use slow temperature ramps ($\lesssim$ 35 °C per hour) to maintain low pressures in our furnace. This annealing procedure, inspired by previous work with SiV[228, 219] and NV[107, 117, 229, 230] centers (see also Sec. 2.2.2), both aids in the formation of SiV centers and also helps remove damage to the crystal lattice, reducing local strain. The residual graphitic carbon produced during these high-temperature anneals was removed by again performing the oxidative acid clean. Before each annealing step, we use X-ray photoelectron spectroscopy to verify that the surface is free of contaminants.

4.3 Results and discussion

4.3.1 SiV centers in bulk diamond

We confirm that the SiV centers exhibit narrow-linewidth optical transitions by performing photo-luminescence excitation (PLE) spectroscopy after 1100 °C annealing. In this experiment, we scan the frequency of a weak resonant laser (New Focus Velocity, linewidth $\Delta f \lesssim 25\,\mathrm{MHz}$ over the course of the experiment, stabilized with a High Finesse WS7 wavemeter) across transition C and monitor the fluorescence on the phonon-sideband (PSB). We integrate over several scans to reconstruct the time-averaged shape and position of the SiV ZPL (Fig. 4.1d). We perform these measurements in a helium flow cryostat at a sample stage temperature of 3.7 K to avoid phonon-induced broadening of the optical transition[226]. The emitters are resonantly excited below saturation to avoid power broadening. (See Appendix B for more experimental details.) We find that SiV centers in bulk diamond have narrow optical transitions with linewidths of $\Gamma/2\pi = 320 \pm 180\,\mathrm{MHz}$ (mean and standard deviation for $\mathrm{N} = 13$ spatially resolved emitters). Almost all SiV centers have a linewidth within a factor of three of the lifetime limit (Fig. 4.1d, inset). As defined here, these linewidths include the effects of phonon broadening and all spectral diffusion that happens at any timescale during the course of the experiment (4–15 minutes).

We characterize the inhomogeneous distribution of the implanted SiV fluorescence wavelengths after each annealing step via photoluminescence spectroscopy. To per-

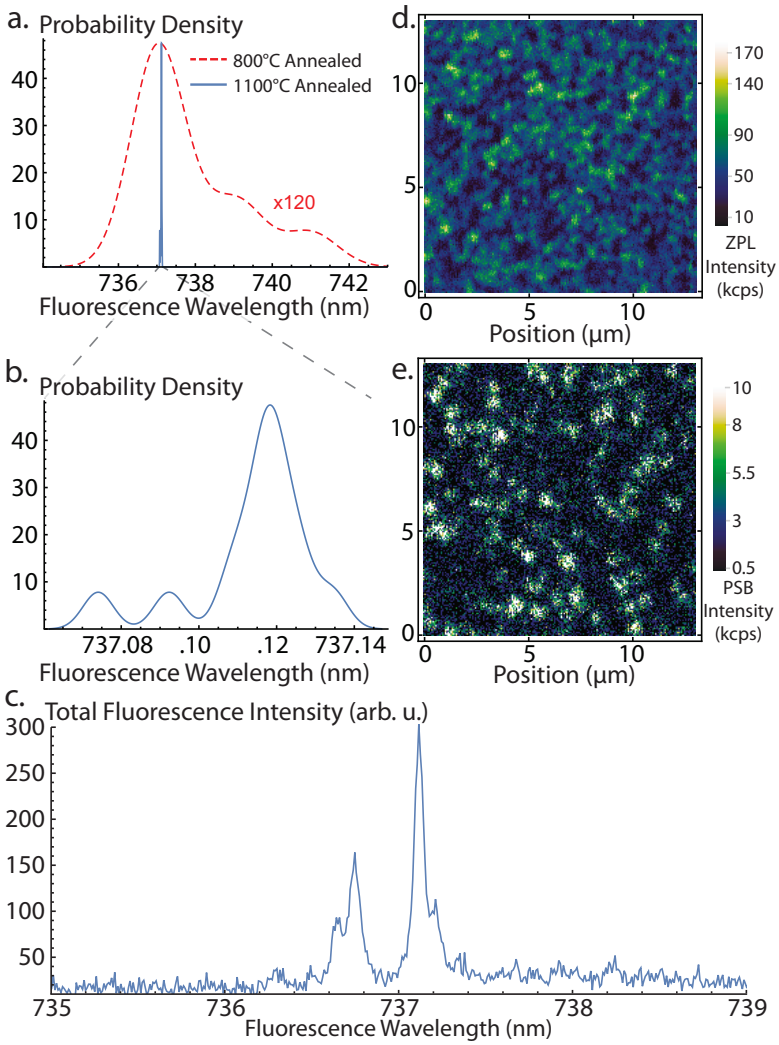

Figure 4.2: Inhomogeneous distribution of fluorescence wavelengths of implanted SiV transitions. **a.** Kernel density estimation of distribution of bulk SiV wavelengths after 800 °C (N = 19, red dashed curve) and 1100 °C (N = 13, blue solid curve) annealing. The distribution narrows from 3–4 nm (800 °C anneal) to 0.03 nm (15 GHz, 1100 °C anneal). **b.** Zoomed-in distribution (transition C) after 1100 °C annealing. Note the smaller wavelength range on the horizontal axis. **c.** Sum of spectra for different SiV centers after 1100 °C annealing. The SiV fine structure is clearly present, demonstrating that the inhomogeneous distribution is small. **d**, **e.** Spatial map of collected fluorescence (thousands of counts per second) over a region of bulk diamond exciting off (d) and on (e) resonance. By comparing the densities of emitters, we estimate that 30 ± 15% of the emitters are nearly resonant. These measurements were taken at 9–15 K.

form these measurements, we excite the SiV centers using off-resonant light from a 700 nm diode laser. Off-resonant excitation at 520 nm is also possible. Using both of these wavelengths together results in a superlinear enhancement in the observed count rate, suggesting that the 520 nm laser may play a role in stabilizing the SiV charge state. The resulting fluorescence is sent to a spectrometer (Horiba iHR550, 0.025 nm resolution). We perform these measurements at 9–15 K.

After annealing at 800 °C, the observed distribution is broad, with about half of the emitter transition wavelengths lying within a 3–4 nm range (Fig. 4.2a, red dashed curve). Transition C was used where unambiguous identification was possible; otherwise, the brightest transition (which should correspond to transition C[211, 210]) was used. After the 1100 °C anneal, the distribution becomes more than 100 times narrower, with about half of the 13 measured emitters (transition C) now lying in a 0.03 nm (15 GHz) window (Fig. 4.2a and 4.2b, blue solid curves). In both cases, we focus on transition C because it is the brightest transition and relatively insensitive to strain[211] and phononic decoherence[226]. The other transitions are also much more narrowly distributed after 1100 °C annealing. In Fig. 4.2c, we plot a composite spectrum constructed by summing over all of the normalized 13 SiV spectra taken after 1100 °C annealing. This composite spectrum is very similar to the spectrum of a single unstrained SiV center (Fig. 4.1c) and shows the expected fine-structure splitting, demonstrating that the inhomogeneous distribution of SiV transition wavelengths is small compared to the fine-structure splitting. This result is comparable to reported

inhomogeneous distributions reported for SiV centers created during CVD growth[210, 212, 211, 214]. It is possible that even higher temperature annealing could further reduce this inhomogeneous distribution[219, 229].

To estimate the yield of conversion from implanted Si^+ ions to SiV centers, we perform scanning confocal microscopy (Fig. 4.2d). Exciting with several milliwatts of off-resonant light (700 nm) gives around 10^5 counts per second (cps) into a single-mode fiber from a single SiV in a 20 nm spectral range around the ZPL. In the resulting microscope image, we count the number of SiV centers and estimate a density of 0.5–1/μm^2. Based on our Si^+ implantation density of 100/μm^2, we estimate our SiV creation yield after 800 °C annealing to be 0.5–1%. There was no clear difference in the yield after performing the 1100 °C anneal. Furthermore, the yield in the sample that was not pre-etched was significantly higher (2–3%). The observations that higher-temperature annealing did not increase the yield and that the sample with greater surface damage had a larger yield both support the model that SiV formation is limited by the presence and diffusion of nearby vacancies[228, 108]. This yield could be increased by electron irradiating the sample to create a higher vacancy density in a controllable way[107, 228, 217].

To visualize the density of nearly resonant SiV centers, we resonantly excited the SiV centers with a Rabi frequency of several GHz using an external-cavity diode laser tuned to the center of the inhomogeneous distribution. We scan spatially over the sample and collect fluorescence on the phonon side-band (PSB). The resulting image

taken in the same region of the sample (Fig. 4.2e) has about a factor of three fewer emitters compared to the image taken with off-resonant excitation (N∼100 vs. ∼340); roughly 30% of the emitters are near-resonant (within our few GHz Rabi frequency).

4.3.2 SiV centers in nanostructures

One major advantage of building quantum devices with solid-state emitters rather than trapped atoms or ions is that solid state systems are typically more easily integrated into nanofabricated electrical and optical structures[231, 232]. The scalability of these systems is important for practical realization of even simple quantum optical devices[233]. Unfortunately, many solid-state systems suffer serious deterioration in their properties when incorporated into nanostructures. For example, the large permanent electric dipole of NV centers in diamond causes coupling of the NV to nearby electric field noise, shifting its optical transition frequency as a function of time. The SiV is immune to this spectral diffusion to first order because of its inversion symmetry[212] and is therefore an ideal candidate for integration into diamond nanophotonic structures. Motivated by these considerations, we fabricated an array of diamond nanophotonic waveguides (Fig. 4.3a) on the pre-etched sample characterized above using previously reported methods[97, 73]. Each waveguide (Fig. 4.3a, inset) is 23 μm long with approximately equilateral-triangle cross sections of side length 300–500 nm. After fabrication, we again performed the same 1100 °C annealing and acid cleaning

procedure. Many SiV centers are visible in a fluorescence image of the final structures (Fig. 4.3b). Photon correlation measurements (Appendix B) verify our ability to create and image single SiV centers.

To characterize the optical coherence properties of SiV centers in nanostructures, we again perform PLE spectroscopy. SiV centers in nanostructures have narrow transitions with a full-width at half-maximum (FWHM) of $\Gamma_n/2\pi = 410 \pm 160\,\mathrm{MHz}$ (mean and standard deviation for $\mathrm{N} = 10$ emitters; see Fig. 4.3c inset for linewidth histogram), only a factor of 4.4 greater than the lifetime limited linewidth $\gamma/2\pi = 94\,\mathrm{MHz}$. The linewidths measured in nanostructures are comparable to those measured in bulk (unstructured) diamond ($\Gamma_b/2\pi = 320 \pm 180\,\mathrm{MHz}$). The ratios Γ_n/γ and Γ_b/γ are much lower than the values for NV centers, where the current state of the art for typical implanted NV centers in nanostructures[71] and in bulk[230] is $\Gamma_n/\gamma \gtrsim 100$–$200$ and $\Gamma_b/\gamma \gtrsim 10$ ($\gamma/2\pi = 13\,\mathrm{MHz}$ for NV centers).

It is possible for the lifetime in nanostructures to be longer than the lifetime in the bulk since the local photonic density of states is generally reduced inside such a structure[234, 235]. This potential change in lifetime would change the lifetime-limited linewidth and can also provide indirect evidence of the SiV quantum efficiency. To probe this effect, we measured the lifetime of nine SiV centers. The lifetime measured in the nanobeam waveguides ($\tau = 1.69 \pm 0.14\,\mathrm{ns}$, $\mathrm{N} = 5$) was not significantly different from the lifetime measured in the bulk-like anchors ($\tau = 1.75 \pm 0.08\,\mathrm{ns}$, $\mathrm{N} = 4$). Both values are in good agreement with the literature[226, 222].

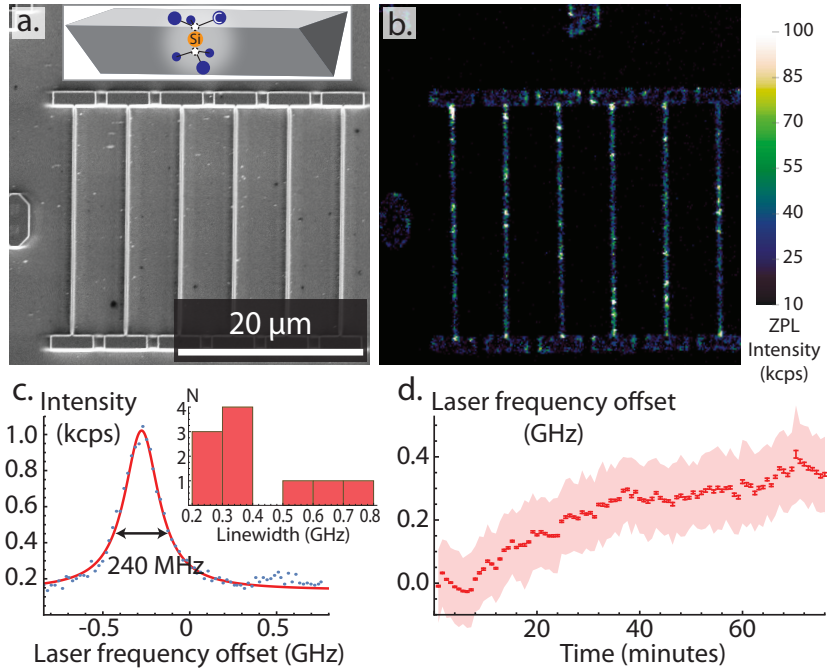

Figure 4.3: SiV centers in nanostructures. **a.** Scanning electron micrograph of six nanobeam waveguides. Inset: schematic of a triangular diamond nanobeam containing an SiV center. **b.** Spatial map of ZPL fluorescence collected by scanning confocal microscopy with off-resonant excitation. Multiple SiV centers are visible in each waveguide. **c.** Linewidth of representative implanted SiV inside a nano-waveguide measured by PLE spectroscopy (blue points: data; red line: Lorentzian fit). Inset: histogram of emitter linewidths in nanostructures. Most emitters have linewidths within a factor of four of the lifetime limit. **d.** Spectral diffusion of the emitter measured in part c. The total spectral diffusion is under 400 MHz even after more than an hour of continuous measurement. This diffusion is quantified by measuring the drift of the fitted center frequency of resonance fluorescence scans as a function of time. Error bars are statistical error on the fitted center position. The lighter outline is the FWHM of the fitted Lorentzian at each time point.

By extracting the center frequency of each individual scan, we also determine the rate of fluctuation of the ZPL frequency and therefore quantify spectral diffusion (Fig. 4.3d). Optical transition frequencies in SiV centers are stable throughout the course of our experiment, with spectral diffusion on the order of the lifetime-limited linewidth even after more than an hour. Characterizing the inhomogeneous distribution of SiV centers in nanostructures is challenging because off-resonant excitation leads to strong background fluorescence, making exhaustive identification of all SiV centers in a given region difficult. Nevertheless, it is easy to find multiple SiV centers in nanostructures at nearly the same resonance frequency: to find the above ten emitters, we scanned the laser frequency over only a 20 GHz range.

The residual broadening of the optical transition can result from a combination of second-order Stark shifts and phonon-induced broadening. The presence of a strong static electric field would result in an induced dipole that linearly couples to charge fluctuations, accounting for the slow diffusion. Finally, we expect that up to 50 MHz of additional broadening could arise from the hyperfine interaction[236] present due to our choice of ^{29}Si ions. Determining the precise mechanisms limiting SiV linewidths is an important topic of future study.

To conclude, we have presented optical emission from implanted SiV centers with a narrow inhomogeneous distribution of SiV optical transition wavelengths and nearly lifetime-limited optical linewidths. These properties persist after nanofabrication, making the SiV center uniquely suited for integration into quantum nanophotonic

devices[223, 237]. Recent advances in diamond fabrication technology[97, 238, 138] suggest the tantalizing possibility of scalably integrating these high-quality implanted SiV centers into nanowire single photon sources[234] or nanocavities[239, 240]. Furthermore, combining our processing procedure with targeted implantation of silicon using a focused ion beam[137] either before or after fabrication[241] could significantly improve photonic device yields and reproducibility by deterministically positioning individual SiV centers in all three dimensions. Our work, combined with the promise of these future advances, could make the SiV center a new workhorse in solid-state quantum optics.

5

An integrated diamond nanophotonics platform for quantum optical networks

Efficient interfaces between photons and quantum emitters are central to applications in quantum science [33, 34] but are challenging to implement due to weak interactions between single photons and individual quantum emitters. Despite advances in the control of microwave and optical fields using cavity and waveguide quantum electrodynamics (QED) [69, 42, 70, 242, 243, 244, 245], the realization of integrated quantum devices where multiple qubits are coupled by optical photons remains an outstanding challenge[44]. In particular, due to their complex environments, solid-state emitters have optical transitions that generally exhibit a large inhomogeneous distribution[246, 44], rapid decoherence[243] and significant spectral diffusion, especially in nanostruc-

tures[71]. Moreover, most solid-state emitters appear at random positions, making the realization of scalable devices with multiple emitters difficult [246, 240].

5.1 Diamond platform for quantum nanophotonics

Our approach uses negatively-charged silicon-vacancy (SiV) color centers[214] integrated into diamond nanophotonic devices. SiV centers in high-quality diamond crystals show nearly lifetime-broadened optical transitions with an inhomogeneous (ensemble) distribution on the order of the lifetime-broadened linewidth[247]. These properties arise from the inversion symmetry of the SiV center which protects the optical transitions from electric field noise in the environment[212, 248].

The stable quantum emitters are integrated into one-dimensional diamond waveguides and photonic-crystal cavities with small mode volumes (V) and large quality factors (Q). These nanophotonic devices are fabricated using angled reactive-ion etching to scalably create free-standing single-mode structures starting from bulk diamond[138]. The fabrication process is described in Appendix C. As an example, Figs. 5.1C and C.3 show structures consisting of a notch for free space-waveguide coupling (at $\sim 1\%$ efficiency), a waveguide section on each side and a cavity (Fig. 5.1B). The measured cavity $Q = 7200\,(500)$ is limited predominantly by decay to the waveg-

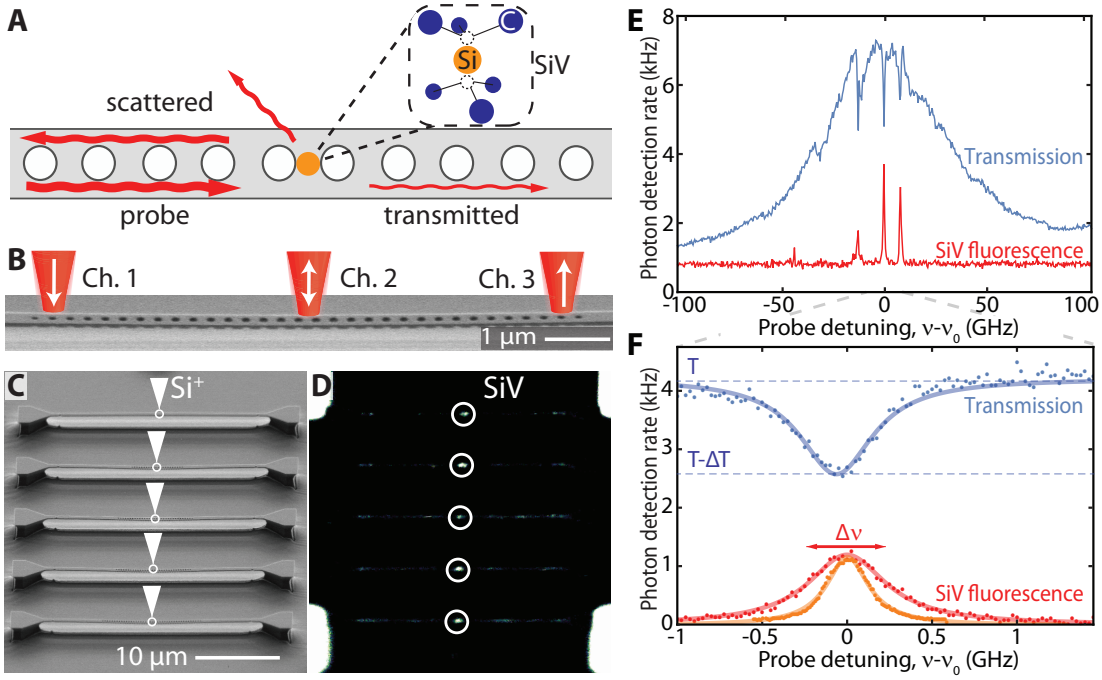

Figure 5.1: Positioning and strong coupling of SiVs in diamond cavities. (A) Schematic of an SiV center in a diamond photonic crystal cavity. (B) Scanning electron micrograph (SEM) of a cavity. (C) SEM of five cavities fabricated out of undoped diamond. After fabrication, SiV centers are deterministically positioned at the center of each cavity using focused Si^+ ion beam implantation. (D) SiV fluorescence is detected at the center of each nanocavity shown in (C). (E) Measured cavity transmission (blue, Ch. 3) and SiV scattered fluorescence (red, Ch. 2) spectrum. Three SiV centers are coupled to the cavity and each results in suppressed transmission. (F) Strong extinction, $\Delta T/T = 38(3)\%$, of probe transmission from a single SiV center. Optical transition linewidths $\Delta\nu$ are measured with the cavity detuned (orange) and on resonance (red, count rate offset by -150 Hz and multiplied by 3.3) with the SiV transition.

uide, so the system has high transmission on resonance. We measure the cavity mode profile and infer $V \sim 2.5(\lambda/n)^3$ using a uniform, high density SiV ensemble (Fig. C.4).

To obtain optimal coupling between an individual SiV and the cavity mode, we use a focused ion beam to implant Si^+ ions at the center of the cavities as illustrated in Fig. 5.1C. To form SiVs and mitigate crystal damage from fabrication and implantation, we subsequently anneal the sample at 1200 °C in vacuum[248]. This targeted implantation technique enables positioning of emitters inside the cavity with close to 40 nm precision in all three dimensions and control over the isotope and average number of implanted Si^+ ions. We fabricate $\sim$ 2000 SiV-cavity nodes on a single diamond sample with optimal spatial alignment. For example, Fig. 5.1D shows fluorescence from the array of cavities implanted with Si^+ ions in Fig. 5.1C. SiV fluorescence is detected at the center of each cavity, demonstrating high-yield creation of SiV-cavity nodes. The number of SiVs created varies based on the number of implanted ions and the $\sim$ 2% conversion yield from Si^+ to SiV. For our experiments, we create an average of $\sim$ 5 SiVs per cavity. Because each SiV can be resolved in the frequency domain, device creation is nearly deterministic: most SiV-cavity nodes can be used for the experiments described below.

We characterize the coupled SiV-cavity system at 4 K using the setup described in Appendix C. As shown in Figs. 5.1B and C.1, three optical beams are focused on the nanostructure to excite the waveguide mode (Channel 1), to detect fluorescence scattering and to control the SiV (Channel 2) and to detect transmission (Channel 3). In

subsequent experiments (Figs. 5.4 and 5.5), efficient collection with a tapered optical fiber is employed. We scan the frequency ν of the weak excitation laser across the SiV resonance $\nu_0 = 406.706\,\text{THz}$ and monitor the transmitted and scattered field intensities (Fig. 5.1E). We observe three fluorescence peaks in Channel 2 from three SiV centers in a single cavity (red curve in Fig. 5.1E). At the same time, within the broad cavity transmission spectrum measured in Channel 3, each of these three resonances results in strong extinction of the cavity transmission indicating that all three SiVs couple to the cavity mode.

The strength of the SiV-cavity coupling is evaluated using the data in Fig. 5.1F. When the cavity is off-resonant with the emitter, the SiV transition linewidth is $\Delta\nu = 298\,(5)\,\text{MHz}$ (orange curve) and the excited state lifetime is $\tau_e = 1.8\,(1)\,\text{ns}$. This is close to the lifetime-broadening limit of 90 MHz with additional nonradiative broadening likely due to a combination of finite-temperature effects[226] and residual spectral diffusion[248]. When the cavity is tuned into resonance, the transition is radiatively broadened to $\Delta\nu = 590\,(30)\,\text{MHz}$ (red curve) with a corresponding measured reduction in lifetime $\tau_e = 0.6\,(1)\,\text{ns}$ (limited by detection bandwidth). At the same time, we find that a single SiV results in 38 (3)% extinction of the probe field in transmission (Fig. 5.1F, blue curve). Based on the radiative broadening shown in Fig. 5.1F, we infer a cooperativity of $C = 4g^2/\kappa\gamma = 1.0\,(1)$ for the SiV-cavity system with cavity QED parameters $\{g, \kappa, \gamma\}/2\pi = \{2.1, 57, 0.30\}\,\text{GHz}$ where g is the single-photon Rabi frequency, κ is the cavity intensity decay rate and γ is the SiV optical transition

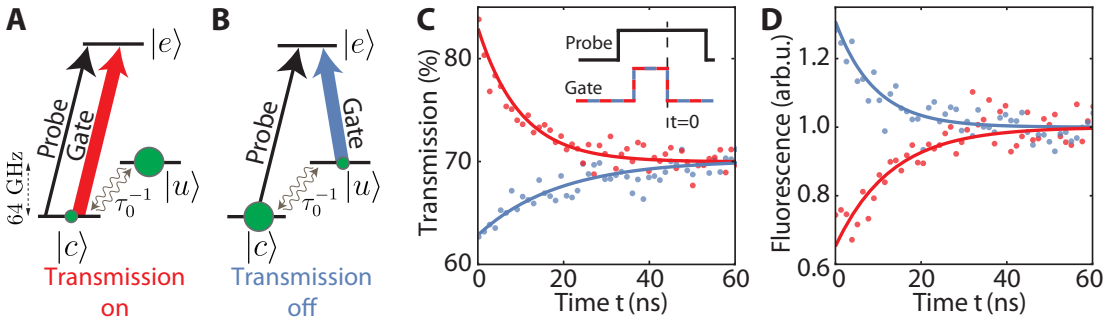

Figure 5.2: An all-optical switch using a single SiV. The transmission of a probe field is modulated using a gate pulse that optically pumps the SiV to state $|u\rangle$ (A) or $|c\rangle$ (B). (C) Probe field transmission measured after the initialization gate pulse. Initialization in state $|u\rangle$ ($|c\rangle$) results in increased (suppressed) transmission, and (D) suppressed (increased) fluorescence.

linewidth.

5.2 Quantum-optical switch based on a single SiV center

The coupled emitter-cavity system can be used to create strong interactions between single photons and achieve single-photon nonlinearities[249, 34]. To probe the nonlinear response of the SiV-cavity system, we repeat the transmission and linewidth measurements of Fig. 5.1F at increasing probe intensities. As expected [250, 249], we find that the system saturates at a level less than a single photon per Purcell-enhanced excited-state lifetime (Fig. 5.3A), resulting in power broadening in fluorescence ($\Delta\nu$) and reduced extinction in transmission ($\Delta T/T$).

We realize an all-optical switch with memory by optically controlling the metastable orbital states[222, 236, 251] of a single SiV (Fig. 5.2). Specifically, we use a 30 ns long gate pulse to optically pump the SiV to an orbital state that is uncoupled ($|u\rangle$, Fig. 5.2A) or coupled ($|c\rangle$, Fig. 5.2B) to a weak probe field resonant with the cavity. The response of the system to the probe field after the gate pulse is monitored both in transmission (Fig. 5.2C) and fluorescence (Fig. 5.2D). If the gate pulse initializes the system in state $|c\rangle$ (blue curves), the transmission is reduced while the fluorescence scattering is increased. Initializing the system in state $|u\rangle$ (red curves) results in increased transmission and reduced fluorescence scattering. The observed modulation demonstrates switching of a weak probe pulse by a classical gate pulse. The switch memory time is limited by a thermal phonon relaxation process between $|c\rangle$ and $|u\rangle$ that depolarizes the system over $\tau_0 \sim 10$ ns at 4 K[226].

To investigate these processes at the single-photon level, we resonantly excite the SiV-cavity system with a weak coherent light and measure photon statistics of the scattered and transmitted fields. To this end, scattered and transmitted light are each split to two detectors (Fig. C.1), allowing us to measure normalized intensity auto-correlations for the scattered ($g^{(2)}_{SS}(\tau)$, Fig. 5.3B) and transmitted ($g^{(2)}_{TT}(\tau)$, Fig. 5.3C) fields as well as cross-correlations between the two channels ($g^{(2)}_{ST}(\tau)$, Fig. 5.3D). At short timescales determined by the excited state lifetime τ_e, we observe strong anti-bunching of photons scattered by the SiV ($g^{(2)}_{SS}(0) = 0.15(4)$), consistent with scattering from a single emitter. In transmission, the photons are strongly bunched with

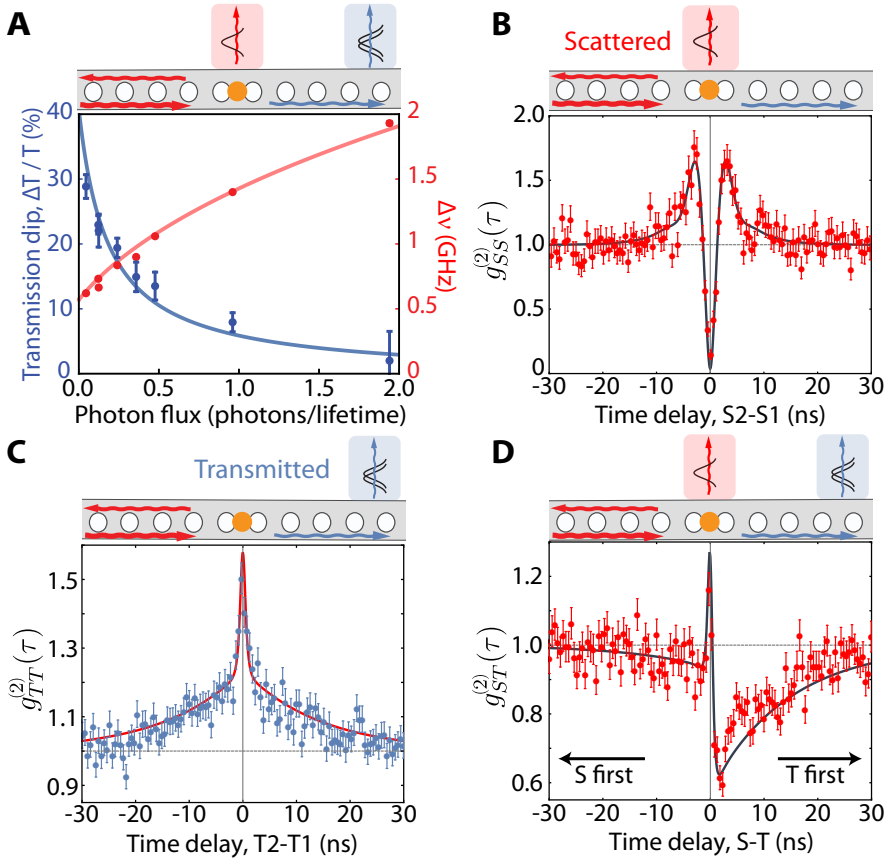

Figure 5.3: Single-photon switching. (A) Cavity transmission and SiV transition linewidth measured at different probe intensities. (B, C) Intensity autocorrelations of the scattered (fluorescence) and transmitted fields. The scattered field shows antibunching (B), while the transmitted photons are bunched with an increased contribution from photon pairs (C). (D) Intensity cross-correlation between the scattered and transmitted fields. $g^{(2)}_{SS}$ is measured under different conditions with above saturation excitation.

$g^{(2)}_{TT}(0) = 1.50(5)$. This photon bunching in transmission results from the interference between the weak probe field and the anti-bunched resonant scattering from the SiV. The destructive interference for single photons yields preferential transmission of photon pairs and is a direct indication of nonlinear response at the single-photon level[250, 249]. In other words, a single photon in an optical pulse switches a second photon, and the system acts as a photon number router where single photons are scattered while photon pairs are preferentially transmitted. Finally, both bunching ($g^{(2)}_{ST}(0) = 1.16(5)$) and anti-bunching are observed for scattering-transmission cross-correlations at fast and slow timescales respectively.

To understand the system saturation and switching responses in Figs. 5.2 and 5.3, we model the quantum dynamics of the SiV-cavity system using the cavity QED parameters measured in Fig. 5.1 and a three-level model of the SiV (Figs. 5.2 and C.7). This model is described in detail in Appendix C. The results of our calculation are in excellent agreement with our observations (solid curves in Figs. 5.1-5.3). Specifically, the presence of a second metastable state, $|u\rangle$, reduces the extinction in linear transmission (Fig. 5.1F) and affects the nonlinear saturation response[249]. The metastable state $|u\rangle$ also causes both slow dynamics in photon correlation measurements (Fig. 5.3) at the metastable orbital relaxation timescale of τ_0 as well as an asymmetry in cross-correlations. In these measurements, the detection of a transmitted (scattered) photon preferentially prepares the SiV in state $|u\rangle$ ($|c\rangle$), resulting in enhanced (reduced) transmission and reduced (enhanced) scattering for τ_0. The per-

formance of our system as an optical switch can be improved by using the spin degree of freedom of the SiV, which can have much longer relaxation and coherence times, especially at low temperatures[252, 214]. We pursue this approach in section 6.4 to realize a switch with longer switching times and higher contrast.

5.3 Tunable single-photon source using Raman transitions.

A key challenge for building scalable quantum networks using solid-state emitters is the spectral inhomogeneity of their optical transitions. Although the inhomogeneous broadening of SiVs is suppressed by inversion symmetry, SiVs inside nanostructures still display a substantial inhomogeneous distribution (seen in Fig. 5.1E) due to residual strain from fabrication[248]. To mitigate this effect, we use Raman transitions between the metastable orbital states of SiV centers. When a single SiV is excited from the state $|u\rangle$ at a detuning Δ (Fig. 4B), the emission spectrum includes a spontaneous component at frequency ν_{ec} and a Raman component at frequency $\nu_{ec} - \Delta$ that is tunable by choosing Δ.

Tunable single-photon emission is experimentally realized by implanting SiVs inside a one-dimensional diamond waveguide and continuously exciting the emitters from free space (Fig. 5.4A). The fluorescence scattering into the diamond waveguide

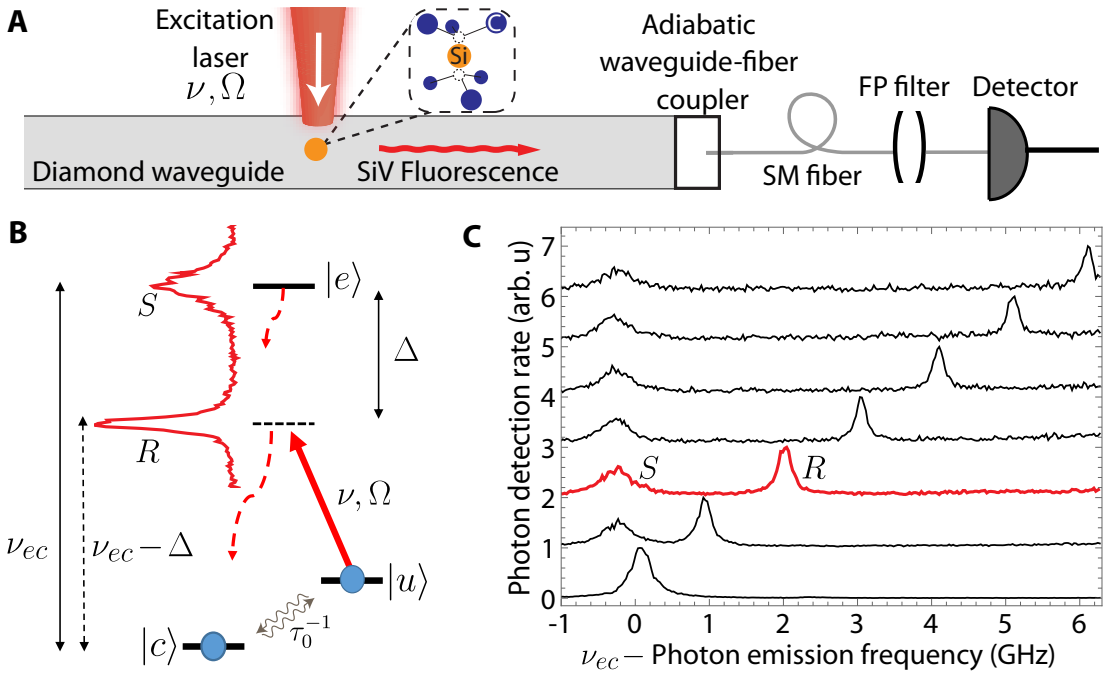

Figure 5.4: Spectrally-tunable single-photons using Raman transitions. (A) Photons scattered by a single SiV into a diamond waveguide are efficiently coupled to a single-mode (SM) fiber. A scanning Fabry-Perot (FP) cavity is used to measure emission spectra. (B) Under excitation at a detuning Δ, the emission spectrum contains spontaneous emission (labeled S) at frequency ν_{ec} and narrow Raman emission (R) at frequency $\nu_{ec} - \Delta$. (C) Δ is varied from 0 to 6 GHz in steps of 1 GHz and a corresponding tuning of the Raman emission frequency is observed. The red curves in (B) and (C) are the same data.

is coupled to a tapered single-mode fiber with $\geq 70\%$ efficiency using adiabatic mode transfer[69, 253, 139]. As we change the excitation frequency from near-resonance to a detuning of $\Delta = 6\,\mathrm{GHz}$, we observe a corresponding tuning of the Raman emission frequency $\nu_{ec} - \Delta$ while the spontaneous emission frequency remains nearly fixed at ν_{ec} up to an AC Stark shift (Figs. 5.4C and C.8).

The Raman linewidth can be controlled by both the detuning and the power of the driving laser, and is ultimately limited by the ground state coherence between states $|u\rangle$ and $|c\rangle$. At large detunings and low power, we measure a subnatural Raman linewidth of less than 30 MHz (Fig. C.8). The nonclassical nature of the Raman emission is demonstrated via photon correlation measurements. The Raman photons from a single SiV are antibunched with $g^{(2)}_{single}(0) = 0.16\,(3)$ (orange curve in Fig. 5.5D) close to the ideal limit $g^{(2)}_{single}(0) = 0$. For the continuous excitation used here, we detect Raman photons at a rate of $\sim 15\,\mathrm{kHz}$ from a single SiV. After a Raman scattering event, the SiV cannot scatter a second photon within the metastable orbital state relaxation timescale τ_0, limiting the Raman emission rate. This rate can be improved using a pulsed excitation scheme where the SiV is first prepared in state $|u\rangle$ via optical pumping and subsequently excited with a pulse of desired shape and duration. Unlike previous demonstrations of Raman tuning of solid-state quantum emitters [254, 255], the tuning range demonstrated here is comparable to the inhomogeneous distribution of the SiV ensemble and can thus be used to tune pairs of SiV centers into resonance.

5.4 Entanglement of two SiV centers in a nanophotonic waveguide

Quantum entanglement is an essential ingredient in quantum networks[33]. Although optical photons were recently used to entangle solid-state qubits over long-distances[64, 256], optically-mediated entanglement of solid-state qubits in a single nanophotonic device has not yet been observed.

Motivated by the proposals for probabilistic entanglement generation based on interference of indistinguishable photons[257], we use two SiV centers inside a diamond waveguide (Fig. 5.5A), continuously excite each SiV on the $|u\rangle \rightarrow |e\rangle$ transition with a separate laser, and measure photon correlations in the waveguide mode. If the Raman transitions of the two SiVs are not tuned into resonance, the photons are distinguishable, resulting in the measured $g^{(2)}_{dist}(0) = 0.63\,(3)$ (blue curve in Fig. 5.5D) close to the conventional limit associated with two single photon emitters $g^{(2)}_{dist}(0) = 0.5$ [212]. Alternatively, if the Raman transitions of the two SiVs are tuned instead into resonance with each other, an interference feature is observed in photon correlations around zero time delay with $g^{(2)}_{ind}(0) = 0.98\,(5)$ (red curve in Fig. 5.5D).

These results can be understood by considering the level diagrams in Figs. 5.5B and 5.5C involving the SiV metastable states $|u\rangle$ and $|c\rangle$[258, 244]. Photon correlation measurements probe the conditional dynamics of the two SiVs starting in state $|uu\rangle$.

In this state, each SiV scatters Raman single photons to the waveguide at a rate Γ_{1D}. However, when the Raman transitions of the two SiVs are tuned into resonance with each other, it is fundamentally impossible to distinguish which of the two emitters produced a waveguide photon. Thus, emission of an indistinguishable single photon leaves the two SiVs prepared in the entangled state $|B\rangle = (|cu\rangle + e^{i\phi}|uc\rangle)/\sqrt{2}$ [257] (Fig. 5.5B), where ϕ is set by the propagation phase between emitters spaced by ΔL and the relative phase of the driving lasers which is constant in each experimental run (Fig. C.9). This state is a two-atom superradiant Dicke state with respect to the waveguide mode, independent of the value of ΔL[258]. This implies that although there is only a single excitation stored in the state $|B\rangle$, it will scatter Raman photons at a rate $2\Gamma_{1D}$ that is twice the scattering rate of a single emitter. This enhanced emission rate into the waveguide mode results in the experimentally observed interference peak at short time delays (Fig. 5.5D) and is a signature of entanglement. Our measured value of $g^{(2)}_{ind}(0) = 0.98\,(5)$ is close to the ideal limit where the factor of two enhancement in the emission from the entangled state $|B\rangle$ yields $g^{(2)}_{ind}(0) = 1$.

The visibility of the interference signal in photon correlation measurements in Fig. 5.5D can be used to evaluate a lower bound on the conditional entanglement fidelity $F = \langle B|\rho|B\rangle$. For experimental runs where we detect a photon coincidence within the interference window (rate $\sim 0.5\,\mathrm{Hz}$), we find that the two SiVs were in an entangled state with $F \geq 82(7)\%$ after the emission of the first photon. This conditional fidelity is primarily limited by laser leakage and scattering from nearby SiVs

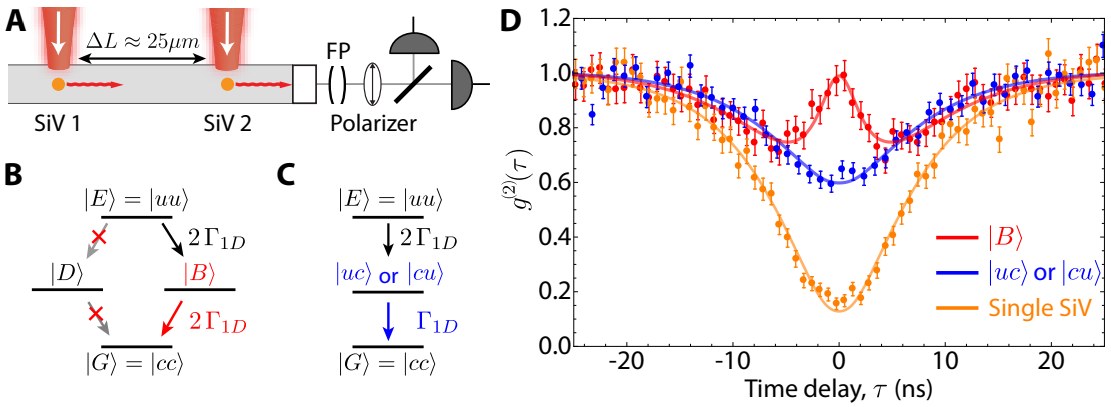

Figure 5.5: Quantum interference and two-SiV entanglement in a nanophotonic waveguide. (A) Photons scattered by two SiV centers into a diamond waveguide are detected after a polarizer. (B) After emission of an indistinguishable photon, the two SiVs are in the entangled state $|B\rangle$ which decays at the collectively enhanced rate of 2 Γ_{1D} into the waveguide. (C) After emission of a distinguishable photon, the two SiVs are in a classical mixture of states $|uc\rangle$ and $|cu\rangle$ which decays at a rate Γ_{1D} into the waveguide. (D) Intensity autocorrelations for the waveguide photons. Exciting only a single SiV yields $g^{(2)}_{single}(0) = 0.16\,(3)$ for SiV1 (orange data), and $g^{(2)}_{single}(0) = 0.16\,(2)$ for SiV2. Blue: Both SiVs excited; Raman photons are spectrally distinguishable. Red: Both SiVs excited; Raman photons are tuned to be indistinguishable. The observed contrast between the blue and the red curves at $g^{(2)}(0)$ is due to the collectively enhanced decay of $|B\rangle$. The solid curves are fits to a model described in Appendix C.

that yield false detection events. Our measurements also demonstrate entanglement generation (rate $\sim 30\,\mathrm{kHz}$) after a single Raman photon emission event. As discussed in Appendix C, using photon correlation data and steady state populations of SiV orbital states, we find that a single photon emission results in an entangled state with positive concurrence $\mathcal{C} > 0.090\,(0.024)$, which is limited by imperfect initialization in state $|uu\rangle$. The width of the interference signal in Fig. 5.5D can be used to extract a lifetime $T_2^* \approx 2.5\,\mathrm{ns}$ of the entangled state $|B\rangle$. This lifetime is mainly limited by imperfect spectral tuning of the two Raman photons from the two SiVs, resulting in a relative frequency detuning δ. In this regime, emission of a first photon results in a state $|\psi(\tau)\rangle = (|cu\rangle + e^{i(\phi-2\pi\delta\tau)}|uc\rangle)/\sqrt{2}$ that oscillates at frequency δ between states $|B\rangle$ and the subradiant state $|D\rangle = (|cu\rangle - e^{i\phi}|uc\rangle)/\sqrt{2}$. Since $|D\rangle$ does not couple to the waveguide mode due to destructive interference, fluctuations in δ over different realizations result in decay of the collectively enhanced signal (central peak in red curve in Fig. 5.5D).

Note that in our experiment, the photon propagation time is longer than T_2^* and the entangled state dephases before it can be heralded by detection of the first photon. To generate useful heralded entanglement with high fidelity[257, 256], a pulsed excitation scheme can be employed where the two SiVs are optically initialized in state $|uu\rangle$ and excited by short pulses. The Raman emission frequencies can be further stabilized using a narrowband reference cavity to extend the lifetime of the entangled state.

5.5 Outlook

The performance of these quantum nanophotonic devices can be improved in several ways. Control over the SiV orbital states is limited by the occupation of ∼50 GHz phonons at 4 K, which causes relaxation between the metastable orbital states $|u\rangle$ and $|c\rangle$ and limits their coherence times to less than 50 ns. Phonon relaxation can be significantly suppressed by operating at temperatures below 500 mK or engineering the phononic density of states to enable millisecond-long coherence times[226, 252]. Even longer-lived quantum memories can potentially be obtained by storing the qubit in the ^{29}Si nuclear spin[236] which is only weakly coupled to the environment[55]. Furthermore, the demonstrated cooperativity in our nanocavity experiment is lower than the theoretical estimate based on an ideal two-level emitter optimally positioned in a cavity. The discrepancy is due to a combination of factors including imperfect spatial and polarization alignment, phonon broadening[226], finite quantum efficiency[240], the branching ratio of the transition and residual spectral diffusion[248]. These imperfections also limit the collection efficiencies obtained in our waveguide experiments. Despite uncertainties in individual contributions which are discussed in Appendix C, operation at lower temperatures and improved cavity designs with higher Q/V ratios should enable spin-photon interfaces with high cooperativity $C \gg 1$. Furthermore, the efficient fiber-diamond waveguide coupling can be improved to exceed 95% efficiency [253]. Despite these areas of potential improvement, this chapter demonstrates

key ingredients required for realizing integrated quantum network nodes and opens up new possibilities for realizing large-scale systems involving multiple emitters strongly interacting via photons.

6

Photon-mediated interactions between two quantum emitters in a diamond nanophotonic cavity

6.1 Introduction

Photon-mediated interactions between quantum emitters are an important building block of many quantum information systems. These interactions enable entanglement generation and quantum logic operations involving both stationary quantum bits (qubits) and photons [33]. Recent progress in the field of cavity quantum electrodynamics (QED) with trapped atoms and ions [42], superconducting qubits [259],

and self-assembled quantum dots [44] has opened up several avenues for engineering and controlling such interactions. In particular, coherent coupling between multiple qubits mediated via a cavity mode has been demonstrated in the microwave domain using circuit QED [260, 261, 262]. This method is now an essential element[263] of superconducting quantum processors[16, 15]. Extending such coherent coupling into the optical domain could enable the implementation of key protocols in long-distance quantum communication and quantum networking [36, 29, 81]. Recently, two-ion[264] and two-atom[265, 266] systems have been used to observe cavity-modified collective scattering. Spectral signatures of cavity-mediated interactions between quantum dots have also been reported [267, 268]. However, the realization of controlled, coherent optical interactions between quantum emitters is challenging. This is especially the case in the solid state due to inhomogeneous broadening of the optical transition and decoherence introduced by the environment [268, 44].

6.2 High-cooperativity SiV-cavity devices

We realize controllable optically-mediated interactions between negatively-charged silicon-vacancy (SiV) color centers coupled to a diamond photonic crystal cavity (Fig. 1A) [269]. The SiV center in diamond is an atom-like quantum emitter featuring nearly lifetime-limited optical linewidths with low inhomogeneous broadening, both in bulk [212] and, crucially, in nanostructures [248]. Moreover, the SiV has electronic spin

states that form a qubit with >10 ms coherence times at temperatures below 500 mK [252]. SiVs are integrated into devices consisting of a one-dimensional freestanding diamond waveguide with an array of holes defining a photonic crystal cavity with quality factor $Q \sim 10^4$ and simulated mode volume $V \sim 0.5 \left(\frac{\lambda}{n=2.4}\right)^3$ (Fig. 1B) [139]. SiVs are positioned in these devices with 40 nm precision by targeted implantation of ^{29}Si ions using a focused ion beam, yielding around 5 SiV centers per device [269]. One end of the diamond waveguide is tapered and adiabatically coupled to a tapered single-mode fiber, enabling collection efficiencies from the waveguide into the fiber of more than 90% [139]. These devices are placed in a dilution refrigerator with an integrated confocal microscope (see section D.1.1). By working at 85 mK, we completely polarize the SiV into the lowest-energy orbital state[252] used in this work. We also apply an up to 10 kG vector magnetic field to lift the SiV spin degeneracy[252, 214]. To control the SiV-cavity detuning ($\Delta = \omega_{\mathrm{SiV}} - \omega_c$), we tune the cavity resonance frequency ω_c using gas condensation (see section D.1.4).

The coupling between SiV centers and the nanophotonic cavity is characterized by scanning the frequency of an excitation laser incident on one side of the device while monitoring the intensity of the transmitted field into the collection fiber. The resulting transmission spectrum of the SiV-cavity system (Fig. 1C, upper spectrum) reveals strong modulation of the bare cavity response resulting from the coupling of multiple spectrally-resolved SiVs to the cavity mode. For instance, two SiVs near the cavity resonance each result in almost-full extinction of the transmission through the

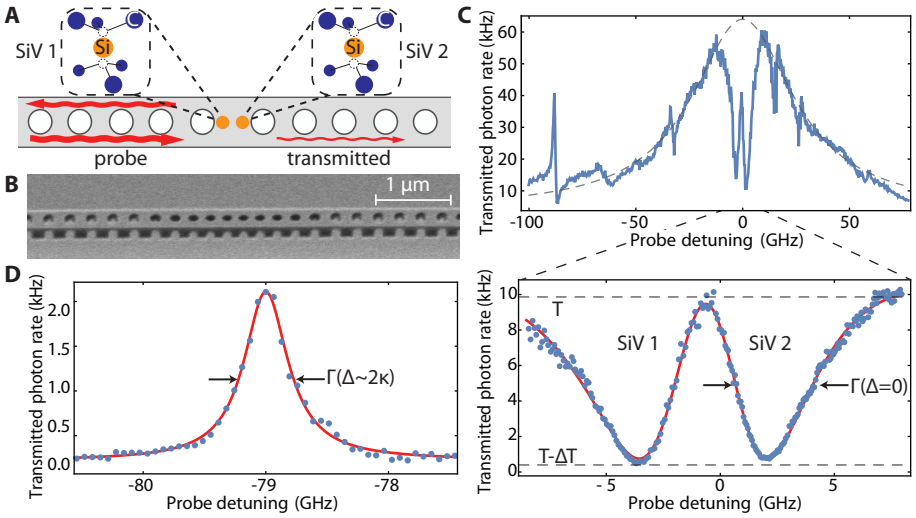

Figure 6.1: **High cooperativity SiV-photon interface. (A)** Multiple SiVs are deterministically positioned in a nanophotonic cavity which is probed in transmission. **(B)** Scanning electron micrograph of a diamond nanophotonic cavity. **(C)** Transmission spectrum of the coupled SiV-cavity system (blue). The broad Lorentzian response of an empty cavity (dashed) is modulated by SiVs coupled to the cavity. Near the cavity resonance (lower panel), two SiVs each result in greater than 95% extinction in transmission and are broadened by the Purcell effect ($\Gamma(\Delta = 0) = 4.6\,\mathrm{GHz}$). **(D)** Far detuned from the cavity resonance ($\Delta = 79\,\mathrm{GHz}$), individual SiVs appear as narrow peaks in transmission ($\Gamma(2\kappa) = 0.5\,\mathrm{GHz}$). The solid lines in (D) and the lower panel of (C) are fits to a model (see section D.2).

cavity ($\Delta T/T > 95\%$; Fig. 1C, lower spectrum) [79]. In contrast, when the cavity frequency is detuned from the SiV by several cavity linewidths (κ), the transmission spectrum shows a narrow peak near each SiV frequency (Fig. 1D). This resonance corresponds to an SiV-like polariton of the strongly-coupled SiV-cavity system featuring a high transmission amplitude. We also observe that the resonance linewidth (Γ) changes by more than an order of magnitude depending on the SiV-cavity detuning (Δ). These observations can be understood in terms of Purcell enhancement, which predicts $\Gamma(\Delta) \approx \gamma + \frac{4g^2}{\kappa}\frac{1}{1+4\Delta^2/\kappa^2}$ where g is the single-photon Rabi frequency, κ is the cavity energy decay rate and γ is twice the decoherence rate due to free-space spontaneous emission and spectral diffusion. For the most strongly-coupled SiV in this device, we measure linewidths ranging from $\Gamma(0) = 2\pi \times 4.6$ GHz on resonance to $\Gamma(7\kappa) = 2\pi \times 0.19$ GHz $\approx \gamma$ when the cavity is far detuned. From these measurements, we extract the cavity QED parameters $\{g, \kappa, \gamma\} = 2\pi \times \{7.5, 50, 0.19\}$ GHz. The key cavity-QED figure of merit is the cooperativity $C = \frac{4g^2}{\kappa\gamma}$, which expresses the coherent interaction rate relative to the decoherence rates. We find $C = 23$ for this SiV (see section D.3). This order-of-magnitude improvement in SiV-cavity cooperativity over previous work [269] primarily results from the decreased mode volume of the cavity.

6.3 Photon-mediated interactions between two SiVs

As is evident from Fig. 1C, SiV centers are subject to inhomogeneous broadening, resulting predominantly from local strain within the nanophotonic device[248]. This broadening is significantly below that of other solid-state emitters[44] when compared to the lifetime-limited emitter linewidths.In fact, the resonance frequencies of some SiVs within the same devices are nearly identical.To study the cavity-mediated interaction between SiVs, we focus on a pair of such nearly-resonant SiVs (two-SiV detuning $\delta = 0.5\,\mathrm{GHz}$) that are coupled to the cavity in the dispersive regime, that is, with large SiV-cavity detuning ($\Delta = 79\,\mathrm{GHz} > \kappa$, Fig. 2A). To identify resonances associated with individual SiVs, we selectively ionize either SiV into an optically-inactive charge state by applying a resonant laser field at powers significantly higher than those used to probe the system. This allows us to measure the transmission spectrum for each SiV individually (Fig. 2A, gray data) while holding fixed the other parameters (such as Δ) in the experiment. The spectrum from each SiV corresponds to transmission via an SiV-like polariton, as in Fig. 1D.

When both SiVs are in the optically-active charge state, we observe an increased splitting of the peaks in transmission. These new resonances (Fig. 2A, black data) display different transmission amplitudes compared with the single-SiV resonances, and are accordingly labeled as superradiant bright ($|S\rangle$) and subradiant dark ($|D\rangle$) states.

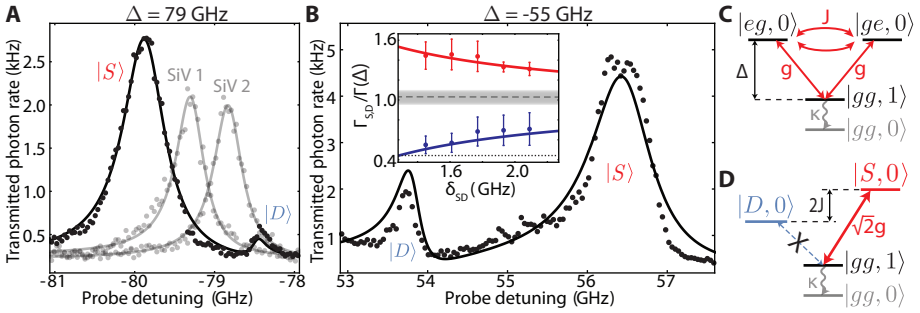

Figure 6.2: **Cavity mediated SiV-SiV interactions. (A)** Transmission spectrum of two nearly-resonant SiVs (SiV-SiV detuning $\delta = 0.56\,\text{GHz}$) at cavity detuning $\Delta = 79\,\text{GHz}$. Individual spectra of non-interacting SiVs are shown in gray. When both SiVs are simultaneously coupled to the cavity, superradiant (bright) $|S\rangle$ and subradiant (dark) $|D\rangle$ collective states are formed (black). **(B)** Transmission spectrum of the same SiVs at an opposite cavity detuning $\Delta = -55\,\text{GHz}$ and $\delta = 2\,\text{GHz}$. The $|S\rangle$ / $|D\rangle$ energy splitting δ_{SD} is reversed. Inset: ratio of $|S\rangle$ (red) and $|D\rangle$ (blue) state linewidths to the single-SiV linewidth at $\Delta = 79\,\text{GHz}$ as a function of δ_{SD}. The resonance frequencies of these SiVs slowly drift due to spectral diffusion[248], allowing us to measure the linewidths of the superradiant and subradiant states at different δ_{SD}. State $|S\rangle$ ($|D\rangle$) has a radiatively enhanced (suppressed) linewidth compared to the measured single-SiV linewidths. The gray dashed line and shaded region are the average and standard deviation of the single-SiV linewidths. The dotted line corresponds to the SiV linewidth γ without Purcell enhancement, demonstrating that the subradiant state at minimum δ_{SD} is almost completely decoupled from the cavity mode. Solid lines in (A) and (B) are predictions based on independently-measured SiV parameters (see section D.4.4). **(C)** SiV-SiV-cavity energy diagram. Two SiVs are detuned from the cavity by Δ, are resonant with each other and are each coupled to the cavity with single-photon Rabi frequency g. The two SiVs interact via exchange of a virtual cavity photon at a rate $J = g^2/\Delta$, forming collective $|S\rangle$ and $|D\rangle$ eigenstates **(D)**.

Moreover, we observe that the amplitudes and linewidths of $|S\rangle$ ($|D\rangle$) are enhanced (suppressed) compared to those of the individual SiVs (Fig. 2B, inset). At a cavity detuning of the opposite sign ($\Delta = -55\,\mathrm{GHz}$), we observe that the sign of the energy splitting δ_{SD} between $|S\rangle$ and $|D\rangle$ is reversed (Fig. 2B), indicating that the cavity resonance affects δ_{SD}.

To understand these observations, we consider the system of two SiV centers coupled to a cavity mode, described by the Hamiltonian[270, 260]:

$$\hat{H}/\hbar = \omega_c \hat{a}^\dagger \hat{a} + \omega_1 \hat{\sigma}_1^\dagger \hat{\sigma}_1 + \omega_2 \hat{\sigma}_2^\dagger \hat{\sigma}_2 + \hat{a}^\dagger \left(g_1 \hat{\sigma}_1 + g_2 \hat{\sigma}_2\right) + \hat{a}(g_1^* \hat{\sigma}_1^\dagger + g_2^* \hat{\sigma}_2^\dagger)$$

where ω_c and ω_i are the frequencies of the cavity and SiV i and the operators $\hat{a}$ and $\hat{\sigma}_i$ are the annihilation operators for the cavity and SiV-i excitations. The coherent evolution of $\hat{H}$ is modified by the decay of the cavity field (κ) and SiV decoherence (γ) (see section D.2). For $C \gg 1$, the coherent SiV-cavity coupling dominates and a single SiV will strongly couple to the cavity mode and significantly modify the cavity response.

In the dispersive regime, $\hat{H}$ yields an effective Hamiltonian for two resonant SiVs[270, 260]: $\hat{H}_{\text{eff}}/\hbar = \hbar J \left(\hat{\sigma}_1 \hat{\sigma}_2^\dagger + \hat{\sigma}_1^\dagger \hat{\sigma}_2\right)$ where $J = \frac{g^2}{\Delta}$. Thus, the two SiVs interact at a rate J via a flip-flop interaction that is mediated by the exchange of cavity photons (Fig. 2C). (In our system, $g_1 \approx g_2 \equiv g$.) This interaction hybridizes the two resonant SiVs, forming collective eigenstates: $|S\rangle = \frac{1}{\sqrt{2}}(|eg\rangle + |ge\rangle)$ and $|D\rangle = \frac{1}{\sqrt{2}}(|eg\rangle - |ge\rangle)$ split in energy by $2J$ (Fig. 2D) [260]. The symmetric superradiant state $|S\rangle$ has an

enhanced coupling to the cavity of $\sqrt{2}g$ and an increased Lamb shift of $2J = 2\frac{g^2}{\Delta}$, whereas the antisymmetric combination $|D\rangle$ is, in the ideal limit, decoupled from the cavity ("dark" in transmission) and has zero Lamb shift [268, 260]. This Lamb shift is always away from the cavity mode, explaining the reversed energy difference δ_{SD} between states $|S\rangle$ and $|D\rangle$ upon changing the sign of Δ (Fig. 2B). By comparing the data for the two nearly-resonant SiVs in Fig. 2 to theoretical predictions (Fig. 2, solid curves) based on independently measured SiV-cavity parameters, we extract the SiV-SiV interaction strength $J = 0.6\,\mathrm{GHz}$. The energy difference $\delta_{SD} \geq 2J$ is larger than the measured state linewidths (for a single SiV, $\Gamma(\Delta) = 0.4\,\mathrm{GHz}$), allowing us to spectrally resolve these states.

6.4 Coupling of the SiV spin degree of freedom to the cavity

We next demonstrate deterministic control over this two-SiV interaction using the long-lived SiV electronic spin degree of freedom[214]. We access the SiV spin by applying a magnetic field to lift the degeneracy of the spin sublevels in the lower-energy orbital branches of the ground (spin states $|\uparrow\rangle$ and $|\downarrow\rangle$) and optically-excited ($|\uparrow'\rangle$ and $|\downarrow'\rangle$) states. The Zeeman shifts are different for each orbital state and depend on both the magnitude and orientation of the field with respect to the SiV symmetry axis,

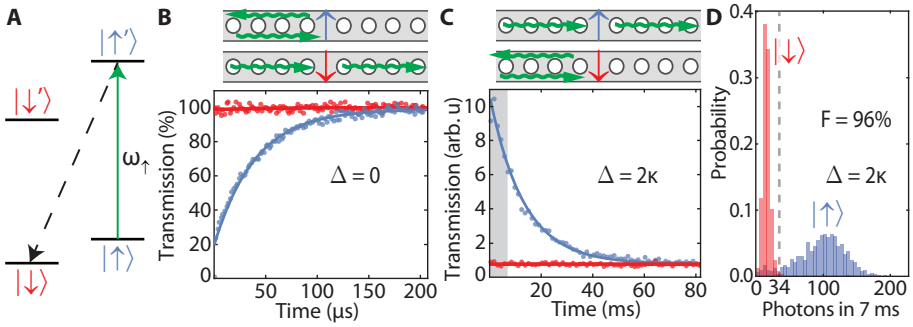

Figure 6.3: **Cavity-assisted spin initialization and readout. (A)** Simplified level structure of the SiV in a magnetic field. An optical transition at frequency $\omega_\uparrow$ (green arrow) is used to initialize the SiV spin into $|\downarrow\rangle$ by optical pumping via a spin-flipping transition (dashed line). Conversely, pumping at frequency $\omega_\downarrow$ (not shown) initializes the spin into $|\uparrow\rangle$. **(B)** Spin-dependent optical switching on cavity resonance. State $|\downarrow\rangle$ is not coupled to the probe field at frequency $\omega_\uparrow$ which is therefore transmitted (red). Initialization into $|\uparrow\rangle$ results in reflection of the probe field (blue). The maximum spin-dependent contrast is 80%. **(C)** Spin-dependent optical switching in the dispersive regime. For state $|\downarrow\rangle$ / $|\uparrow\rangle$, the probe is reflected/transmitted (red/blue). **(D)** Photon number distributions for transmission in the dispersive regime for initialization into $|\uparrow\rangle$ (blue) and $|\downarrow\rangle$ (red). The distributions are well-resolved (mean $n_\uparrow = 96$, $n_\downarrow = 16$) in a 7 ms readout window (gray region in **(C)**), demonstrating single-shot spin-state readout with 96% fidelity.

yielding spectrally-distinguishable spin-selective optical transitions at frequencies $\omega_\uparrow$ and $\omega_\downarrow$ (Fig. 3B). In general, the splitting between these frequencies is maximized for large off-axis magnetic fields[214]. Also, any off-axis magnetic field component, the optical transitions are not perfectly cycling. The presence of this spin-flipping decay means the SiV spin can be initialized into $|\uparrow\rangle$ by pumping at $\omega_\downarrow$ and vice versa[236, 222]. Both spin-selective transitions couple to the cavity mode with a similar strength $\sim g$, enabling high-contrast spin-dependent modulation of the cavity transmission.

We demonstrate this effect by focusing on a single SiV in both the resonant-cavity and dispersive regimes. For the first case, we tune the cavity near the SiV resonance. In this regime, the SiV optical transitions are Purcell-broadened, so we apply a large off-axis magnetic field to resolve them. We then initialize the SiV in either $|\downarrow\rangle$ or $|\uparrow\rangle$ via optical pumping (Fig. 3A). Finally, we probe the cavity at frequency $\omega_\uparrow$, which is resonant with both the cavity and the $|\uparrow\rangle \rightarrow |\uparrow'\rangle$ transition (Fig. 3B). When the spin is prepared in the state $|\downarrow\rangle$, the probe field at $\omega_\uparrow$ is detuned from the SiV transition and is transmitted (red curve). When the spin is prepared in $|\uparrow\rangle$, it couples to the probe field at frequency $\omega_\uparrow$ and the incoming light is reflected (blue curve) [79]. We observe a maximum spin-dependent transmission contrast of 80%, limited by spectral overlap between the two spin transitions. The memory time of this modulation (50 μs) is limited by the cyclicity of the spin-conserving optical transition addressed by the probe pulse in this highly off-axis field. By repeating this experiment in the dispersive regime ($\Delta \sim 2\kappa$), we can reverse the behavior of the cavity-spin system (Fig. 3C). Here, the SiV linewidth is narrow, allowing us to resolve the optical transitions in a 9 kG magnetic field aligned along the SiV axis. In this regime, the transitions are highly ($\sim 10^4$) cycling[252].When the spin is in $|\downarrow\rangle$, the interaction with the field at $\omega_\uparrow$ is negligible and the probe is reflected by the detuned cavity (red curve). When the spin is in $|\uparrow\rangle$, single photons at frequency $\omega_\uparrow$ are transmitted via the SiV-like polariton (blue curve) for a time (12 ms) determined by the higher aligned-field cyclicity [252]. We construct a histogram of photons detected in a 7 ms window when the spin

is initialized in $|\uparrow\rangle$ (red) and $|\downarrow\rangle$ (blue) (Fig. 3D). The photon count distributions for the two spin states are well-resolved, allowing us to determine the spin state in a single shot with 96% fidelity (see section D.5).

6.5 A spin-dependent photon-mediated interaction between two SiVs

The combination of spin control, high-cooperativity coupling and a relatively small inhomogeneous distribution of SiVs provides a platform for controlling optically-mediated interactions between multiple SiVs. We focus on two SiVs (SiV 1 and 2 in Fig. 1) in the dispersive regime ($\Delta = 109\,\text{GHz}$) with cavity QED parameters $\{g_1 \approx g_2, \kappa, \gamma_1 \approx \gamma_2\} = 2\pi \times \{7.3, 39, 0.5\}$ GHz that are initially detuned from one another by $\delta = 5\,\text{GHz}$. We sweep the magnitude of a magnetic field oriented almost orthogonal to the SiV symmetry axis and tune transitions $|\uparrow_1\rangle \rightarrow |\uparrow_1'\rangle$ and $|\downarrow_2\rangle \rightarrow |\downarrow_2'\rangle$ (which have opposite Zeeman shifts) in and out of resonance (Fig. 4A). At each magnetic field, we use a continuous field Ω_1 or Ω_2 to pump either SiV 1 or SiV 2 into the spin state resonant with a weak probe field Ω_p. We then measure the transmission spectrum of the system. This allows us to perform control measurements where only one spin is addressed by Ω_p at a time (gray data in Fig. 4B). The single-spin transmission spectra at each field are summed to form a composite spectrum of the non-interacting

two-SiV system (Fig. 4C). This composite spectrum shows a crossing of the two SiV transitions.

Next, we measure the system in the interacting case by pumping the spins into the state $|\uparrow_1\rangle|\downarrow_2\rangle$ by applying both Ω_1 and Ω_2, and probe the system transmission using probe field Ω_p. The two-SiV transmission spectrum demonstrates the formation of superradiant and subradiant states (Fig. 4B, black) that exist only for this combination of spin states. Transmission spectra as a function of the applied magnetic field are shown in (Fig. 4D), demonstrating an avoided crossing of the spin-selective optical transitions arising from the interaction between the spins[260]. We use the independently-measured SiV-cavity parameters to calculate the energies of $|S\rangle$ and $|D\rangle$ (red and blue solid lines) and the full avoided-crossing (Fig. 4E). We find good agreement with the experimental data. These observations were reproduced in a separate device on the same chip (see section D.6.5).

6.6 Outlook

The optically-mediated interaction between quantum emitters observed here could be used to realize key quantum information protocols, including cavity-assisted entanglement generation[270, 81], efficient Bell-state measurements[79, 36] and robust photon-mediated gates between emitters in distant cavities [32, 29]. To efficiently implement these schemes, qubits should be encoded in long-lived SiV electronic spin

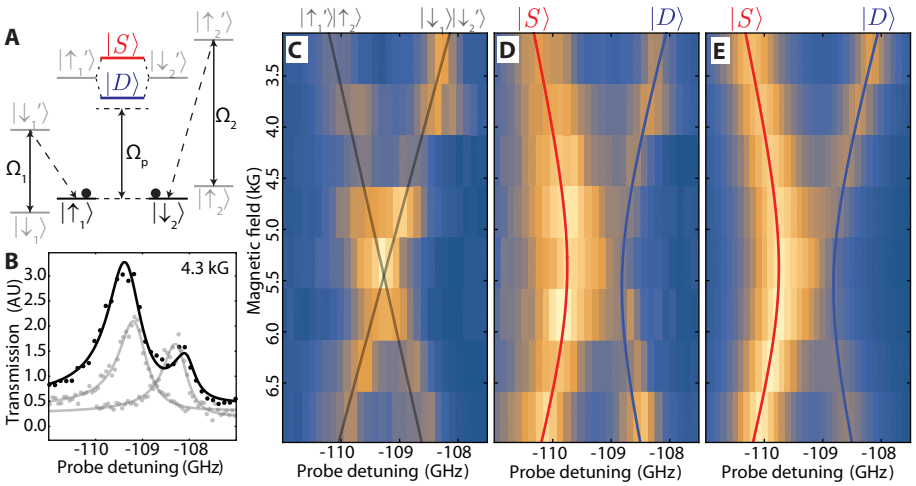

Figure 6.4: **Spin-dependent avoided crossing. (A)** Two-SiV level structure in a magnetic field. The $|\uparrow_1\rangle \rightarrow |\uparrow_1'\rangle$ and $|\downarrow_2\rangle \rightarrow |\downarrow_2'\rangle$ transitions are tuned by sweeping a magnetic field. The spins are pumped with control fields Ω_1 and Ω_2, and the cavity transmission spectrum is measured by sweeping the frequency of a weak probe field Ω_p. When the spins are initialized in $|\uparrow_1\rangle|\downarrow_2\rangle$, collective super- ($|S\rangle$) and subradiant ($|D\rangle$) states are formed. **(B)** Spin-dependent transmission spectra at a magnetic field of 4.3 kG. Spectra of single SiVs in the noninteracting case are shown in gray. The spectrum of two interacting SiVs (black) demonstrates formation of $|S\rangle$ and $|D\rangle$. **(C)** Composite spectrum of the non-interacting system at different two-SiV detunings. The solid lines are the fitted single-SiV energies of $|\uparrow_1'\rangle|\uparrow_2\rangle$ and $|\downarrow_1\rangle|\downarrow_2'\rangle$ as a function of magnetic field. **(D)** An avoided crossing is visible in cavity transmission when we prepare the spins in the interacting state $|\uparrow_1\rangle|\downarrow_2\rangle$. **(E)** Predicted transmission spectrum for independently measured SiV-cavity parameters. The red and blue solid lines in (D) and (E) are predicted energies of $|S\rangle$ and $|D\rangle$ based on these parameters (see section D.6).

states. Recent work has already demonstrated that the SiV spin can be used as a long-lived quantum memory[252] that can be coherently manipulated with both microwave[252, 271] and optical fields[251]. The fidelity associated with cavity-mediated quantum operations between such qubit states is critically limited by the cavity cooperativity[36, 81]. While the cooperativity $C \sim 20$ achieved in this work is among the largest demonstrated in the optical domain, it can be further improved by at least two orders of magnitude by increasing the cavity Q/V or by reducing sources of spectral diffusion which limit γ. Alternatively, the cooperativity could be enhanced by using different quantum emitters, such as GeV[100] or SnV[103] centers in diamond, which feature significantly higher quantum efficiencies[101]. Furthermore, more efficient protocols have recently been suggested, enabling high fidelity operations even with the present cooperativity levels. For example, near-unity fidelities are possible with existing cooperativities using heralded schemes where gate errors can be limited by error detection using an auxilary qubit[272]. In addition, our system could be used to efficiently generate non-classical states of light [273], which can be useful in, for example, measurement-based quantum computing. In particular, high photon bandwidth and on-chip scalability make our system particularly well-suited for quantum networking, paving the way for implementation of efficient quantum repeaters[37, 36] and distributed quantum computing[29].

7

Conclusion

The challenge of creating a scalable platform for quantum networking is considerable and requires simultaneously satisfying many diverse requirements. In some ways, building a quantum network is an even more formidable task than building a quantum computer; in addition to requiring a system of well-controlled qubits, a quantum network must also couple such qubits strongly to optical photons. As we saw in chapter 2, although nitrogen-vacancy centers are long-lived spin qubits, engineering coherent optical properties for implanted NVs even in bulk diamond is a major challenge. The limitations on the NV center optical coherence allowed us to achieve only a low cooperativity of $C \sim 3 \times 10^{-3}$, despite significant work understanding the sources of electronic noise (and other negative effects) from the diamond surface (chapter 3).

In the later chapters of the thesis, we used the silicon-vacancy center to circumvent these challenges by relying on its insensitivity to environmental electric-field noise.

First, we demonstrated the production of SiVs with coherent optical properties and a low inhomogeneous distribution of optical transition wavelengths, even for implanted SiVs in nanostructures (chapter 4). This opened up the possibility of engineering a high-cooperativity interface between SiVs and photons using a diamond nanophotonics platform (chapter 5).[1] Finally, by achieving higher cooperativities and working at lower temperatures, we were able to demonstrate spin-dependent optically-mediated interactions between two SiVs in a single diamond nanocavity (chapter 6).

In the introduction (Section 1.1), we discussed three criteria for an effective node of a quantum network: high-cooperativity qubit-photon interactions, a long-lived spin-degree of freedom and controllable interactions between multiple qubits within the node. In this framework, we can understand the advantage of the NV center as fulfilling the second (and, under some circumstances, the third[65]) of these criteria, with the spin-selective optical transitions of the NV suggesting that the first could also be achieved. Unfortunately, spectral- and charge- stability in nanostructures precluded straightforward realization of this goal. By using the SiV center, on the other hand, we were able to fulfill the first criterion and additionally harness the strong SiV-photon coupling to achieve the third criterion.

To address the second criterion, it was predicted[226] and then experimentally con-

[1]The key advance enabling this work was indeed the intrinsically superior optical properties of the SiV arising from its inversion symmetry. In fact, the diamond cavity fabrication process [138] described in chapter 5 (and section C.2.2) was already fairly mature at the time of the work described in chapter 2 with NVs.

firmed[252] that by working at temperatures less than 500 mK, the SiV spin degree of freedom can be used as a qubit with coherence times exceeding 10 ms. In our most recent work (chapter 6), we are in fact working at these temperatures with the hope of combining our advances with control over the SiV spin degree of freedom. Integrating microwave[252, 271] and/or optical[251] control over the SiV spin with our nanophotonics platform is an exciting direction of active research. This would allow the three criteria for a quantum network node to be realized in a single solid-state platform for the first time.

The work presented in this thesis opens up new possibilities for scalable quantum networking and quantum information processing. In particular, our system of multiple qubits interacting with optical photons is an essential element for local protocols important for quantum repeater architectures, including deterministic cavity-assisted entanglement generation[270, 81] and efficient Bell-state measurements[36]. These schemes can be readily extended to implement robust photon-mediated gates between emitters in distant cavities [32, 29, 274]. Finally, this system could be used for efficient generation of squeezed[275] states and 2D cluster states[273] of light, which are useful resources for metrology and measurement-based quantum computing[276]. These proposals are feasible with the cavity QED parameters demonstrated in chapter 6 when combined with spin control, and their fidelities can be further enhanced by increasing the cooperativity of the SiV-cavity system. The cooperativity can be improved by increasing the cavity Q/V or by reducing sources of spectral diffusion

which limit γ. Achieving the latter goal will require renewed focus on the material properties of the diamond, possibly using some of the tools developed in chapter 3 for the NV center.

Alternatively, the cooperativity could be enhanced by using different quantum emitters, such as GeV[100] or SnV[103] centers in diamond, which are also spin-$\frac{1}{2}$ systems featuring inversion symmetry and therefore have many similar properties to the SiV. Both the GeV and SnV feature significantly higher quantum efficiencies[101] than the SiV, directly translating into an improvement in the cooperativity of the system via a decrease in the nonradiative decay rate contributing to γ (see section 2.3). Finally, there is the possibility of discovering novel color centers that have even more advantageous properties. Recent work on the SiV^0 (as opposed to the SiV^- discussed here) has suggested that the SiV^0 has both a spin-triplet ground state (like the NV^-) and also features inversion symmetry (like the SiV^-)[277, 217, 278]. In such a spin-triplet system, the spin and orbital components of the wavefunction are decoupled, allowing for long spin coherence times at non-cryogenic temperatures. Although it has not yet been confirmed that the SiV^0 has suitable optical properties, exploring the large space of vacancy-impurity complexes in diamond[279, 50] represents a promising avenue of future research.

A different direction for work with the SiV color center is to harness the large ground-state coupling between the orbital and spin degrees of freedom. Although for most applications this coupling is a nuisance that decreases the SiV spin coherence

time[226], it can be an asset when the SiV electronic orbital degrees of freedom are manipulated deliberately using mechanical (strain) fields. The simplest example of this is the use of static strain fields to tune the optical transitions of multiple SiVs into resonance, effectively circumventing the inhomogeneous distribution of optical transition wavelengths[280, 68]. Higher levels of strain can enable longer spin coherence times by increasing the splitting, and therefore the relevant energy and temperature scale, between the orbital levels that participate in phonon-induced spin decoherence[280]. Finally, the large coupling strength of the SiV spin to strain can be used to realize direct spin-phonon interactions where phonons are used as a bus for transporting quantum information within a local device [281, 282, 283]. The SiV is therefore a promising system for optomechanics and quantum acoustics.

Looking forward, the work presented in this thesis acts both as a template for future work with the SiV and, in contrast, as a reminder about the importance of exploring new systems. Feedback between the fundamental physics of these systems and their applications in quantum information processing is essential. For example, our attempts to develop a platform for solid-state quantum optics based on the NV center led us to a particular appreciation of having a system insensitive to electric-field noise. Future developments with the SiV should therefore go hand-in-hand with a flexible exploration of new color centers and platforms for nanophotonics.

A

Supporting material for Chapter 3

A.1 RHEED Calibration

To calibrate the length scales observed in our RHEED patterns, we analyze a sample with a known structure, orientation, and diffraction pattern. Then we measure the distance in pixels from the center of the specular spot to the diffraction streak. This distance is compared to the known periodicity of the sample. This measurement gives a conversion factor between pixels and inverse Ångströms that can be applied to other samples. This procedure can be repeated with different substrates at different angles to independently compute this conversion factor. This calibration factor was used to determine the distances found in section 3.3.5.

In this case, we performed our calibration with gadolinium scandate and lanthanum strontium aluminum tantalum oxide (LSAT) bulk crystal substrates along the (100)

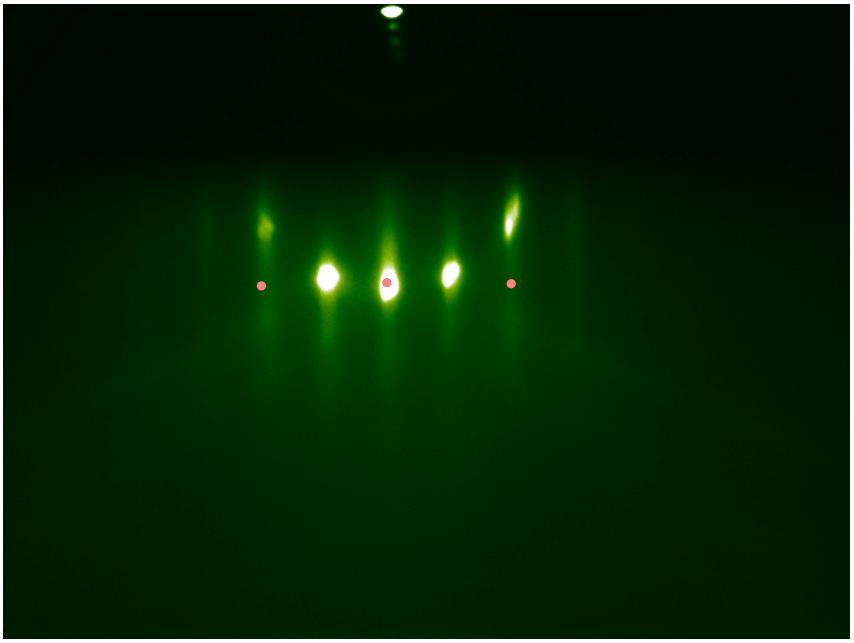

Figure A.1: RHEED pattern produced by gadolinium scandate ($GdScO_3$) (100), looking along the [100] direction. The spots used for calibration are marked in pink. This distance corresponds to a known periodicity of 3.965 Å.

and (110) directions for each. These four measurements give a conversion factor of 368.0 ± 5.6Å·pixels. The uncertainty in this calibration corresponds to 1.5%. This error could probably be improved with more robust fitting methods. See Figures A.1 to A.4.

Using different substrates for the calibration also helps eliminate the possibly that a single particular substrate or orientation is misidentified. In our case, all four images across two samples gave the same calibration factor within 2%. Only a systematic failure to properly identify *any* of the four patterns (*i.e.* misidentifying all of them) could explain this calibration error.

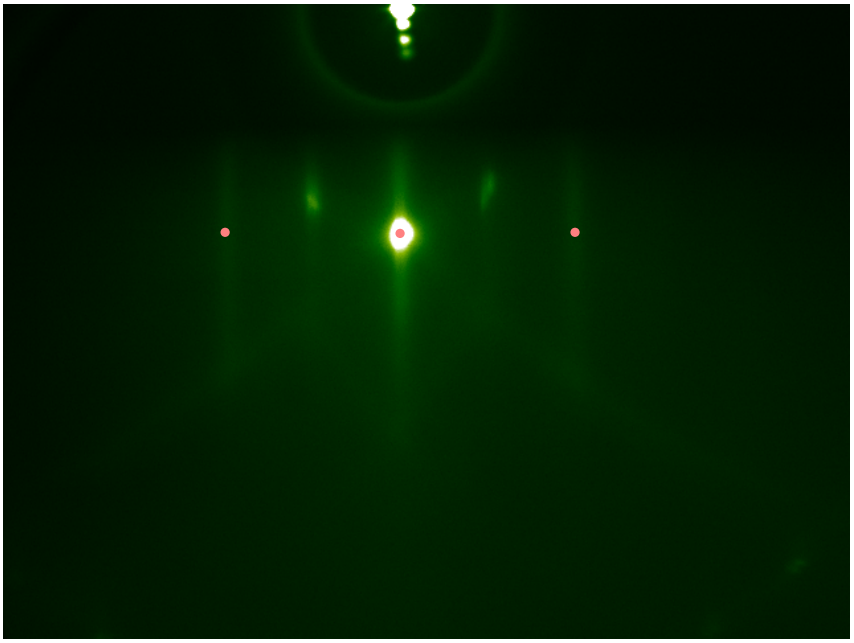

Figure A.2: RHEED pattern produced by gadolinium scandate ($GdScO_3$) (100), looking along the [110] direction. The spots used for calibration are marked in pink. This distance corresponds to a known periodicity of 2.8037 Å.

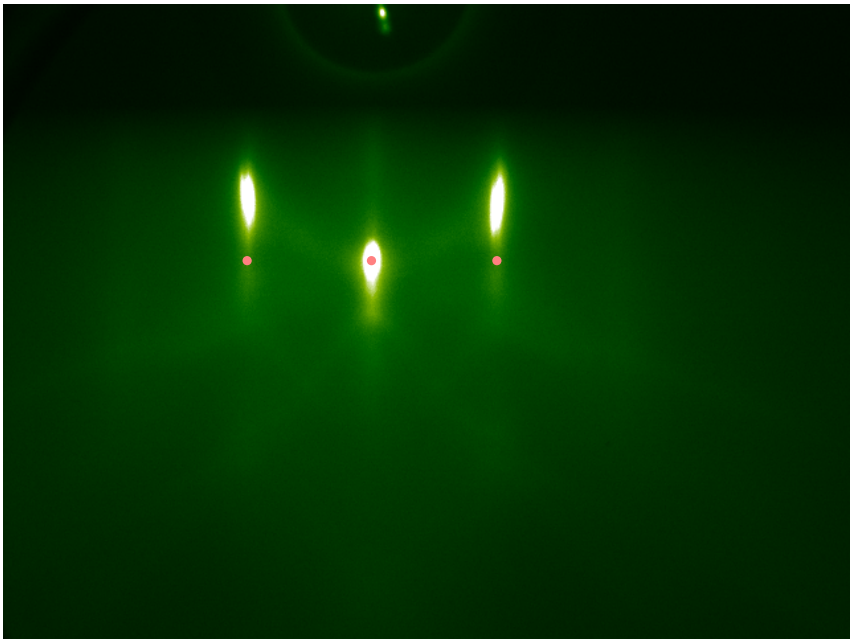

Figure A.3: RHEED pattern produced by lanthanum strontium aluminum tantalum oxide (LSAT) (110), looking along the [100] direction. The spots used for calibration are marked in pink. This distance corresponds to a known periodicity of 3.868 Å.

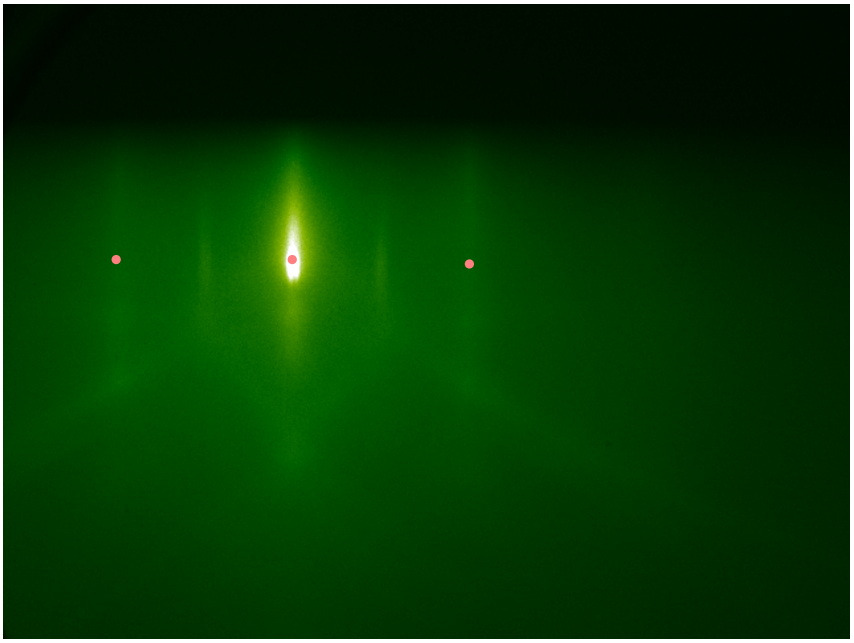

Figure A.4: RHEED pattern produced by lanthanum strontium aluminum tantalum oxide (LSAT) (100), looking along the [110] direction. The spots used for calibration are marked in pink. This distance corresponds to a known periodicity of 2.6987 Å.

A.2 XPS Background and methodology

This section includes additional technical details on fitting the XPS spectra in section 3.4. First, we will the physical processes that contribute to the shapes of the XPS peaks and background and discuss some of the challenges of developing good models for XPS data. Then, we will discuss an implementation of these techniques and our general strategy for data analysis.

A.2.1 An overview of peak shapes and fitting in XPS

Ideally, all peaks in the XPS spectra are lifetime-limited Lorentzians with peak widths around 0.1 eV. However, any distribution in the excitation photons, lack of precision in the energy electron analyzer or charging effects from an insulating sample can all broaden the peak further. Typically, these broadening effects contribute Gaussian noise. Hence the observed lineshape is typically a Lorentzian profile from the intrinsic lifetime convolved with a Gaussian profile from the instrumental response. The resulting curve is known as a Voigt profile[284] and is frequently used in the spectroscopy community[285, 286, 287]. Unfortunately, there is no closed-form analytic expression for the Voigt profile, which makes numerical peak-fitting more challenging. Over the years, many excellent approximations to the Voigt profile have been developed to aid peak fitting[287, 288, 289]. More complicated asymmetric peak profiles are necessary to fit conductive samples.

Background subtraction also plays an important role in fitting XPS data and can introduce some additional subtleties, in spectra with a large number of peaks. Using a linear background can give acceptable results, but is often replaced with the Shirley background. In the Shirley background the total background level is proportional to the integrated peak area at higher kinetic energies (lower binding energies)[290, 291, 292]. This technique has the great advantages of being generally effective, well-motivated physically and relatively simple to implement. More sophisticated methods are also sometimes used[293, 294, 295, 296, 297].

Even with proper background subtraction and a robust peak fitting procedure, interpreting XPS spectra is challenging, especially when several subpeaks are fitted to a single broad peak to extract quantitative information about the peak's constituent chemical components. Fortunately, there are many formal[158] and informal resources[298, 299, 300] available. Here are a few guidelines extracted from these sources and tailored towards fitting peaks on diamond with the Thermo-Fisher Kα XPS system available at Harvard.

1. When fitting multiple subpeaks to a single peak to extract chemical state information, all of the subpeaks should have similar widths. In general, the broadening mechanisms that apply to one species will apply to another.
2. Peak positions and widths should not change appreciably when looking at similar samples. In fact, a "standard" sample can be used to fix the relative peak positions (and possibly widths) which can then be constrained and used to fit the other samples.
3. Instrumental response and charging seem to be significant. As a result, Lorentzians

often produce quite poor fits to the data. Gaussians do much better while (necessarily), Voigt functions do the best. If the instrumental response dominates, Gaussians are sometimes sufficient.

A.2.2 Peak fitting methodology

To aid in peak fitting, I have developed a package for *Mathematica* that performs Multi-peak-fitting for Gaussian, Lorentzian, and Voigt functions quickly and efficiently with few free parameters. It includes options to import the data from the Microsoft Excel files outputted by our Thermo-Fisher Kα XPS instrument as well as tools to constrain the positions of peaks and perform Shirley background subtraction. More information, including the code, documentation and example files is freely available[301].

The general fitting procedure is as follows:

1. Import the uncorrected data from the files exported by the instrument.
2. For each peak, recenter the data around its maximum value and normalize it. This makes fitting the data more reliable.
3. Remove the extreme boundaries of the data by looking at only $\pm 5\,\mathrm{eV}$ around the peak. This makes the fitting less sensitive to variations in the background far away from the peak itself.
4. Perform a Shirley background subtraction.
5. Fit peaks to this corrected spectrum:

(a) Write down a sum of several peaks with variable amplitudes, widths, and positions as a model

(b) Constrain these parameters to lie within physically reasonable boundaries.

(c) Use differential evolution to minimize the RMS difference between the model and the data. Typical values are around 1-2%.

(d) Check to make sure that the constraints in (b) are not reached, in other words that we have reached at least a local minimum, and that this local minimum is as good or better than a fit without constraints.

(e) Check to make sure that an equally good fit is not obtained with fewer peaks, *i.e.* that the model is the most parsimonious for the given data. See figure A.5. Figure A.6 includes goodness-of-fit data for the fits to our spectra.

6. Once the fit is performed, the global positions of the subpeaks across different datasets can be compared by adding back the value subtracted in step 2. Alternatively, the subpeak positions can all be compared to the central peak position in each dataset.

7. Statistical tests can be performed to compare various properties of the models for different samples, process histories, or dates. In particular, we examine the:

   (a) Relative weights and positions of different subpeaks within the carbon and oxygen peaks

   (b) Carbon-oxygen peak separation

   (c) Carbon-oxygen peak weights

A.2.3 Statistical tests

We use the Komolgorov-Smirnov test to distinguish between the various distributions of peaks corresponding to different process histories. This is a (parameter free) test

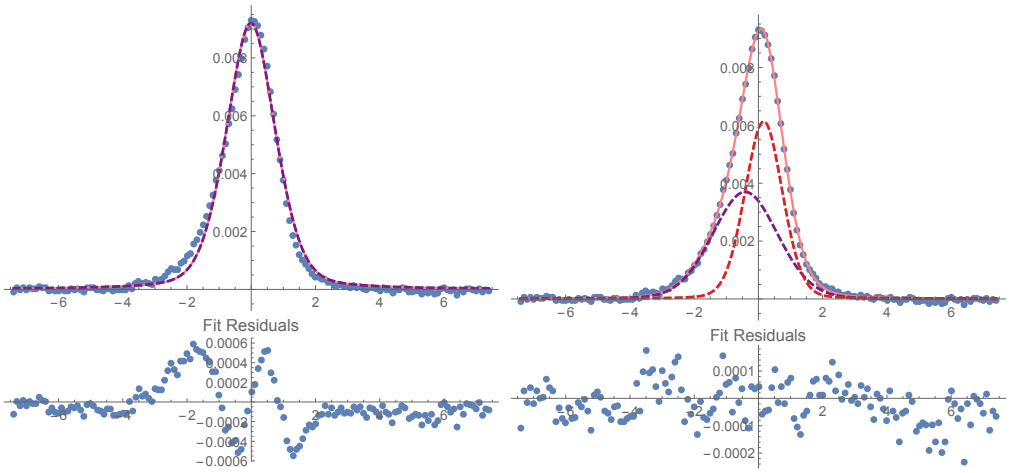

(a) Single peak fit (b) Double peak fit

Figure A.5: Comparison between single- and double-peak fits for an example O(1s) spectrum after Shirley background subtraction. The fit quality improves for the double-peak fit. Quantitatively, the average (across many fits) RMS residual value decreases from 8.2% to 2.8%. There is no significant improvement from adding additional peaks: going from two to five peaks only decreases the average RMS residual value from 2.76% to 2.65%.

that tells us the likelihood that two distributions are the same. We are also interested in knowing if the two distributions have statistically distinct means, which is a stricter condition. To answer this question, we use the Kruskal-Wallis one-way analysis of variance.

Note that the standard t-test is appropriate only if the data are normally distributed. Our data often fail standard tests for normality, so the t-test is not appropriate.[1] If it is used, however, it gives results that qualitatively agree with the Komolgorov-Smirnov test.

[1]This is why we use the nonparametric Kruskal–Wallis one-way analysis of variance instead of the traditional (parametric) ANOVA which is equivalent to a t-test for two samples.

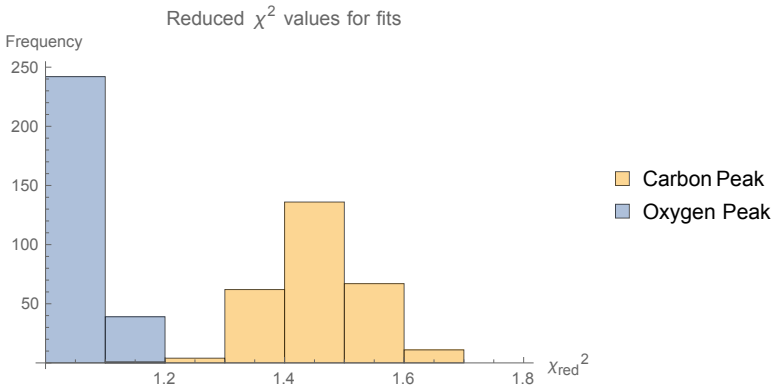

(a) Histogram of χ^2_{reduced} values. The mean is $\chi^2 = 1.455$ for the carbon peak and 1.084 for the oxygen peak.

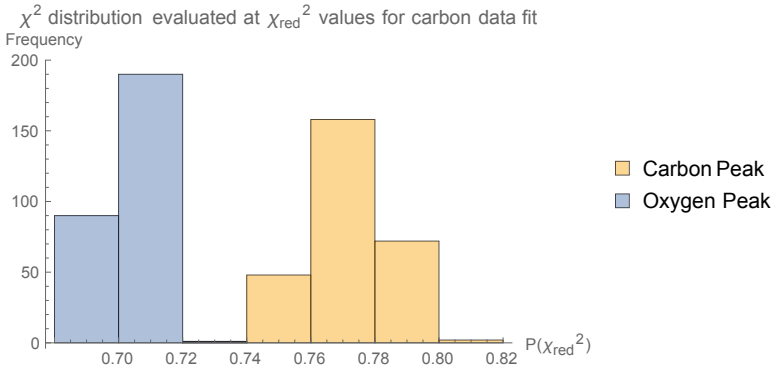

(b) Histogram of p values taken from the χ^2 distribution. The mean is $p = 77.2\%$ for the carbon peak and 70.2% for the oxygen peak.

Figure A.6: Histogram of χ^2_{reduced} values and corresponding p values for fits to the carbon and oygen peaks. There are 78 degrees of freedom for each of the carbon fits and 140 for each of the oxygen fits.

In all of these cases, we perform the tests only on the relative weights of the different sub-peaks and not their positions. This should constitute a strictly more challenging test of statistical significance than including all of the multidimensional data, and in any case it is not clear what physical meaning to assign to small differences in the

sub-peak positions.

	ta	t	an	ae	f
ta	μ=0.052214 σ=0.00747727 N=15	p_{K-S}=0.729e p_{K-W}=0.503e	p_{K-S}=1.56e-8 p_{K-W}=2.35e-9	p_{K-S}=0.00477e p_{K-W}=0.0222e	p_{K-S}=3.62e-6 p_{K-W}=0.0000554e
t	p_{K-S}=0.729e p_{K-W}=0.503e	μ=0.0539461 σ=0.00825004 N=33	p_{K-S}=2.68e-11 p_{K-W}=6.05e-15	p_{K-S}=0.000841e p_{K-W}=0.0323e	p_{K-S}=1.03e-7 p_{K-W}=9.36e-6
an	p_{K-S}=1.56e-8 p_{K-W}=2.35e-9	p_{K-S}=2.68e-11 p_{K-W}=6.05e-15	μ=0.0758427 σ=0.00639081 N=26	p_{K-S}=4.68e-7 p_{K-W}=3.81e-10	p_{K-S}=2.39e-7 p_{K-W}=5.08e-7
ae	p_{K-S}=0.00477e p_{K-W}=0.0222e	p_{K-S}=0.000841e p_{K-W}=0.0323e	p_{K-S}=4.68e-7 p_{K-W}=3.81e-10	μ=0.0536495 σ=0.00185293 N=7	p_{K-S}=0.000503e p_{K-W}=0.00147e
f	p_{K-S}=3.62e-6 p_{K-W}=0.0000554e	p_{K-S}=1.03e-7 p_{K-W}=9.36e-6	p_{K-S}=2.39e-7 p_{K-W}=5.08e-7	p_{K-S}=0.000503e p_{K-W}=0.00147e	μ=0.0104839 σ=0.0223401 N=11

Figure A.7: Summary statistical data for oxygen concentrations described in figure 3.13 and table 3.4. The sample processes are as follows: “ta” means terminated then acid cleaned, “t” means terminated, “an” means annealed and then acid cleaned, “ae” means etched and then acid cleaned and “f” means annealed and then immediately analyzed without acid cleaning. For each of the processing histories, the diagonal gives the mean oxygen concentration, standard deviation, and size of each dataset. The off-diagonal elements give the Komolgorov–Smirnov and Kruskal–Wallis p-values comparing each of the processing steps. The off-diagonal elements are displayed in red when the p-values are less than 0.05.

A.3 Infrared Spectroscopy

I will first provide a very brief overview of infrared spectroscopy with an emphasis on diamond surface analysis. Then, I’ll focus on previous work on understanding diamond surface chemistry with infrared spectroscopy.

A.3.1 Details of the technique

Fourier-transform infrared spectroscopy, or FTIR, is a technique to determine the chemical composition of a sample by measuring the vibrational excitations of func-

	Term	Anneal-Acid	Term-Acid	Etch-Acid
Term	μ=0.218654 σ=0.116805 N=33	p_{K-S}=2.47e-9 p_{K-W}=1.53e-8	p_{K-S}=0.237e p_{K-W}=0.423e	p_{K-S}=0.274e p_{K-W}=0.162e
Anneal-Acid	p_{K-S}=2.47e-9 p_{K-W}=1.53e-8	μ=0.419895 σ=0.0774526 N=26	p_{K-S}=3.66e-8 p_{K-W}=1.38e-11	p_{K-S}=3.75e-6 p_{K-W}=1.95e-7
Term-Acid	p_{K-S}=0.237e p_{K-W}=0.423e	p_{K-S}=3.66e-8 p_{K-W}=1.38e-11	μ=0.203575 σ=0.0573041 N=15	p_{K-S}=0.868e p_{K-W}=0.659e
Etch-Acid	p_{K-S}=0.274e p_{K-W}=0.162e	p_{K-S}=3.75e-6 p_{K-W}=1.95e-7	p_{K-S}=0.868e p_{K-W}=0.659e	μ=0.214676 σ=0.0461908 N=7

(a) Carbonyl peak at -1.1 eV

	Term	Anneal-Acid	Term-Acid	Etch-Acid
Term	μ=0.781346 σ=0.116805 N=33	p_{K-S}=2.47e-9 p_{K-W}=1.53e-8	p_{K-S}=0.237e p_{K-W}=0.423e	p_{K-S}=0.274e p_{K-W}=0.162e
Anneal-Acid	p_{K-S}=2.47e-9 p_{K-W}=1.53e-8	μ=0.580105 σ=0.0774526 N=26	p_{K-S}=3.66e-8 p_{K-W}=1.38e-11	p_{K-S}=3.75e-6 p_{K-W}=1.95e-7
Term-Acid	p_{K-S}=0.237e p_{K-W}=0.423e	p_{K-S}=3.66e-8 p_{K-W}=1.38e-11	μ=0.796425 σ=0.0573041 N=15	p_{K-S}=0.868e p_{K-W}=0.659e
Etch-Acid	p_{K-S}=0.274e p_{K-W}=0.162e	p_{K-S}=3.75e-6 p_{K-W}=1.95e-7	p_{K-S}=0.868e p_{K-W}=0.659e	μ=0.785324 σ=0.0461908 N=7

(b) C-O peak

Figure A.8: Summary statistical data for relative oxygen subpeak concentrations described in figure 3.14 and table 3.5.

tional groups. Bonds between the atoms in these functional groups can stretch and bend with resonant frequencies that depend on the stiffness of the bond and the masses of the atoms making up the bond. Double bonds are stiffer than single bonds, and masses of common chemical species can be quite different (compare hydrogen to oxygen). FTIR makes it easy to distinguish among C-H bonds, C-O bonds, and C=O bonds, for example. Because these vibrational modes are localized, the oscillator strength of a given excitation is generally independent of the rest of the molecule. It is therefore possible to quantitatively determine which functional groups are present in the sample and in what ratio.

The energy scales of infrared photons in FTIR spectra are usually expressed in terms of inverse centimeters, often called wavenumbers. Wavenumbers are units of

energy; 100 cm^{-1} corresponds to a wavelength of $\lambda = \frac{1}{100 cm^{-1}} = 100\mu m$. FTIR spectra typically run from 500 cm^{-1} = 20 μm = 62 meV = 720 K = 15 THz to 3000 cm^{-1}= 3.3 μm = 372 meV = 4370 K = 90 THz.

In addition to localized modes, extended vibrations (the fundamental modes of a whole molecule, for example) can also be excited by infrared light. These low-energy modes are difficult to interpret, but often act as a "fingerprint" of the molecule as a whole. These modes are often well separated spectrally from the high-energy localized vibrational modes of single functional groups; the region from 500 cm^{-1} to 1500 cm^{-1} is called the "fingerprint region" for this reason.

A.3.2 IR Reflection Spectroscopies

Instead of measuring absorption, the reflection from the surface of a sample can be measured; in the case of diffuse reflection, this technique is known as Diffuse Reflection InfraRed Fourier Transform (DRIFT) spectroscopy. For measuring thick samples on top of a reflective surface (for example, a dielectric deposited on a metal), a reflection measurement at near-normal incidence is essentially a double-pass transmission measurement. Finally, grazing angles can be used to probe very thin films on reflective surfaces. Like all useful surface characterization tecniques, this method has several acronyms. It is known as reflection-absorption infrared spectroscopy (RAIRS) or occasionally IR Reflection Absorption Spectroscopy (IRRAS). RAIRS is a highly

sensitive technique, capable of detecting sub-monolayer coverage[302] on reflective substrates. (More specialized techniques—such as SNIFTIRS—can be identified by their increasingly baroque acronyms.)

RAIRS has a few geometrical considerations that make it different from transmission spectroscopy in some important respects. First, recall that the component of the electric field in the plane of the surface undergoes a π phase shift upon reflection. At a grazing angle, *s*-polarized light has the electric field nearly in the plane of the sample, so at the point of contact the sum of electric fields from the incident and reflected photon go nearly to zero, wheras *p*-polarized light has its interaction enhanced. [2] Hence, RAIRS is only sensitive to vibrations where the transition dipole is perpendicular to the surface. This fact is known as the "surface selection rule."

Nonreflective surfaces can be directly analyzed by exploiting total internal reflection. In this technique, known as attenuated total reflection (ATR), the sample is brought into contact with a high-index crystal, typically germanium (n = 4) or diamond (n = 2.47 in the visible and IR[303]). The IR light is reflected off of the surface of the crystal that is in contact with the sample. As a result, only an evanescent wave escapes into the sample, characterizing only the surface of the sample.

The penetration depth into the crystal (the $\frac{1}{e}$ decay distance of the amplitude) is given by:

[2] See Figures 7.11 and 7.12 in Ref. [158].

$$d = \frac{\lambda}{2\pi n_1 \sqrt{\sin^2\theta - (n_2/n_1)^2}}$$

where n_1 is the index of the substrate, n_2 is the index of the sample, and λ is the wavelength of light (which varies from 3-20 μm in a single measurement.)

In practice, this means that ATR relies crucially on two factors: the angle of incidence and the index mismatch between the sample and the ATR crystal. Both of these should be large. For a diamond sample and a germanium ATR crystal, the angle inside the germanium crystal must be greater than about 38°. Finally, note that because the penetration depth depends strongly on the wavelength, an isotropic sample will show more absorption (due to greater optical depth) at longer wavelengths. [3] Although the penetration depth can still be large compared to the true surface of the sample, it is still possible to use standard ATR techniques to characterize the top few nanometers of the sample.[199]

A.3.3 Previous work on diamond surfaces with IR spectroscopy

The possible FTIR peaks for diamond are summarized in table A.1. Pioneering work by Ando et al. on diamond powder gives a good overview of possible surface functionalizations[204]. In particular, the authors perform oxygen annealing at a wide

[3] Most FTIR analysis packages have a tool to correct for this effect.

Table A.1: Table of FTIR peaks in diamond and other useful materials. Theoretical values can differ substantially (more than 100 cm^{-1}) from experimental values.

$\tilde{\nu}$ (cm^{-1})	Assignment	Notes
891	Si-C on DLC film	Questionable Reference.[304]
1000-1250	C-H on diamond surface	Theory. Should also see peak at 2800-2970.[305]
1068	Si-O-Si asymmetric stretch	Not on diamond surface.[205]
1106	C-O-C stretch on diamond surface	Should also see peak at 1264.[204] Possibly Si-O-Si?[304]
1264	C-O-C stretch on diamond surface	Should also see peak at 1106.[204]
1332	C-C lattice peak from defects	A perfect diamond lattice has inversion symmetry.[204]
1360-1500	Oxygen related. Ionic carbonate?	Peak of band is at 1444. Assignment disputed.[204, 306]
1405	C-H bend in bulk	Not correlated with total concentration.[153]
1570	C=C Stretch in DLC film	Often many peaks. Assignment uncertainty.[304]
1594	Water	Present if poor background correction
1640-1660	C-O bend, diamond powder	Should see broad peak at 3280-3675.[307]
1640-1850	C=O stretch on diamond surface	Oxygen annealing. Pos. indicates ox. state.[204, 205, 307, 308]
1800-2700	Multiphonon bands from lattice	Broad hump at 2500, doublet ∼2000, sharp peak at ∼2200.[306]
2300-2400	CO_2 doublet	Present if poor background correction
2800-2970	C-H stretch on diamond surface	H term.[204, 205, 307, 308, 309] Pos. indicates reconstruction.[305]
3000-3200	Aromatic C-H stretch on diamond surf.	Theoretical?[204]
3280-3675	Broad O-H stretch, diamond powder	Adsorbed material? Corresponding bend at 1640-1660.[307]
3710	Narrow O-H stretch from surf. COOH	Should see bend at 1640.[204]
3657	Water	Present if poor background correction
3755	Water	Present if poor background correction

range of temperatures up to 1000°C for 20 minutes each. This work is particularly relevant given the possibly-important temperature dependence of our oxygen annealing procedure. Above 310°C, the C-H stretch bands from 2800-2970 cm^{-1} decrease in intensity, reaching a minimum at and above 410°C annealing. Calculations by Zhigilei et al. suggest that the C{100}/(2×1)H surface reconstruction should have a peak at 2960 cm^{-1}, a triplet with maximum value around 2860 cm^{-1}, and a number of peaks from 1000–1250 cm^{-1}. Other surface reconstructions have similar but distinct peaks in these regions[305].

While the C-H stretch bands disappear above 310°C, a new set of oxygen-related bands emerge. The authors assign peaks at 1106 and 1264 cm^{-1} to C-O-C stretches

and the doublet at 1650-1850 cm^{-1} to a C=O stretch. In this stretch region, peaks at 1710 and 1770 cm^{-1} first appear at 330°C. Both peaks shift to higher wavenumbers, with the 1770 cm^{-1} peak increasing in relative intensity, until 480°Cwhere the peaks begin shifting back to longer wavelengths. The authors hypothesize that decomposition begins above this temperature, with this peak shift corresponding to cyclic ketones at lower temperatures that convert into lactone -(CO)O- and finally carboxylic anhydride -CO(O)CO- at higher temperatures. Finally, the authors note an increase in the intensity of the band from 1360-1500 cm^{-1} (maximum at 1444 cm^{-1}) with increasing temperature. Although the assignment of this band is open to debate, the authors reject the hypothesis of an aromatic C-H vibration in favor of an oxygen-containing feature, perhaps an ionic carbonate.To test this hypothesis of carbonate formation, the authors attempt to hydrolyze these carbonates with NaOH. They appear to be successful: one C=O peak shifts back to the red and they get a new C=O peak at 1640 cm^{-1} corresponding to carboxylic acid C=O or O-H. Most notably, they also get a new O-H stretch at 3710 cm^{-1}. They reasonably conclude that they are forming acid groups. Based on all of this evidence, they suggest that they begin to form ether and ketone groups at around 300°C that both turn into lactone and then eventually carboxylic anhydride over the range 380-480°C. These hypothesis are summed up in schemes 1 and 2. Figure four is a good overview of the temperature dependence of this oxygenation effect.

Similar work by Osswald et al. on oxidation of detonation nanodiamonds (includ-

ing both XANES and FTIR analysis) also indicates an enhancement and oxidation-related blue-shift of C=O stretch modes after annealing at 425°Cin air.[307] This peak disappears after hydrogen gas flow at 800°C. This study assigns the peaks at 1640-1660 cm^{-1} to an O-H stretch mode which is unchanged by the hydrogen anneal. This peak does not seem to be present in the work of Ando[204]; otherwise, these hypothesis are consistent with that work. Interestingly, the authors claim that in the range 400-430°C they can selectively remove sp^2 diamond from their nanodiamonds.

Previous work on thermally oxidized MPECVD diamond crystallites indicates that annealing diamonds in a dry oxgygen environment at above 500°Cgives carboynl peaks in DRIFT spectra[205]. The authors' primary conclusion is the presence of a C=O stretch at 1731 cm^{-1} and a large broad C-H stretching mode at 2870 cm^{-1}. This work also notes peaks at 1464, 1373, 1253, 1165, and 1104 cm^{-1} that are unassigned, though perhaps they could correspond to the theorized C-H stretch modes of Zhigilei[305]. Finally, they note a Si-O-Si asymmetric stretch mode at 1068 cm^{-1} from their substrate. They claim that the lack of a defect-induced lattice peak at 1332 cm^{-1} is evidence of the quality of their material.

A.3.4 Conclusion and outlook

Our attempts to use FTIR on bulk diamond surfaces was largely unsuccessful, probably due to the low IR cross-section achievable from the diamond surface in ATR

mode. In such an experiment, we are essentially attempting to detect a signal from a single plane of atoms in a single pass. The intrinsic difficulty of this tasks is probably the reason why essentially all previous studies on diamond use a powder of micro- or nanodiamonds. Moreover, the high index of the diamond means that even in the best case the penetration depth is at least 100 nm. Although bulk diamond itself has no IR signal due to its inversion symmetry, the presence of even a relatively small fraction of IR-active defects in the bulk could dominate the signal. Regardless of our experimental difficulties, the background information presented in this section may be useful for future studies.

	Term	Anneal -Acid	Term -Acid	Etch -Acid
Term	μ=0.0119131 σ=0.0128813 N=33	p_{K-S}=9.18e-9 p_{K-W}=1.12e-10	p_{K-S}=4.41e-6 p_{K-W}=9.26e-6	p_{K-S}=0.68 e p_{K-W}=0.517 e
Anneal -Acid	p_{K-S}=9.18e-9 p_{K-W}=1.12e-10	μ=0.0449794 σ=0.0192307 N=26	p_{K-S}=0.0259 e p_{K-W}=0.0713 e	p_{K-S}=0.0000562 e p_{K-W}=0.0000204 e
Term -Acid	p_{K-S}=4.41e-6 p_{K-W}=9.26e-6	p_{K-S}=0.0259 e p_{K-W}=0.0713 e	μ=0.0361793 σ=0.02157 N=15	p_{K-S}=0.0000938 e p_{K-W}=0.000111 e
Etch -Acid	p_{K-S}=0.68 e p_{K-W}=0.517 e	p_{K-S}=0.0000562 e p_{K-W}=0.0000204 e	p_{K-S}=0.0000938 e p_{K-W}=0.000111 e	μ=0.00825704 σ=0.00763523 N=7

(a) Unknown peak at -1.9 eV

	Term	Anneal -Acid	Term -Acid	Etch -Acid
Term	μ=0.0428082 σ=0.0162614 N=33	p_{K-S}=0.0173 e p_{K-W}=0.113 e	p_{K-S}=0.533 e p_{K-W}=0.606 e	p_{K-S}=0.149 e p_{K-W}=0.0983 e
Anneal -Acid	p_{K-S}=0.0173 e p_{K-W}=0.113 e	μ=0.0345273 σ=0.0206857 N=26	p_{K-S}=0.067 e p_{K-W}=0.254 e	p_{K-S}=0.165 e p_{K-W}=0.0164 e
Term -Acid	p_{K-S}=0.533 e p_{K-W}=0.606 e	p_{K-S}=0.067 e p_{K-W}=0.254 e	μ=0.0414947 σ=0.0140401 N=15	p_{K-S}=0.265 e p_{K-W}=0.153 e
Etch -Acid	p_{K-S}=0.149 e p_{K-W}=0.0983 e	p_{K-S}=0.165 e p_{K-W}=0.0164 e	p_{K-S}=0.265 e p_{K-W}=0.153 e	μ=0.0584975 σ=0.0275775 N=7

(b) Graphitic peak at -0.9 eV

	Term	Anneal -Acid	Term -Acid	Etch -Acid
Term	μ=0.862954 σ=0.0312842 N=33	p_{K-S}=0.0149 e p_{K-W}=0.000239 e	p_{K-S}=0.28 e p_{K-W}=0.117 e	p_{K-S}=0.572 e p_{K-W}=0.836 e
Anneal -Acid	p_{K-S}=0.0149 e p_{K-W}=0.000239 e	μ=0.825849 σ=0.041425 N=26	p_{K-S}=0.322 e p_{K-W}=0.102 e	p_{K-S}=0.0384 e p_{K-W}=0.0346 e
Term -Acid	p_{K-S}=0.28 e p_{K-W}=0.117 e	p_{K-S}=0.322 e p_{K-W}=0.102 e	μ=0.846981 σ=0.0339579 N=15	p_{K-S}=0.204 e p_{K-W}=0.294 e
Etch -Acid	p_{K-S}=0.572 e p_{K-W}=0.836 e	p_{K-S}=0.0384 e p_{K-W}=0.0346 e	p_{K-S}=0.204 e p_{K-W}=0.294 e	μ=0.865936 σ=0.0471994 N=7

(c) sp^3 peak

	Term	Anneal -Acid	Term -Acid	Etch -Acid
Term	μ=0.0566369 σ=0.0173917 N=33	p_{K-S}=0.107 e p_{K-W}=0.00979 e	p_{K-S}=0.874 e p_{K-W}=0.564 e	p_{K-S}=0.0738 e p_{K-W}=0.0725 e
Anneal -Acid	p_{K-S}=0.107 e p_{K-W}=0.00979 e	μ=0.0697825 σ=0.0203678 N=26	p_{K-S}=0.0863 e p_{K-W}=0.0163 e	p_{K-S}=0.0021 e p_{K-W}=0.0044 e
Term -Acid	p_{K-S}=0.874 e p_{K-W}=0.564 e	p_{K-S}=0.0863 e p_{K-W}=0.0163 e	μ=0.0533469 σ=0.0198482 N=15	p_{K-S}=0.104 e p_{K-W}=0.268 e
Etch -Acid	p_{K-S}=0.0738 e p_{K-W}=0.0725 e	p_{K-S}=0.0021 e p_{K-W}=0.0044 e	p_{K-S}=0.104 e p_{K-W}=0.268 e	μ=0.0425693 σ=0.0225218 N=7

(d) C-O peak at +1.0 eV

	Term	Anneal -Acid	Term -Acid	Etch -Acid
Term	μ=0.0256879 σ=0.00729961 N=33	p_{K-S}=0.553 e p_{K-W}=0.689 e	p_{K-S}=0.0592 e p_{K-W}=0.111 e	p_{K-S}=0.812 e p_{K-W}=0.746 e
Anneal -Acid	p_{K-S}=0.553 e p_{K-W}=0.689 e	μ=0.0248616 σ=0.00847532 N=26	p_{K-S}=0.335 e p_{K-W}=0.281 e	p_{K-S}=0.556 e p_{K-W}=0.972 e
Term -Acid	p_{K-S}=0.0592 e p_{K-W}=0.111 e	p_{K-S}=0.335 e p_{K-W}=0.281 e	μ=0.021998 σ=0.00729109 N=15	p_{K-S}=0.397 e p_{K-W}=0.381 e
Etch -Acid	p_{K-S}=0.812 e p_{K-W}=0.746 e	p_{K-S}=0.556 e p_{K-W}=0.972 e	p_{K-S}=0.397 e p_{K-W}=0.381 e	μ=0.0247401 σ=0.0049947 N=7

(e) C=O peak at +2.4 eV

Figure A.9: Summary statistical data for relative carbon subpeak concentrations described in figure 3.15 and table 3.6.

B

Supporting material for Chapter 4

B.1 Experimental setup

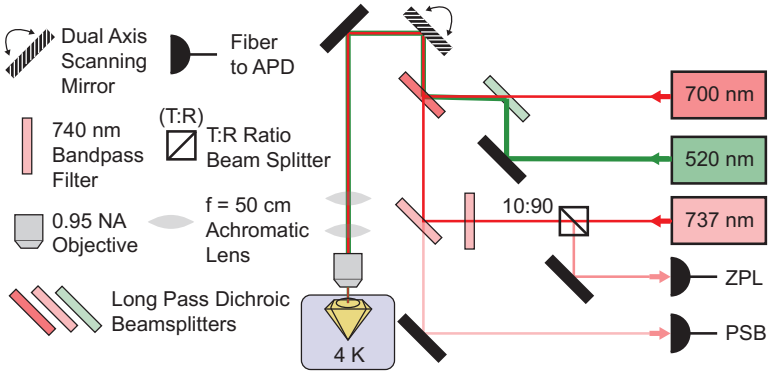

Figure B.1: Confocal microscope design. The 520 nm and 700 nm lasers are used to excite the SiV off-resonantly. The 737 nm external-cavity diode laser is used to excite the SiV resonantly. Collection can be performed either on the ZPL (if the excitation is off-resonance) or the PSB (in either excitation scheme).

The experiments were carried out using home-built scanning confocal microscopes

as illustrated in Fig. B.1. The three lasers used for excitation (520 nm and 700 nm diode lasers used for off resonant excitation, 737 nm external-cavity diode laser used for resonant excitation) are combined using dichroic beamsplitters. A 760 nm long-pass dichroic beamsplitter separates the PSB fluorescence from the rest of the optical channels. An additional bandpass filter (740 ± 13 nm) is used on the ZPL channel. Single photons are detected using single photon counting modules (Picoquant τ-SPAD and Excelitas SPCM-NIR). The cryogenic measurements were performed in 4 K helium flow cryostats. We used a 0.95 NA microscope objective (Nikon CFI LU Plan Apo Epi 100×) in all experiments. During the cryogenic measurements, the objective was inside the vacuum chamber and the sample was clamped with an indium foil spacer to the cold finger of the cryostat. During the PLE measurements, the 520 nm laser is pulsed at a $\sim 5\%$ duty cycle to stabilize the charge state of the SiV center[71, 230]. The detectors are gated off during these pulses.

B.2 Fluorescence autocorrelation measurements

To verify our ability to create single SiV centers, we performed fluorescence autocorrelation measurements on SiV centers inside diamond nanobeams. We performed this measurement by exciting the SiV centers off resonantly as described above and splitting the emission between two detectors in a Hanbury-Brown–Twiss configuration. The relative arrival times of the photons on the two detectors were recorded using

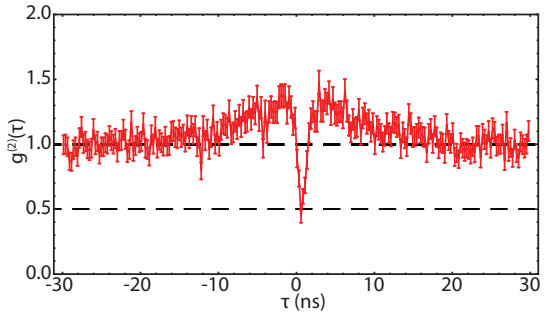

Figure B.2: Fluorescence autocorrelation measurement of a SiV center inside a diamond nanobeam as described in the text. Error bars are estimated assuming the noise on the number of detected photons follows a Poisson distribution (shot noise). The extent of the dip at $\tau = 0$ is limited by finite detector bandwidth: we measure $g^{(2)}(0) = 0.45$; deconvolving the detector response yields $g^{(2)}(0) = 0.15$.

fast acquisition electronics (PicoQuant HydraHarp 400) with a resolution better than 128 ps. In this experiment, our total average photon count rate from this SiV was 9×10^4 counts per second.

The relative photon detection times $g^{(2)}(\tau)$ (normalized by defining $g^{(2)}(\infty) = 1$) from a representative SiV are displayed in Fig. D.3. A value of $g^{(2)}(0) < 0.5$ would confirm that we are measuring emitters producing single photons. Finite jitter on our detectors of around 350 ps causes the measured arrival times of our photons to be convolved with the detector response, hence limiting the sharpness and minimum value of our dip. Fitting the data (including the detector response) using previously reported methods[212] gives a value $g^{(2)}(0) = 0.45$. Deconvolving the detector response gives a value $g^{(2)}(0) = 0.15$, indicating that the extent of our $g^{(2)}(0)$ dip is limited primarily

by detector response as expected.

C

Supporting material for Chapter 5

C.1 Setup description

The experiments in Chapter 5 are carried out in a confocal microscope consisting of a modified 4 K liquid helium flow probe-station (Desert Cryogenics model TTP4) and a 0.95 NA microscope objective (Nikon CFI LU Plan Apo Epi 100×) inside the vacuum chamber. The layout of the setup is shown in Fig. C.1. Three ports are used to excite the system (Ch. 1), control the SiV and detect fluorescence (Ch. 2) and measure transmission (Ch. 3).

For the coarse characterization of the diamond nanocavity resonances, we excite the system with a broadband supercontinuum laser (NKT Photonics SuperKExtreme). The transmitted light is sent to a spectrometer (Horiba iHR550 with Synapse CCD and 1800 gr/mm) with a spectral resolution of 0.025 nm. To obtain high resolution

spectra of the system in Fig. 5.1, we scanned a Ti:Sapphire laser (Probe laser: M-Squared SolsTiS-2000-PSX-XF) across the cavity and atomic resonance. For all frequency scans, the instantaneous laser frequency was monitored using a high resolution wavemeter (High Finesse WS7) with 10 MHz resolution and 50 MHz accuracy. We used a laser noise eater (Thorlabs LCC3112H) to stabilize laser power to less than 1% during frequency scans.

We use a home-built external-cavity diode laser (Opnext Diode HL7302MG, Littrow configuration) with an electro-optical modulator (EOM: EOSPACE interferometric electro-optical amplitude modulator, model AZ-AV5-40-PFA-PFA-737 with 40 GHz bandwidth) to apply short (minimum pulse duration ∼500 ps) optical pulses for the lifetime measurements and switching experiment (Figs. 5.1 and 5.2). The interferometer of the EOM was stabilized using a lock-in amplifier (SRS model SR830) and short driving electrical pulses were generated using an arbitrary waveform generator (Tektronix AWG710, 4 GSa/s). Off-resonant excitation of the SiV was performed with 700 nm (Thorlabs LP705-SF15) and 520 nm (Thorlabs LP520-SF15) diode lasers. Single photons were counted using single-photon detectors (2× PicoQuant τ-SPAD, and 2× Excelitas SPCM-NIR) and time tagged using fast acquisition electronics (PicoQuant HydraHarp 400).

The waveguides described in Sec. C.2 support two modes with different polarizations. In our design, the cavity mode is a transverse-electric-like (TE) mode. At the cavity resonance frequency, there is a high-transmission passband for transverse-magnetic-

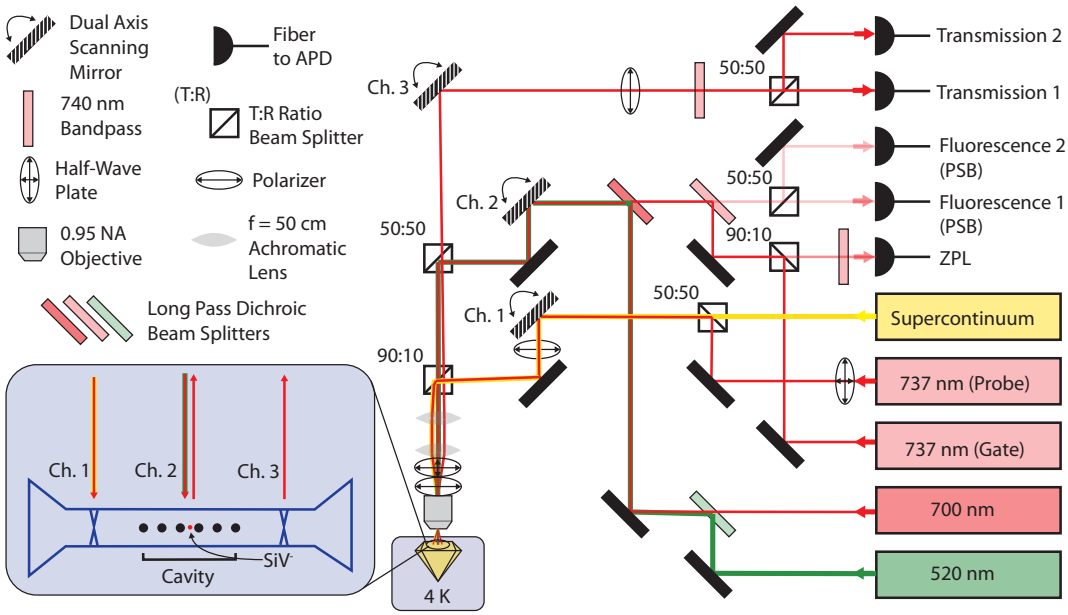

Figure C.1: Optical configuration for the three-port measurements described in Chapter 5. Each port has its own dual-axis scanning galvo mirror system (Thorlabs GVS012) labeled Ch. 1–Ch. 3. The first port, Ch. 1, is used to excite the waveguide mode and contains both a supercontinuum light source and a narrowband Ti:Saph laser used for broadband and narrowband characterization of the system response respectively. The second port, Ch. 2, is used to control the SiV (as described in Sec. C.4) and monitor the SiV fluorescence scattering in the phonon-sideband (PSB). The third port, Ch. 3, is used to measure the transmission through the cavity mode. The objective and the sample are in vacuum, and the sample is cooled to 4 K. Shaded blue inset: schematic of the spatial position of the focal spots of the three channels relative to the SiV-cavity system.

like (TM) modes. (Our conventions for TE and TM in this context are described in Section C.2.1.) In order to only excite the relevant (TE) cavity mode, we place a polarizer immediately before the objective.

The in- and out-coupling efficiencies between free-space and waveguide modes are each of order 1% based on simulations. In order to isolate transmission from the diamond nanocavity and mitigate residual reflection from free-space optics, we use a cross-polarization scheme between the excitation (Ch. 1) and transmission (Ch. 3) channels.

C.2 Device design, fabrication and characterization

C.2.1 Cavity design

The one-dimensional diamond photonic-crystal cavity ("nanobeam cavity" hereafter) used here (based on previous designs[138]) consists of a diamond waveguide with a triangular cross-section perforated by a chirped 1D lattice of elliptically-shaped air holes. The unit cell of the lattice (Fig. C.2A) is parameterized by the etch angle (θ), width (w), lattice constant (a) and major (transverse) and minor (longitudinal) elliptical air hole diameters (d_z, d_x). The unit cell etch angle (the half-angle at the bottom apex of the triangular cross-section) was fixed at $\theta = 50$ in the design to ease fabrication.

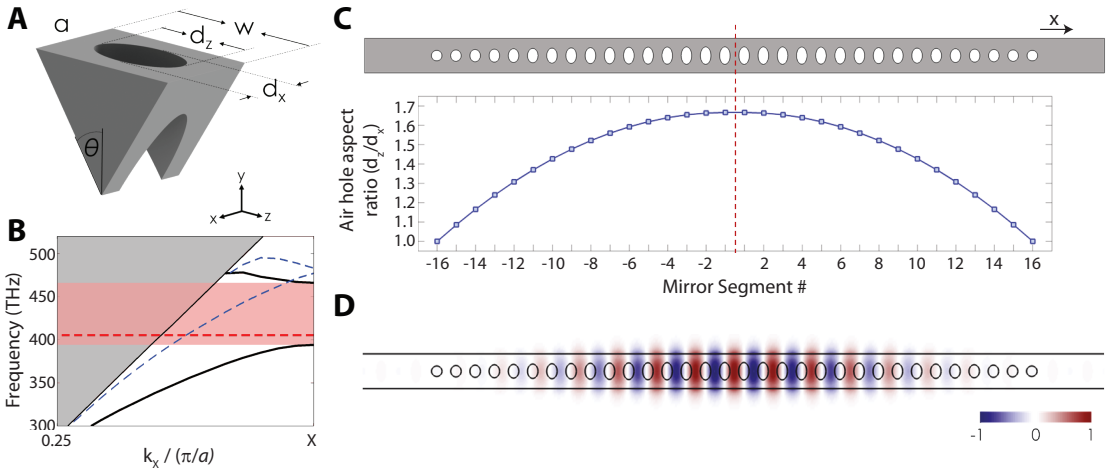

Figure C.2: (A)Schematic of a triangular cross-section diamond unit cell parameterized by the etch angle (θ), width (w), lattice constant (a), and major and minor elliptical air hole diameters (d_z, d_x). (B) Corresponding photonic bandstructure of a nominal unit cell with $\theta = 50$ and $(a, w, d_z, d_x) = (260, 470, 140, 140)$ nm. The gray shaded region indicates the continuum of radiation and leaky modes that exist above the light line. Below the light line, supported transverse-electric-like (TE) and transverse-magnetic-like (TM) guided modes are indicated by solid black and dashed blue lines, respectively. A quasi-bandgap based on symmetry for the TE guided modes is indicated by the pink shaded region. The fundamental cavity resonance at $\lambda_{TE} = 743$ nm is designated by the dashed red line. (C) Schematic of the 16-hole-array cavity design with the air hole aspect ratio (d_z/d_x) plotted as a function of mirror segment number. (D) Normalized optical E_y field profile of the fundamental localized cavity mode of diamond nanobeam cavity design in (C).

Fig. C.2B shows the photonic band structure for a nominal unit cell with $\theta = 50$ and $(a, w, d_z, d_x) = (260, 470, 140, 140)$ nm. Here, transverse-electric-like (TE, solid black lines) and transverse-magnetic-like (TM, dashed blue lines) guided modes give rise to symmetry based quasi-bandgaps sufficient to realize highly localized resonances. In our convention, the TE modes have odd vector symmetry with respect to reflection across the $z = 0$ longitudinal symmetry plane of the nanobeam (see Fig. C.2 for coordinate conventions). In other words, the electric field of a TE (TM) mode is mostly perpendicular (parallel) to the $z = 0$ plane. At the center of the beam, the electric field vector of the TE modes matches the transition dipole moment of two (out of four possible) orientations of the SiV center up to a factor of cos(35).

We parameterized the nanobeam cavity design by the target fundamental TE cavity mode resonance wavelength in free space, λ_{TE}. Our final design has the following parameters: a nanobeam width $w = 0.635\,\lambda_{TE}$, lattice constant (hole spacing) $a = 0.349\,\lambda_{TE}$ and elliptical hole minor diameter $d_x = 0.191\,\lambda_{TE}$, with the major diameter of the elliptical hole increased quadratically, from $d_z = d_x = 0.191\,\lambda_{TE}$ at the end of the cavity, to $d_z = 0.317\,\lambda_{TE}$ at the center. This quadratically tapering major diameter is schematically displayed in Fig. C.2C for a 16 hole array on each side of the cavity x-axis mirror plane. For the unit cell dimensions used to calculate the bandstructure in Fig. C.2A, the fundamental TE cavity resonance is located at $\lambda_{TE} = 743\,\text{nm}$, which is designated by the dashed red line in Fig. C.2B.

The total cavity loss is comprised of both radiation losses into free-space (Q_{rad})

and coupling losses to the feeding waveguide (Q_{wg}). For the cavity design used in the experiment, the cavity figures of merit generated from FDTD simulations are the cavity mode volume ($V = 1.8\,(\lambda_{TE}/n)^3$ with $n = 2.4$) and the partial optical Q-factors ($Q_{rad} \approx 320000$, $Q_{wg} \approx 10000$). From the partial optical Q-factors, the total cavity loss (Q_{tot}) is given by the relation $Q_{tot} = (Q_{rad}^{-1} + Q_{wg}^{-1})^{-1} \approx 10000$. Additionally, the predicted on-resonance transmission of the fundamental cavity mode was calculated by the relation: $T = Q_{tot}^2/Q_{wg}^2 \approx 94\%$. It is important for this transmission to be high because it is directly proportional the number of photons we are able to measure experimentally.

In order to estimate the transmission of the cavities used in the experiment, the cavity transmission was normalized to transmission through a diamond waveguide (no holes) with identical in- and out-coupling structures. Using this approach, we found that the cavity transmission on resonance was $\geq 85\%$ of the waveguide transmission.

C.2.2 Cavity fabrication

Electronic grade, $\langle 100 \rangle$-normal oriented, single-crystal diamond substrates (CVD grown, < 5 ppb [N], Element Six), were first polished to a surface roughness < 5 nm RMS, followed by an acid treatment ("tri-acid clean" hereafter) in a boiling mixture consisting of equal parts conc. sulfuric acid, conc. nitric acid, and 70% (aqueous) perchloric acid. Prior to device fabrication, approximately the top six microns of the

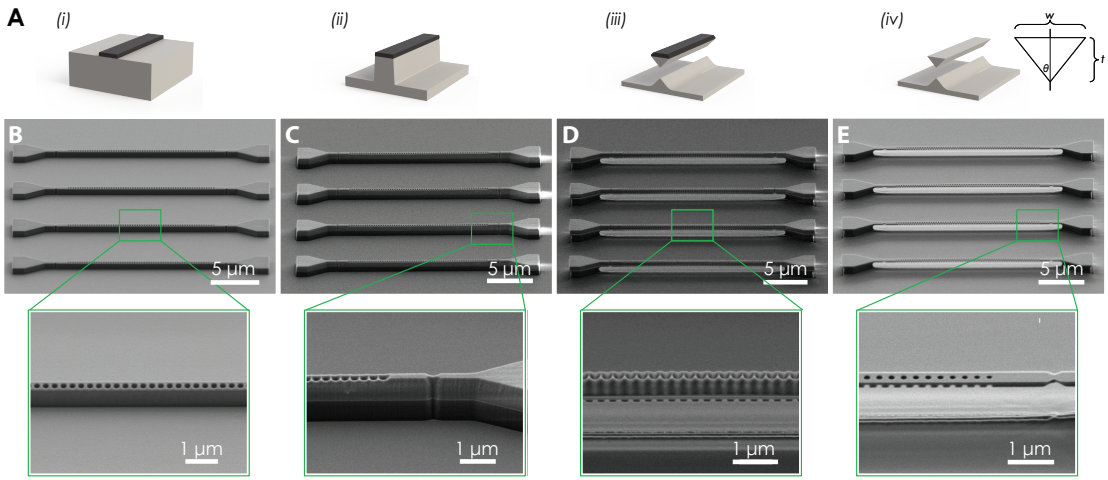

Figure C.3: (A) Illustration of the angled-etching technique used to fabricate free-standing optical nanocavity structures in bulk single-crystal diamond. Angled-etching fabrication steps with corresponding SEM images: (i) define an etch mask on substrate via standard fabrication techniques (panel (B)), (ii) transfer etch mask pattern into the substrate by top-down plasma etching (panel (C)), (iii) employ angled-etching to realize suspended nanobeam structures (panel (D)), (iv) remove residual etch mask (panel (E)). All SEM images taken at a stage tilt of 60.

diamond surface were removed in a standard inductively-coupled-plasma reactive-ion etcher (ICP-RIE, Unaxis Shuttleline). This pre-fabrication etch consisted of an Ar/Cl_2 etch (30 minutes, 400 W ICP power, 250 W RF power, 25 sccm Ar flow rate, 40 sccm Cl_2 flow rate, 8 mTorr chamber pressure) followed by an O_2 etch (30 minutes, 700 W ICP power, 100 W RF power, 50 sccm O_2 flow rate, 10 mTorr chamber pressure). This pre-fabrication etch removes polishing-induced mechanical strain near the top surface of the diamond and reduces the final surface roughness of the diamond substrate to < 1 nm RMS (confirmed by AFM).

Our nanofabrication procedure is outlined schematically in Fig. C.3. First, a silica

etch mask was patterned on the prepared diamond substrates using electron-beam lithography on a 650 nm spin-coated layer of 83% hydrogen silsesquioxane (HSQ, FOX-16 from Dow Corning) negative resist in methyl isobutyl ketone (MIBK). Exposed HSQ was developed in tetramethylammonium hydroxide (TMAH, 25% diluted aqueous solution) to yield the final mask used for etching (Fig. C.3B).

We then performed a conventional top-down anisotropic plasma etch (Unaxis Shuttleline ICP-RIE, 700 W ICP power, 100 W RF power, 50 sccm O_2 flow rate, 2 sccm Ar flow rate, 10 mTorr chamber pressure) to first transfer the silica etch mask pattern into the diamond to a depth of approximately 600 nm (Fig. C.3C). We then etched the sample at an angle using the same ICP-RIE parameters as the initial top down etch, but instead housing the sample inside a macroscopic aluminum Faraday cage[97, 138] to direct the plasma ions to the substrate surface at the intended angle (Fig. C.3D). Finally, the remaining etch mask was removed in concentrated hydrofluoric acid, followed by 1 : 3 hydrogen peroxide : conc. sulfuric acid ("piranha") solution leaving freestanding diamond nanocavities (Fig. C.3E).

After the cavities are fabricated, SiV centers are created by targeted implantation using a focused ion beam. This technique will be described in Section C.2.5. Implantation is followed by a tri-acid clean and a three-stage ultra-high-vacuum (maximum pressure 5×10^{-9} Torr) anneal at 400°C (3°C per minute ramp, 8 hour dwell time), 800°C (1°C per minute ramp, 8 hour dwell time), and 1200°C (1°C per minute ramp, 4 hour dwell time). This annealing introduces a small amount of graphitic carbon on

the surface of the sample. The tri-acid clean is repeated after annealing to remove this carbon. We do not perform a low temperature oxygen anneal. The effect of each post-implantation step is described in more detail in References [230, 248].

C.2.3 Tuning the cavity resonance wavelength

Fabrication imperfections usually result in cavity resonances that are typically of order 10 nm away from the desired resonance position. Moreover, cooling the sample to 4K introduces additional irreproducible shifts due to thermal contraction of diamond and condensation of residual gas onto the sample surface. Thus, it is highly desirable to have a method to tune the resonance frequency of the cavity *in situ* during the course of our experiment.

To accomplish this goal, we deliberately introduce a controlled amount of inert gas into the chamber. This gas freezes on the surface of the sample, increasing the local refractive index and shifting the resonance frequency of the cavity to longer wavelengths. Using this technique, we can tune the cavity resonance by more than 20 nm with no deterioration of the cavity quality factor.

Thermal desorption of the tuning gas provides a simple technique to reverse the tuning. Either the sample can be heated up locally using an intense laser field, and/or the whole sample can be heated using a resistive heater mounted on the sample stage. The tuning procedure is very robust and was implemented on the same diamond

nanophotonic device many times over several months. For our experiment, we use carbon dioxide as the tuning gas which does not desorb under typical experimental conditions but can be desorbed deliberately using the above methods.

C.2.4 Cavity mode characterization using SiV centers

We estimate the mode volume of the nanobeam cavity experimentally by probing the local photonic density of states, which is in turn measured via the spontaneous emission rate of SiV centers into the cavity mode. To implement this novel technique, we use a sample with a similar cavity design but a very high density of SiV centers created by uniform high-density ion implantation (implantation flux $3 \times 10^{11}\,\mathrm{cm}^{-2}$, implantation energy 150 keV, performed by Innovion corporation). We then tune the cavity as described in the previous section until the ensemble of SiV centers is on resonance with the fundamental mode of the cavity. Next, we excite the SiV centers in the cavity by scanning over the entire nanostructure with an off-resonant excitation laser at 700 nm (Ch. 2 in Fig. C.1 and C.4). We measure the fluorescence into the cavity mode via the outcoupling notch at the end of the cavity (Ch. 3). To produce a one-dimensional plot of the mode density along the beam, we integrate along the direction (z) orthogonal to the beam. We then repeat this procedure for the second-order cavity mode by tuning the mode into resonance with the SiV ensemble.

Figure C.4C shows this integrated line cut superimposed with the same integrated

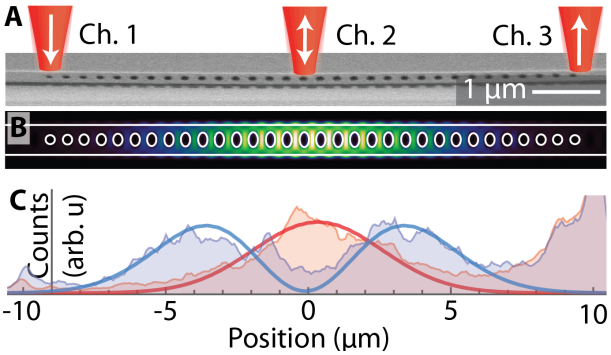

Figure C.4: (A) Scanning electron micrograph of nanophotonic crystal cavity and (B) simulated energy density profile of the cavity mode. (C) Experimentally measured energy density profile for the cavity mode in part B. Photons are detected in the waveguide mode (Ch. 3) as the excitation laser (Ch. 2) is spatially scanned across the nanocavity.

line cut taken from our FDTD simulations (see Section C.2.1) where the horizontal axis has been scaled by a fitted parameter to estimate the agreement between simulations and experiment. We assume that the transverse mode profile is given by our simulated value since that mode profile is determined primarily by the size and refractive index of the beam which are well controlled. Before fitting, the simulated data has been convolved with a Gaussian point-spread function ($2\sigma \approx 600\,\mathrm{nm}$) with width extracted from an image of a single emitter.

We find that the measured mode volume is 35% larger for the first mode and 46% larger for the second mode than predicted by our simulations. Under the assumption that this scaling is similar for the devices used in the main text, we estimate an experimental mode volume for the first mode of $V \sim 2.5\,(\lambda/n)^3$ (here, $n = 2.4$). Discrepancies in the mode volume can result from fabrication imperfections which can reduce

longitudinal confinement. This mechanism is plausible since we have observed lower quality factors than predicted in our simulations (see Section C.2.1).

C.2.5 Deterministic SiV positioning using focused Si ion beam implantation

SiV centers were introduced at the center of the diamond nanocavities by targeted implantation using Sandia National Lab's nanoImplanter, a custom focused-ion-beam system made by the A&D Corporation (Tokyo). This instrument employs a 100 kV accelerating potential, an E×B mass velocity filter with $m/\Delta m = 60$, a laser interferometry controlled stage and a Raith Elphy Plus pattern generator. A AuSiSb liquid metal alloy is used to generate the Si^+ ion beam. We controlled the ion fluence with a combination of beam current and dwell time at each targeted implantation site. The implantation position was aligned to <1 nm.

This combination of controlled ion fluence, energy and positioning allows for precise control over the number, depth and lateral position of SiV centers inside the nanophotonic structure. The number of implanted ions obeys a Poisson distribution; the error in the number of implanted ions scales as the square root of the average number of implanted ions. The expected positioning error is dominated by the ion spot size (40 nm). The range (depth) of the ions is predicted to be 68 nm with a ±13 nm straggle. The positioning error is about a factor of two smaller than the relevant cavity

mode dimensions: the mode oscillates at about 100 nm peak-to-peak in the longitudinal direction and has a similar extent in the transverse directions.

Using this approach, we chose an intended dose of between 10 to 500 ions (equivalent fluence 8×10^{11} to 4×10^{13} ions/cm^2) for different nanocavities on the diamond sample. The nanocavity used in the experiment was implanted with 350 Si^+ ions and contains more than 5 SiV centers (Fig. C.5) after high temperature annealing. These measurements demonstrate greater than 1.5% conversion yield from Si^+ ions to SiV centers, comparable to what has been realized in the bulk[248]. The yield of conversion from Si^+ ions to SiV centers is limited by the vacancy density in the diamond crystal. Electron irradiation has been shown to improve the SiV creation yield by more than an order of magnitude[217] and could be used to enable operation with fewer number of implanted ions, reduced damage to the crystal and reduced inhomogeneous distribution.

C.2.6 Adiabatic fiber-waveguide coupling for high-efficiency photon extraction

For the diamond nano-waveguides used in the Raman tuning and two-SiV entanglement experiments, we collect the Raman emission of SiV centers by adiabatically transferring the photons from the waveguide mode into a single-mode optical fiber[253]. In this technique, a tapered optical fiber is brought into physical contact with a ta-

pered section of a diamond waveguide. For an appropriate choice of the diamond and fiber geometries, the composite structure supports a single optical mode along its entire length, allowing a photon emitted by a SiV center inside the diamond waveguide to be transfered to the optical fiber. This technique can achieve high absolute coupling efficiencies and requires no realignment over the course of several days.

To achieve this goal, we use a wet-etching procedure to create conical tapers on conventional single-mode optical fibers (Thorlabs SM600) with a taper angle of approximately 1.5(per side; 3full angle). The triangular diamond waveguide is designed with a similar taper angle of 2 Fiber coupling is achieved by positioning a tapered optical fiber in physical contact with the tapered section of the diamond waveguide using piezoelectric nanopositioners (Attocube ANPx101/ANPz101). The coupling efficiency from single-mode fiber to the diamond waveguide is calculated by sending light into a 90:10 fiber beamsplitter (Thorlabs TW670R5A2), with 90% of the input light sent to a reference photodiode (Thorlabs PDA100A), and the remaining 10% to the coupled fiber-waveguide structure. We use a Bragg mirror section of holes (similar to the mirror used to create the photonic crystal cavities above) in the waveguide to reflect the incoming light, 90% of which is sent to a calibrated measurement photodiode via the final beamsplitter port. By comparing the reflected power with the incoming power, we infer a lower bound on the fiber-diamond coupling efficiency of 70%.

C.3 Identifying single SiV centers inside nanocavities

The electronic structure of the SiV center consists of spin-orbit doublets in the ground and excited states. Optical dipole transitions between the doublets result in four transition frequencies which are labeled A–D in order of decreasing frequency[214]. The presence of strain in the crystal changes the energy splittings, resulting in inhomogeneous broadening[211]. However, the difference in the transition frequencies always obeys the energy conservation constraints: $\Delta^i_{A-B} = \Delta^i_{C-D} = \Delta^i_{gs}$ and $\Delta^i_{A-C} = \Delta^i_{B-D} = \Delta^i_{es}$, where Δ^i_{es} and Δ^i_{gs} are the excited and ground state splittings, corresponding to an individual emitter labeled i.

To determine the set of four transitions corresponding to a single emitter at the center of our cavity, we scanned the Ti:Sapphire laser over a 700 GHz range centered around 406.8 THz at $\sim$ 100 MHz resolution. We recorded the fluorescence counts in the PSB as a function of excitation frequency to obtain a list of all emitter resonances in this cavity. The resulting spectrum (Fig. C.5A) indicates that there are several near-resonant SiV centers at the center of the cavity where each SiV results in four lines A^i–D^i. We fit the frequency of each line in the Fig. C.5A and calculate the energy differences Δ between all pairs of lines. From this list, we find sets of four frequencies A^i-D^i that consist of pairs of transitions with matching Δ, i.e.

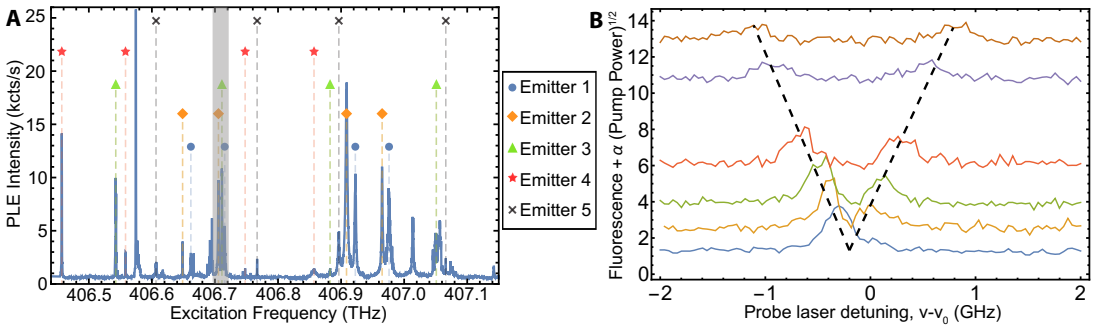

Figure C.5: (A) Fluorescence counts from the center of the cavity as a function of excitation frequency. Colored symbols correspond to emitter frequencies determined by the algorithm described in the text. Emitters 1 and 2 are at low strain, and emitters 3–5 are at higher strain. The shaded region indicates a typical inhomogeneous distribution range of transition C ($|c\rangle \leftrightarrow |e\rangle$) frequencies. The cavity QED experiments in the main text were carried out using Emitter 2. (B) The identification procedure was verified by measuring Autler-Townes splitting for the Λ-type system. A pump laser of varying intensity was fixed on transition D ($|u\rangle \leftrightarrow |e\rangle$) at 406.649 THz, and a weak probe was scanned across transition C at 406.705 THz. The line splitting on transition C scales with the square root of the applied power on transition D (illustrated with dashed black line), confirming that the two transitions form an optical lambda system.

$|\Delta^i_{A-B} - \Delta^i_{C-D}| < \epsilon$ where $\epsilon \sim 300\,\mathrm{MHz}$ is limited by experimental error in frequency estimation.

The results of this approach are indicated in Fig. C.5A where we have drawn colored symbols over the sets of lines presumably corresponding to the same SiV. (Only five emitters are labeled.) To verify that these lines correspond to the same SiV, we apply a strong driving field on transition D^i (B^i) and probe the response on transition C^i (A^i). We observe that the probed transition undergoes a splitting proportional to the square root of the power of the driving field (Fig. C.5B). This signature of the Autler-Townes effect confirms that the two transitions share an excited state as expected. When the two lines do not correspond to the same SiV, there is no observable splitting. For the optical switch experiment shown in Fig. 2 of the main manuscript, transitions C ($|c\rangle \leftrightarrow |e\rangle$) and D ($|u\rangle \leftrightarrow |e\rangle$) were used to realize an optical lambda system.

C.4 SiV charge state control: high fidelity initialization and single-shot readout

The SiV can be occasionally ionized from the SiV^- charge state to other charge states (SiV^0 or SiV^{2-}) which are dark in our measurement scheme. It is highly desirable to know when the SiV is in the correct charge state and to actively control the charge

state. To accomplish these tasks, we performed the cavity transmission experiment in Fig. 1D with both the cavity and emitter on resonance with the probe laser. At first, only the weak, resonant probe laser was used for driving the system.

We recorded both the transmission photons collected through the cavity and the fluorescence photons collected in the phonon-sideband (PSB), and binned them in 15 ms intervals as shown in the blue curves in Fig. C.6A. The SiV jumps between a bright state (SiV^-) where the transmission intensity (thick blue trace) is low and the PSB fluorescence intensity (thin blue trace) is high and a dark state (not coupled to the probe field) with high transmission and no fluorescence. These jumps are clearly resolved on the timescale of seconds, allowing single-shot readout of the charge state of the SiV.

To rule out the possibility of faster ionization dynamics that we could not resolve with this slow technique, we performed a similar experiment but recorded the time-tagged photon arrival times with the fast acquisition electronics described above. We observed no features slower than tens of nanoseconds, indicating that the complete electronic dynamics are limited to those of the three-level optical system plus a slow charge switching process at the timescale of seconds for the laser intensities used in the experiment.

We then repeat the first experiment, with the addition of a 10 μs pulse of around 0.4 mW green light (520 nm) every 100 μs. The detectors are gated off during the green pulse. The timetraces recorded with this scheme (and with the same duty cycle

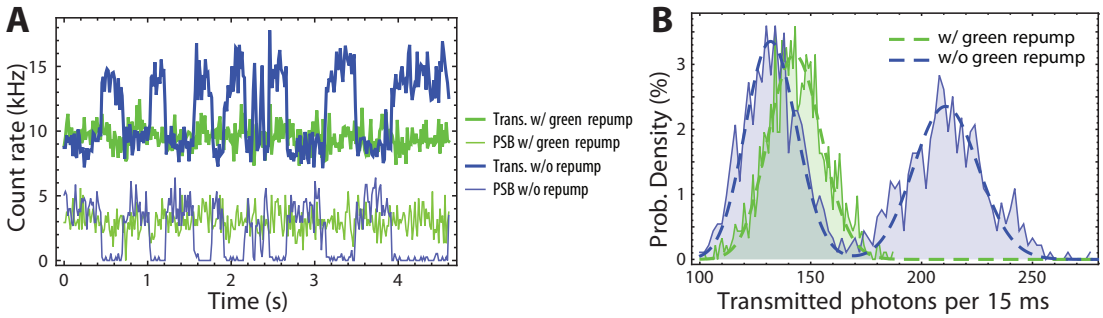

Figure C.6: Charge state initialization with and without a green repump pulse. (A) Timetraces of transmission (upper thick curves) and phonon sideband (PSB, lower thin curves) photon detection events as a function of time. The data are taken both with (green) and without (blue) the presence of a 520 nm repump laser at approximately 10% duty cycle. Clear jumps are present in the case of no green repump, indicating single-shot readout of charge-state fluctuations. (B) Histograms of timetraces in A with Poissonian fits. The ratio of the two blue peak positions gives a direct measurement of the transmission dip of 37%. The mean number of transmitted photons in the case with green repump can be decomposed into 85% of the low-transmission peak and 15% of the high transmission peak in the case of no green repump. This implies an 85% charge state initialization fidelity.

and data processing as above) are shown in the green timetraces (thick: transmission, thin: PSB fluorescence) in Fig. C.6A. These traces are flat and close to the values when the SiV is in the correct charge state, illustrating that there are no dynamics on the millisecond timescale and that the green pulse effectively repumps the SiV into the desired charge state.

To quantify this effect, we make histograms of photons detected per 15 ms bin for the transmission counts both with and without green repump (Fig. C.6B). We fit a Poisson distribution to the histogram of counts taken with green repump and two Poisson distributions to the histogram of counts taken with no repump. Based on the relative amplitude of the two peaks without green repump, we estimate that the SiV is in the correct charge state 53% of the time. The average counts for the data taken with the green repump pulse can be decomposed into 85% of the low-transmission (SiV on) case and 15% of the high-transmission (SiV off) case, implying a charge-state initialization fidelity of 85%. A similar analysis using the PSB fluorescence has more noise but is consistent with the above estimate. The close fit of these Poisson distributions to our data also indicates that there is no significant noise above shot noise on this timescale.

Finally, by measuring the contrast between the transmission counts in the bright and dark cases (i.e. the mean values of the peaks in Fig. C.6B) we also have a simple and direct measurement of the transmission extinction from a single SiV. The value of the transmission dip extracted from this measurement is 37%, consistent with the

measurement in Fig. 1F of the main manuscript. While the single-shot readout of the charge state shown in Fig. C.6 can be used to initialize the system with near-perfect fidelity, further research is necessary to understand the microscopic mechanism for charge dynamics and develop higher fidelity control techniques.

C.5 Model description for a SiV center inside an optical cavity

In this section, we describe the theoretical model used to describe the dynamics of the SiV-cavity system measured in Figs. 5.1–5.3 of Chapter 5. We show how to calculate the saturation response of the transmission and fluorescence of the system (Fig. 5.3A) and the different intensity correlation functions between detection events (Figs. 3B–D).

C.5.1 Three level dynamics with dissipation

The system is modeled by a three level atom inside a driven cavity as depicted in Fig. C.7. In a frame rotating with the probe frequency, the Hamiltonian is

$$\hat{H} = \Delta_e \left|e\right\rangle \left\langle e\right| + \Delta_c \hat{a}^\dagger \hat{a} + i\xi \left(\hat{a}^\dagger - \hat{a}\right) + ig \left(\hat{a} \left|e\right\rangle \left\langle c\right| - \hat{a}^\dagger \left|c\right\rangle \left\langle e\right|\right) \tag{C.5.1}$$

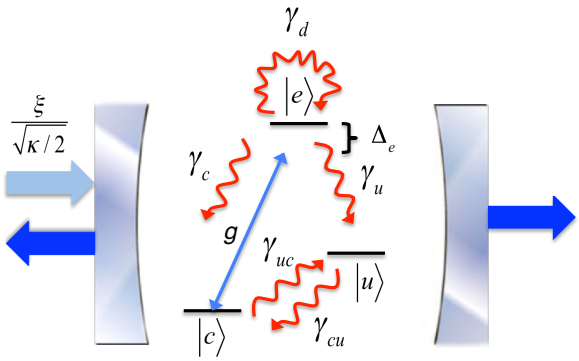

Figure C.7: Setup for the coupled SiV-cavity system with dissipation. $\xi/\sqrt{\kappa/2}$ is the flux amplitude of the weak coherent probe field, and κ is the total decay rate of the symmetric cavity. Dissipation channels are characterized by decay rates γ. The cavity drives the $|c\rangle \quad \leftrightarrow \quad |e\rangle$ transition with a single-photon Rabi frequency g and a detuning Δ_e.

where $\Delta_e = \omega_{ec} - \omega_p$, $\Delta_c = \omega_c - \omega_p$, ω_{ec} is the transition frequency between level $|e\rangle$ and $|c\rangle$, and ω_c is the resonance frequency of the cavity. The coupling between the cavity field and the SiV is given by the single-photon Rabi frequency g. The driving probe field is in a weak coherent state with a flux amplitude $\xi/\sqrt{\kappa/2}$ and frequency ω_p. The bosonic annihilation operator $\hat{a}$ describes the cavity field. The dissipation in the system is described by the Lindblad operators

$$\begin{aligned} \hat{L}_1 &= \sqrt{\gamma_c}\,|c\rangle\langle e|\,, & \hat{L}_4 &= \sqrt{\gamma_{uc}}\,|u\rangle\langle c|\,, \\ \hat{L}_2 &= \sqrt{\gamma_u}\,|u\rangle\langle e|\,, & \hat{L}_5 &= \sqrt{\gamma_d}\,|e\rangle\langle e|\,, \\ \hat{L}_3 &= \sqrt{\gamma_{cu}}\,|c\rangle\langle u|\,, & \hat{L}_6 &= \sqrt{\kappa}\hat{a} \end{aligned} \tag{C.5.2}$$

where γ_{uc} and γ_{cu} are the nonradiative decay rates between states $|c\rangle$ and $|u\rangle$, γ_c (γ_u) is the decay rate from state $|e\rangle$ to state $|c\rangle$ ($|u\rangle$), γ_d is the dephasing rate of state $|e\rangle$ and κ is the total decay rate of the cavity field. The Markovian approximation for the nonradiative relaxation rates ($\gamma_{uc}, \gamma_{cu}, \gamma_d$) is justified by recent measurements of dephasing (γ_d) and depolarization (γ_{cu}) induced by a thermal phonon bath[226]. Experimentally, we find that the optical transitions can be well described by Lorentzian profiles (see Fig. 5.1F), and that the slow non-Markovian dephasing (spectral diffusion) has a small contribution to the total linewidth.

The master equation describing the atom-cavity system can be written formally as

$$\dot{\rho} = -i\left[\hat{H}, \rho\right] + \sum_{x=1}^{6} \hat{L}_x \rho \hat{L}_x^\dagger - \frac{1}{2}\left(\hat{L}_x^\dagger \hat{L}_x \rho + \rho \hat{L}_x^\dagger \hat{L}_x\right) \tag{C.5.3}$$

We work in the weak driving regime ($\xi \ll \kappa$) and can therefore truncate the Hilbert space. To lowest order, we assume that at most two excitations are present in the system such that we can describe the system in the basis

$$\{|0,c\rangle, |0,e\rangle, |0,u\rangle, |1,c\rangle, |1,e\rangle, |1,u\rangle, |2,c\rangle, |2,u\rangle\}. \tag{C.5.4}$$

We label these states $\{|1\rangle \ldots |8\rangle\}$.

C.5.2 System saturation response

To model the saturation response of the transmission and fluorescence measured in Fig. 5.3A, we look at the steady state of the system. For this calculation, we assume that the cavity is driven resonantly ($\Delta_c = 0$) and we are in the regime where $\kappa \gg g, \Delta_e, \xi, \gamma$ and $g \gg \gamma$. This makes it possible to approximately solve the master equation for the steady state density matrix elements $\rho_{i,j}^{(s)} = \langle i| \rho^{(s)} |j\rangle$ analytically. The expressions for $\rho_{i,j}^{(s)}$ can be found in Sec. C.9.1.

The transmission is then given by

$$\mathcal{T} = \frac{\kappa_b \langle \hat{a}^\dagger \hat{a} \rangle_s}{\langle \hat{a}_{\text{in}}^\dagger \hat{a}_{\text{in}} \rangle} \approx \frac{\kappa_a \kappa_b \left(\rho_{4,4}^{(s)} + \rho_{6,6}^{(s)} \right)}{\xi^2}, \tag{C.5.5}$$

where κ_a (κ_b) describes the cavity decay rate to the input (output) waveguide mode. The total cavity decay rate is $\kappa = \kappa_a + \kappa_b + \kappa'$, where κ' is the loss rate out of the cavity not collected by the input and output waveguide modes. In our experiment, we use a waveguide damped symmetric cavity with $\kappa_a \approx \kappa_b \approx \kappa/2$. $\langle \hat{a}_{\text{in}}^\dagger \hat{a}_{\text{in}} \rangle = 2\xi^2/\kappa$ is the photon flux of the input coherent state. The fluorescence scattering is given by

$$\mathcal{F} = \frac{\langle \sigma_{e,e} \rangle_s}{\langle \hat{a}_{\text{in}}^\dagger \hat{a}_{\text{in}} \rangle} \approx \frac{(\gamma_c + \gamma_u)\kappa}{2\xi^2} \left(\rho_{2,2}^{(s)} + \rho_{5,5}^{(s)} \right) \tag{C.5.6}$$

where $\hat{\sigma}_{e,e} = |e\rangle \langle e|$. We note that the observed saturation response differs from the two-level system response due to the presence of a second metastable level $|u\rangle$.

These expressions for $\mathcal{T}$ and $\mathcal{F}$ successfully capture the experimentally measured saturation response in fluorescence and transmission (see Fig. 5.3A) using the system parameters given in Section C.5.4. In Fig. 5.3A, we express the photon flux, $2\xi^2/\kappa$, in terms of number of photons per Purcell-reduced excited-state lifetime τ_e. The experimental data (dots) were fit to the theoretical curves (solid curves) using a single fit parameter for the scaling between the photon flux at the cavity (horizontal scale in the figure) and the photon detection rate. We find that a photon detection rate of approximately 110 kHz corresponds to a photon flux of 1 photon per lifetime. This scaling parameter accounts for the detection efficiency in the experiment, and the fit result is in agreement with our independent estimates of the detection efficiency ($\sim 10^{-4}$).

C.5.3 Calculation of intensity correlation functions

In order to calculate the intensity correlation functions measured in Fig. 5.3, we need to evaluate the response of the system following the detection of either a cavity photon or a scattered photon. Since we work below saturation, the evolution of the metastable states ($|0,c\rangle, |0,u\rangle$) are approximately determined solely by the dissipative coupling

between these two states such that

$$\dot{\rho}_{1,1} \approx \gamma_{cu}\rho_{3,3} - \gamma_{uc}\rho_{1,1} \tag{C.5.7}$$

$$\dot{\rho}_{3,3} \approx \gamma_{uc}\rho_{1,1} - \gamma_{cu}\rho_{3,3}. \tag{C.5.8}$$

This can be solved to yield $\rho_{1,1}(t) = \alpha + \beta e^{-\tilde{\gamma}t}, \rho_{3,3}(t) = \alpha_2 - \beta e^{-\tilde{\gamma}t}$, where $\alpha = \frac{\gamma_{cu}(\rho_{1,1}(0)+\rho_{3,3}(0))}{\tilde{\gamma}}$, $\beta = \frac{\gamma_{uc}\rho_{1,1}(0)-\gamma_{cu}\rho_{3,3}(0)}{\tilde{\gamma}}$, $\alpha_2 = \frac{\gamma_{uc}(\rho_{1,1}(0)+\rho_{3,3}(0))}{\tilde{\gamma}}$ and $\tilde{\gamma} = \gamma_{cu} + \gamma_{uc}$. In steady state, the populations are given by $\rho_{1,1}^{(s)} \approx \gamma_{cu}/(\gamma_{cu} + \gamma_{uc})$ and $\rho_{3,3}^{(s)} \approx \gamma_{uc}/(\gamma_{cu} + \gamma_{uc})$. The ratio of γ_{uc}/γ_{cu} is determined by the thermal distribution[226]. Using data from the optical pumping experiment shown in Fig. 5.2, we infer $\rho_{1,1} \sim 64\%$ and $\rho_{3,3} \sim 36\%$ in steady state. These values are in good agreement with a thermal distribution of population at 4K for the two metastable states that are split by 64 GHz.

Using these expressions for the metastable state populations, we can analytically solve the equations of motion for the populations in the other levels to the leading order in the probe field amplitude. We use the assumption of weak resonant driving ($\Delta_c = 0$) and that we are in the bad cavity regime ($\kappa \gg g \gg \gamma \gg \xi$,) to identify the dominant terms and adiabatically eliminate all states containing cavity photons. As a result, we are left with only three coupled differential equations that we need to solve

between $\dot{\rho}_{2,2}$ and $\dot{\rho}_{1,2}, \dot{\rho}_{2,1}$. Solving the equations, we obtain the following expressions:

$$\rho_{1,2}(t) \approx \mathcal{A}_1 + \mathcal{A}_2 e^{-\tilde{\gamma}t} + \mathcal{A}_3 e^{a_1 t}, \qquad \rho_{6,6}(t) \approx \frac{4\xi^2}{\kappa^2}\rho_{3,3}(t), \tag{C.5.9}$$

$$\rho_{2,2}(t) \approx \mathcal{B}_1 + \mathcal{B}_2 e^{-\tilde{\gamma}t} + \mathcal{B}_3 e^{a_1 t} + \mathcal{B}_4 e^{b_1 t}, \quad \rho_{7,7}(t) \approx \frac{4(\xi^2\rho_{4,4}(t) + g^2\rho_{5,5}(t))}{3\kappa^2} \tag{C.5.10}$$

$$\rho_{4,4}(t) \approx \mathcal{C}_1 + \mathcal{C}_2 e^{-\tilde{\gamma}t} + \mathcal{C}_3 e^{a_1 t} + \mathcal{C}_4 e^{b_1 t}, \quad \rho_{8,8}(t) \approx \frac{6\xi^2}{3\kappa^2}\rho_{6,6}(t), \tag{C.5.11}$$

$$\rho_{5,5}(t) \approx \frac{4\xi^2}{\kappa^2}\rho_{2,2}(t). \tag{C.5.12}$$

The coefficients a_i, b_i, $\mathcal{A}_i$, $\mathcal{B}_i$ and $\mathcal{C}_i$ are defined in Sec. C.9.2.

From Eqs. (C.5.9)–(C.5.12), it is straightforward to get the steady state population of the different levels by taking the limit $t \to \infty$. From the steady state populations we can calculate $\langle \hat{a}^\dagger \hat{a} \rangle \approx \rho^{(s)}_{4,4} + \rho^{(s)}_{6,6}$ and $\langle \hat{\sigma}_{e,e} \rangle \approx \rho^{(s)}_{2,2}$. The normalized transmission–transmission intensity correlation function (Fig. 5.3C) is given by

$$g^{(2)}_{TT}(\tau) = \frac{\langle \hat{a}^\dagger(0)\hat{a}^\dagger(\tau)\hat{a}(\tau)\hat{a}(0)\rangle}{\langle \hat{a}^\dagger \hat{a}\rangle^2}, \tag{C.5.13}$$

where $\langle \hat{a}^\dagger(0)\hat{a}^\dagger(\tau)\hat{a}(\tau)\hat{a}(0)\rangle \approx \rho_{4,4}(\tau) + \rho_{6,6}(\tau)$ can be calculated from Eqs. (C.5.9) and (C.5.11) with initial conditions given by the detection of a cavity photon at time $t = 0$, i.e. $\rho(0) = \hat{a}\rho^{(s)}\hat{a}^\dagger$. Consequently, $\rho_{1,1}(0) = \rho^{(s)}_{4,4}, \rho_{3,3}(0) = \rho^{(s)}_{6,6}$, $\rho_{2,2}(0) = \rho^{(s)}_{5,5}$ and $\rho_{1,2}(0) = (4\xi^2\rho^{(s)}_{1,2} + 2\xi g\rho^{(s)}_{4,4} - 4\xi g\rho^{(s)}_{2,2})/\kappa^2$. The normalized intensity autocorrelation

function for the scattered (fluorescence) field (see Fig. 5.3B)

$$g^{(2)}_{SS}(\tau) = \frac{\gamma_u^{(rad)}}{\gamma_c^{(rad)}+\gamma_u^{(rad)}}\frac{\langle\hat{\sigma}_{e,u}(0)\hat{\sigma}_{e,e}(\tau)\hat{\sigma}_{u,e}(0)\rangle}{\langle\hat{\sigma}_{e,e}\rangle^2} + \frac{\gamma_c^{(rad)}}{\gamma_c^{(rad)}+\gamma_u^{(rad)}}\frac{\langle\hat{\sigma}_{e,c}(0)\hat{\sigma}_{e,e}(\tau)\hat{\sigma}_{c,e}(0)\rangle}{\langle\hat{\sigma}_{e,e}\rangle^2}, \tag{C.5.14}$$

and the normalized intensity correlation function between the scattered and transmitted fields (see Fig. 5.3D)

$$g^{(2)}_{ST}(\tau=\tau_F-\tau_T>0) = \frac{\langle\hat{a}^\dagger(0)\hat{\sigma}_{e,e}(\tau)\hat{a}(0)\rangle}{\langle\hat{a}^\dagger\hat{a}\rangle\langle\hat{\sigma}_{e,e}\rangle} \tag{C.5.15}$$

$$g^{(2)}_{ST}(\tau<0) = \frac{\gamma_u^{(rad)}}{\gamma_c^{(rad)}+\gamma_u^{(rad)}}\frac{\langle\hat{\sigma}_{e,u}(0)\hat{a}^\dagger(-\tau)\hat{a}(-\tau)\hat{\sigma}_{u,e}(0)\rangle}{\langle\hat{a}^\dagger\hat{a}\rangle\langle\hat{\sigma}_{e,e}\rangle} + \frac{\gamma_c^{(rad)}}{\gamma_c^{(rad)}+\gamma_u^{(rad)}}\frac{\langle\hat{\sigma}_{e,c}(0)\hat{a}^\dagger(-\tau)\hat{a}(-\tau)\hat{\sigma}_{c,e}(0)\rangle}{\langle\hat{a}^\dagger\hat{a}\rangle\langle\hat{\sigma}_{e,e}\rangle} \tag{C.5.16}$$

can be calculated in a similar way where $\hat{\sigma}_{u,e} = |u\rangle\langle e|$ and $\hat{\sigma}_{c,e} = |c\rangle\langle e|$. Equations (C.5.15) and (C.5.16) correspond to cases where a transmitted or a scattered photon was detected first, respectively. Note that for correlations involving the fluorescence field, detection of photons emitted in $|e\rangle \rightarrow |u\rangle$ (detection probability $\sim \gamma_u^{(rad)}$) or $|e\rangle \rightarrow |c\rangle$ (detection probability $\sim \gamma_c^{(rad)}$) can result in different dynamics and two separate terms. While these photons (or two paths) are in principle distinguishable by frequency, in our experiment both paths were detected without frequency filtering. For this reason, a photon detection in fluorescence leaves the SiV in some classical

mixture of states $|c\rangle$ (with probability $\gamma_c^{(rad)}/(\gamma_c^{(rad)}+\gamma_u^{(rad)})$) and $|u\rangle$ (with probability $\gamma_u^{(rad)}/(\gamma_c^{(rad)}+\gamma_u^{(rad)})$). On the other hand, the detection of a cavity photon preferentially leaves the SiV in state $|u\rangle$. This results in the asymmetry in the fluorescence–transmission intensity cross-correlation function measured in Fig. 5.3D.

The observed dynamics in photon correlations in Fig. 5.3, can be understood based on these multivel dynamics. Upon detection of a transmitted photon, the SiV has an increased likelihood to be projected into state $|u\rangle$, where the SiV is not excited by laser light. Consequently, for a time period ($\sim \tau_0$) given by the lifetime of state $|u\rangle$, the SiV-cavity system will have higher transmission and reduced scattering resulting in enhanced $g_{TT}^{(2)}$ and suppressed $g_{ST}^{(2)}$. If instead a scattered photon is detected first, the SiV is preferentially projected to the coupled state $|c\rangle$. This state undergoes two-level dynamics associated with decreased scattering and enhanced transmission at short times on the order of the excited state lifetime τ_e. At longer times of order τ_0 while the system is more likely to remain in the coupled state $|c\rangle$, it exhibits enhanced scattering ($g_{SS}^{(2)}$, Fig. 5.3A) and somewhat reduced transmission ($g_{ST}^{(2)}$, Fig. 5.3C). These results are also consistent with the optical switching dynamics in Fig. 2 where the system is polarized using a classical gate pulse instead of a single photon detection event and the relaxation dynamics at the same timescale τ_0 are observed.

C.5.4 Extraction of system parameters

The data shown in Figs. 5.1–5.3 of the main manuscript can be modeled using a single set of intrinsic system parameters. The cavity decay rate κ is measured from the envelope of the cavity transmission curve in Fig. 5.1E (blue curve). The dephasing rate γ_d of the SiV optical transition ($|c\rangle \rightarrow |u\rangle$) is measured from the SiV linewidth in Fig. 5.1F when the cavity is off resonance with the SiV (orange curve), while the single-photon Rabi frequency g is determined by the Purcell-broadened linewidth when the cavity is on resonance with the SiV (red curve). These values are consistent with the independent time-domain lifetime measurement described in the main text. These values (which suffice to determine the cooperativity) are then taken as fixed; the remaining parameters are extracted from the photon correlation measurements in Figs. 5.3C and 5.3D. (The data in Fig. 5.3B were taken above saturation with large cavity detuning ($\Delta_e = 0, \Delta_c >> \kappa$) and were modeled separately as a three-level atom in a classical field.) The optical switching experiment (Fig. 5.2) provides an independent measurement of the ground-state relaxation rates γ_{uc} and γ_{cu} and is consistent with the values extracted from the photon correlation measurements.

The following parameters (defined in Fig. C.7) accurately describe the system dynamics: $\{\kappa = 1150\,\gamma_0, \gamma_d = 4\,\gamma_0, \gamma_u = \gamma_0, \gamma_c = \gamma_0, \gamma_{uc} = 0.10\,\gamma_0, \gamma_{cu} = 0.15\,\gamma_0, g = \gamma_0(1.5\kappa/\gamma_0)^{1/2}, \gamma_c^{(rad)}/\gamma_u^{(rad)} = 2\}$ where we defined $\gamma_0 = 2\pi \times 50\,\text{MHz}$. Of these parameters, $\{\kappa, \gamma_d, \gamma_{uc}, \gamma_{cu}, g\}$ are consistent with independently measured values in

Figs. 5.1–5.3. The detected ratio of $\gamma_c^{(rad)}/\gamma_u^{(rad)}$ determines the asymmetry of $g^2_{ST}(\tau)$ and was fit separately using the data in Fig. 5.3D. The theoretical expressions for photon correlations were convolved with the detector timing response (300 ps timing jitter per APD) to obtain the solid curves in Fig. 5.3. Intensity correlation measurements were normalized using intensity averages; we do not observe excess noise due to incoherent dynamics at slow timescales.

C.5.5 Measured vs. expected cooperativity

Our measured cooperativity of $C \sim 1$ differs substantially from the cooperativity $C = \frac{4g^2}{\kappa\gamma} = \frac{3}{4\pi^2}\frac{Q}{V}\left(\frac{\lambda}{n}\right)^3 \sim 275$ in the ideal case of a perfect emitter coupled optimally to our cavity with measured quality factor $Q \sim 7200$ and dimensionless mode volume $\frac{V}{(\lambda/n)^3} \sim 3$. In this section, we discuss the discrepancies leading to this disagreement. See also section 2.5 where we describe some similar errors for the hybrid nanocavity/NV system described in chapter 2.

First, the emitter is not optimally aligned with the cavity mode. Based on the crystallographic orientation of our sample and the electric field mode profile inside the cavity, the maximal overlap between the atomic transition dipole and the cavity mode is roughly 2/3. The positioning of the SiV center can be a separate source of error. The accuracy of FIB-based implantation (Section C.2.5) is around 40 nm, including straggle. This is a significant fraction of the spatial extent of the local cavity field

antinode that extends in about 100 nm in all three dimensions. This positioning error can reduce the atom–photon coupling and hence the cooperativity by roughly 20–40%.[1]

In addition to reductions in the cooperativity due to emitter positioning errors, the SiV is not a perfect optical emitter. The atomic decay rate γ in the cooperativity includes all photon emission and decoherence rates, whereas the single-photon Rabi frequency g includes only the contribution from the dipole transition ($|c\rangle \leftrightarrow |e\rangle$) that couples to the cavity mode. The cooperativity is therefore reduced by imperfections in the optical transitions of the SiV center. First, the Debye-Waller factor ($\gamma_{ZPL}^{(rad)}/\gamma^{(rad)}$) for the SiV ZPL is around 70%. Next, our linewidth is broadened by phonon processes and spectral diffusion to approximately three times the lifetime-limited linewidth ($\gamma_0/\gamma_{exp} \approx 0.3$). For the lambda system used in the experiment, the branching ratio of the $|e\rangle \rightarrow |c\rangle$ and $|e\rangle \rightarrow |u\rangle$ ZPL transitions are about 80% and 20% respectively[225]. Finally, if there is a significant nonradiative decay rate limiting the quantum efficiency (QE) of the SiV, our observed cooperativity could be substantially reduced.

Taking conservative estimates for the parameters other than an unknown quantum efficiency, our estimated cooperativity is around $C \sim 10 \times$ QE (Table C.1). A quan-

[1]The story is similar for the NV center system in chapter 2, except the positioning error there is set by our ability to localize the NV in the dimension along the beam axis when designing the optical cavities, as well as any alignment error in our lithography process. This positioning error is difficult to estimate, but is probably on the order of 100–200 nm.

$$C = \overbrace{\frac{3}{4\pi^2}\left(\frac{\lambda_0}{n}\right)^3 \frac{Q}{V}}^{\text{cavity properties}} \quad \overbrace{\frac{\gamma_{ZPL}^{(rad)}}{\gamma^{(rad)}} \frac{\gamma_0}{\gamma_{exp}} \text{QE}}^{\text{atomic properties}} \quad \overbrace{\begin{pmatrix}\text{dipole}\\ \text{orient.}\end{pmatrix}\begin{pmatrix}\text{SiV}\\ \text{position}\end{pmatrix}}^{\text{atomic position and orientation}}$$

$$C \approx \frac{1}{13} \quad \frac{7200}{3} \quad 0.7 \quad 0.3 \ \text{QE} \quad 0.4\text{–}0.8 \quad 0.4\text{–}1 \quad \sim 10 \times \text{QE}$$

Table C.1: Cooperativity estimate based on SiV and experimental parameters described in the text

tum efficiency of around 10% is therefore consistent with the discrepancy between our expected and observed cooperativity. Note that the quantum efficiency of the NV is believed to be larger, perhaps of order unity.

C.6 Subnatural-linewidth Raman single photons

The Raman tuning demonstrated in Fig. 5.4 uses off-resonant laser excitation to generate spectrally-tunable subnatural linewidth single photons. In this section, we discuss technical considerations that enable us to isolate single photons under off-resonant excitation and present data that support our claims about subnatural linewidths for Raman photons. The SiV centers used for the Raman tuning and entanglement experiments have a ground state frequency splitting of $\approx 50\,\text{GHz}$. When we excite the $|u\rangle \rightarrow |e\rangle$ transition with a laser at frequency ν, the Raman photons are at a frequency $\approx \nu + 50\,\text{GHz}$. We use separate spatial modes for laser excitation (free-space,

see Fig. 5.4) and Raman photon detection (waveguide mode collected via fiber). This allows us to significantly suppress leakage from the excitation laser into our collection mode. Despite this suppression, the scattering at the diamond-vacuum interface results in laser leakage into the collection mode. When we excite the $|u\rangle \rightarrow |e\rangle$ transition on resonance, we find that the typical signal to noise ratio between the Raman single-photons and laser background is about ~ 1.

To obtain Raman single-photons with high purity, we use a home-built scanning Fabry-Perot (FP) filter cavity designed to have high transmission for Raman photons at frequency $\approx \nu + 50\,\mathrm{GHz}$ while suppressing laser photons at frequency ν. To achieve this, we built a cavity with a free spectral range (FSR) of 37 GHz which maximally suppresses the laser field (by putting the laser line in the middle of the FSR, exactly between two cavity resonances) while maintaining a high cavity bandwidth of 150 MHz (FWHM, ringdown time 1.05 ns). We note that the high bandwidth is necessary to be able to measure the dynamics observed at the ≈ 2.5 ns timescale in Fig. 5.5D. The fit functions used for the data in Fig. 5.5D are convolved with the combined timing response of the cavity and the detectors.

The use of the FP cavity allows us to obtain a signal to noise ratio of ~ 1000 under resonant excitation. At increased detunings Δ, the scattering cross section of the SiV reduces according to $\sim \frac{1}{(\Gamma/2)^2+\Delta^2}$, where Γ is the $|u\rangle \leftrightarrow |e\rangle$ transition linewidth. This scaling is confirmed with the measurements shown Fig. C.8A where we measure the Raman emission intensity at different detunings for a fixed laser power. The reduced

scattering cross section at large detunings necessitates an increased laser power to maintain a fixed photon scattering and detection rate. The extinction ratio of the FP cavity ($\sim 10^4$ for current device) is therefore a crucial parameter that sets the practical limit on the extent of Raman tuning. With the cavity used in the experiments, we are able to tune the Raman photons by 10 GHz in each direction while maintaining a signal to noise ratio above 1 (see extended data in Fig. C.8). The tuning range could be further extended by using a higher finesse cavity (or a second filter cavity) or cavity-enhanced Raman scattering.

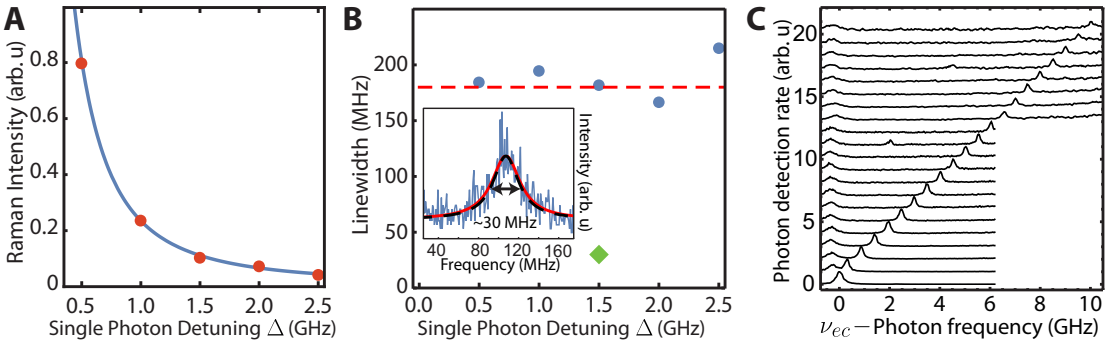

Figure C.8: (A) Raman fluorescence intensity for a fixed laser power measured at different single photon detunings Δ. The solid line is a fit with the form $\frac{A}{(\Gamma/4\pi)^2+(\Delta)^2}$ with $\Gamma/2\pi = 440$ MHz. (B) Raman emission linewidth as a function of detuning. At all detunings, the Raman emission linewidth (blue circles) is limited by the cavity linewidth (dashed red line). When a narrow-linewidth cavity with FWHM$\sim$30 MHz is used to measure the Raman linewidth, the linewidth is significantly narrower (green diamond). Inset: Raman fluorescence intensity as a function of narrow-linewidth cavity frequency. The fitted Lorentzian response (solid red curve) is almost identical to the measured cavity transfer function (dashed black curve) indicating that the Raman linewidth is less than the 30 MHz cavity bandwidth. (C) Extended data for Fig. 5.4C, showing Raman tuning over 10 GHz on the red sideband.

Under off-resonant excitation with $\Omega, \Gamma << \Delta$, the linewidth of the Raman photons is determined by the coherence between the metastable states $|u\rangle$ and $|c\rangle$. In this limit, it is therefore possible to achieve subnatural linewidth photons, that is, photons that are narrower than the natural spontaneous emission linewidth of 90 MHz (corresponding lifetime $\tau_e \approx 1.8$ ns). When we measure the linewidth of the Raman photons in Fig. C.8B, we find that the linewidth is limited by the resolution of the FP cavity 180 MHz. When we use a different FP cavity with a resolution of 30 MHz, we find that the Raman linewidth is less than 30 MHz (inset of Fig. C.8B), demonstrating subnatural-linewidth Raman photon emission.

C.7 Experimental procedure for entanglement generation

To generate entanglement between two SiV centers, we perform the same Raman tuning technique simultaneously on two spatially-separated SiV centers in a single diamond waveguide. The waveguide is again adiabatically coupled to a single-mode optical fiber as described in Sec. C.2.6. The collected photons are frequency filtered (see below) and then sent to a Hanbury Brown-Twiss setup to measure the photon autocorrelation function using the detectors and electronics described in Sec. D.1. The theoretical analysis of the system will be presented in Sec. C.8.

For the photon autocorrelation measurements performed when the two SiV centers are Raman-tuned onto resonance (Fig. 5.5B, red curve in Fig. 5.5D), the Raman fluorescence from both SiV centers passes through the FP cavity (FWHM: 150 MHz, FSR: 37 GHz, Transmission: 80%), ensuring frequency indistinguishability. For the two SiVs used in the entanglement experiment, the transition frequencies ν_{ec} were detuned by about 1 GHz. The emitters were excited below saturation using two frequency stabilized lasers at single photon detunings $\Delta_1 = 1.3$ GHz for SiV1 and $\Delta_2 = 2.3$ GHz for SiV2, and the Raman emission frequencies and intensities were matched. During the course of the measurement, the Raman emission frequency for the SiV centers underwent slow spectral drifts of order 100 MHz at the $\sim$ 10 minute timescale that were compensated by the frequency of the excitation lasers. In other words, effects of slow spectral diffusion were mitigated using the Raman tuning technique. The Raman emission rates into the waveguide mode from each SiV were independently monitored to assure balanced emission. For these measurements, it is also important that the relative phase of the two driving lasers does not drift over the $\sim$ 10 ns lifetime of the entangled state (see Sec. C.8.1 for a theoretical discussion). This requirement is fulfilled by the frequency stabilization scheme described in Sec. D.1. We experimentally verify the relative phase stability of the two driving fields by performing a time-domain interference measurement (Fig. C.9). For applications where it is necessary to achieve phase stability over longer timescales, the two excitation frequencies could be generated from a single laser using electrooptical modulation.

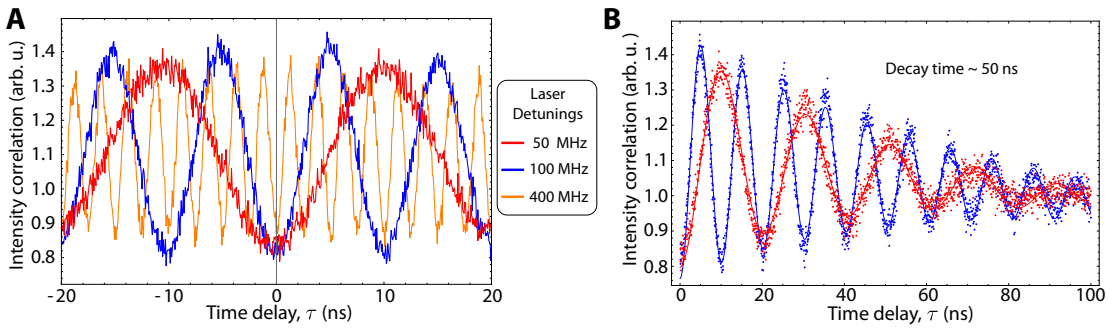

Figure C.9: Phase stability of the two Raman excitation lasers. The two lasers are combined on a beamsplitter and the intensity correlations are measured at the two output ports. (A) When the two lasers are detuned, intensity beats are observed. For the timescales considered in the entanglement experiment ($\tau < 10$ ns, see Fig. 5.5D), the laser beats do not decay and the relative phase of the two lasers is stable. (B) The laser beats decay at a longer timescale of ~ 50 ns that is determined by the relative linewidths of the two lasers.

For the autocorrelation measurements performed in the distinguishable case (Fig. 5.5C, blue curve in Fig. 5.5D), the frequencies of the Raman photons from the two SiV centers are not tuned on resonance and differ by about 1 GHz. In this measurement, we split the fluorescence from the two SiV centers using a 50/50 beamsplitter and send each path to a separate FP cavity: FP1 (FWHM: 150 MHz, FSR: 37 GHz, Transmission: 80%) is tuned to SiV1 Raman emission, FP2 (solid etalon with FWHM: 800 MHz, FSR: 20.3 GHz, Transmission: 80%) is tuned to SiV2 Raman emission. The two paths are then recombined on a second 50/50 beamplitter and sent to two detectors to measure photon correlations.

C.8 Model description for entanglement in a two-SiV system

In this Section, we analyze entanglement generation and verification for two SiV centers coupled to a waveguide. Specifically, we first use a simple model to describe the two-SiV entanglement generation process (Sec. C.8.1). We next extend this model in Sec. C.8.2 to include dissipation and show that it can be used to describe the observations reported in the main text. We next present the analyses showing how the photon correlation measurements can be used to verify entanglement generation. Specifically, in Sec. C.8.3.1, we derive an expression for the concurrence of the two-SiV system after emission of a single photon. We show that the concurrence is positive, demonstrating the presence of entanglement after a single photon emission. In Sec. C.8.3.2, we use a more specific model for our system to estimate the fidelity of the entangled state $|B\rangle$ conditioned on detection of two photons within a short time delay. The resulting fidelity also demonstrates creation of an entangled state.

C.8.1 Simple model

The process of entanglement generation can be understood through a simple model of the system. The two SiVs in the waveguide can be modeled as two three-level systems in a lossy cavity as in Sec. C.5. In a proper rotating frame, the Hamilton of the

system is

$$\begin{aligned}\hat{H} &= \Delta_1 |e\rangle_1 \langle e| + \Delta_2 |e\rangle_2 \langle e| + (\Omega_1 |e\rangle_1 \langle u| + \Omega_2 |e\rangle_2 \langle u| + h.c.) \\ &\quad + (g_1 |e\rangle_1 \langle c| \hat{a} + g_2 |e\rangle_2 \langle c| \hat{a} + h.c.), \end{aligned} \tag{C.8.1}$$

where we have assumed that both Raman transitions are on resonance and defined $\Delta_i = \omega_{ei} - \omega_{Li}$ where ω_{ei} is the frequency of level $|e\rangle_i$ and ω_{Li} is the frequency of the laser associated with the coupling Ω_i, which we assume to be real. The photonic operator $\hat{a}$ describes the single mode field that both emitters couple to. Since we are operating in the far detuned regime, we can adiabatically eliminate the excited states, which results in an effective Hamiltonian

$$\hat{H}_{\text{eff}} \approx -\tilde{g}_1 \hat{\sigma}_{uc}^{(1)} \hat{a} - \tilde{g}_2 \hat{\sigma}_{uc}^{(2)} \hat{a} + h.c \tag{C.8.2}$$

where $\tilde{g}_i \approx \frac{\Omega_i g_i}{\Delta_i}$ and we have defined $\hat{\sigma}_{uc}^{(i)} = |u\rangle_i \langle c|$. We have neglected any shifts of the ground states due to laser and cavity couplings since we are far detuned.

To understand entanglement generation, we consider the initial state of the SiVs $|u\rangle_1 |u\rangle_2$ since this is the only state that can emit two Raman photons. The evolution of this initial state under the above Hamiltonian is

$$U(\epsilon) |u\rangle_1 |u\rangle_2 |0\rangle \approx |u\rangle_1 |u\rangle_2 |0\rangle + i\epsilon (\tilde{g}_1 |c\rangle_1 |u\rangle_2 + \tilde{g}_2 |u\rangle_1 |c\rangle_2) |1\rangle, \tag{C.8.3}$$

where $U(t) = e^{-i\hat{H}t}$, $|0\rangle$ ($|1\rangle$) is the vacuum (single photon) state of the waveguide mode and we have expanded the time evolution assuming that we are looking at a time $\epsilon \ll 1/\tilde{g}_{1,2}$. In the experiment, the strength of the lasers is tuned such that $|\tilde{g}_1| = |\tilde{g}_2| = \tilde{g}$ and we write $g_2 = g_1 e^{i\phi}$ where ϕ results from the propagation phase between the emitters in the waveguide and the relative phase of the two driving lasers. As described above, the two driving lasers are frequency stabilized such that the phase ϕ is constant over timescales much longer than any other system dynamics. Under these conditions, we have

$$U(\epsilon)\,|u\rangle_1\,|u\rangle_2\,|0\rangle \approx |u\rangle_1\,|u\rangle_2\,|0\rangle + i\epsilon\tilde{g}\left(|c\rangle_1\,|u\rangle_2 + e^{i\phi}\,|u\rangle_1\,|c\rangle_2\right)|1\rangle\,. \tag{C.8.4}$$

The emission of the first photon thus prepares the SiVs in the entangled state

$$|B\rangle = \left(|c\rangle_1\,|u\rangle_2 + e^{i\phi}\,|u\rangle_1\,|c\rangle_2\right)/\sqrt{2}. \tag{C.8.5}$$

This state $|B\rangle$ is a superradiant state, which emits photons at a rate which is twice that of a single emitter in state $|u\rangle$. This can be seen from the evolution of this state under the Hamiltonian in Eq. (C.8.2):

$$U(\epsilon)\,|B\rangle\,|0\rangle \approx |B\rangle\,|0\rangle - \sqrt{2}i\epsilon\tilde{g}e^{i\phi}\,|c\rangle_1\,|c\rangle_2\,|1\rangle\,. \tag{C.8.6}$$

The $\sqrt{2}$ prefactor of $|c\rangle_1\,|c\rangle_2\,|1\rangle$ corresponds to a factor of 2 enhancement of the emis-

sion rate compared to that of a single emitter in state $|u\rangle$. It is this enhanced emission rate that results in the measured peak in the normalized photon correlation function $g^{(2)}$ at zero delay time in Fig. 5.5D.

C.8.2 Detailed model

We next present a more detailed model of the waveguide experiment including various dissipation channels in order to model the time-dependent $g^{(2)}$-correlation functions. We describe the unitary dynamics using Eq. (C.8.1) and the dissipation in the system using the Lindblad operators defined in Eq. (C.5.2) for each atom. The only exception is that we now define $\hat{L}_{5,i} = \sqrt{\gamma_d}\,|u\rangle_i\,\langle u|$ because we scatter Raman photons at a large detuning ($\Delta_i \gg \gamma_u$) where the contribution from excited state dephasing can be neglected and ground state dephasing dominates. Furthermore, we assume that the two atoms have equal decay rates. Since $\Delta_i \gg \Omega_i, g_i$, we can again adiabatically eliminate the excited states, which results in the effective Hamiltonian in Eq. (C.8.2). The effective Lindblad operators are $\hat{L}_{3,i}$ through $\hat{L}_{6,i}$ and

$$\hat{L}_{1,i}^{\text{eff}} \approx \frac{\sqrt{\gamma_c}}{\Delta_i}\left(\Omega_i\,|c\rangle_i\,\langle u| + g_i\,|c\rangle_i\,\langle c|\,\hat{a}\right) \tag{C.8.7}$$

$$\hat{L}_{2,i}^{\text{eff}} \approx \frac{\sqrt{\gamma_u}}{\Delta_i}\left(\Omega_i\,|u\rangle_i\,\langle u| + g_i\,|u\rangle_i\,\langle c|\,\hat{a}\right). \tag{C.8.8}$$

Since we operate in the weak-driving regime, we can truncate the Hilbert space assuming that at most two photons are present in the system. In this case, the system can

be described in a basis of the states

$$\Big\{ |uu\rangle|0\rangle, |uc\rangle|0\rangle, |cu\rangle|0\rangle, |cc\rangle|0\rangle, |uu\rangle|1\rangle, |uc\rangle|1\rangle, \\ |cu\rangle|1\rangle, |cc\rangle|1\rangle, |uu\rangle|2\rangle, |uc\rangle|2\rangle, |cu\rangle|2\rangle, |cc\rangle|2\rangle \Big\}, \tag{C.8.9}$$

which we label $\{|1\rangle, \ldots, |12\rangle\}$. The notation is such that $|uc\rangle|1\rangle$ denotes atomic state $|u\rangle_1 |c\rangle_2$ and one photon in mode $\hat{a}$. In this basis, we can solve the master equation for the system by adiabatically eliminating all states containing cavity photons since the cavity mode models, in this experiment a waveguide, and therefore has extremely fast decay. We also assume that the dynamics of the ground states $\{|1\rangle, \ldots, |4\rangle\}$ are governed solely by the dissipative couplings between them (similar to the procedure in Sec. C.5.3) since we are in the weak driving regime and that $|g_i|^2/(\kappa\gamma_u) \ll 1$.

Under these conditions, we find that the photon intensity correlation function can be expressed as

$$g^{(2)}(\tau) \approx \frac{(\alpha_1+\alpha_2)\rho_{1,1}(\tau) + \alpha_1\rho_{2,2}(\tau) + \alpha_2\rho_{3,3}(\tau) + 2\alpha_3\rho_{2,3}(\tau)}{\Big((\alpha_1+\alpha_2)(\rho^{(s)}_{1,1}+\rho^{(s)}_{2,2})\Big)^2}, \tag{C.8.10}$$

where $\rho_{i,j} = \langle i|\rho|j\rangle$ and $\rho^{(s)}$ denotes the steady state density matrix of the system and $\rho = \hat{a}\rho^{(s)}\hat{a}^\dagger$. The matrix elements and constants are defined in Sec. C.9.3. The peak in the $g^{(2)}$ function at zero time-delay originates from the coherence $\alpha_3\rho_{2,3}(\tau)$ between the two ground states. This is consistent with the simple model description

in Sec. C.8.1: If the laser strengths are tuned such that $\left|\frac{\Omega_1^* g_1}{\Delta_1}\right| = \left|\frac{\Omega_2^* g_2}{\Delta_2}\right|$ and $g_2 = g_1 e^{i\phi}$ then $\rho_{1,1}(0) = 0$ and $\alpha_1\rho_{2,2}(0) = \alpha_2\rho_{3,3}(0) = \alpha_3\rho_{2,3}(0)$, which means that the peak is a result of the enhanced emission rate of the entangled state $|B\rangle$. The coherence $\rho_{2,3}(\tau)$ decays with a rate $\Gamma \approx \gamma_{cu} + \gamma_{uc} + \gamma_d$, which determines the width of the peak. We note that under the continuous driving used in our experiment, the optical pumping rate out of state $|u\rangle$ determines the lower limit on this decoherence rate.

Eq. (C.8.10) corresponds to the ideal limit where no noise photons, e.g. originating from scattering of laser light, are detected. The effect of noise photons changes the correlation function into

$$g^{(2)}_{\text{noise}}(\tau) \approx \frac{g^{(2)}(\tau) + (2 + p_n)p_n}{(1 + p_n)^2}, \tag{C.8.11}$$

where p_n is the relative rate (odds) of detecting noise photons compared to Raman photons and we have assumed that the noise photons are completely classical and uncorrelated. The results of this model are in good agreement with the measured data as shown in Fig. C.10. The solid curves in Fig. 5.5D are a simple phenomenological model assuming exponential decay with a single timescale for the distinguishable and single-SiV cases and two timescales for the indistinguishable case. All models are convolved with the (independently measured) temporal response of the cavity and photon detectors.

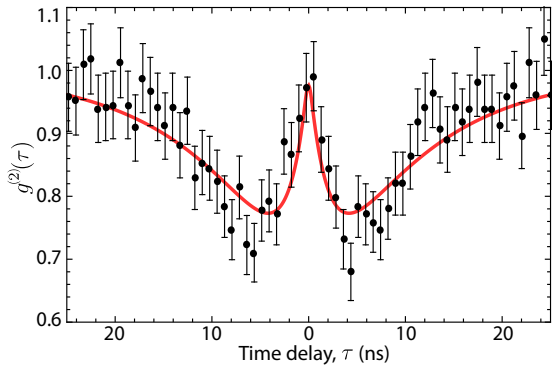

Figure C.10: Comparison of model (solid red curve) to data (black points) using the following parameters (defined in Eq. (C.5.2)): $\{\Delta_1, \Delta_2, \gamma_{cu}, \gamma_{uc}, \gamma_{uu}, \Omega_1, \Omega_2\} = \{22, 14, 0.10, 0.06, 0.66, 0.23, 0.15\} \times \gamma_0$ with $\gamma_0 = 2\pi \times 94\,\text{MHz}$. The model has been convolved with a Gaussian to account for the finite detector jitter present in the experiment. Of these parameters, Δ_1, Δ_2 and the odds of detecting a noise photon $p_n = 0.09$ are fixed based on single-photon detunings and single SiV $g^{(2)}$ measurements; the other parameters are estimated by fitting the data to the model under conservative physical constraints. The data correspond to the red curve in Fig. 5D in the main text.

C.8.3 Entanglement analysis

We verify entanglement generation through the two-photon correlation function of the emitted field from the SiVs. The SiVs are excited by weak continuous-wave lasers and the corresponding emitted field is a stationary field such that the photon correlation function of the field can be written as

$$g^{(2)}(\tau) = \frac{\text{tr}\hat{A}^\dagger\hat{A}^\dagger(\tau)\hat{A}(\tau)\hat{A}\rho}{\text{tr}\hat{A}^\dagger\hat{A}\rho^2} = \frac{\text{tr}\hat{A}^\dagger\hat{A}e^{\mathcal{L}\tau}\left[\hat{A}\rho\hat{A}^\dagger\right]}{\text{tr}\hat{A}^\dagger\hat{A}\rho^2} \tag{C.8.12}$$

$$= \frac{\text{tr}\hat{A}^\dagger\hat{A}\tilde{\rho}(\tau)}{\text{tr}\hat{A}^\dagger\hat{A}\rho}, \tag{C.8.13}$$

where $\hat{A} = \hat{A}(0)$ is the annihilation operator of the field and ρ is the density matrix describing the stationary field, i.e. the steady state density matrix of the system. We have defined $\tilde{\rho}(\tau)$ as the conditional density matrix at time τ with initial condition $\tilde{\rho}(0) = \frac{1}{\mathrm{tr}\hat{A}^\dagger\hat{A}\rho}\hat{A}\rho\hat{A}^\dagger$ and time evolution described by some Lindblad super-operator $\mathcal{L}\tau$. $\tilde{\rho}(\tau)$ thus describes the state of the system at time τ conditioned on having emitted a photon at time $\tau = 0$. Note that in the experiment, the photon is detected with a fixed time delay after being emitted into into the waveguide. However, the detection still heralds that the photon was emitted into the waveguide at the earlier time. The photon correlation function $g^{(2)}(\tau)$ thus directly probes the ratio between photon emission from the conditionally prepared state after emission of a photon into the waveguide and the stationary state ρ.

C.8.3.1 Concurrence

The degree of entanglement of an arbitrary two qubit state can be quantified by the concurrence of the corresponding density matrix, $\mathcal{C}(\rho)$ [310]. All separable states have $\mathcal{C}(\rho) = 0$ while a maximally entangled state has $\mathcal{C}(\rho) = 1$. Following the procedure of Ref. [311], we derive a lower bound on the concurrence of the state of the two SiVs conditioned on a photon emission into the waveguide. We show that the concurrence is positive, demonstrating the presence of entanglement after a single photon emission.

As a general model for the SiVs, we describe them as qubits with states $|c\rangle$ and $|u\rangle$

where a photon can be emitted from state $|u\rangle$ with some fixed probability while $|c\rangle$ is dark. Let $p_{u,i}^{(0)}$ be the probability of the i^{th} SiV to be in state $|u\rangle$ in the steady state. According to Eq. (C.8.13), the corresponding single SiV photon correlation function can then be written as

$$g_i^{(2)}(\tau) = \frac{p_{u,i}(\tau)}{p_{u,i}^{(0)}}, \tag{C.8.14}$$

where $p_{u,i}(\tau)$ is the probability of the SiV to be in state $|u\rangle$ time τ after the emission of the first photon. If both SiVs are continuously excited, we can write the density matrix following the emission of a photon as

$$\tilde{\rho} = \begin{pmatrix} p_{cc} & 0 & 0 & 0 \\ 0 & p_{uc} & d & 0 \\ 0 & d^* & p_{cu} & 0 \\ 0 & 0 & 0 & p_{uu} \end{pmatrix}, \tag{C.8.15}$$

in the basis $\{|cc\rangle, |cu\rangle, |uc\rangle, |uu\rangle\}$. Here, p_{cu} is the (time-dependent) probability of the first SiV being in state $|c\rangle$ and the second SiV being in state $|u\rangle$, and so on. Note that we have assumed there is no coherence in the system except between states $|cu\rangle$ and $|uc\rangle$. This assumption gives a lower bound on the actual amount of entanglement in the system since any coherences could be removed with local operations on the SiVs and classical communication, which can never increase the amount of entanglement as described in Ref. [311]. The concurrence of the conditional density matrix is

[311]

$$\mathcal{C}(\tilde{\rho}) = \max\left(2\left|d\right| - 2\sqrt{p_{cc}p_{uu}}, 0\right). \tag{C.8.16}$$

We assume that the two SiVs are completely uncorrelated in the steady state before a photon emission and that we are detecting a mode $\hat{A} \sim \hat{S}_1 + e^{i\phi}\hat{S}_2$, where $\hat{S}_i$ is the operator associated with emission of a photon from the i^{th} SiV. The $g^{(2)}$ function can then be written as

$$g^{(2)}(\tau) = \frac{p_{cu} + p_{uc} + 2\left|d\right|\cos(\theta - \phi) + 2p_{uu}}{p_{u,1}^{(0)} + p_{u,2}^{(0)}}, \tag{C.8.17}$$

where we have written the coherences as $d = \left|d\right| e^{i\theta}$. From this, we obtain a lower bound on the coherences

$$2\left|d\right| \geq \left|g_{\text{indist}}^{(2)}(\tau)\left(p_{u,1}^{(0)} + p_{u,2}^{(0)}\right) - 1 - p_{uu} + p_{cc}\right|, \tag{C.8.18}$$

where we have used that $p_{uc} + p_{cu} = 1 - p_{cc} - p_{uu}$. The diagonal elements p_{uu} and p_{cc} can be obtained from the single-SiV $g_i^{(2)}$ functions as

$$p_{uu} = \frac{p_{u,1}^{(0)}p_{u,2}^{(0)}}{p_{u,1}^{(0)} + p_{u,2}^{(0)}}\left(p_{u,1}(\tau) + p_{u,2}(\tau)\right) = \frac{p_{u,1}^{(0)}p_{u,2}^{(0)}}{p_{u,1}^{(0)} + p_{u,2}^{(0)}}\left(g_1^{(2)}(\tau)p_{u,1}^{(0)} + g_2^{(2)}(\tau)p_{u,2}^{(0)}\right), \tag{C.8.19}$$

and

$$p_{cc} = \frac{1}{p_{u,1}^{(0)} + p_{u,2}^{(0)}} \left(p_{c,1}(\tau) p_{c,2}^{(0)} p_{u,1}^{(0)} + p_{c,2}(\tau) p_{c,1}^{(0)} p_{u,2}^{(0)} \right) \tag{C.8.20}$$

$$= \frac{1}{p_{u,1}^{(0)} + p_{u,2}^{(0)}} \left((1 - g_1^{(2)}(\tau) p_{u,1}^{(0)})(1 - p_{u,2}^{(0)}) p_{u,1}^{(0)} + (1 - g_2^{(2)}(\tau) p_{u,2}^{(0)})(1 - p_{u,1}^{(0)}) p_{u,2}^{(0)} \right) \tag{C.8.21}$$

where we have used that $p_{c,i}^{(0)} = 1 - p_{u,i}^{(0)}$ and $p_{c,i} = 1 - p_{u,i}$. Combining Eqs. (C.8.18)-(C.8.20) with Eq. (C.8.16) gives a lower bound on the concurrence. For the experiment, the photon detection rates from the SiVs were balanced such that $p_{u,1}^{(0)} = p_{u,2}^{(0)} = p_u^{(0)}$ and the lower bound becomes

$$\mathcal{C}(\tilde{\rho}) \geq \max\left(0, \left| 2 g_{\text{indist}}^{(2)}(\tau) p_u^{(0)} - \frac{1}{2} \left(2 + g_1^{(2)}(\tau) + g_2^{(2)}(\tau) \right) p_u^{(0)} \right| \right.$$
$$\left. - p_u^{(0)} \sqrt{ \left(g_1^{(2)}(\tau) + g_2^{(2)}(\tau) \right) \left(2 - (g_1^{(2)}(\tau) + g_2^{(2)}(\tau)) p_u^{(0)} \right) (1 - p_u^{(0)}) } \right) \tag{C.8.22}$$

We estimate the concurrence generated in our experiment by directly evaluating Eq. (C.8.22) using experimentally measured values of $g^{(2)}(\tau)$ at short time delays $\tau \sim 0$ (Fig. 5.5). We estimate the error assuming the photon count rates follow a Poisson distribution. (This assumption has been verified via similar measurements on the same apparatus). By taking the thermal distribution at 4 K and measured saturation associated with weak optical pumping during the measurement into account, we obtain a lower bound of $p_u^{(0)} \geq 0.34$ for each SiV in steady state. From fits of the autocorrelation functions shown in Fig. 5.5D, we obtain the concurrence

$\mathcal{C}(\tau = 0) > 0.090\,(0.024)$ demonstrating entanglement generation in the system. Around $\tau = 0$ the concurrence is fairly insensitive to this window size and is positive for window sizes up to 8 ns. All uncertainties given in parentheses here and throughout the manuscript are the one-standard-deviation level. Note that the extracted value of concurrence is limited by imperfect initial state preparation of the SiV centers. This can be circumvented by either working with the pulsed excitation or via post-selection as discussed in the following section.

C.8.3.2 Conditional fidelity estimate

The lower bound on the concurrence extracted above verifies that entanglement is created by emission of the first photon into the waveguide. In order to relate this entanglement to the theoretical model presented previously, we now estimate the fidelity of the conditional state with state $|B\rangle$ given that a second photon is detected at a time ϵ after the first. Here, ϵ is much shorter than the decoherence rate of the ground states, which ensures that any dynamics of the conditional state can be neglected and we therefore post-select on events where the initial state of the SiVs was $|uu\rangle$ to good approximation.

While the measurement of the correlation function of a single SiV individually shows a strong anti-bunching at $\tau = 0$ (orange curve in Fig. 5.5D), the correlation functions do not completely vanish as expected for an ideal single photon source. What is detected is therefore not only the field from the Raman transition of the

SiV but also noise photons originating primarily from the scattering of frequency-distinguishable laser light. From the single-emitter $g_i^{(2)}$ functions, we can estimate the ratio, $p_{n,i}$ between the detection rate of noise photons and Raman photons assuming that the noise photons are classical and uncorrelated. From Eq. (C.8.11), we find that

$$g_i^{(2)}(0) = \frac{p_{n,i}(2 + p_{n,i})}{(1 + p_{n,i})^2}, \tag{C.8.23}$$

which for the measured single emitter $g^{(2)}$ functions of $g_1^{(2)}(0) = g_2^{(2)}(0) = 0.16(3)$ gives $p_{n,1} = p_{n,2} = p_n = 0.09(2)$.

To calculate the $g^{(2)}$ function when both emitters are excited, we assume that the emitters are completely uncorrelated in the steady state. Consequently, the rate of Raman photons γ_R is simply the sum of the Raman photon rates from the single emitters in the steady state. Furthermore, the rate of noise photons γ_{noise} is also assumed to be the sum of the noise photon rates for the single emitters. In the experiments, the photon detection rate from the two emitters was balanced, which means that the ratio between the detection rate of Raman photons and noise photons is still p_n. The total rate of photons from the steady state can thus be written as $\gamma_{\text{total}} = \gamma_R + \gamma_{\text{noise}} = 2\gamma_r p_u^{(0)}(1 + p_n)$, where we have written the single emitter Raman photon rate as $\gamma_r p_u^{(0)}$ where $p_u^{(0)}$ is the steady state probability of an emitter to be in state $|u\rangle$.

The conditional density matrix upon emission of the first photon can be parameter-

ized as

$$\tilde{\rho} = \frac{1}{1+p_n}\left(p_u^{(0)}\tilde{F}\left|B\right\rangle\left\langle B\right| + (1-p_u^{(0)}\tilde{F})\rho_d\right) + \frac{p_n}{1+p_n}\rho, \tag{C.8.24}$$

where ρ is the steady state density matrix of the SiVs and ρ_d describes all states that cannot emit Raman photons, i.e. $|cc\rangle$ and $|D\rangle = \frac{1}{\sqrt{2}}\left(|uc\rangle - e^{i\phi}|cu\rangle\right)$. The first term proportional to $\frac{1}{1+p_n}$ can be viewed as the conditional density matrix if the first detected photon was a Raman photon while the second term proportional to $\frac{p_n}{1+p_n}$ is where the first detected photon was a noise photon. This conditional density matrix results in a $g^{(2)}$ function

$$g^{(2)}(0) = \frac{\tilde{F} + p_n(2+p_n)}{(1+p_n)^2}. \tag{C.8.25}$$

$\tilde{F}$ can thus be extracted from the the measured value of $g^{(2)}(0)$ in Fig. 5.5D. $\tilde{F}$ can be viewed as the fidelity with state $|B\rangle$ if the two SiVs were initially in state $|uu\rangle$.

In the $g^{(2)}$ measurements, we postselect for experimental runs that result in a two-photon coincidence. For these runs, the overlap with state $|B\rangle$ after the emission of the first photon is then given by $F = p_{uu}^{(c)}\tilde{F}$, where $p_{uu}^{(c)}$ is the probability of the initial state being $|uu\rangle$ given that we detected the second photon ϵ after the first photon. This probability can be bounded from below by the relative rate of detecting two Raman photons compared to the total rate of detecting two photons. From Eq. (C.8.24),

we find that this is

$$p_{uu}^{(c)} \geq \frac{\frac{1}{1+p_n} 2\tilde{F} p_u^{(0)} \gamma_s}{\frac{1}{1+p_n} 2\tilde{F} p_u^{(0)} \gamma_s + 2p_n p_u^{(0)} \gamma_s + \frac{p_n}{1+p_n} 2\gamma_s p_u^{(0)}} = \frac{\tilde{F}}{\tilde{F} + (2+p_n)p_n}. \tag{C.8.26}$$

Consequently, we find a lower bound on the fidelity of the conditional state

$$F \geq \frac{\left(g^{(2)}(0)(1+p_n)^2 - p_n(2+p_n)\right)^2}{g^{(2)}(0)(1+p_n)^2}. \tag{C.8.27}$$

From the measured value of $g^{(2)}(0) = 0.98(5)$, we obtain $F \geq 82(7)\%$.

C.9 Analytical expressions for density matrix elements

C.9.1 Steady-state density matrix expressions

The analytical expression for the matrix elements $\rho_{i,j}^{(s)} = \langle i | \rho^{(s)} | j \rangle$ in Sec. C.5.2 are given by:

$$\rho_{1,1}^{(s)} \approx \frac{1}{\mathcal{A}+\mathcal{B}/\mathcal{C}} \tag{C.9.1}$$

$$\rho_{1,2}^{(s)} \approx \frac{-4\xi g\rho_{1,1}^{(s)}}{\mathcal{C}}$$

$$\times(16\xi^2g^2-\kappa((4\Delta_e^2+\kappa^2)(\gamma_c+\gamma_u)+4g^2(\kappa+\gamma_c+\gamma_u)))(4g^2+\kappa(2i\Delta_e+\Gamma)) \tag{C.9.2}$$

$$\rho_{2,2}^{(s)} \approx \frac{16\xi^2g^2\kappa(\kappa+\Gamma)(4g^2+\kappa\Gamma)\rho_{1,1}^{(s)}}{\mathcal{C}}, \tag{C.9.3}$$

$$\rho_{3,3}^{(s)} \approx \frac{\gamma_u\rho_{2,2}^{(s)}+\gamma_{uc}\rho_{1,1}^{(s)}}{\gamma_{cu}} \tag{C.9.4}$$

$$\rho_{4,4}^{(s)} \approx \frac{4\xi^2\rho_{1,1}^{(s)}}{\mathcal{C}}\Big(16\Delta_e^4\kappa(\gamma_c+\gamma_u)+(4g^2+\kappa\Gamma)(16\xi^2g^2+\kappa(4g^2(\gamma_d+\gamma_{uc})+\kappa(\gamma_c+\gamma_u)\Gamma))$$

$$+4\Delta_e^2\kappa(\gamma_c+\gamma_u)(\kappa^2+\Gamma^2)+4\Delta_e^2(-16\xi^2g^2+4g^2(\kappa^2+(\kappa+\Gamma)(\gamma_c+\gamma_u)))\Big) \tag{C.9.5}$$

$$\rho_{5,5}^{(s)} \approx \frac{4\xi^2}{\kappa^2}\rho_{2,2}^{(s)} \tag{C.9.6}$$

$$\rho_{6,6}^{(s)} \approx \frac{4\xi^2}{\kappa^2}\rho_{3,3}^{(s)} \tag{C.9.7}$$

$$\rho_{7,7}^{(s)} \approx \frac{4\xi^2\rho_{4,4}^{(s)}+4g^2\rho_{5,5}^{(s)}}{3\kappa^2}-\frac{8}{27\kappa^4}\Big(-9\xi^4\rho_{1,1}^{(s)}+45\xi^3g(\rho_{1,2}^{(s)}+\rho_{2,1}^{(s)})$$

$$+12\xi^2g^2(-9\rho_{2,2}^{(s)}+7\rho_{4,4}^{(s)})+2g^2(\Delta_e^2+3g^2)\rho_{5,5}^{(s)}\Big)+\frac{392i\Delta_e\xi^3g}{9\kappa^5}(\rho_{1,2}^{(s)}-\rho_{2,1}^{(s)}) \tag{C.9.8}$$

$$\rho_{8,8}^{(s)} \approx \frac{6\xi^2}{3\kappa^2}\rho_{6,6}^{(s)}, \tag{C.9.9}$$

where we have defined

$$\mathcal{A} = \frac{\gamma_{cu}+\gamma_{uc}}{\gamma_{cu}} + \left(\frac{8\xi^4+4\xi^2\kappa^2}{\kappa^4}\right)\frac{\gamma_{uc}}{\gamma_{cu}} \tag{C.9.10}$$

$$\begin{aligned}\mathcal{B} = {} & \frac{16g^2\xi^2}{3\kappa^3\gamma_{cu}}\left(24\xi^4\gamma_u + 3\kappa^4(\gamma_{cu}+\gamma_u) + 4\xi^2(4g^2\gamma_{cu} + 3\kappa^2(\gamma_{cu}+\gamma_u))\right)(\kappa+\Gamma)(4g^2+\kappa\Gamma) \\ & + \left(4\xi^2 + \frac{16\xi^4}{3\kappa^2}\right)\Big(16\Delta_e^4\kappa(\gamma_c+\gamma_u) + (4g^2+\kappa\Gamma)(16\xi^2g^2 + \kappa(4g^2(\gamma_d+\gamma_{uc}) + \kappa(\gamma_c+\gamma_u)\Gamma)) \\ & + 4\Delta_e^2(-16\xi^2g^2 + 4g^2(\kappa^2 + (\kappa+\Gamma)(\gamma_c+\gamma_u)) + \kappa(\gamma_u+\gamma_c)(\kappa^2+\Gamma^2))\Big)\end{aligned} \tag{C.9.11}$$

$$\begin{aligned}\mathcal{C} = {} & -16\xi^2g^2(4\Delta_e^2\kappa^2 + (4g^2-\kappa^2)(4g^2+\kappa\Gamma)) \\ & + \kappa((4\Delta_e^2+\kappa^2)(\gamma_c+\gamma_u) + 4g^2(\kappa+\gamma_c+\gamma_u))(4\Delta_e^2\kappa^2 + (4g^2+\kappa\Gamma)^2).\end{aligned} \tag{C.9.12}$$

C.9.2 Coefficients in the expressions for the time-dependent density matrix elements

Here, we give explicit expressions for the coefficients a_i, b_i, $\mathcal{A}_i$, $\mathcal{B}_i$ and $\mathcal{C}_i$ in the time-dependent density matrix elements described in Sec. C.5.3:

$$\mathcal{A}_1 = -\frac{a_2}{a_1 + i\Delta_e}, \qquad \mathcal{C}_1 = \frac{1}{\kappa^2 + 4g^2}\left(4\xi^2\alpha - 4\xi g\left(\mathcal{A}_1 + \mathcal{A}_1^*\right) + 4g^2\mathcal{B}_1\right), \tag{C.9.13}$$

$$\mathcal{A}_2 = -\frac{a_3}{a_1 + i\Delta_e + \tilde{\gamma}}, \qquad \mathcal{C}_2 = \frac{1}{\kappa^2 + 4g^2}\left(4\xi^2\beta - 4\xi g\left(\mathcal{A}_2 + \mathcal{A}_2^*\right) + 4g^2\mathcal{B}_2\right), \tag{C.9.14}$$

$$\mathcal{A}_3 = \left(-\mathcal{A}_1 - \mathcal{A}_2 + \rho_{1,2}(0)\right)e^{i\Delta_e t}, \quad \mathcal{C}_3 = \frac{1}{\kappa^2 + 4g^2}\left(-4\xi g\left(\mathcal{A}_3 + \mathcal{A}_3^*\right) + 4g^2\mathcal{B}_3\right), \tag{C.9.15}$$

$$\mathcal{B}_1 = \frac{2a_1a_2b_2}{b_1\left(a_1^2 + \Delta_e^2\right)} - \frac{b_3}{b_1}, \qquad \mathcal{C}_4 = \frac{4g^2}{\kappa^2 + 4g^2}\mathcal{B}_4, \tag{C.9.16}$$

$$\mathcal{B}_2 = \frac{-\left(a_1^2 + \Delta_e^2\right)b_4 + a_1a_3b_2}{(b_1 + \tilde{\gamma})\left(\Delta_e^2 + (a_1 + \tilde{\gamma})^2\right)} - \frac{\left(b_4(2a_1 + \tilde{\gamma}) - 2a_3b_2\right)(\tilde{\gamma})}{(b_1 + \tilde{\gamma})\left(\Delta_e^2 + (a_1 + \tilde{\gamma})^2\right)}, \qquad \mathcal{B}_4 = -\left(\mathcal{B}_1 + \mathcal{B}_2\right) + \rho_{2,2}(0) - 2\Re\left[\frac{b_2}{a_1 + i\Delta_e - b_1}\mathcal{A}_3 e^{-i\Delta_e t}\right], \tag{C.9.17}$$

$$\mathcal{B}_3 = 2\Re\left[\frac{b_2}{a_1 + i\Delta_e - b_1}\mathcal{A}_3\right], \tag{C.9.18}$$

and

$$b_1 = -\gamma_c - \gamma_u - \frac{4g^2\kappa}{\kappa^2 + 4g^2}, \qquad a_1 = -\frac{\gamma_u + \gamma_c + \gamma_d + \gamma_{uc}}{2} - \frac{2g^2}{\kappa}, \tag{C.9.19}$$

$$b_2 = \frac{2\xi g}{\kappa} - \frac{16g^3\xi}{\kappa\left(\kappa^2 + 4g^2\right)}, \qquad a_2 = \frac{2g\xi}{\kappa}\alpha, \tag{C.9.20}$$

$$b_3 = \frac{16\xi^2 g^2}{\kappa\left(\kappa^2 + 4g^2\right)}\alpha, \qquad a_3 = \frac{2g\xi}{\kappa}\beta, \tag{C.9.21}$$

$$b_4 = \frac{16\xi^2 g^2}{\kappa\left(\kappa^2 + 4g^2\right)}\beta. \tag{C.9.22}$$

C.9.3 Coefficents and matrix elements for the two-SiV model

The constants and matrix elements appearing in Sec. C.8.2 are defined as

$$\alpha_1 = \frac{4\left|g_1\right|^2\left|\Omega_1\right|^2}{\Delta_1^2\kappa^2}, \qquad \alpha_2 = \frac{4\left|g_2\right|^2\left|\Omega_2\right|^2}{\Delta_2^2\kappa^2}, \tag{C.9.23}$$

$$\alpha_3 = \frac{4g_1^* g_2 \Omega_2^* \Omega_1}{\Delta_1\Delta_2\kappa^2}, \qquad \rho_{1,1}^{(s)} \approx \frac{\gamma_{uc}^2}{(\gamma_{uc} + \gamma_{cu})^2} \tag{C.9.24}$$

$$\rho_{2,2}^{(s)} \approx \frac{\gamma_{uc}\gamma_{cu}}{(\gamma_{uc} + \gamma_{cu})^2}, \qquad \rho_{4,4}^{(s)} \approx \frac{\gamma_{cu}^2}{(\gamma_{uc} + \gamma_{cu})^2} \tag{C.9.25}$$

$$\rho_{1,1}(\tau) \approx \beta_1\left(1 - e^{-\tilde{\gamma}\tau}\right), \qquad \rho_{2,2}(\tau) \approx \beta_2 + e^{-\tilde{\gamma}\tau}\beta_3 \tag{C.9.26}$$

$$\rho_{3,3}(\tau) \approx \beta_2 + e^{-\tilde{\gamma}\tau}\beta_4, \qquad \rho_{2,3}(\tau) \approx \alpha_3^*\rho_{1,1}^{(s)}e^{-\Gamma\tau}, \tag{C.9.27}$$

where

$$\tilde{\gamma} = \gamma_{cu} + \gamma_{uc}, \tag{C.9.28}$$

$$\Gamma = \tilde{\gamma} + \gamma_d \tag{C.9.29}$$

$$\beta_1 = (\alpha_1 + \alpha_2)(\rho_{1,1}^{(s)} + \rho_{2,2}^{(s)})\rho_{1,1}^{(s)}, \tag{C.9.30}$$

$$\beta_2 = (\alpha_1 + \alpha_2)(\rho_{1,1}^{(s)} + \rho_{2,2}^{(s)})\rho_{2,2}^{(s)}, \tag{C.9.31}$$

$$\beta_3 = -\alpha_1\rho_{2,2}^{(s)}(\rho_{1,1}^{(s)} + \rho_{2,2}^{(s)}) + \alpha_2\left(\left(\rho_{1,1}^{(s)}\right)^2 - \left(\rho_{2,2}^{(s)}\right)^2 + \rho_{1,1}^{(s)}\left(\rho_{2,2}^{(s)} + \rho_{4,4}^{(s)}\right)\right), \tag{C.9.32}$$

$$\beta_4 = -\alpha_2\rho_{2,2}^{(s)}(\rho_{1,1}^{(s)} + \rho_{2,2}^{(s)}) + \alpha_1\left(\left(\rho_{1,1}^{(s)}\right)^2 - \left(\rho_{2,2}^{(s)}\right)^2 + \rho_{1,1}^{(s)}\left(\rho_{2,2}^{(s)} + \rho_{4,4}^{(s)}\right)\right), \tag{C.9.33}$$

D

Supporting material for Chapter 6

D.1 Setup

D.1.1 Confocal microscopy inside a dilution refrigerator

All experiments are carried out in a dilution refrigerator (DR: BlueFors BF-LD250) with free-space optical access (see Fig. D.1). To perform scanning confocal microscopy, we use a dual-axis scanning galvonometer mirror system (Thorlabs GVS012), two concatenated 4f lens systems ($f_1 = 20\,\text{cm}$, $f_2 = 25\,\text{cm}$) consisting of anti-reflection coated, 40 mm-diameter cemented achromatic doublets (VIS-NIR, Edumund Optics) and a vacuum- and cryo-compatible objective (Attocube LT-APO-VISIR, NA = 0.82) to deliver light to the diamond nanodevice. Light reflected from the sample through the microscope is partially reflected by a 33:67 pellicle beam splitter to a CCD camera for

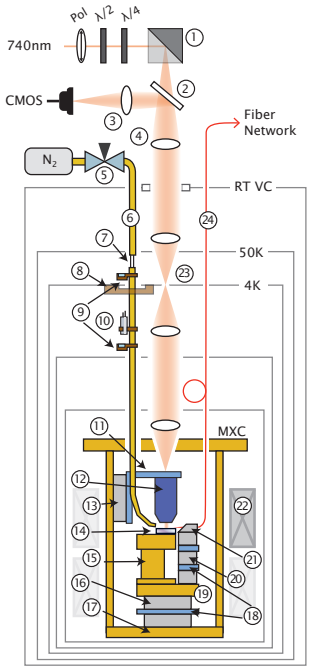

Figure D.1: Schematic of the confocal microscope inside a dilution refrigerator (DR). RT VC: Outer vacuum can; 50K: 50K plate; 4K: 4K plate; MXC: Mixing chamber plate; CMOS: CMOS camera; Pol, $\lambda/2$, $\lambda/4$: Polarizer, half-wave plate, quarter-wave plate; 1: dual-axis scanning galvonometer mirror system (Thorlabs GVS012); 2: 33:67 pellicle beam splitter; 3: achromatic lens (f=10 cm); 4: 40 mm diameter achromatic lens ($f_1 = 20$ cm, $f_2 = 25$ cm); 5: tunable leak valve (VAT Series 211 DN 16 No. 21124-KE0X-000); 6: Copper tube which delivers the N_2 for gas tuning; 7: PTFE thermal break; 8: copper thermal link; 9: temperature sensors (Lake Shore DT-670); 10: resistive cartridge heater (Lake Shore HTR-50); 11: objective L-bracket; 12: vacuum- and cryo-compatible objective (Attocube LT-APO-VISIR, NA = 0.82, focal length = 2.87 mm); 13: Attocube stepper ANPx311 which positions the objective; 14: diamond nanodevice; 15: sample stage; 16: Attocube steppers ANPx311 which position the stage and fiber mount laterally; 17: base plate; 18: aluminum thermalization plates; 19: science plate; 20: Attocube steppers (2× ANPx101, 1× ANPz101) which position the fiber mount; 21: fiber mount; 22: 6-1-1 T superconducting vector magnet with persistent switches (American Magnetics Inc. MAxes); 23: 10 mm aperture at 4 K plate of the DR; 24: single-mode fiber (S630-HP). All parts shown in brown or gold are copper (C101). All parts shown in light blue are aluminum (Al 6061).

imaging.

A 6-1-1 T superconducting vector magnet (American Magnetics Inc.) is mounted below the mixing chamber (MXC) and thermally linked to the 4 K plate of the DR. The magnet is operated in persistent current mode to maximize the stability of the applied field used for Zeeman splitting of the SiV spin states. The diamond nanodevice is soldered with indium to a copper sample stage and placed inside the magnet bore on the base plate. A temperature sensor (Lake Shore Cryotronics, RX-102B-CB) is attached to the sample holder and measures a base temperature of 85 mK.

The objective lens is mounted on a piezo stepper (Attocube ANPx311) via an L-bracket. We use the stepper to move the objective to adjust the focus. The sample stage sits directly beneath the objective, next to an aluminum mount which holds the tapered tip of the optical fiber, through which light exits (and, in some experiments, enters) the DR. The fiber holder is mounted on a stack of 3-axis piezo steppers (2× Attocube ANPx101, 1× Attocube ANPz101). These steppers are used to position the fiber relative to the nanodevice, allowing us to maximize the coupling efficiency to the tapered diamond waveguide. The sample stage and fiber mount stepper stack are both on the copper science plate, which is attached to a separate stack of x- and y-axis piezo steppers (2× Attocube ANPx311) on top of the base plate. These steppers are used for simultaneous coarse positioning of both the sample stage and the fiber mount relative to the microscope objective.

The base plate is connected to the MXC via thick copper beams which provide a

thermal connection as well as a rigid mechanical link, minimizing vibrations mostly propagating from the pulse tube and hence reducing the pointing error of the confocal microscope to approximately ∼1 um in amplitude. The sample stage, objective L-bracket and aluminum thermalization plates (inserted between neighboring base steppers) are also thermally anchored to the MXC via connection to the base plate by oxygen-free copper braids (Copper Braid Products—not shown in Fig. D.1). This ensures rapid thermalization of the entire sample stage setup and inhibits slow mechanical drift of the fiber and objective during the experiment.

D.1.2 Excitation and readout of the diamond nanodevice

A full description of the diamond nanodevice and its fabrication procedure are presented elsewhere [139]. The nanodevice consists of a 1D photonic crystal cavity symmetrically coupled to a waveguide. The waveguide has two ports. The first port is a notch that couples the light entering through the confocal microscope into the waveguide. Light entering through this path is used for resonant excitation of the SiV and cavity modes and comes from narrowband lasers [Newport TLB-6711, M-Squared SolsTiS-2000-PSX-XF and a home-built external-cavity diode laser (Opnext Diode HL7302MG, Littrow configuration)]. In some experiments (see Sec. D.6.1), these lasers are modulated using an electro-optic phase modulator (EOSPACE model PM-0S5-10-PFA-PFA-740-SUL) with microwave sources (MW: Agilent 83732B and Hit-

tite HMC-T2220) to generate additional optical frequencies. The second port is the tapered end of the nanobeam waveguide, which is positioned in contact with the tapered tip of a single mode optical fiber. The coupled fiber is then used to collect light from the cavity mode propagating out of the waveguide. Our techniques for chemically fabricating the tapered fiber and performing the coupling are described in previous works [139, 269]. We also apply pulses from a 520 nm diode laser (Thorlabs LP520-SF15) via the tapered fiber, as shown in Fig. D.2 for charge-state control of the SiV, described in detail in Sec. D.6.1.

D.1.3 Fiber-based photon collection and polarization control

A fiber network is used to efficiently collect light transmitted through the waveguide, as well as measure the fiber-waveguide coupling efficiency and control the polarization of the input and output light.

To couple the tapered fiber to the waveguide, we first send light from a supercontinuum light source (NKT Photonics SuperKExtreme) into the fiber network. As shown in Fig. D.2, the input light is sent into a 90:10 fiber beamsplitter, with 90% of the light sent to a calibration photodiode, and the remaining 10% sent into the diamond waveguide through the tapered fiber contact. The light reflected from the cavity is then split by two other 90:10 beam splitters, which send 1% of the final output light

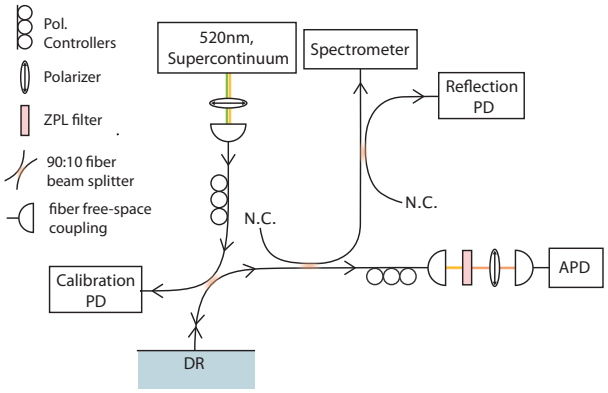

Figure D.2: Schematic of the fiber network used for efficient collection of light from the diamond waveguide. The polarization of the input and output light of the diamond nanocavity inside the DR is tuned via separate sets of polarizers and polarization controllers. The fiber-waveguide coupling efficiency is measured by splitting the light entering and exiting the DR to a calibration photodiode and a reflection photodiode, respectively, and comparing the two signals. The collected light is filtered through a narrowband filter (Semrock FF01-740/13-25) centered around the SiV ZPL wavelength before being detected.

to a reflection photodiode. The efficiency of the coupling between the fiber and the tapered end of the waveguide is calculated by comparing the incoming power and the reflected power, measured from the two photodiodes. For this experiment, the frequency of the light is within the stopband of the photonic crystal cavity, and the polarization of the light is adjusted so that it couples only to the correct mode of the device. Imperfections in either of these areas will cause us to underestimate the coupling efficiency. For the experiments in this paper, we infer a fiber-waveguide coupling efficiency of approximately 50%.

We measure a transmission efficiency of approximately 10% along the fiber collection path, which accounts for losses from beam splitters, four fiber splices with an average efficiency of 80% per splice and the free-space frequency frequency-filtering stage. With the fiber-waveguide coupling efficiency of around 50% described above and an APD efficiency of around 50%, the total detection efficiency of light from the diamond nanocavity is approximately 2.5%.

The waveguide supports two polarization modes: a transverse-electric-like (TE) mode corresponding to the cavity polarization and a transverse-magnetic-like (TM) mode whose transmission is largely unaffected by the presence of the cavity. Control over the polarization of the input and output light of the diamond waveguide allows us to optimize intensity in the relevant (TE) cavity mode by maximizing the contrast of the cavity resonance. The input resonant-excitation light beam consists of light from different narrowband lasers joined via fiber-based beamsplitters, and couples

from free space into the waveguide. We control the polarization of this input field using a polarizer, half wave-plate, and a quarter wave-plate placed in the beam path as shown in Fig. D.1.

Polarization control of the output light transmitted through the diamond waveguide is achieved using the fiber network: First, light propagating out from the diamond waveguide couples to the tapered optical fiber which exits the DR. The light then passes through a polarizer and a set of polarization controllers before being filtered to a frequency range around the ZPL via a bandpass filter (Semrock FF01-740/13-25) in free-space and coupled back into a fiber and collected by a single-photon detector (Excelitas SPCM-NIR). By tuning the polarizer and polarization controllers while monitoring the photon detection rate, we can minimize the detection rate at a frequency far detuned from the cavity resonance, where a non-zero spectrally-flat background signal indicates transmission of the TM mode. As a result, the relative signal from the cavity (TE) mode of interest is maximized.

This is primarily useful for characterizing the spectrum of the diamond nanocavity via reflection. For low-resolution characterization of the diamond nanocavity, light from the broadband supercontinuum laser is sent in from the fiber for non-resonant excitation of the system. A separate polarizer and set of polarization controllers tune the polarization of this input light to selectively address the nanocavity mode. Reflected light from the cavity is coupled back into the tapered fiber and collected through the fiber and sent to a spectrometer (Horiba iHR550 with Synapse CCD and 1800 gr/mm)

with a spectral resolution of 0.025 nm.

D.1.4 Gas tuning

We tune the resonance wavelength of the diamond nanocavity by depositing solid N_2 on the diamond waveguide to change its refractive index. As shown in Fig. D.1, N_2 gas is extracted from a reservoir at atmospheric pressure via a tunable leak valve (VAT Series 211 DN 16 No. 21124-KE0X-000) into a copper tube. A vacuum gauge attached to the top of the tube is used to read out the pressure of the gas inside the tube. The tube extends into the DR and terminates at the sample stage, where N_2 exits and deposits onto the diamond nanocavity. To start the N_2 deposition, the temperature of the tube is increased by applying power of around 10 W to a heater resistor, attached to the tube directly below the 4 K stage, and monitored by several temperature sensors (Lake Shore DT-670SD) placed along the tube. As the temperature of the tube increases, the pressure inside the tube, monitored on the vacuum gauge, initially rises. When the tube reaches a temperature of roughly 80-100 K near the 4 K plate, the pressure reaches a maximum and then starts to decrease. At this time, residual frozen N_2 has unclogged inside the tube and begins to flow out and deposit onto the nanodevice. We then open the leak valve to let more N_2 into the tube while monitoring the cavity spectrum, and close the leak valve once we have observed a satisfactory shift in the cavity resonance wavelength. The leak rate is on the order

of 10^{-2} mbar L/s, corresponding to a cavity resonance tuning rate of approximately 0.01 nm/s. The leak rate can be adjusted in real time to control the tuning rate. The heater is then switched off and the system equilibrates.

Crucially, the copper tube has a weak but non-negligible thermal link to the 4 K plate, while being thermally isolated from the room-temperature environment via a PTFE thermal break below the 50 K plate (see Fig. D.1). The copper tube is also carefully thermally isolated from the components of the experiment that are below 4 K. Therefore, when the heater is off, the tube equilibriates to around 4 K. Since this is well below the N_2 freezing point, N_2 cannot leak out of the tube. Thus, after gas tuning, the cavity resonance wavelength experiences no drift and has been measured to be stable (to within 5 GHz or better) over several weeks.

While deposition of N_2 on the device increases the resonance wavelength, the amount of N_2 can also be reduced to incrementally decrease the resonance wavelength and thus back-tune the cavity resonance. This is done using the supercontinuum laser, which is typically used for low-resolution cavity spectra measurements through the tapered fiber connected to the diamond waveguide as described in Sec. D.1.3. By applying this laser at higher power, we heat up the nanobeam and thus evaporate the deposited N_2. We can therefore tune the resonance wavelength of the cavity in both directions while simultaneously monitoring the cavity spectrum on the spectrometer.

D.2 Model for two SiV centers inside an optical cavity

To theoretically describe the transmission measurements described in Figures 1, 2, and 4 of the main text, we model the steady-state response of the SiV-cavity system in the linear regime using a non-Hermitian effective Hamiltonian. This approach accounts for photon loss through the cavity (decay rate κ) and through spontaneous emission (γ_i for SiV i). Because there is no distinction in this formalism between photon loss and pure dephasing of the optical excited state, the γ_i include all sources of decay and decoherence for these states.[1] Recalling the Tavis-Cummings Hamiltonian for the N-emitter case,

$$H_{\mathrm{TC,N}}/\hbar = \omega_c \hat{a}^\dagger \hat{a} + \sum_i^N \omega_i \hat{\sigma}_i^\dagger \hat{\sigma}_i + \sum_i^N g_i \left(\hat{a}^\dagger \hat{\sigma}_i + \hat{\sigma}_i^\dagger \hat{a} \right) \tag{D.2.1}$$

we write a non-Hermitian two-emitter Tavis-Cummings Hamiltonian [312]:

$$\hat{H}_{\mathrm{TC}} = (\omega_0 + \Delta - \frac{\delta}{2} - i\gamma_1)\hat{\sigma}_1^\dagger \hat{\sigma}_1 + (\omega_0 + \Delta + \frac{\delta}{2} - i\gamma_2)\hat{\sigma}_2^\dagger \hat{\sigma}_2 + (\omega_0 - i\kappa)\hat{a}^\dagger \hat{a} + \left[\hat{a}^\dagger \left(g_1 \hat{\sigma}_1 + g_2 \hat{\sigma}_2 \right) + h.c. \right] \tag{D.2.2}$$

[1] Note that for consistency with the literature, we have taken γ_i to be the *energy* decay rate, which therefore enters with a factor of $\frac{1}{2}$ in the non-Hermitian Hamiltonian (Eqn. D.2.1)for the field amplitudes. However, this means that pure dephasing at a rate γ_d should be included as $\gamma_i \to \gamma_i + 2\gamma_d$.

where ω_0 is the frequency of the cavity, Δ is the detuning between the center-of-mass frequency of the two SiVs $(\omega_1+\omega_2)/2$ and the cavity mode, $\delta = \omega_1 - \omega_2$ is the detuning between the two SiVs and g_j is the single-photon Rabi frequency for SiV $j \in \{1, 2\}$. The operators $\hat{a}$ and $\hat{\sigma}_j$ are the annihilation operators for the cavity and SiV j excitations. The spectrum of this Hamiltonian gives the bright and dark state energies *e.g.* the red and blue lines in Fig. 4D/E.

To calculate the transmission of the system, we use the input-output formalism[313] to solve for the dynamics of the cavity field $\hat{a}$:

$$\dot{\hat{a}}(t) = -i\left[\hat{H}_{\mathrm{TC}}, \hat{a}(t)\right] + \sqrt{\kappa_{\mathrm{a}}}\hat{a}_{in}(t) + \sqrt{\kappa_{\mathrm{b}}}\hat{b}_{in}(t) - \frac{1}{2}(\kappa_{\mathrm{a}} + \kappa_{\mathrm{b}})\hat{a}(t), \tag{D.2.3}$$

Here, we have defined $\hat{a}_{\mathrm{in}}$ and $\hat{b}_{\mathrm{in}}$ as the input fields on either side of the cavity with κ_{a} and κ_{b} as the corresponding cavity energy decay rates and thus the total decay rate $\kappa = \kappa_{\mathrm{a}} + \kappa_{\mathrm{b}}$ We write down the equations of motion in the frequency domain, using

$$\hat{a}(t) = \int d\omega e^{-i\omega t}\hat{a}(\omega) \tag{D.2.4}$$

to arrive at:

$$\begin{aligned} -i\omega\hat{a}(\omega) &= \left(-i\omega_0 - \frac{\kappa_{\mathrm{a}} + \kappa_{\mathrm{b}}}{2}\right)\hat{a} + \sqrt{\kappa_{\mathrm{a}}}\hat{a}_{\mathrm{in}} + \sqrt{\kappa_{\mathrm{b}}}\hat{b}_{\mathrm{in}} - ig_1\sigma_-^{(1)} - ig_2\sigma_-^{(2)} \\ -i\omega\hat{\sigma}_j(\omega) &= \left(-i\left(\omega_0 + \Delta + (-1)^j\frac{\delta}{2}\right) - \frac{\gamma_j}{2}\right)\hat{\sigma}_j - ig_j\hat{a} \end{aligned} \tag{D.2.5}$$

Eliminating the SiV degrees of freedom and solving for the cavity mode gives:

$$\hat{a}(\omega) = \frac{\sqrt{\kappa_{\mathrm{a}}}\hat{a}_{in}(\omega) + \sqrt{\kappa_{\mathrm{b}}}\hat{b}_{in}(\omega)}{D}, \tag{D.2.6}$$

where we have defined

$$D \equiv -i(\omega_0 - \omega) - \frac{\kappa_{\mathrm{a}} + \kappa_{\mathrm{b}}}{2} + \left(\frac{g_1^2}{-i\left(\omega_0 - \omega + \Delta - \frac{\delta}{2}\right) - \frac{\gamma_1}{2}} + \frac{g_2^2}{-i\left(\omega_0 - \omega + \Delta + \frac{\delta}{2}\right) - \frac{\gamma_2}{2}} \right). \tag{D.2.7}$$

In our case of interest, $\langle \hat{b}_{\mathrm{in}} \rangle = 0$, and the transmission coefficient is $t = \langle \hat{b}_{\mathrm{out}} \rangle / \langle \hat{a}_{\mathrm{in}} \rangle$. Using the input-output relations $\hat{a}_{\mathrm{out}} + \hat{a}_{\mathrm{in}} = \sqrt{\kappa_{\mathrm{a}}}\hat{a}$ and $\hat{b}_{\mathrm{out}} + \hat{b}_{\mathrm{in}} = \hat{b}_{\mathrm{out}} = \sqrt{\kappa_{\mathrm{b}}}\hat{a}$, we have

$$t(\omega) = \frac{\sqrt{\kappa_{\mathrm{b}}\kappa_{\mathrm{a}}}}{D}, \tag{D.2.8}$$

and thus the transmission intensity for the cavity field $T(\omega) = |t(\omega)|^2$ is,

$$T(\omega) = \frac{\kappa_{\mathrm{a}}\kappa_{\mathrm{b}}}{|D|^2} \tag{D.2.9}$$

This transmission response is accurate in both the resonant and detuned regime and agrees with numerical solutions of the master equation to better than a few percent. However, to more accurately model the spectra measured in the experiment, we additionally include a background term corresponding to the leakage of coherent laser

light into our detection path, resulting in a measured transmission intensity of

$$T(\omega) = |t(\omega) + Ae^{i\phi}|^2 \tag{D.2.10}$$

where A and ϕ are the amplitude and phase of the of the background field. This coherent background term, which has a flat frequency spectrum corresponding to, for example, transmission of the TM cavity mode, is necessary to account for the lineshapes we observe, which do not agree perfectly with the prediction from Eqn. D.2.9. Addition of an incoherent background term does not appreciatively improve the agreement between the model and experiment. The solid curves in **Figs. 1, 2** and **4** in the main text are all generated via this model.

D.3 Single-SiV measurements

D.3.1 Verification of single emitters

In order to verify that the two emitters used in the measurements described in the main text are indeed single emitters, we separately measure the second-order correlation function $g^{(2)}(\tau)$ of the light transmitted via each of the two SiV-like polaritons in the dispersive regime ($\Delta > \kappa$). Here, τ is the delay time between detection of the second and first photon. We measure under conditions where the two SiVs are far detuned from one another ($\delta \sim 2\pi\times 5\,\mathrm{GHz}$), allowing us to measure one SiV at a time with negligible effects from their interaction. In this regime, each single SiV is

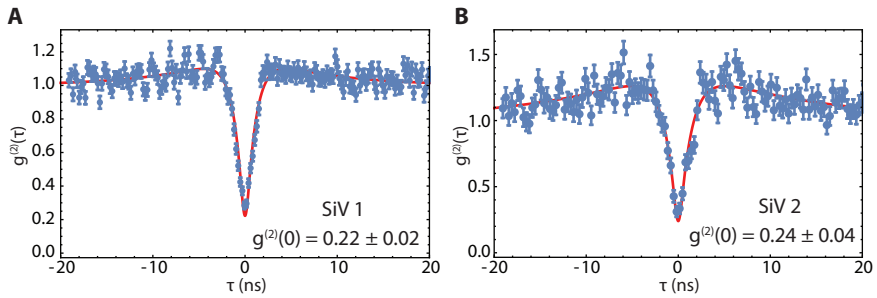

Figure D.3: **Verification of single emitters.** $g^{(2)}(\tau)$ for SiV 1 **(A)** and SiV 2 **(B)** in the main text. Error bars are given by shot noise, and red solid lines are a double-exponential fit convolved with a Gaussian of 350 ps width to account for finite APD timing resolution. From the fits, we extract timescales for antibunching and bunching $\{\tau_{a1}, \tau_{a2}, \tau_{b1}, \tau_{b2}\} = \{1.0, 1.3, 7.7, 13.4\}$ ns.

only slightly dressed by the cavity mode, and acts as a transmission channel for single photons far detuned from cavity resonance. Therefore, in the ideal case, we expect $g^{(2)}(\tau = 0) \approx 0$ in transmission for single SiV-like polaritons. As explained below, a background field or limited cooperativity can increase the measured value of $g^{(2)}(0)$, but a value of $g^{(2)}(0) < 0.5$ confirms that the measured field corresponds to a single-photon emitter.

We employ an active preselection sequence described in detail in Sec. D.6.1 in order to ensure initialization of each SiV in the correct charge and frequency state. These measurements are done at zero magnetic field when the spin sublevels are degenerate and only a single laser is needed to continuously scatter photons from a single SiV. The transmitted light is split on a beamsplitter and sent to two APDs. Photon detection times are logged using fast acquisition hardware (PicoQuant HydraHarp 400). We construct a histogram as a function of τ and normalize it to the background signal at long time delays.

We measure $g^{(2)}(0) = 0.22 \pm 0.02$ and $g^{(2)}(0) = 0.24 \pm 0.04$ in transmission on resonance with SiV 1 and SiV 2 respectively (Fig. D.3), with SiV-cavity detunings of $\Delta = 2\pi\times$ 156 GHz at a sample temperature of 5 K. No background subtraction or postselection is used. We measure bunching on a timescale significantly longer than the excited state lifetime for both SiVs, likely due to optical pumping into the metastable higher-energy orbital branch of the ground state [214, 269]. The finite value of $g^{(2)}(0)$ primarily arises from the coherent laser background, which is minimized relative to the single-photon transmission when the SiV is excited in the linear regime (low laser power). In this regime and at large SiV-cavity detuning Δ, the contrast between single-photon transmission and the coherent laser background (which has $g^{(2)}(0) = 1$) scales with the cooperativity. Thus, the $g^{(2)}(0)$ value measured for each SiV is fundamentally limited by the SiV-cavity cooperativity.

D.3.2 Extraction of cavity QED parameters

In this section, we describe the measurements used to extract the cavity QED parameters (g, κ, γ). We extract $\kappa = 2\pi\times$ 48 GHz, the cavity decay rate, by fitting the cavity spectrum to a Lorentzian when it is detuned from the SiV resonance by more than 5 cavity linewidths (Fig. D.4A). The measured cavity linewidth κ can change after the gas-tuning process, where the cavity loss rate can increase due to scattering or absorption introduced by the deposited material. This effect is not perfectly reproducible and may depend on the details of the gas deposition process. As a result, κ can vary by tens of perecent between different experiments. In order to account for this, we measure the full cavity spectrum before each experiment and use the corresponding

measured cavity linewidth as κ in the model for that particular experiment.

We extract $\gamma_1 = 2\pi\times 0.19\,\mathrm{GHz}$, the bare (not cavity-enhanced) linewidth of the SiV, by fitting a Lorentzian to the transmission spectrum near the resonance of SiV 1 when the cavity is detuned by $\Delta = 6.8\kappa$ (Fig. D.4C). In this measurement, extra care was taken to reduce the laser linewidth and power in order to prevent broadening of the measured SiV linewidth from either power broadening or spectral diffusion. Although the linewidth of SiV 2 was not measured carefully in this regime, we measured similar linewidths for the two SiVs (*cf.* Fig. 2A or Fig. 4B) at a variety of detunings, suggesting that $\gamma_1 \approx \gamma_2$. We extract $g_1 \sim g_2 = 2\pi\times 7.3\,\mathrm{GHz}$, the single-photon Rabi frequencies for SiV 1 and SiV 2, by fitting Eqn. D.2.10 to the measurement in the bottom panel of Fig. 1C of the main text with the other CQED parameters fixed.

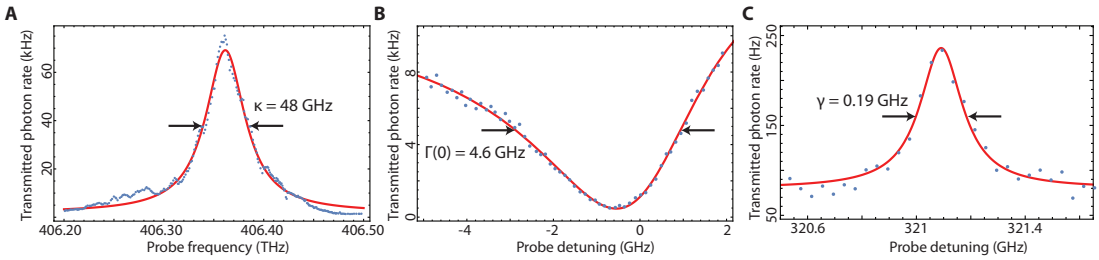

Figure D.4: **Measurement of cavity and emitter linewidths (A)** Typical measurement of cavity transmission spectrum far detuned from the emitter resonance, used to extract κ. **(B)** Lorentzian with coherent background (see Sec. D.2) fit to on-resonance cavity transmission near SiV 1. The data (blue points) are the same as in the lower panel of Fig. 1C of the main text. **(C)** Linewidth measurement of SiV 1 when the cavity is $\sim 6.8\kappa$ detuned from the SiV resonance.

D.3.3 Additional factors influencing cavity transmission spectrum

As discussed in Sec. D.2, the transmission of a system consisting of a single, ideal, two-level emitter coupled to a cavity is determined solely by the cooperativity C. In the linear regime at $\Delta = 0$ the transmission through the cavity is given by $T \approx (1+C)^{-2}$ [249]. For the cooperativity $C = 23$ inferred here, the expected on-resonance transmission is $T = 0.002$, corresponding to a single-SiV cavity extinction of $\Delta T/T = 99.8\%$. This is more than the roughly 95% extinction demonstrated in Fig. 1C of the main text. This discrepancy is primarily due to imperfect polarization of the laser field. For our device (*cf.* Sec. D.1.3), the TM polarization has high transmission, resulting in the addition of a coherent background that limits the transmission contrast $\Delta T/T$. This background is accounted for in Eq. D.2.10, which fits the data in Fig. 1C well. Additional factors that could contribute to the background include improper charge-state initialization (blinking) and slow-timescale (non-Markovian) broadening of the line beyond $\gamma = 2\pi\times\ 0.19\,\mathrm{GHz}$ due to spectral diffusion [269, 248]. This measurement was done at low laser power (see Sec. D.4.1-D.4.2) to minimize these effects.

In the dispersive regime ($\Delta \gg \kappa$), the contrast of the peak increases with the cooperativity. However, the same mechanisms described above also result in a reduction of contrast in this regime. We find that the model including the coherent background term (Eqn. D.2.10) accurately predicts the measured spectra in this regime as well. For example, the solid line shown in Fig. 1D of the main text is a fit to Eqn. D.2.10 with the background amplitude and phase as the only free parameters (for the exact

cavity QED parameters and atom cavity detuning in this fit, see Sec. D.4.4). The background amplitude determined from this fit is 12% of the amplitude of the correctly polarized SiV-cavity signal.

We also note that since both the input and output fields are each independently filtered through a polarizer, the transmission contrast in the dispersive regime can be artificially enhanced through cross-polarization effects. While our model does not account for the two polarization modes independently, as would be necessary to completely describe the transmission signal due to this effect, our single-mode model fits the measured transmission spectra well with reasonable extracted background amplitudes.

D.4 Two-SiV transmission measurements in zero magnetic field

D.4.1 Charge-state control of nanocavity-integrated SiVs

Continuous resonant excitation results in selective ionization (blinking) of each SiV [269, 248]. The ionization timescale varies among emitters, but at low laser powers this timescale is much longer than the time needed to measure the transmission spectrum corresponding to an SiV. This timescale can be reduced by increasing the resonant laser power, allowing us to selectively ionize a particular SiV by applying high laser power on resonance with that SiV. We can therefore ionize one of a pair of nearly-resonant SiVs into its optically-inactive charge state and, in this way, measure

the spectrum corresponding to transmission from a single SiV even when there are multiple SiVs present (gray data in Fig. 2A). SiVs can then be reinitialized with high fidelity ($\sim 80\%$) into the optically active charge state by applying a 520 nm laser pulse for roughly 10 μs. With both SiVs initialized in the correct charge state, we measure the two-SiV spectrum (black data in Fig. 2A). Because the charge state is stable over timescales longer than a single run of the experiment, we can also post-select for runs in the experiment where the two SiVs are in the desired charge state.

D.4.2 Spectral hopping of nanocavity-integrated SiVs

The SiV optical transition frequency can also drift as a function of time (spectral diffusion), possibly resulting from higher-order Stark effects [248]. While these dynamics vary from emitter to emitter, for the SiVs studied here, we find that spectral diffusion occurs primarily in discrete spectral jumps on a timescale that increases with reduced resonant (and off-resonant repump) laser powers. For all measurements of the two-SiV system at zero magnetic field (Fig. 2), we work at laser intensities where the spectral diffusion timescale is much slower than the measurement timescale. In other words, we can obtain several high signal-to-noise transmission spectra before a spectral jump occurs. For example, the data in the case of two interacting SiVs (black curves in Fig. 2A,B) were each acquired over roughly 1 minute, in which time there was no measurable spectral hopping.

We also note that SiVs can undergo significant spectral jumps when the sample is warmed up to room temperature and then cooled down again (thermally cycled). This means that after thermal cycling the setup, the same SiVs can have resonance

frequencies that differ on the order of $\sim 5\,\mathrm{GHz}$. This is a much larger frequency scale than the typical slow, laser-induced spectral hopping described above ($\sim 1\,\mathrm{GHz}$). As an example, the experiments in Fig. 2 and Fig. 4 of the main text were performed with the same pair of SiVs (also labelled as SiV 1 and 2 in Fig. 1C of the main text). The average SiV-SiV detuning in Fig. 2 is $\delta \sim 1\,\mathrm{GHz}$, whereas the average SiV-SiV detuning (at zero magnetic field) in Fig. 4 is $\delta \sim 5\,\mathrm{GHz}$ due to this type of spectral jump. Understanding and limiting sources of spectral diffusion is an important task for future work. However, the frequency scales of all spectral hopping processes are still smaller than or comparable to that of the magnetic field tuning mechanism demonstrated here ($\sim 5\,\mathrm{GHz}$) and the Raman tuning process previously demonstrated [269] ($\sim 20\,\mathrm{GHz}$).

D.4.3 Bright and dark state linewidth measurement

The spectral hopping of SiVs provides an opportunity to measure the interacting two-SiV spectra as a function of splitting between the bright and dark states by simply integrating for a long time period and binning spectra into individual sets in which no spectral hop has occured. For the measurement presented in the inset of Fig. 2B, we do this over the course of roughly 12 hours and fit each binned spectrum to a double Lorentzian model (see Fig. D.5B for some example spectra at different bright-dark splittings). To produce the plot shown in the inset of Fig. 2B, we bin each set of spectra based on the frequency difference between peaks obtained from the fit and plot the average width of the left (red) and right (blue) peaks in each bin. The error bars are the standard deviation within each bin. The gray dashed line and shaded region

represent the mean and standard deviation of the single-SiV (that is, where the other SiV is ionized) linewidths obtained from single Lorentzian fits.

D.4.4 Cavity QED parameters for the two-SiV measurements in zero magnetic field

We determine the atom-cavity detuning Δ relative to the center-of-mass frequency of the two SiVs using a Lorentzian fit to the spectrum shown in Fig. D.5A ($\Delta = 2\pi\times -79\,\mathrm{GHz}$) for the measurements in Fig. 2A and the inset of Fig. 2B. Using the same technique after tuning the cavity to the opposite side of the SiV resonance (for measurement in main panel of Fig. 2B), we estimate an SiV-cavity detuning of $\Delta = 2\pi\times 55\,\mathrm{GHz}$. The cavity spectrum during these experiments ($\kappa = 2\pi\times 30\,\mathrm{GHz}$) was measured to be slightly narrower than in the measurements presented in Fig. 1 (see Sec. D.3.2).

Based on these cavity spectra and the measurements described in Sec. D.3, the following cavity QED parameters for the coupled SiV-cavity system are kept fixed: $\{g_1, g_2, \kappa, \gamma_1, \gamma_2\} = 2\pi \times \{7.3, 7.3, 30, 0.19, 0.19\}$ GHz yielding $C = 37$ for these SiVs. As explained above, we set $\Delta = 2\pi\times -79\,\mathrm{GHz}$ for Fig. 2A and the inset of Fig. 2B and $\Delta = 2\pi\times 55\,\mathrm{GHz}$ for the main panel of Fig. 2B. The solid gray curves in Fig. 2A are single-SiV spectra obtained from Eqn. D.2.10 by setting either g_1 or g_2 to zero. From these fits we extract the SiV-SiV detuning $\delta = 2\pi\times 0.56\,\mathrm{GHz}$.

With Δ and δ fixed, we fit the two-SiV spectrum shown in black in Fig. 2A to Eqn. D.2.10 with only the background terms as free parameters to obtain the solid

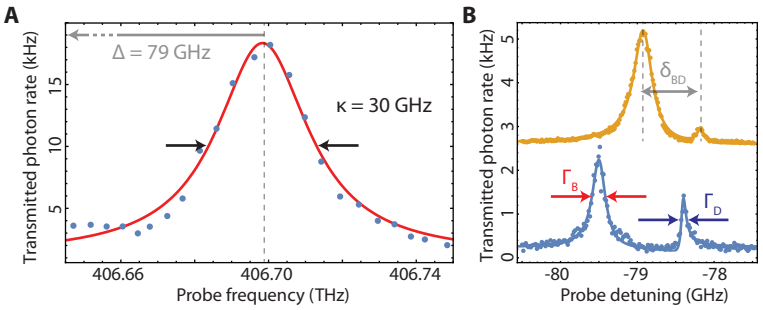

Figure D.5: **Two-SiV measurement in zero magnetic field (A)** Measurement of cavity linewidth (κ) and detuning from SiV (Δ) for the measurements presented in (Fig. 1D, 2) of the main text. The solid red line is a Lorentzian fit. **(B)** Example 2-SiV transmission spectra at different bright-dark state detunings (δ_{SD}). The solid lines are a bi-Lorentzian fit with coherent background, and are used to extract δ_{SD} and the superradiant (bright) and subradiant (dark) state linewidths, Γ_S and Γ_D, plotted in the inset of (Fig. 3B) in the main text.

black curve, which agrees well with the data. The close agreement between theory and experiment also validates our independently measured g_i and γ_i. Since individual ionized control spectra similar to the gray data in Fig. 2A were not taken for the data shown in the main panel of Fig. 3B, δ was left as a free parameter for the fit shown in black in Fig. 2B, and was determined to be $\delta = 2\pi\times\, 2\,\mathrm{GHz}$, which is different from the measured value of δ at the other cavity detuning due to the spectral diffusion process described in Sec. D.4.2.

The solid lines in the inset of Fig. 2B are calculated using Eqn. D.2.2 with the above SiV-cavity parameters at the SiV-cavity detuning $\Delta = 2\pi\times\, -79\,\mathrm{GHz}$, but at various δ. We first calculate the energy difference between the superradiant (bright) and subradiant (dark) states as a function of SiV-SiV detuning (using the real part of the eigenvalues of $\hat{H}_{\mathrm{TC}}$). We then calculate the $|S\rangle$ and $|D\rangle$ state linewidths (the

imaginary eigenvalues of $\hat{H}_{\mathrm{TC}}$ arising from non-hermitian terms in Eqn. D.2.5) as a function of SiV-SiV detuning. This allows us to plot the theoretical bright and dark state linewidths as a function of bright and dark state energy difference, which is the parameter determined from the fitting procedure described in Sec. D.4.3 above. The solid curves in the inset of Fig. 2 are predictions from the independently-measured cavity QED parameters (*cf.* Sec. D.3.2) with no free parameters. This is because in the linear regime, the bright and dark state linewidths do not depend on the signal amplitude, laser power or background, which are the only free parameters in most of the other fits.

D.5 Fidelity calculation for single-shot readout

We read out the SiV spin state in the dispersive regime using spin-dependent transmission (Fig. 3 main text). The full experimental pulse sequence is shown in Fig. D.6. The main sequence consists of a pulse at frequency $\omega_{\downarrow}$ which initializes the spin in $|\uparrow\rangle$ via optical pumping and a readout pulse at $\omega_{\uparrow}$. We build a histogram of photons in the first δt seconds, when the state is assumed to be $|\uparrow\rangle$, as well as in the last δt

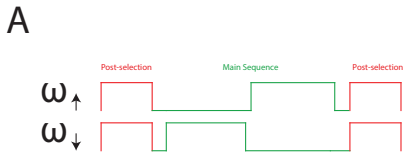

Figure D.6: **Measurement of cavity and emitter linewidths (A)** Pulse sequence used to measure single shot readout

seconds after the system has been pumped into $|\downarrow\rangle$. These histograms represent the distribution of photon numbers we expect to observe in a single run of the experiment. Since these histograms are well separated, we can define a threshold photon number n such that if in a time bin δt we detect more (fewer) than n photons, the state is $|\uparrow\rangle$ ($|\downarrow\rangle$). We numerically optimize our choice for δt and n to maximize the single-shot readout fidelity:

$$\mathcal{F} = \mathrm{Max}_{n,\delta t}\{(1 - \sum_{m=n}^{\infty} P_{\downarrow}(m, \delta t)) + (1 - \sum_{1}^{m=n} P_{\uparrow}(m, \delta t))\}/2. \tag{D.5.1}$$

To account for SiV blinking and spectral diffusion (sec. D.4), we implement pre-sequence and post-sequence pulses. Applying two laser fields at $\omega_{\uparrow}$ and $\omega_{\downarrow}$, continuously cycles the spin. If the SiV is in the correct charge state and at the correct frequency, transmission will be higher than if the SiV is in the wrong charge state or if the SiV has drifted to a different frequency. We use this pulse both at the start of the experiment, to ensure we start in the correct state, and at the end to ensure the readout itself did not ionize the SiV.

The optimal fidelity occurs at $\delta t = 7\,\mathrm{ms}$ and $n = 34$ as stated in the main text. Without post-selection, the $|\uparrow\rangle$ histogram is bimodal, limiting the readout fidelity to 89%. With post-selection, the lower lobe of the histogram is removed, and the reported fidelity $\mathcal{F} = 96.8\%$ is achieved. Of note, the fidelity presented here is not strictly readout fidelity, but the combined initialization and readout fidelity. Thus, the fidelity is predominately limited by the non-zero overlap of the spin-cycling transitions used in the experiment, which can result in off-resonant pumping limiting the initialization of the spin into $|\uparrow\rangle$. Based on the measured splitting, we expect a maxi-

mum fidelity of 97.4%.

D.6 Two-SiV transmission measurements in nonzero magnetic fields

D.6.1 SiV frequency stabilization based on active preselection

SiV optical transitions are narrow and stable for timescales long enough to enable the measurements described in Fig. 1-3 of the main text. In order to achieve stable optical transitions over longer timescales, we use an active preselection sequence for the measurements described in Fig. 4 of the main text. This preselection technique effectively fixes the optical transition frequencies of the emitters to desired frequencies at the expense of a slight reduction in duty cycle.

In order to cycle photons continuously from both SiVs in a magnetic field, we apply two tones simultaneously at frequencies $\omega_{\uparrow/\downarrow,i}$ for SiV i (four total tones) as described in the previous section. Each SiV is addressed by a separate resonant laser, with each laser modulated by an EOM to produce a sideband at the appropriate frequency. For example, lasers at $\omega_{\uparrow,1}$ and $\omega_{\downarrow,2}$ have corresponding sidebands $\omega_{\downarrow,1}$ and $\omega_{\uparrow,2}$. Each SiV is separately addressed for 1 ms and the number of transmitted photons is recorded using a field-programmable gate array (Lattice Diamond MachXO2).

We set a photon number threshold based on observed photon count rates for these

SiVs under conditions similar to those used in the experiment. If the threshold photon number is exceeded for both SiVs, we proceed with the experiment (typical duration: $\sim 50\,\mathrm{ms}$). If not, we apply a relatively strong ($\sim 1\,\mu\mathrm{W}$) 520 nm laser pulse for $100\,\mu\mathrm{s}$ to induce spectral hopping of the SiV optical frequencies. Using this technique, we are able to measure with duty cycle $\sim 50\%$ and measure linewidths ($\sim 0.5\,\mathrm{GHz}$) that are significantly narrower than the long-timescale integrated linewidth of the SiV centers without any preselection ($\sim 2\,\mathrm{GHz}$). The gray data in Fig. 4B are an example of narrow lines measured using this preselection sequence.

D.6.2 Zeeman splitting calibration

We determine the frequencies of all spin-selective transitions $\omega_{\uparrow/\downarrow,i}$ as a function of magnetic field at a sample temperature of 5 K. A complete description of the magnetic-field dependence of the SiV optical transitions can be found elsewhere[214]. At temperatures above 500 mK where the relevant phonon modes are populated, working in a magnetic field misaligned with respect to the SiV symmetry axis yields a relatively short spin population relaxation rate $T_1 \sim 100\,\mathrm{ns}$ in contrast to the $50\,\mu\mathrm{s}$ for a similarly misaligned field at 85 mK (Fig. 3B) [252]. As a result, optical pumping from a single laser at $\omega_{\uparrow/\downarrow}$ is minimal, allowing us to scatter photons at a sufficient rate to easily observe all spin transitions $\omega_{\uparrow/\downarrow,i}$ in transmission spectrum with a single laser (in other words, with no repumping laser). We measure the transmission spectra around SiVs 1 and 2 at various magnetic fields from 0 kG to 8 kG. For an example calibration transmission spectrum at 5 K (taken in a different device), see Fig. D.7A.

D.6.3 Spin-dependent measurement of the two-SiV transmission spectra

For the measurements presented in Fig. 4, at each magnetic field value we first probe the response of SiV 1 alone by applying Ω_1 continuously (to ensure initialization in $|\uparrow_1\rangle$ via optical pumping) and scanning Ω_p across the resonance. Although Ω_1 is applied continuously at $\omega_{\downarrow,1}$, we only scatter photons continuously when Ω_p is on resonance with $\omega_{\uparrow,1}$. Otherwise, Ω_1 probes a population that is predominantly in $|\uparrow_1\rangle$ which scatters relatively few photons in the steady state. We then repeat the same measurement for SiV 2, applying Ω_2 and scanning Ω_p. One example dataset is shown in gray in Fig. 4B. The individual transmission spectra are then normalized to the laser background to compensate for slight differences in laser power and summed (incoherently) at each field to produce the data shown in Fig. 4C. At each field, we fit a Lorentzian to the single-spin spectra to determine the center frequency of the spin-selective transitions. The solid gray lines in Fig. 4C are linear fits to the extracted center frequencies as a function of magnetic field.

To study the two-spin interacting system, we apply Ω_1 and Ω_2 continuously to ensure spin initialization in $|\uparrow_1\rangle|\downarrow_2\rangle$ and measure the transmission spectrum of Ω_p. Again, we normalize the data at each field to the background, which is primarily set by the stronger pump lasers Ω_1 and Ω_2. An example spectrum at a single magnetic field is shown in black in Fig. 4B, and the full avoided crossing (transmission spectra as a function of magnetic field) is shown in Fig. 4D. In all measurements (single spin and two-spin), we adjust our laser intensities such that Ω_1 and Ω_2 are roughly 3 times

larger than Ω_p, so that each SiV spin is polarized in the desired spin state (spin polarization $P \sim |\Omega_{1,2}/\Omega_p|^2 \sim 90\%$).

D.6.4 Cavity QED parameters for the two-SiV measurements in a non-zero magnetic field

Despite our use of the preselection sequence described in Sec. D.6.1, SiV optical transitions are broadened non-radiatively beyond the linewidth $2\pi\times$ 0.19 GHz measured on short timescales without preselection. Although this broadening has both Markovian and non-Markovian sources, to good approximation it can simply be included as an increased decoherence rate contributing to γ. Note that this approximation leads us to underestimate the SiV-cavity cooperativity.

We determine the SiV-polariton linewidth (and by extension, γ) under preselection using the single-spin transmission spectra plotted in Fig. 4C. By fitting Lorentzians to the individual spectra at each magnetic field (*cf.* gray data in Fig. 4B), we determine the mean single-SiV linewidths to be $\{\Gamma_1(\Delta), \Gamma_2(\Delta)\} = 2\pi \times \{0.77 \pm 0.14, 0.58 \pm 0.12\}$ GHz. We measure a cavity linewidth $\kappa = 2\pi\times$ 39 GHz and SiV-cavity detuning $\Delta = 2\pi\times$ 109 GHz during this measurement (not shown; see (Fig. D.5A) for an example measurement) and fix $g_1 = g_2 = 2\pi\times$ 7.3 GHz as determined before. From the observed Purcell enhancement, we can extract the bare SiV linewidth γ

$$\gamma_i = \Gamma_i(\Delta) - \frac{4g^2}{\kappa}\frac{1}{1+4\Delta^2/\kappa^2}, \tag{D.6.1}$$

yielding $\{\gamma_1, \gamma_2\} = 2\pi \times \{0.6, 0.42\}$ GHz over long timescales under preselection. We use the complete cavity QED parameters $\{g_1, g_2, \kappa, \gamma_1, \gamma_2\} = 2\pi \times \{7.3, 7.3, 39, 0.6, 0.42\}$ GHz to calculate the eigenvalues of $\hat{H}_{TC}$ (Eqn. D.2.1) at various 2-SiV detunings δ (extracted from Fig. 4C) which are the bright and dark state energies (solid red and blue curves in Fig. 4D, E). We note that these are computed using no free parameters.

In order to compare the measured data to a theoretical prediction for the full avoided-crossing transmission spectrum shown in Fig. 4E, we also need to include in our model effects arising from imperfect polarization P into the desired spin state ($P \sim 0.9$, see Sec. D.6.2) and laser background (see Sec. D.2). We calculate the transmission spectrum with imperfect polarization $T_P(\omega)$ by computing a weighted average of transmission spectra:

$$T_P(\omega) = P^2 T(\omega) + P(1-P)T_1(\omega) + (1-P)PT_2(\omega) + (1-P)^2 T_0(\omega), \qquad \text{(D.6.2)}$$

where $T(\omega)$, $T_1(\omega)$, $T_2(\omega)$ and $T_0(\omega)$ are all given by Eqn. D.2.10 with $\{g_1, g_2\}$ set to $2\pi \times \{7.3, 7.3\}$, $\{7.3, 0\}$, $\{0, 7.3\}$ and $\{0, 0\}$ GHz respectively. At each field we fit Eqn. D.6.2 to the two-spin transmission data with only the background amplitude and phase as free parameters (for an example fit, see solid black curve in Fig. 4B). We determine an average background amplitude and phase over all magnetic fields (data in Fig. 4D) and use these average values in our model. We then use Eqn. D.6.2 at various δ (which are determined at each magnetic field based on the linear fits shown in Fig. 4C) with the above cavity QED parameters, $P = 0.9$ and estimated background

parameters to produce the theoretical avoided-crossing transmission spectrum shown in Fig. 4E.

D.6.5 Measurement of collective-state formation in an independent device

We also measure the formation of superradiant and subradiant states with a pair of SiVs located in a different device on the same diamond chip. A transmission spectrum at 5 K near both SiV and cavity resonance is shown in Fig. D.7A. From this measurement, we extract Purcell enhanced linewidths of $\{\Gamma_1(0), \Gamma_2(0)\} = 2\pi \times \{1.78, 2.43\}$ GHz. To measure the cavity mediated interaction between these SiVs, we work at an atom-cavity detuning of $\Delta = 2\pi \times 70$ GHz. To demonstrate that we can bring spin-selective transitions from each SiV into resonance, we first measure the transmission spectrum of all transitions at a temperature of 5 K (Fig. D.7C) as the magnetic field is ramped from 0 kG to 6.7 kG. In this measurement, the spins are unpolarized, which allows us to see all spin-preserving transitions without a second pumping field. However, this random polarization causes us to average over the different combination of spin states (*e.g.* $P \sim 0.5$ in Eqn. D.6.2), limiting the visibility of the cavity-mediated interaction.

As evident from the data Fig. D.7C, there is no significant spectral diffusion for this pair of SiVs, and we therefore choose not to implement the preselection sequence described in Sec. D.6.1. Instead, to ensure proper initialization of both SiVs into the correct charge state, we simply apply a $\sim 1\,\mu$W green pulse every ~ 5 ms[269]. At a

temperature of 85 mK, the spins can be polarized by applying pump lasers Ω_1 and Ω_2. By polarizing the spins individually, we measure the single SiV linewidths over long timescales under this periodic green illumination (similar to gray data in Fig. 4B): $\{\Gamma_1(\Delta), \Gamma_2(\Delta)\} = 2\pi \times \{0.65, 1.01\}$ GHz (Fig. D.7B). Using the SiV linewidth data in Fig. D.7A and Fig. D.7B, the measured cavity linewidth (not shown), and Eqn. D.6.1, we can extract the full cavity QED parameters: $\{g_1, g_1, \kappa, \gamma_1, \gamma_2\} = 2\pi \times \{5.7, 6.4, 85, 0.23, 0.49\}$ GHz.

Fig. D.7D shows the spectrum of the two interacting spins at 85 mK (with both pump fields Ω_1 and Ω_2 applied), taken as a function of the magnitude of an external magnetic field oriented roughly 70° from the SiV symmetry axis. Although the avoided crossing is not as well resolved as in Fig. 4D of the main text due to the lower cooperativity (7 and 4) of these SiVs, the formation of superradiant and subradiant states near the two-SiV resonance is evident from the enhanced intensity and broader linewidth of the superradiant state that remains on the positive-frequency side of the density plot in Fig. D.7D. The theoretical spectrum (Fig. D.7E) is calculated as in Sec. D.6.4.

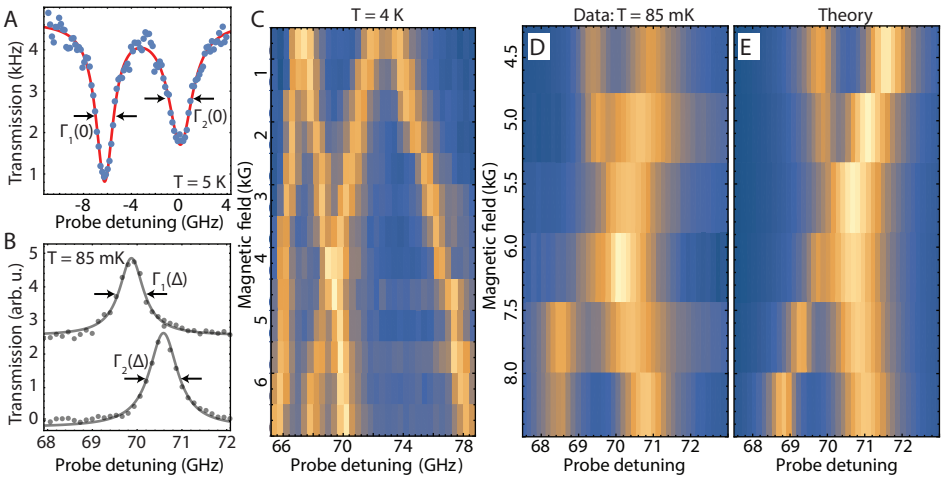

Figure D.7: **SiV-SiV interaction measurement in a different device (A)** Transmission spectrum near cavity resonance ($\Delta \sim 0\,\text{GHz}$). The red line shows a Bi-Lorentzian fit used to extract the Purcell-enhanced linewidths $\Gamma_1(0)$ and $\Gamma_2(0)$. **(B)** Single SiV linewidth measurements at 85 mK in a magnetic field oriented roughly 70 (similar to the gray data in Fig. 4B). The lower data is taken at $B = 6.6\,\text{kG}$ and is used to extract $\Gamma_1(\Delta)$ and the upper data (shifted vertically for clarity) is taken at $B = 8.3\,\text{kG}$ and is used to extract $\Gamma_2(\Delta)$. **(C)** Zeeman calibration transmission spectrum taken as from 0 kG to 6.7 kG roughly orthogonal to the SiV symmetry axis. **(D)** Spin dependent SiV-SiV interaction at $T = 85\,\text{mK}$ with both SiVs initialized into spin states that couple to the probe field. **(E)** Theoretical SiV-SiV interaction spectrum for the cavity parameters given in the text, assuming spin polarization of 90% (see Sec. D.6.4).

Bibliography

[1] D. A. Neamen and B. Pevzner. *Semiconductor physics and devices: basic principles*. Vol. 3. McGraw-Hill New York, 2003 (cited on pp. 1, 43).

[2] L. Pauling. *The Nature of the Chemical Bond*. Vol. 260. Cornell University Press, Ithaca, NY, 1960 (cited on p. 1).

[3] A. D. Ludlow, M. M. Boyd, J. Ye, E. Peik, and P. O. Schmidt. "Optical atomic clocks". *Reviews of Modern Physics* 87.2 (2015), p. 637 (cited on p. 2).

[4] B. Bloom, T. Nicholson, J. Williams, S. Campbell, M. Bishof, X. Zhang, W. Zhang, S. Bromley, and J. Ye. "An optical lattice clock with accuracy and stability at the 10- 18 level". *Nature* 506.7486 (2014), p. 71 (cited on p. 2).

[5] I. Lovchinsky, A. Sushkov, E. Urbach, N. de Leon, S. Choi, K. De Greve, R. Evans, R. Gertner, E. Bersin, C. Müller, et al. "Nuclear magnetic resonance detection and spectroscopy of single proteins using quantum logic". *Science* 351.6275 (2016), pp. 836–841 (cited on pp. 2, 6, 41, 46).

[6] C. L. Degen, F. Reinhard, and P. Cappellaro. "Quantum sensing". *Rev. Mod. Phys.* 89 (3 2017), p. 035002 (cited on p. 2).

[7] N. Gisin, G. Ribordy, W. Tittel, and H. Zbinden. "Quantum cryptography". *Rev. Mod. Phys.* 74 (1 2002), pp. 145–195 (cited on pp. 2, 3).

[8] M. A. Nielsen and I. L. Chuang. *Quantum computation and quantum information*. Cambridge university press, 2010 (cited on p. 2).

[9] P. W. Shor. "Polynomial-time algorithms for prime factorization and discrete logarithms on a quantum computer". *SIAM review* 41.2 (1999), pp. 303–332 (cited on p. 2).

[10] S. Lloyd. “Universal quantum simulators”. *Science* (1996), pp. 1073–1078 (cited on p. 2).

[11] A. Aspuru-Guzik, A. D. Dutoi, P. J. Love, and M. Head-Gordon. “Simulated quantum computation of molecular energies”. *Science* 309.5741 (2005), pp. 1704–1707 (cited on p. 2).

[12] J. Preskill. “Quantum computing and the entanglement frontier”. *arXiv preprint arXiv:1203.5813* (2012) (cited on p. 2).

[13] S. Boixo, S. V. Isakov, V. N. Smelyanskiy, R. Babbush, N. Ding, Z. Jiang, J. M. Martinis, and H. Neven. “Characterizing quantum supremacy in near-term devices”. *arXiv preprint arXiv:1608.00263* (2016) (cited on p. 2).

[14] T. Monz, P. Schindler, J. T. Barreiro, M. Chwalla, D. Nigg, W. a. Coish, M. Harlander, W. Hänsel, M. Hennrich, and R. Blatt. “14-Qubit Entanglement: Creation and Coherence”. *Phys. Rev. Lett.* 106.13 (2011), p. 130506 (cited on p. 2).

[15] R. Barends, J. Kelly, A. Megrant, A. Veitia, D. Sank, E. Jeffrey, T. C. White, J. Mutus, A. G. Fowler, B. Campbell, et al. “Superconducting quantum circuits at the surface code threshold for fault tolerance”. *Nature* 508.7497 (2014), pp. 500–503 (cited on pp. 2, 131).

[16] M. Devoret and R. Schoelkopf. “Superconducting circuits for quantum information: an outlook”. *Science* 339.6124 (2013), pp. 1169–1174 (cited on pp. 2, 131).

[17] C. Monroe and J. Kim. “Scaling the ion trap quantum processor”. *Science* 339.6124 (2013), pp. 1164–1169 (cited on p. 2).

[18] J. Zhang, G. Pagano, P. W. Hess, A. Kyprianidis, P. Becker, H. Kaplan, A. V. Gorshkov, Z.-X. Gong, and C. Monroe. “Observation of a many-body dynamical phase transition with a 53-qubit quantum simulator”. *Nature* 551.7682 (2017), p. 601 (cited on p. 2).

[19] N. M. Linke, D. Maslov, M. Roetteler, S. Debnath, C. Figgatt, K. A. Landsman, K. Wright, and C. Monroe. “Experimental comparison of two

quantum computing architectures". *Proceedings of the National Academy of Sciences* (2017), p. 201618020 (cited on p. 2).

[20] M. Greiner, O. Mandel, T. Esslinger, T. W. Hänsch, and I. Bloch. "Quantum phase transition from a superfluid to a Mott insulator in a gas of ultracold atoms". *Nature* 415.6867 (2002), p. 39 (cited on p. 3).

[21] I. Bloch, J. Dalibard, and W. Zwerger. "Many-body physics with ultracold gases". *Reviews of modern physics* 80.3 (2008), p. 885 (cited on p. 3).

[22] J. Simon, W. S. Bakr, R. Ma, M. E. Tai, P. M. Preiss, and M. Greiner. "Quantum simulation of antiferromagnetic spin chains in an optical lattice". *Nature* 472.7343 (2011), p. 307 (cited on p. 3).

[23] H. Bernien, S. Schwartz, A. Keesling, H. Levine, A. Omran, H. Pichler, S. Choi, A. S. Zibrov, M. Endres, M. Greiner, et al. "Probing many-body dynamics on a 51-atom quantum simulator". *Nature* 551.7682 (2017), p. 579 (cited on p. 3).

[24] M. Aidelsburger, M. Atala, M. Lohse, J. T. Barreiro, B. Paredes, and I. Bloch. "Realization of the Hofstadter Hamiltonian with ultracold atoms in optical lattices". *Physical review letters* 111.18 (2013), p. 185301 (cited on p. 3).

[25] J. Struck, C. Ölschläger, R. Le Targat, P. Soltan-Panahi, A. Eckardt, M. Lewenstein, P. Windpassinger, and K. Sengstock. "Quantum simulation of frustrated classical magnetism in triangular optical lattices". *Science* 333.6045 (2011), pp. 996–999 (cited on p. 3).

[26] D. S. Weiss and M. Saffman. "Quantum computing with neutral atoms". *Physics Today* 70.7 (2017), p. 44 (cited on p. 3).

[27] M. Saffman, T. G. Walker, and K. Mølmer. "Quantum information with Rydberg atoms". *Reviews of Modern Physics* 82.3 (2010), p. 2313 (cited on p. 3).

[28] C. R. Monroe, R. J. Schoelkopf, and M. D. Lukin. "Quantum connections". *Sci. Amer.* 314.5 (2016), pp. 50–57 (cited on p. 3).

[29] C. Monroe, R. Raussendorf, A. Ruthven, K. Brown, P. Maunz, L.-M. Duan, and J. Kim. "Large-scale modular quantum-computer architecture with atomic memory and photonic interconnects". *Phys. Rev. A* 89.2 (2014), p. 022317 (cited on pp. 3, 4, 131, 142, 144, 147).

[30] A. Broadbent, J. Fitzsimons, and E. Kashefi. "Universal blind quantum computation". In: *Foundations of Computer Science, 2009. FOCS'09. 50th Annual IEEE Symposium on*. IEEE. 2009, pp. 517–526 (cited on p. 3).

[31] S. Barz, E. Kashefi, A. Broadbent, J. F. Fitzsimons, A. Zeilinger, and P. Walther. "Demonstration of blind quantum computing". *Science* 335.6066 (2012), pp. 303–308 (cited on p. 3).

[32] J. I. Cirac, P. Zoller, H. J. Kimble, and H. Mabuchi. "Quantum state transfer and entanglement distribution among distant nodes in a quantum network". *Physical Review Letters* 78.16 (1997), p. 3221 (cited on pp. 3, 142, 147).

[33] H. J. Kimble. "The quantum internet". *Nature* 453.7198 (2008), pp. 1023–1030 (cited on pp. 3, 112, 124, 130).

[34] D. E. Chang, V. Vuletić, and M. D. Lukin. "Quantum nonlinear optics—photon by photon". *Nature Photonics* 8.9 (2014), p. 685 (cited on pp. 4, 112, 117).

[35] H. Briegel, W. Dür, J. I. Cirac, and P. Zoller. "Quantum Repeaters : The Role of Imperfect Local Operations in Quantum Communication". *Phys. Rev. Lett.* 81.26 (1998), pp. 5932–5935 (cited on p. 4).

[36] J. Borregaard, P. Kómár, E. M. Kessler, M. D. Lukin, and A. S. Sørensen. "Long-distance entanglement distribution using individual atoms in optical cavities". *Phys. Rev. A* 92 (1 2015), p. 012307 (cited on pp. 4, 13, 25, 131, 142, 144, 147).

[37] S. Muralidharan, L. Li, J. Kim, N. Lütkenhaus, M. D. Lukin, and L. Jiang. "Optimal architectures for long distance quantum communication". *Scientific reports* 6 (2016), p. 20463 (cited on pp. 4, 144).

[38] L. Childress, J. M. Taylor, A. S. Sørensen, and M. D. Lukin. "Fault-tolerant quantum repeaters with minimal physical resources and implementations based on single-photon emitters". *Phys. Rev. A* 72.5 (2005), p. 052330 (cited on pp. 4, 13, 25).

[39] R. W. Andrews, R. W. Peterson, T. P. Purdy, K. Cicak, R. W. Simmonds, C. A. Regal, and K. W. Lehnert. "Bidirectional and efficient conversion between microwave and optical light". *Nat. Phys.* 10.4 (2014), pp. 321–326 (cited on p. 5).

[40] J. D. Thompson, T. G. Tiecke, N. P. de Leon, J. Feist, A. V. Akimov, M. Gullans, A. S. Zibrov, V. Vuletic, and M. D. Lukin. "Coupling a Single Trapped Atom to a Nanoscale Optical Cavity." *Science* 1202 (2013) (cited on p. 5).

[41] S. Ritter, C. Nölleke, C. Hahn, A. Reiserer, A. Neuzner, M. Uphoff, M. Mücke, E. Figueroa, J. Bochmann, and G. Rempe. "An elementary quantum network of single atoms in optical cavities". *Nature* 484.7393 (2012), pp. 195–200 (cited on p. 5).

[42] A. Reiserer, N. Kalb, G. Rempe, and S. Ritter. "A quantum gate between a flying optical photon and a single trapped atom". *Nature* 508.7495 (2014), pp. 237–240 (cited on pp. 5, 13, 112, 130).

[43] P. Michler, A. Kiraz, C. Becher, W. Schoenfeld, P. Petroff, L. Zhang, E. Hu, and A. Imamoglu. "A quantum dot single-photon turnstile device". *Science* 290.5500 (2000), pp. 2282–2285 (cited on p. 5).

[44] P. Lodahl, S. Mahmoodian, and S. Stobbe. "Interfacing single photons and single quantum dots with photonic nanostructures". *Rev. Mod. Phys.* 87.2 (2015), p. 347 (cited on pp. 5, 33, 97, 112, 131, 135).

[45] A. I. Lvovsky, B. C. Sanders, and W. Tittel. "Optical quantum memory". *Nat. Photon.* 3.12 (2009), pp. 706–714 (cited on p. 5).

[46] T. Zhong, J. M. Kindem, E. Miyazono, and A. Faraon. "Nanophotonic coherent light–matter interfaces based on rare-earth-doped crystals". *Nature communications* 6 (2015), p. 8206 (cited on p. 5).

[47] W. E. Moerner and L. Kador. “Optical detection and spectroscopy of single molecules in a solid”. *Physical review letters* 62.21 (1989), p. 2535 (cited on p. 5).

[48] M. Orrit and J. Bernard. “Single pentacene molecules detected by fluorescence excitation in ap-terphenyl crystal”. *Phys. Rev. Lett.* 65.21 (1990), pp. 2716–2719 (cited on p. 5).

[49] W. P. Ambrose and W. E. Moerner. “Fluorescence spectroscopy and spectral diffusion of single impurity molecules in a crystal”. *Nature* 349.6306 (1991), pp. 225–227 (cited on pp. 5, 15).

[50] A. M. Zaitsev. *Optical properties of diamond: a data handbook*. Springer Science & Business Media, 2001 (cited on pp. 5, 19, 102, 148).

[51] D. Press, K. D. Greve, P. L. McMahon, T. D. Ladd, B. Friess, C. Schneider, M. Kamp, S. Höfling, A. Forchel, and Y. Yamamoto. “Ultrafast optical spin echo in a single quantum dot”. *Nat. Photon.* 4.6 (2010), pp. 367–370 (cited on p. 5).

[52] A. Bechtold, D. Rauch, F. Li, T. Simmet, P.-L. Ardelt, A. Regler, K. Müller, N. A. Sinitsyn, and J. J. Finley. “Three-stage decoherence dynamics of an electron spin qubit in an optically active quantum dot”. *Nat. Phys.* 11.12 (2015), pp. 1005–1008 (cited on p. 5).

[53] R. Stockill, C. L. Gall, C. Matthiesen, L. Huthmacher, E. Clarke, M. Hugues, and M. Atatüre. “Quantum dot spin coherence governed by a strained nuclear environment”. *Nat. Commun.* 7 (2016), p. 12745 (cited on p. 5).

[54] G. Balasubramanian, P. Neumann, D. Twitchen, M. Markham, R. Kolesov, N. Mizuochi, J. Isoya, J. Achard, J. Beck, J. Tissler, et al. “Ultralong spin coherence time in isotopically engineered diamond”. *Nature materials* 8.5 (2009), p. 383 (cited on pp. 6, 12).

[55] P. C. Maurer, G. Kucsko, C. Latta, L. Jiang, N. Y. Yao, S. D. Bennett, F. Pastawski, D. Hunger, N. Chisholm, M. Markham, et al. “Room-temperature quantum bit memory exceeding one second”. *Science* 336.6086 (2012), pp. 1283–1286 (cited on pp. 6, 128).

[56] S. Castelletto, B. Johnson, V. Ivády, N. Stavrias, T. Umeda, A. Gali, and T. Ohshima. "A silicon carbide room-temperature single-photon source". *Nature materials* 13.2 (2014), p. 151 (cited on p. 6).

[57] W. F. Koehl, B. B. Buckley, F. J. Heremans, G. Calusine, and D. D. Awschalom. "Room temperature coherent control of defect spin qubits in silicon carbide". *Nature* 479.7371 (2011), p. 84 (cited on p. 6).

[58] J. Maze, P. Stanwix, J. Hodges, S. Hong, J. Taylor, P. Cappellaro, L. Jiang, M. G. Dutt, E. Togan, A. Zibrov, et al. "Nanoscale magnetic sensing with an individual electronic spin in diamond". *Nature* 455.7213 (2008), p. 644 (cited on p. 6).

[59] G. Kucsko, P. Maurer, N. Y. Yao, M. Kubo, H. Noh, P. Lo, H. Park, and M. D. Lukin. "Nanometre-scale thermometry in a living cell". *Nature* 500.7460 (2013), p. 54 (cited on p. 6).

[60] F. Dolde, H. Fedder, M. W. Doherty, T. Nöbauer, F. Rempp, G. Balasubramanian, T. Wolf, F. Reinhard, L. C. Hollenberg, F. Jelezko, et al. "Electric-field sensing using single diamond spins". *Nature Physics* 7.6 (2011), p. 459 (cited on p. 6).

[61] E. Togan, Y. Chu, A. S. Trifonov, L. Jiang, J. Maze, L. Childress, M. V. G. Dutt, A. S. Sørensen, P. R. Hemmer, A. S. Zibrov, and M. D. Lukin. "Quantum entanglement between an optical photon and a solid-state spin qubit". *Nature (London)* 466.7307 (2010), pp. 730–734 (cited on pp. 6, 13, 25).

[62] S. D. Barrett and P. Kok. "Efficient high-fidelity quantum computation using matter qubits and linear optics". *Physical Review A* 71.6 (2005), p. 060310 (cited on pp. 6, 13, 25).

[63] H. Bernien, B. Hensen, W. Pfaff, G. Koolstra, M. S. Blok, L. Robledo, T. H. Taminiau, M. Markham, D. J. Twitchen, L. Childress, and R. Hanson. "Heralded entanglement between solid-state qubits separated by three metres". *Nature* 497.7447 (2013), pp. 86–90 (cited on pp. 6, 13, 25, 97).

[64] B. Hensen, H. Bernien, A. Dréau, A. Reiserer, N. Kalb, M. Blok, J. Ruitenberg, R. Vermeulen, R. Schouten, C. Abellán, et al. "Loophole-free Bell inequality violation using electron spins separated by 1.3 kilometres". *Nature* 526.7575 (2015), pp. 682–686 (cited on pp. 6, 13, 25, 97, 124).

[65] F. Dolde, I. Jakobi, B. Naydenov, N. Zhao, S. Pezzagna, C. Trautmann, J. Meijer, P. Neumann, F. Jelezko, and J. Wrachtrup. "Room-temperature entanglement between single defect spins in diamond". *Nature Physics* 9.3 (2013), p. 139 (cited on pp. 7, 146).

[66] M. W. Doherty, N. B. Manson, P. Delaney, F. Jelezko, J. Wrachtrup, and L. C. Hollenberg. "The nitrogen-vacancy colour centre in diamond". *Physics Reports* 528.1 (2013), pp. 1–45 (cited on pp. 7, 12, 14, 15, 21, 32).

[67] C. Hepp. "Electronic structure of the silicon vacancy color center in diamond". PhD thesis. Saarland University, 2014 (cited on p. 7).

[68] S. Meesala, Y.-I. Sohn, B. Pingault, L. Shao, H. A. Atikian, J. Holzgrafe, M. Gundogan, C. Stavrakas, A. Sipahigil, C. Chia, M. J. Burek, M. Zhang, L. Wu, J. L. Pacheco, J. Abraham, E. Bielejec, M. D. Lukin, M. Atature, and M. Loncar. "Strain engineering of the silicon-vacancy center in diamond". *ArXiv e-prints* (2018) (cited on pp. 7, 149).

[69] T. Tiecke, J. D. Thompson, N. P. de Leon, L. Liu, V. Vuletić, and M. D. Lukin. "Nanophotonic quantum phase switch with a single atom". *Nature* 508.7495 (2014), pp. 241–244 (cited on pp. 13, 112, 123).

[70] D. Englund, A. Faraon, I. Fushman, N. Stoltz, P. Petroff, and J. Vučković. "Controlling cavity reflectivity with a single quantum dot". *Nature* 450.7171 (2007), pp. 857–861 (cited on pp. 13, 33, 112).

[71] A. Faraon, C. Santori, Z. Huang, V. M. Acosta, and R. G. Beausoleil. "Coupling of Nitrogen-Vacancy Centers to Photonic Crystal Cavities in Monocrystalline Diamond". *Phys. Rev. Lett.* 109 (3 2012), p. 033604 (cited on pp. 13, 17, 97, 108, 113, 172).

[72] D. Englund, B. Shields, K. Rivoire, F. Hatami, J. Vuckovic, H. Park, and M. D. Lukin. "Deterministic coupling of a single nitrogen vacancy cen-

ter to a photonic crystal cavity". *Nano Lett.* 1 (2010), pp. 1–10 (cited on p. 13).

[73] B. J. M. Hausmann, B. J. Shields, Q. Quan, Y. Chu, N. P. de Leon, R. Evans, M. J. Burek, A. S. Zibrov, M. Markham, D. J. Twitchen, H. Park, M. D. Lukin, and M. Loncar. "Coupling of NV Centers to Photonic Crystal Nanobeams in Diamond". *Nano Letters* 13.12 (2013), pp. 5791–5796 (cited on pp. 13, 34, 35, 37, 107).

[74] R. Albrecht, A. Bommer, C. Deutsch, J. Reichel, and C. Becher. "Coupling of a single nitrogen-vacancy center in diamond to a fiber-based microcavity". *Phys. Rev. Lett.* 110.24 (2013), p. 243602 (cited on pp. 13, 33).

[75] S. Bogdanovic. "Diamond-based Fabry-Perot microcavities for quantum networks". PhD thesis. Delft University of Technology, 2017 (cited on pp. 13, 33).

[76] E. Janitz, M. Ruf, M. Dimock, A. Bourassa, J. Sankey, and L. Childress. "Fabry-Perot microcavity for diamond-based photonics". *Physical Review A* 92.4 (2015), p. 043844 (cited on pp. 13, 33).

[77] D. Riedel, I. Söllner, B. J. Shields, S. Starosielec, P. Appel, E. Neu, P. Maletinsky, and R. J. Warburton. "Deterministic enhancement of coherent photon generation from a nitrogen-vacancy center in ultrapure diamond". *Physical Review X* 7.3 (2017), p. 031040 (cited on pp. 13, 33).

[78] H. Kaupp, T. Hümmer, M. Mader, B. Schlederer, J. Benedikter, P. Haeusser, H.-C. Chang, H. Fedder, T. W. Hänsch, and D. Hunger. "Purcell-enhanced single-photon emission from nitrogen-vacancy centers coupled to a tunable microcavity". *Physical Review Applied* 6.5 (2016), p. 054010 (cited on pp. 13, 33).

[79] E. Waks and J. Vuckovic. "Dipole induced transparency in drop-filter cavity-waveguide systems". *Physical review letters* 96.15 (2006), p. 153601 (cited on pp. 13, 26, 134, 140, 142).

[80] L.-M. Duan and H. J. Kimble. “Scalable photonic quantum computation through cavity-assisted interactions”. *Phys. Rev. Lett.* 92.12 (2004), p. 127902 (cited on pp. 13, 25).

[81] M. J. Kastoryano, F. Reiter, and A. S. Sørensen. “Dissipative Preparation of Entanglement in Optical Cavities”. *Phys. Rev. Lett.* 106 (9 2011), p. 090502 (cited on pp. 13, 25, 131, 142, 144, 147).

[82] A. Jarmola, V. Acosta, K. Jensen, S. Chemerisov, and D. Budker. “Temperature- and magnetic-field-dependent longitudinal spin relaxation in nitrogen-vacancy ensembles in diamond”. *Physical review letters* 108.19 (2012), p. 197601 (cited on p. 15).

[83] M. Kim, H. Mamin, M. Sherwood, K. Ohno, D. Awschalom, and D. Rugar. “Decoherence of near-surface nitrogen-vacancy centers due to electric field noise”. *Physical review letters* 115.8 (2015), p. 087602 (cited on p. 15).

[84] B. A. Myers, M. C. Dartiailh, K. Ohno, A. Das, D. D. Awschalom, and A. C. B. Jayich. “Probing surface noise with depth-calibrated spins in diamond”. *arXiv preprint arXiv:1402.5392* (2014) (cited on p. 15).

[85] Y. Romach, C. Müller, T. Unden, L. J. Rogers, T. Isoda, K. M. Itoh, M. Markham, A. Stacey, J. Meijer, S. Pezzagna, B. Naydenov, L. P. McGuinness, N. Bar-Gill, and F. Jelezko. “Spectroscopy of Surface-Induced Noise Using Shallow Spins in Diamond”. *Phys. Rev. Lett.* 114 (1 2015), p. 017601 (cited on p. 15).

[86] P. Tamarat, T. Gaebel, J. Rabeau, M. Khan, A. Greentree, H. Wilson, L. Hollenberg, S. Prawer, P. Hemmer, F. Jelezko, et al. “Stark shift control of single optical centers in diamond”. *Physical review letters* 97.8 (2006), p. 083002 (cited on p. 15).

[87] H. D. Robinson and B. B. Goldberg. “Light-induced spectral diffusion in single self-assembled quantum dots”. *Phys. Rev. B* 61 (8 2000), R5086–R5089 (cited on p. 15).

[88] H. Bernien, L. Childress, L. Robledo, M. Markham, D. Twitchen, and R. Hanson. “Two-Photon Quantum Interference from Separate Nitrogen

Vacancy Centers in Diamond". *Phys. Rev. Lett.* 108 (4 2012), p. 043604 (cited on pp. 15, 23).

[89] V. M. Acosta, C. Santori, A. Faraon, Z. Huang, K.-M. C. Fu, A. Stacey, D. A. Simpson, K. Ganesan, S. Tomljenovic-Hanic, A. D. Greentree, S. Prawer, and R. G. Beausoleil. "Dynamic Stabilization of the Optical Resonances of Single Nitrogen-Vacancy Centers in Diamond". *Phys. Rev. Lett.* 108 (20 2012), p. 206401 (cited on pp. 15, 23).

[90] P. Tamarat, T. Gaebel, J. R. Rabeau, M. Khan, A. D. Greentree, H. Wilson, L. C. L. Hollenberg, S. Prawer, P. Hemmer, F. Jelezko, and J. Wrachtrup. "Stark Shift Control of Single Optical Centers in Diamond". *Phys. Rev. Lett.* 97 (8 2006), p. 083002 (cited on pp. 15, 16, 97).

[91] Y. Shen, T. M. Sweeney, and H. Wang. "Zero-phonon linewidth of single nitrogen vacancy centers in diamond nanocrystals". *Phys. Rev. B* 77 (3 2008), p. 033201 (cited on p. 16).

[92] P. Siyushev, H. Pinto, M. Vörös, A. Gali, F. Jelezko, and J. Wrachtrup. "Optically Controlled Switching of the Charge State of a Single Nitrogen-Vacancy Center in Diamond at Cryogenic Temperatures". *Phys. Rev. Lett.* 110 (16 2013), p. 167402 (cited on pp. 16, 17, 25, 45, 97).

[93] N. Aslam, G. Waldherr, P. Neumann, F. Jelezko, and J. Wrachtrup. "Photo-induced ionization dynamics of the nitrogen vacancy defect in diamond investigated by single-shot charge state detection". *New Journal of Physics* 15.1 (2013), p. 013064 (cited on p. 16).

[94] L. C. Bassett, F. J. Heremans, C. G. Yale, B. B. Buckley, and D. D. Awschalom. "Electrical Tuning of Single Nitrogen-Vacancy Center Optical Transitions Enhanced by Photoinduced Fields". *Phys. Rev. Lett.* 107 (26 2011), p. 266403 (cited on p. 16).

[95] A. Stacey, D. A. Simpson, T. J. Karle, B. C. Gibson, V. M. Acosta, Z. Huang, K. M. C. Fu, C. Santori, R. G. Beausoleil, L. P. McGuinness, K. Ganesan, S. Tomljenovic-Hanic, A. D. Greentree, and S. Prawer. "Near-Surface Spectrally Stable Nitrogen Vacancy Centres Engineered in Sin-

gle Crystal Diamond". *Advanced Materials* 24.25 (2012), pp. 3333–3338 (cited on pp. 16, 23).

[96] J. Meijer, B. Burchard, M. Domhan, C. Wittmann, T. Gaebel, I. Popa, F. Jelezko, and J. Wrachtrup. "Generation of single color centers by focused nitrogen implantation". *Applied Physics Letters* 87.26 (2005), p. 261909 (cited on pp. 17, 34).

[97] M. J. Burek, N. P. de Leon, B. J. Shields, B. J. Hausmann, Y. Chu, Q. Quan, A. S. Zibrov, H. Park, M. D. Lukin, and M. Lončar. "Free-standing mechanical and photonic nanostructures in single-crystal diamond". *Nano Lett.* 12.12 (2012), pp. 6084–6089 (cited on pp. 18, 34, 36, 101, 107, 111, 183).

[98] J. F. Ziegler. *PARTICLE INTERACTIONS WITH MATTER*. http://www.srim.org. 2013 (cited on p. 18).

[99] D. M. Toyli, C. D. Weis, G. D. Fuchs, T. Schenkel, and D. D. Awschalom. "Chip-scale nanofabrication of single spins and spin arrays in diamond". *Nano letters* 10.8 (2010), pp. 3168–3172 (cited on p. 18).

[100] T. Iwasaki, F. Ishibashi, Y. Miyamoto, Y. Doi, S. Kobayashi, T. Miyazaki, K. Tahara, K. D. Jahnke, L. J. Rogers, B. Naydenov, et al. "Germanium-Vacancy Single Color Centers in Diamond". *Sci. Rep.* 5 (2015), p. 12882 (cited on pp. 19, 144, 148).

[101] M. K. Bhaskar, D. D. Sukachev, A. Sipahigil, R. E. Evans, M. J. Burek, C. T. Nguyen, L. J. Rogers, P. Siyushev, M. H. Metsch, H. Park, F. Jelezko, M. Lon čar, and M. D. Lukin. "Quantum Nonlinear Optics with a Germanium-Vacancy Color Center in a Nanoscale Diamond Waveguide". *Phys. Rev. Lett.* 118 (22 2017), p. 223603 (cited on pp. 19, 144, 148).

[102] P. Siyushev, M. H. Metsch, A. Ijaz, J. M. Binder, M. K. Bhaskar, D. D. Sukachev, A. Sipahigil, R. E. Evans, C. T. Nguyen, M. D. Lukin, P. R. Hemmer, Y. N. Palyanov, I. N. Kupriyanov, Y. M. Borzdov, L. J. Rogers, and F. Jelezko. "Optical and microwave control of germanium-vacancy

center spins in diamond". *Phys. Rev. B* 96 (8 2017), p. 081201 (cited on p. 19).

[103] T. Iwasaki, Y. Miyamoto, T. Taniguchi, P. Siyushev, M. H. Metsch, F. Jelezko, and M. Hatano. "Tin-Vacancy Quantum Emitters in Diamond". *Phys. Rev. Lett.* 119 (25 2017), p. 253601 (cited on pp. 19, 144, 148).

[104] D. Twitchen, D. Hunt, C. Wade, M. Newton, J. Baker, T. Anthony, and W. Banholzer. "The production and annealing stages of the self-interstitial (R2) defect in diamond". *Physica B: Condensed Matter* 273 - 274.0 (1999), pp. 644–646 (cited on p. 19).

[105] G. Davies, S. C. Lawson, A. T. Collins, A. Mainwood, and S. J. Sharp. "Vacancy-related centers in diamond". *Phys. Rev. B* 46.20 (1992), p. 13157 (cited on pp. 19, 102).

[106] P. Deák, B. Aradi, M. Kaviani, T. Frauenheim, and A. Gali. "Formation of NV centers in diamond: A theoretical study based on calculated transitions and migration of nitrogen and vacancy related defects". *Phys. Rev. B* 89.7 (2014), p. 075203 (cited on pp. 19, 20, 44, 102).

[107] V. Acosta, E. Bauch, M. Ledbetter, C. Santori, K.-M. Fu, P. Barclay, R. Beausoleil, H. Linget, J. Roch, F. Treussart, et al. "Diamonds with a high density of nitrogen-vacancy centers for magnetometry applications". *Phys. Rev. B* 80.11 (2009), p. 115202 (cited on pp. 19, 20, 102, 106).

[108] T. Yamamoto, C. Müller, L. P. McGuinness, T. Teraji, B. Naydenov, S. Onoda, T. Ohshima, J. Wrachtrup, F. Jelezko, and J. Isoya. "Strongly coupled diamond spin qubits by molecular nitrogen implantation". *Phys. Rev. B* 88.20 (2013), p. 201201 (cited on pp. 19, 106).

[109] M. A. Lea-wilsonf [*sic*], J. N. Lomer, and J. A. Van Wyk. "Electron spin resonance of the R4/W6 defect in irradiated diamond". *Philosophical Magazine Part B* 72.1 (1995), pp. 81–89 (cited on p. 19).

[110] D. J. Twitchen, M. E. Newton, J. M. Baker, T. R. Anthony, and W. F. Banholzer. "Electron-paramagnetic-resonance measurements on the divacancy defect center $R4/W6$ in diamond". *Phys. Rev. B* 59 (20 1999), pp. 12900–12910 (cited on p. 19).

[111] D. F. Talbot-Ponsonby, M. E. Newton, J. M. Baker, G. A. Scarsbrook, R. S. Sussmann, and A. J. Whitehead. "EPR and optical studies on polycrystalline diamond films grown by chemical vapor deposition and annealed between 1100 and 1900 K". *Phys. Rev. B* 57 (4 1998), pp. 2302–2309 (cited on p. 19).

[112] B. Naydenov, F. Reinhard, A. Laemmle, V. Richter, R. Kalish, U. F. S. D'Haenens-Johansson, M. Newton, F. Jelezko, and J. Wrachtrup. "Increasing the coherence time of single electron spins in diamond by high temperature annealing". *Applied Physics Letters* 97.24 (2010), p. 242511 (cited on p. 20).

[113] H. Pinto, R. Jones, D. Palmer, J. P. Goss, P. R. Briddon, and S. Öberg. "On the diffusion of NV defects in diamond". *physica status solidi (a)* 209.9 (2012), pp. 1765–1768 (cited on p. 20).

[114] M. Hauf, B. Grotz, B. Naydenov, M. Dankerl, S. Pezzagna, J. Meijer, F. Jelezko, J. Wrachtrup, M. Stutzmann, F. Reinhard, et al. "Chemical control of the charge state of nitrogen-vacancy centers in diamond". *Phys. Rev. B* 83.8 (2011), p. 081304 (cited on p. 20).

[115] K.-M. C. Fu, C. Santori, P. E. Barclay, and R. G. Beausoleil. "Conversion of neutral nitrogen-vacancy centers to negatively charged nitrogen-vacancy centers through selective oxidation". *Applied Physics Letters* 96.12, 121907 (2010), p. 121907 (cited on p. 20).

[116] M. Kim, H. Mamin, M. Sherwood, C. Rettner, J. Frommer, and D. Rugar. "Effect of oxygen plasma and thermal oxidation on shallow nitrogen-vacancy centers in diamond". *Appl. Phys. Lett.* 105.4 (2014), p. 042406 (cited on p. 20).

[117] S. Pezzagna, B. Naydenov, F. Jelezko, J. Wrachtrup, and J. Meijer. "Creation efficiency of nitrogen-vacancy centres in diamond". *New J. Phys.* 12.6 (2010), p. 065017 (cited on pp. 22, 102).

[118] S. Haroche and J.-M. Raimond. *Exploring the quantum: atoms, cavities, and photons (oxford graduate texts)*. Oxford University Press, USA, 2013 (cited on p. 26).

[119] D. F. Walls and G. J. Milburn. *Quantum optics*. Springer Science & Business Media, 2007 (cited on p. 26).

[120] H. Tanji-Suzuki, I. D. Leroux, M. H. Schleier-Smith, M. Cetina, A. T. Grier, J. Simon, and V. Vuletic. "Interaction between atomic ensembles and optical resonators: classical description". *arXiv preprint arXiv:1104.3594* (2011) (cited on p. 26).

[121] H. Carmichael. *An open systems approach to quantum optics: lectures presented at the Université Libre de Bruxelles, October 28 to November 4, 1991*. Vol. 18. Springer Science & Business Media, 2009 (cited on p. 28).

[122] E. T. Jaynes and F. W. Cummings. "Comparison of quantum and semiclassical radiation theories with application to the beam maser". *Proceedings of the IEEE* 51.1 (1963), pp. 89–109 (cited on p. 28).

[123] E. M. Purcell. "Spontaneous emission probabilities at radio frequencies". *Phys. Rev.* 69 (1946), p. 681 (cited on p. 30).

[124] C. Sauvan, J.-P. Hugonin, I. Maksymov, and P. Lalanne. "Theory of the spontaneous optical emission of nanosize photonic and plasmon resonators". *Physical Review Letters* 110.23 (2013), p. 237401 (cited on p. 31).

[125] V. R. Almeida, Q. Xu, C. A. Barrios, and M. Lipson. "Guiding and confining light in void nanostructure". *Optics letters* 29.11 (2004), pp. 1209–1211 (cited on p. 31).

[126] H. Choi, M. Heuck, and D. Englund. "Self-similar nanocavity design with ultrasmall mode volume for single-photon nonlinearities". *Physical review letters* 118.22 (2017), p. 223605 (cited on p. 31).

[127] W. L. Barnes, A. Dereux, and T. W. Ebbesen. "Surface plasmon subwavelength optics". *nature* 424.6950 (2003), p. 824 (cited on p. 31).

[128] R. F. Oulton, V. J. Sorger, D. Genov, D. Pile, and X. Zhang. "A hybrid plasmonic waveguide for subwavelength confinement and long-range propagation". *nature photonics* 2.8 (2008), p. 496 (cited on p. 31).

[129] A. Blanco, E. Chomski, S. Grabtchak, M. Ibisate, S. John, S. W. Leonard, C. Lopez, F. Meseguer, H. Miguez, and J. P. Mondia. "Large-scale synthesis of a silicon photonic crystal with a complete three-dimensional bandgap near 1.5 micrometres". *Nature* 6785 (2000), pp. 437–440 (cited on p. 33).

[130] J. D. Joannopoulos, S. G. Johnson, J. N. Winn, and R. D. Meade. *Photonic Crystals: Molding the Flow of Light*. Princeton University Press, 2008 (cited on p. 33).

[131] J. Chan. *Laser cooling of an optomechanical crystal resonator to its quantum ground state of motion*. California Institute of Technology, 2012 (cited on p. 33).

[132] A. Faraon, P. Barclay, C. Santori, K. Fu, and R. Beausoleil. "Resonant enhancement of the zero-phonon emission from a colour centre in a diamond cavity". *Nat. Photon.* 5.5 (2011), pp. 301–305 (cited on p. 34).

[133] N. H. Wan, S. Mouradian, and D. Englund. "Two-dimensional photonic crystal slab nanocavities on bulk single-crystal diamond". *Applied Physics Letters* 112.14 (2018), p. 141102 (cited on p. 34).

[134] P. Spinicelli, A. Dréau, L. Rondin, F. Silva, J. Achard, S. Xavier, S. Bansropun, T. Debuisschert, S. Pezzagna, J. Meijer, et al. "Engineered arrays of nitrogen-vacancy color centers in diamond based on implantation of CN- molecules through nanoapertures". *New Journal of Physics* 13.2 (2011), p. 025014 (cited on p. 34).

[135] S. Pezzagna, D. Rogalla, H.-W. Becker, I. Jakobi, F. Dolde, B. Naydenov, J. Wrachtrup, F. Jelezko, C. Trautmann, and J. Meijer. "Creation of colour centres in diamond by collimated ion-implantation through nanochannels in mica". *Physica Status Solidi (a)* 208.9 (2011), pp. 2017–2022 (cited on p. 34).

[136] J. Meijer, S. Pezzagna, T. Vogel, B. Burchard, H. Bukow, I. Rangelow, Y. Sarov, H. Wiggers, I. Plümel, F. Jelezko, J. Wrachtrup, F. Schmidt-Kaler, W. Schnitzler, and K. Singer. "Towards the implanting of ions and

positioning of nanoparticles with nm spatial resolution". *Applied Physics A* 91.4 (2008), pp. 567–571 (cited on p. 34).

[137] S. Tamura, G. Koike, A. Komatsubara, T. Teraji, S. Onoda, L. P. McGuinness, L. Rogers, B. Naydenov, E. Wu, L. Yan, et al. "Array of bright silicon-vacancy centers in diamond fabricated by low-energy focused ion beam implantation". *Appl. Phys. Express* 7.11 (2014), p. 115201 (cited on pp. 34, 98, 111).

[138] M. J. Burek, Y. Chu, M. S. Liddy, P. Patel, J. Rochman, S. Meesala, W. Hong, Q. Quan, M. D. Lukin, and M. Lončar. "High quality-factor optical nanocavities in bulk single-crystal diamond". *Nat. Commun.* 5 (2014), p. 5718 (cited on pp. 34, 111, 113, 146, 178, 183).

[139] M. J. Burek, C. Meuwly, R. E. Evans, M. K. Bhaskar, A. Sipahigil, S. Meesala, B. Machielse, D. D. Sukachev, C. T. Nguyen, J. L. Pacheco, et al. "Fiber-Coupled Diamond Quantum Nanophotonic Interface". *Physical Review Applied* 8.2 (2017), p. 024026 (cited on pp. 34, 123, 132, 237, 238).

[140] S. Mosor, J. Hendrickson, B. C. Richards, J. Sweet, G. Khitrova, H. M. Gibbs, T. Yoshie, A. Scherer, O. B. Shchekin, and D. G. Deppe. "Scanning a photonic crystal slab nanocavity by condensation of xenon". *Applied Physics Letters* 87.14, 141105 (2005), p. 141105 (cited on p. 37).

[141] A. T. Collins. "The Fermi level in diamond". *Journal of Physics: Condensed Matter* 14.14 (2002), p. 3743 (cited on p. 44).

[142] A. Gali and J. R. Maze. "Ab initio study of the split silicon-vacancy defect in diamond: Electronic structure and related properties". *Phys. Rev. B* 88.23 (2013), p. 235205 (cited on pp. 44, 100).

[143] M. Grinolds, M. Warner, K. De Greve, Y. Dovzhenko, L. Thiel, R. Walsworth, S. Hong, P. Maletinsky, and A. Yacoby. "Subnanometre resolution in three-dimensional magnetic resonance imaging of individual dark spins". *Nat. Nanotechnol.* 9.4 (2014), pp. 279–284 (cited on p. 45).

[144] M. Loretz, T. Rosskopf, and C. Degen. “Radio-frequency magnetometry using a single electron spin”. *Phys. Rev. Lett.* 110.1 (2013), p. 017602 (cited on p. 45).

[145] T. Rosskopf, A. Dussaux, K. Ohashi, M. Loretz, R. Schirhagl, H. Watanabe, S. Shikata, K. Itoh, and C. Degen. “Investigation of Surface Magnetic Noise by Shallow Spins in Diamond”. *Phys. Rev. Lett.* 112.14 (2014), p. 147602 (cited on pp. 45, 46).

[146] S. Sque, R. Jones, and P. R. Briddon. “Structure, electronics, and interaction of hydrogen and oxygen on diamond surfaces”. *Phys. Rev. B* 73.8 (2006), p. 085313 (cited on pp. 46, 49, 50, 54, 56, 57, 91).

[147] S. J. Harris and D. Goodwin. “Growth on the reconstructed diamond (100) surface”. *The Journal of Physical Chemistry* 97.1 (1993), pp. 23–28 (cited on pp. 46, 47).

[148] S. Iarlori, G. Galli, F. Gygi, M. Parrinello, and E. Tosatti. “Reconstruction of the diamond (111) surface”. *Phys. Rev. Lett.* 69.20 (1992), p. 2947 (cited on pp. 47–49).

[149] L. V. Zhigilei, D. Srivastava, and B. J. Garrison. “Intermediate metastable structure of the C {111}/(1× 1) HC {111}/(2× 1) surface phase transition”. *Phys. Rev. B* 55.3 (1997), p. 1838 (cited on p. 47).

[150] G. Kern, J. Hafner, and G. Kresse. “Atomic and electronic structure of diamond (111) surfaces I. Reconstruction and hydrogen-induced dereconstruction of the one dangling-bond surface”. *Surface science* 366.3 (1996), pp. 445–463 (cited on pp. 47, 52).

[151] G. Kern, J. Hafner, and G. Kresse. “Atomic and electronic structure of diamond (111) surfaces II.(2× 1) and (√ 3×√ 3) reconstructions of the clean and hydrogen-covered three dangling-bond surfaces”. *Surface science* 366.3 (1996), pp. 464–482 (cited on pp. 47, 48, 52).

[152] A. Hamza, G. Kubiak, and R. Stulen. “The role of hydrogen on the diamond C (111)-(2× 1) reconstruction”. *Surface science* 206.1 (1988), pp. L833–L844 (cited on pp. 47–49).

[153] A. V. Hamza, G. D. Kubiak, and R. H. Stulen. “Hydrogen chemisorption and the structure of the diamond C (100)-(2× 1) surface”. *Surface science* 237.1 (1990), pp. 35–52 (cited on pp. 47–49, 51, 52, 66, 89, 166).

[154] P. Lurie and J. Wilson. “The diamond surface: I. The structure of the clean surface and the interaction with gases and metals”. *Surface Science* 65.2 (1977), pp. 453–475 (cited on pp. 47, 48, 50, 58, 66).

[155] T. Frauenheim, U. Stephan, P. Blaudeck, D. Porezag, H.-G. Busmann, W. Zimmermann-Edling, and S. Lauer. “Stability, reconstruction, and electronic properties of diamond (100) and (111) surfaces”. *Phys. Rev. B* 48.24 (1993), p. 18189 (cited on p. 47).

[156] P. Baumann and R. Nemanich. “Surface cleaning, electronic states and electron affinity of diamond (100),(111) and (110) surfaces”. *Surface science* 409.2 (1998), pp. 320–335 (cited on p. 47).

[157] R. Graupner, F. Maier, J. Ristein, L. Ley, and C. Jung. “High-resolution surface-sensitive C 1 s core-level spectra of clean and hydrogen-terminated diamond (100) and (111) surfaces”. *Phys. Rev. B* 57.19 (1998), p. 12397 (cited on pp. 47–50, 85).

[158] J. C. Vickerman and I. S. Gilmore. *Surface analysis: the principal techniques*. Vol. 2. Wiley Online Library, 2009 (cited on pp. 48, 49, 78–80, 82, 156, 164).

[159] B. B. Pate. “The diamond surface: atomic and electronic structure”. *Surface science* 165.1 (1986), pp. 83–142 (cited on p. 48).

[160] J. Lander and J. Morrison. “Low energy electron diffraction study of the (111) diamond surface”. *Surface Science* 4.3 (1966), pp. 241–246 (cited on pp. 48, 50, 58).

[161] F. Himpsel, D. Eastman, P. Heimann, and J. Van der Veen. “Surface states on reconstructed diamond (111)”. *Phys. Rev. B* 24.12 (1981), p. 7270 (cited on pp. 49, 71).

[162] B. Rezek, C. Sauerer, C. Nebel, M. Stutzmann, J. Ristein, L. Ley, E. Snidero, and P. Bergonzo. “Fermi level on hydrogen terminated diamond surfaces”. *Appl. Phys. Lett.* 82.14 (2003), pp. 2266–2268 (cited on p. 49).

[163] J. Ristein. “Diamond surfaces: familiar and amazing”. *Applied Physics A* 82.3 (2006), pp. 377–384 (cited on pp. 49, 52–54, 67).

[164] S. Cui and E. L. Hu. “Increased negatively charged nitrogen-vacancy centers in fluorinated diamond”. *Appl. Phys. Lett.* 103.5 (2013), p. 051603 (cited on pp. 49, 55).

[165] A. Stacey, T. Karle, L. McGuinness, B. Gibson, K. Ganesan, S. Tomljenovic-Hanic, A. Greentree, A. Hoffman, R. Beausoleil, and S. Prawer. “Depletion of nitrogen-vacancy color centers in diamond via hydrogen passivation”. *Appl. Phys. Lett.* 100.7 (2012), pp. 071902–071902 (cited on pp. 49, 50).

[166] M. Nimmrich, M. Kittelmann, P. Rahe, A. Mayne, G. Dujardin, A. von Schmidsfeld, M. Reichling, W. Harneit, and A. Kühnle. “Atomic-resolution imaging of clean and hydrogen-terminated C (100)-(2× 1) diamond surfaces using noncontact AFM”. *Phys. Rev. B* 81.20 (2010), p. 201403 (cited on pp. 50, 66, 83).

[167] J. Furthmüller, J. Hafner, and G. Kresse. “Structural and electronic properties of clean and hydrogenated diamond (100) surfaces”. *EPL (Europhysics Letters)* 28.9 (1994), p. 659 (cited on pp. 50, 89).

[168] J. Furthmüller, J. Hafner, and G. Kresse. “Dimer reconstruction and electronic surface states on clean and hydrogenated diamond (100) surfaces”. *Physical Review B* 53.11 (1996), p. 7334 (cited on pp. 50–52, 66).

[169] J. Ristein. “Electronic properties of diamond surfaces—blessing or curse for devices?” *Diamond Relat. Mater.* 9.3 (2000), pp. 1129–1137 (cited on p. 52).

[170] M. Kaviani, P. Deák, B. Aradi, T. Frauenheim, J.-P. Chou, and A. Gali. “The proper surface termination for luminescent near-surface NV-centres in diamond”. *Nano Lett.* (2014) (cited on pp. 52, 54, 55, 57, 77, 89, 91).

[171] P. John, N. Polwart, C. Troupe, and J. Wilson. "The oxidation of (100) textured diamond". *Diamond Relat. Mater.* 11.3 (2002), pp. 861–866 (cited on pp. 52, 82, 85).

[172] S. Torrengo, L. Minati, M. Filippi, A. Miotello, M. Ferrari, A. Chiasera, E. Vittone, A. Pasquarelli, M. Dipalo, E. Kohn, et al. "XPS and UPS investigation of the diamond surface oxidation by UV irradiation". *Diamond Relat. Mater.* 18.5 (2009), pp. 804–807 (cited on p. 52).

[173] G. Speranza, S. Torrengo, L. Minati, M. Filippi, M. Castellino, C. Manfredotti, C. Manfredotti, M. Dipalo, A. Pasquarelli, E. Kohn, et al. "Characterization of UV irradiated nanocrystalline diamond". *Diamond Relat. Mater.* 17.7 (2008), pp. 1194–1198 (cited on p. 52).

[174] P. E. Pehrsson and T. W. Mercer. "Oxidation of the hydrogenated diamond (100) surface". *Surface science* 460.1 (2000), pp. 49–66 (cited on p. 52).

[175] P. E. Pehrsson and T. W. Mercer. "Oxidation of heated diamond C (100): H surfaces". *Surface science* 460.1 (2000), pp. 74–90 (cited on p. 52).

[176] T. Szilvási and A. Gali. "Fluorine Modification of the Surface of Diamondoids: A Time-Dependent Density Functional Study". *The Journal of Physical Chemistry C* 118.8 (2014), pp. 4410–4415 (cited on p. 58).

[177] A. Ichimiya and P. I. Cohen. *Reflection high-energy electron diffraction*. Cambridge University Press, 2004 (cited on pp. 59, 64, 69, 75).

[178] W. Braun. *Applied RHEED: reflection high-energy electron diffraction during crystal growth*. 154. Springer, 1999 (cited on pp. 59, 62, 69, 75).

[179] J. Li, W. Peng, K. Chen, P. Wang, H. Chu, Y. Chen, and D. Zheng. "Growth and in situ high-pressure reflection high energy electron diffraction monitoring of oxide thin films". *Science China Physics, Mechanics and Astronomy* 56.12 (2013), pp. 2312–2326 (cited on p. 59).

[180] I. Hernandez-Calderon and H. Höchst. "New method for the analysis of reflection high-energy electron diffraction: α-S n (001) and InSb (001) surfaces". *Phys. Rev. B* 27.8 (1983), p. 4961 (cited on pp. 62, 63).

[181] A. Goswami and N. Lisgarten. “The measurement of the inner potential of diamond”. *Journal of Physics C: Solid State Physics* 13.8 (1980), p. 1381 (cited on p. 64).

[182] D. Ashenford and N. Lisgarten. “The measurement of inner potential for diamond, germanium and silicon”. *Acta Crystallographica Section A: Foundations of Crystallography* 39.3 (1983), pp. 311–314 (cited on p. 64).

[183] H. Nakahara. *KikuchiLines X: Kikuchi Lines and RHEED Pattern Calculator*. 2018. URL: http://www.surf.nuqe.nagoya-u.ac.jp/~nakahara/Software/KikuchiLinesX/index-e.html (visited on 04/12/2018) (cited on p. 65).

[184] Wikipedia. *Structure Factor*. 2018. URL: https://en.wikipedia.org/wiki/Structure_factor (visited on 04/17/2018) (cited on p. 66).

[185] M. Nishitani-Gamo, K. P. Loh, I. Sakaguchi, T. Takami, I. Kusunoki, and T. Ando. “Surface morphology of homoepitaxially grown (111),(001), and (110) diamond studied by low energy electron diffraction and reflection high-energy electron diffraction”. *Journal of Vacuum Science & Technology A* 17.5 (1999), pp. 2991–3002 (cited on pp. 66, 70, 73, 74).

[186] T. Takami, I. Kusunoki, M. Nishitani-Gamo, and T. Ando. “Homoepitaxial diamond (001) thin film studied by reflection high-energy electron diffraction, contact atomic force microscopy, and scanning tunneling microscopy”. *Journal of Vacuum Science & Technology B* 18.3 (2000), pp. 1198–1202 (cited on pp. 66, 70).

[187] J. Zheng, X. Xie, A. Wee, and K. P. Loh. “Oxygen-induced surface state on diamond (100)”. *Diamond Relat. Mater.* 10.3 (2001), pp. 500–505 (cited on p. 66).

[188] N. de Leon. Personal communication based on NEXAFS studies. 15, 2014 (cited on pp. 71, 90).

[189] R. Ramsier and J. Yates Jr. “Electron-stimulated desorption: principles and applications”. *Surface Science Reports* 12.6 (1991), pp. 246–378 (cited on p. 71).

[190] T. L. Barr and S. Seal. “Nature of the use of adventitious carbon as a binding energy standard”. *Journal of Vacuum Science & Technology A* 13.3 (1995), pp. 1239–1246 (cited on pp. 76, 81, 85, 90).

[191] H. Piao and N. McIntyre. “Adventitious carbon growth on aluminium and gold–aluminium alloy surfaces”. *Surface and interface analysis* 33.7 (2002), pp. 591–594 (cited on p. 76).

[192] D. Miller, M. Biesinger, and N. McIntyre. “Interactions of CO2 and CO at fractional atmosphere pressures with iron and iron oxide surfaces: one possible mechanism for surface contamination?” *Surface and interface analysis* 33.4 (2002), pp. 299–305 (cited on p. 76).

[193] N. Stojilovic. “Why Can’t We See Hydrogen in X-ray Photoelectron Spectroscopy?” *Journal of Chemical Education* 89.10 (2012), pp. 1331–1332 (cited on p. 78).

[194] S. Evans and C. E. Riley. “Angular dependence of X-ray-excited valence-band photoelectron spectra of diamond”. *Journal of the Chemical Society, Faraday Transactions 2: Molecular and Chemical Physics* 82.4 (1986), pp. 541–550 (cited on p. 78).

[195] G. Francz, P. Kania, G. Gantner, H. Stupp, and P. Oelhafen. “Photoelectron spectroscopy study of natural (100),(110),(111) and CVD diamond surfaces”. *physica status solidi (a)* 154.1 (1996), pp. 91–108 (cited on p. 78).

[196] W. Lau, L. Huang, I. Bello, Y. Yiu, and S.-T. Lee. “Modification of surface band bending of diamond by low energy argon and carbon ion bombardment”. *J. Appl. Phys.* 75.7 (1994), pp. 3385–3391 (cited on p. 79).

[197] B. Tyler, D. Castner, and B. Ratner. “Regularization: A stable and accurate method for generating depth profiles from angle-dependent XPS data”. *Surface and Interface Analysis* 14.8 (1989), pp. 443–450 (cited on p. 79).

[198] G. P. López, D. G. Castner, and B. D. Ratner. “XPS O 1s binding energies for polymers containing hydroxyl, ether, ketone and ester groups”.

Surface and interface analysis 17.5 (1991), pp. 267–272 (cited on pp. 80, 84, 85).

[199] R. Morent, N. De Geyter, C. Leys, L. Gengembre, and E. Payen. "Comparison between XPS-and FTIR-analysis of plasma-treated polypropylene film surfaces". *Surface and Interface Analysis* 40.3-4 (2008), pp. 597–600 (cited on pp. 80, 85, 165).

[200] K. Siegbahn. *Electron spectroscopy for atoms, molecules and condensed matter*. Tech. rep. Uppsala Univ.(Sweden). Fysiska Institutionen, 1981 (cited on p. 80).

[201] S. Kumaragurubaran, T. Yamada, and S. Shikata. "Annealing effects in H-and O-terminated P-doped diamond (111) surfaces". *Diamond Relat. Mater.* 17.4 (2008), pp. 472–475 (cited on pp. 82, 85).

[202] C. Baldwin, J. Downes, C. McMahon, C. Bradac, and R. Mildren. "Nanostructuring and oxidation of diamond by two-photon ultraviolet surface excitation: An XPS and NEXAFS study". *Phys. Rev. B* 89.19 (2014), p. 195422 (cited on pp. 83, 85, 86, 92).

[203] K. Bobrov, A. J. Mayne, and G. Dujardin. "Atomic-scale imaging of insulating diamond through resonant electron injection". *Nature* 413.6856 (2001), pp. 616–619 (cited on p. 83).

[204] T. Ando, K. Yamamoto, M. Ishii, M. Kamo, and Y. Sato. "Vapour-phase oxidation of diamond surfaces in O2 studied by diffuse reflectance Fourier-transform infrared and temperture-programmed desorption spectroscopy". *Journal of the Chemical Society, Faraday Transactions* 89.19 (1993), pp. 3635–3640 (cited on pp. 83, 165, 166, 168).

[205] P. John, N. Polwart, C. E. Troupe, and J. I. Wilson. "The oxidation of diamond: the geometry and stretching frequency of carbonyl on the (100) surface". *Journal of the American Chemical Society* 125.22 (2003), pp. 6600–6601 (cited on pp. 91, 166, 168).

[206] J. L. O'Brien, A. Furusawa, and J. Vučković. "Photonic quantum technologies". *Nat. Photon.* 3.12 (2009), pp. 687–695 (cited on pp. 96, 100).

[207] M. W. Doherty, N. B. Manson, P. Delaney, F. Jelezko, J. Wrachtrup, and L. C. Hollenberg. "The nitrogen-vacancy colour centre in diamond". *Phys. Rep.* 528.1 (2013), pp. 1–45 (cited on p. 97).

[208] W. Pfaff, B. J. Hensen, H. Bernien, S. B. van Dam, M. S. Blok, T. H. Taminiau, M. J. Tiggelman, R. N. Schouten, M. Markham, D. J. Twitchen, and R. Hanson. "Unconditional quantum teleportation between distant solid-state quantum bits". *Science* 345.6196 (2014), pp. 532–535 (cited on p. 97).

[209] E. Neu, D. Steinmetz, J. Riedrich-Möller, S. Gsell, M. Fischer, M. Schreck, and C. Becher. "Single photon emission from silicon-vacancy colour centres in chemical vapour deposition nano-diamonds on iridium". *New J. Phys.* 13.2 (2011), p. 025012 (cited on p. 97).

[210] L. J. Rogers, M. W. Doherty, M. S. J. Barson, S. Onoda, T. Ohshima, and N. B. Manson. "Singlet levels of the NV^- centre in diamond". *New J. Phys.* 17.1 (2014), p. 013048 (cited on pp. 97–99, 101, 105, 106).

[211] H. Sternschulte, K. Thonke, R. Sauer, P. C. Münzinger, and P. Michler. "1.681-eV luminescence center in chemical-vapor-deposited homoepitaxial diamond films". *Phys. Rev. B* 50.19 (1994), pp. 14554–14560 (cited on pp. 97–99, 101, 105, 106, 190).

[212] A. Sipahigil, K. D. Jahnke, L. J. Rogers, T. Teraji, J. Isoya, A. S. Zibrov, F. Jelezko, and M. D. Lukin. "Indistinguishable Photons from Separated Silicon-Vacancy Centers in Diamond". *Phys. Rev. Lett.* 113 (11 2014), p. 113602 (cited on pp. 98, 106, 107, 113, 124, 131, 173).

[213] T. Müller, C. Hepp, B. Pingault, E. Neu, S. Gsell, M. Schreck, H. Sternschulte, D. Steinmüller-Nethl, C. Becher, and M. Atatüre. "Optical signatures of silicon-vacancy spins in diamond". *Nat. Comm.* 5 (2014), p. 3328 (cited on pp. 98, 101).

[214] C. Hepp, T. Müller, V. Waselowski, J. N. Becker, B. Pingault, H. Sternschulte, D. Steinmüller-Nethl, A. Gali, J. R. Maze, M. Atatüre, and C. Becher. "Electronic Structure of the Silicon Vacancy Color Center in Di-

amond". *Phys. Rev. Lett.* 112.3 (2014), p. 036405 (cited on pp. 98–101, 106, 113, 121, 132, 138, 139, 190, 249, 260).

[215] C. Lo. "Natural Colorless Type IaB Diamond with Silicon-Vacancy Defect Center". *Gems and Gemology* L (2014), p. 293 (cited on p. 98).

[216] A. M. Edmonds, M. E. Newton, P. M. Martineau, D. J. Twitchen, and S. D. Williams. "Electron paramagnetic resonance studies of silicon-related defects in diamond". *Phys. Rev. B* 77.24 (2008), p. 245205 (cited on p. 98).

[217] U. D'Haenens-Johansson, A. Edmonds, B. Green, M. Newton, G. Davies, P. Martineau, R. Khan, and D. Twitchen. "Optical properties of the neutral silicon split-vacancy center in diamond". *Physical Review B* 84.24 (2011), p. 245208 (cited on pp. 98, 106, 148, 188).

[218] E. Neu, C. Hepp, M. Hauschild, S. Gsell, M. Fischer, H. Sternschulte, D. Steinmüller-Nethl, M. Schreck, and C. Becher. "Low-temperature investigations of single silicon vacancy colour centres in diamond". *New J. Phys.* 15.4 (2013), p. 043005 (cited on p. 98).

[219] C. D. Clark, H. Kanda, I. Kiflawi, and G. Sittas. "Silicon defects in diamond". *Phys. Rev. B* 51 (23 1995), pp. 16681–16688 (cited on pp. 98, 102, 106).

[220] J. L. Zhang, H. Ishiwata, T. M. Babinec, M. Radulaski, K. Müller, K. G. Lagoudakis, C. Dory, J. Dahl, R. Edgington, V. Soulière, G. Ferro, A. A. Fokin, P. R. Schreiner, Z.-X. Shen, N. A. Melosh, and J. Vučković. "Hybrid Group IV Nanophotonic Structures Incorporating Diamond Silicon-Vacancy Color Centers". *Nano Lett.* 16.1 (2016), pp. 212–217 (cited on p. 98).

[221] C. Wang, C. Kurtsiefer, H. Weinfurter, and B. Burchard. "Single photon emission from SiV centres in diamond produced by ion implantation". *J. Phys. B* 39.1 (2006), p. 37 (cited on p. 98).

[222] B. Pingault, J. N. Becker, C. H. Schulte, C. Arend, C. Hepp, T. Godde, A. I. Tartakovskii, M. Markham, C. Becher, and M. Atatüre. "All-optical formation of coherent dark states of silicon-vacancy spins in diamond".

Phys. Rev. Lett. 113.26 (2014), p. 263601 (cited on pp. 100, 108, 118, 139).

[223] I. Aharonovich, A. D. Greentree, and S. Prawer. "Diamond photonics". *Nat. Photon.* 5.7 (2011), pp. 397–405 (cited on pp. 100, 111).

[224] J. P. Goss, R. Jones, S. J. Breuer, P. R. Briddon, and S. Öberg. "The twelve-line 1.682 eV luminescence center in diamond and the vacancy-silicon complex". *Phys. Rev. Lett.* 77.14 (1996), p. 3041 (cited on p. 100).

[225] L. J. Rogers, K. D. Jahnke, M. W. Doherty, A. Dietrich, L. P. McGuinness, C. Müller, T. Teraji, H. Sumiya, J. Isoya, N. B. Manson, and F. Jelezko. "Electronic structure of the negatively charged silicon-vacancy center in diamond". *Phys. Rev. B* 89.23 (2014), p. 235101 (cited on pp. 100, 207).

[226] K. D. Jahnke, A. Sipahigil, J. M. Binder, M. W. Doherty, M. Metsch, L. J. Rogers, N. B. Manson, M. D. Lukin, and F. Jelezko. "Electron–phonon processes of the silicon-vacancy centre in diamond". *New J. Phys.* 17.4 (2015), p. 043011 (cited on pp. 101, 103, 105, 108, 116, 118, 128, 146, 149, 198, 201).

[227] J. F. Ziegler, M. D. Ziegler, and J. P. Biersack. "SRIM–The stopping and range of ions in matter (2010)". *Nucl. Instrum. Meth. B* 268.11 (2010), pp. 1818–1823 (cited on p. 102).

[228] C. D. Clark and C. Dickerson. "The 1.681 eV centre in polycrystalline diamond". *Surf. Coat. Tech.* 47.1 (1991), pp. 336–343 (cited on pp. 102, 106).

[229] J. Orwa, C. Santori, K. Fu, B. Gibson, D. Simpson, I. Aharonovich, A. Stacey, A. Cimmino, P. Balog, M. Markham, et al. "Engineering of nitrogen-vacancy color centers in high purity diamond by ion implantation and annealing". *J. Appl. Phys.* 109.8 (2011), p. 083530 (cited on pp. 102, 106).

[230] Y. Chu, N. P. de Leon, B. J. Shields, B. Hausmann, R. Evans, E. Togan, M. J. Burek, M. Markham, A. Stacey, A. S. Zibrov, A. Yacoby, D. J. Twitchen, M. Lončar, H. Park, P. Maletinsky, and M. D. Lukin. "Coher-

ent Optical Transitions in Implanted Nitrogen Vacancy Centers". *Nano Lett.* 14.4 (2014), pp. 1982–1986 (cited on pp. 102, 108, 172, 184).

[231] T. D. Ladd, F. Jelezko, R. Laflamme, Y. Nakamura, C. Monroe, and J. L. O'Brien. "Quantum computers". *Nature* 464.7285 (2010), pp. 45–53 (cited on p. 107).

[232] K. J. Vahala. "Optical microcavities". *Nature* 424.6950 (2003), pp. 839–846 (cited on p. 107).

[233] Y. Li, P. C. Humphreys, G. J. Mendoza, and S. C. Benjamin. "Resource Costs for Fault-Tolerant Linear Optical Quantum Computing". *Phys. Rev. X* 5 (4 2015), p. 041007 (cited on p. 107).

[234] T. Babinec, B. Hausmann, M. Khan, Y. Zhang, J. Maze, P. Hemmer, and M. Lončar. "A diamond nanowire single-photon source". *Nat. Nanotechnol.* 5.3 (2010), pp. 195–199 (cited on pp. 108, 111).

[235] Y. Chu and M. D. Lukin. "Quantum optics with nitrogen-vacancy centers in diamond". *arXiv preprint arXiv:1504.05990* (2015) (cited on p. 108).

[236] L. J. Rogers, K. D. Jahnke, M. H. Metsch, A. Sipahigil, J. M. Binder, T. Teraji, H. Sumiya, J. Isoya, M. D. Lukin, P. Hemmer, and F. Jelezko. "All-optical initialization, readout, and coherent preparation of single silicon-vacancy spins in diamond". *Phys. Rev. Lett.* 113.26 (2014), p. 263602 (cited on pp. 110, 118, 128, 139).

[237] B. J. M. Hausmann, B. Shields, Q. Quan, P. Maletinsky, M. McCutcheon, J. T. Choy, T. M. Babinec, A. Kubanek, A. Yacoby, M. D. Lukin, and M. Loncar. "Integrated diamond networks for quantum nanophotonics." *Nano Lett.* 12.3 (2012), pp. 1578–82 (cited on p. 111).

[238] J. Riedrich-Möller, L. Kipfstuhl, C. Hepp, E. Neu, C. Pauly, F. Mücklich, A. Baur, M. Wandt, S. Wolff, M. Fischer, S. Gsell, M. Schreck, and C. Becher. "One- and two-dimensional photonic crystal microcavities in single crystal diamond". *Nat. Nanotechnol.* 7.1 (2012), pp. 69–74 (cited on p. 111).

[239] J. C. Lee, I. Aharonovich, A. P. Magyar, F. Rol, and E. L. Hu. "Coupling of silicon-vacancy centers to a single crystal diamond cavity". *Opt. Express* 20.8 (2012), pp. 8891–8897 (cited on p. 111).

[240] J. Riedrich-Möller, C. Arend, C. Pauly, F. Mücklich, M. Fischer, S. Gsell, M. Schreck, and C. Becher. "Deterministic Coupling of a Single Silicon-Vacancy Color Center to a Photonic Crystal Cavity in Diamond". *Nano Lett.* 14.9 (2014), pp. 5281–5287 (cited on pp. 111, 113, 128).

[241] A. Sipahigil, R. E. Evans, D. D. Sukachev, M. J. Burek, J. Borregaard, M. K. Bhaskar, C. T. Nguyen, J. L. Pacheco, H. A. Atikian, C. Meuwly, R. M. Camacho, F. Jelezko, E. Bielejec, H. Park, M. Lončar, and M. D. Lukin. "An integrated diamond nanophotonics platform for quantum-optical networks". *Science* 354.6314 (2016), pp. 847–850 (cited on p. 111).

[242] A. Javadi, I. Sollner, M. Arcari, S. L. Hansen, L. Midolo, S. Mahmoodian, G. Kirsanske, T. Pregnolato, E. H. Lee, J. D. Song, S. Stobbe, and P. Lodahl. "Single-photon non-linear optics with a quantum dot in a waveguide". *Nat. Commun.* 6 (2015), p. 8655 (cited on p. 112).

[243] S. Sun, H. Kim, G. S. Solomon, and E. Waks. "A quantum phase switch between a single solid-state spin and a photon". *Nat. Nanotechnol.* 11 (2016), pp. 539–544 (cited on p. 112).

[244] J. Mlynek, A. Abdumalikov, C. Eichler, and A. Wallraff. "Observation of Dicke superradiance for two artificial atoms in a cavity with high decay rate". *Nat. Commun.* 5 (2014) (cited on pp. 112, 124).

[245] B. Casabone, A. Stute, K. Friebe, B. Brandstätter, K. Schüppert, R. Blatt, and T. Northup. "Heralded entanglement of two ions in an optical cavity". *Phys. Rev. Lett.* 111.10 (2013), p. 100505 (cited on p. 112).

[246] A. Badolato, K. Hennessy, M. Atatüre, J. Dreiser, E. Hu, P. M. Petroff, and A. Imamoğlu. "Deterministic coupling of single quantum dots to single nanocavity modes". *Science* 308.5725 (2005), pp. 1158–1161 (cited on pp. 112, 113).

[247] L. J. Rogers, K. D. Jahnke, T. Teraji, L. Marseglia, C. Müller, B. Naydenov, H. Schauffert, C. Kranz, J. Isoya, L. P. McGuinness, and F. Jelezko.

"Multiple intrinsically identical single-photon emitters in the solid state". *Nat. Commun.* 5 (2014), p. 4739 (cited on p. 113).

[248] R. E. Evans, A. Sipahigil, D. D. Sukachev, A. S. Zibrov, and M. D. Lukin. "Narrow-Linewidth Homogeneous Optical Emitters in Diamond Nanostructures via Silicon Ion Implantation". *Phys. Rev. Appl.* 5.4 (2016), p. 044010 (cited on pp. 113, 115, 116, 121, 128, 131, 135, 136, 184, 188, 251–253).

[249] D. E. Chang, A. S. Sørensen, E. A. Demler, and M. D. Lukin. "A single-photon transistor using nanoscale surface plasmons". *Nat. Phys.* 3.11 (2007), pp. 807–812 (cited on pp. 117, 120, 251).

[250] P. R. Rice and H. J. Carmichael. "Single-atom cavity-enhanced absorption. I. Photon statistics in the bad-cavity limit". *IEEE J. Quantum Elect.* 24.7 (1988), pp. 1351–1366 (cited on pp. 117, 120).

[251] J. N. Becker, J. Görlitz, C. Arend, M. Markham, and C. Becher. "Ultrafast all-optical coherent control of single silicon vacancy colour centres in diamond". *Nat. Commun.* 7 (2016), p. 13512 (cited on pp. 118, 144, 147).

[252] D. Sukachev, A. Sipahigil, C. Nguyen, M. Bhaskar, R. Evans, F. Jelezko, and M. Lukin. "Silicon-Vacancy Spin Qubit in Diamond: A Quantum Memory Exceeding 10 ms with Single-Shot State Readout". *Physical review letters* 119.22 (2017), p. 223602 (cited on pp. 121, 128, 132, 140, 144, 147, 260).

[253] T. Tiecke, K. Nayak, J. Thompson, T. Peyronel, N. de Leon, V. Vuletić, and M. Lukin. "Efficient fiber-optical interface for nanophotonic devices". *Optica* 2.2 (2015), pp. 70–75 (cited on pp. 123, 128, 188).

[254] G. Fernandez, T. Volz, R. Desbuquois, A. Badolato, and A. Imamoglu. "Optically tunable spontaneous raman fluorescence from a single self-assembled InGaAs quantum dot". *Phys. Rev. Lett.* 103.8 (2009), p. 087406 (cited on p. 123).

[255] T. M. Sweeney, S. G. Carter, A. S. Bracker, M. Kim, C. S. Kim, L. Yang, P. M. Vora, P. G. Brereton, E. R. Cleveland, and D. Gammon. "Cavity-stimulated Raman emission from a single quantum dot spin". *Nat. Photon.* 8.6 (2014), pp. 442–447 (cited on p. 123).

[256] A. Delteil, Z. Sun, W.-b. Gao, E. Togan, S. Faelt, and A. Imamoğlu. "Generation of heralded entanglement between distant hole spins". *Nat. Phys.* 12 (3 2015), pp. 218–223 (cited on pp. 124, 127).

[257] C. Cabrillo, J. Cirac, P. Garcia-Fernandez, and P. Zoller. "Creation of entangled states of distant atoms by interference". *Phys. Rev. A* 59.2 (1999), p. 1025 (cited on pp. 124, 125, 127).

[258] R. Wiegner, S. Oppel, D. Bhatti, J. von Zanthier, and G. Agarwal. "Simulating superradiance from higher-order-intensity-correlation measurements: Single atoms". *Phys. Rev. A* 92.3 (2015), p. 033832 (cited on pp. 124, 125).

[259] A. Wallraff, D. I. Schuster, A. Blais, L. Frunzio, R.-S. Huang, J. Majer, S. Kumar, S. M. Girvin, and R. J. Schoelkopf. "Strong coupling of a single photon to a superconducting qubit using circuit quantum electrodynamics". *Nature* 431.7005 (2004), pp. 162–167 (cited on p. 130).

[260] J. Majer, J. Chow, J. Gambetta, J. Koch, B. Johnson, J. Schreier, L. Frunzio, D. Schuster, A. Houck, A. Wallraff, et al. "Coupling superconducting qubits via a cavity bus". *Nature* 449.7161 (2007), pp. 443–447 (cited on pp. 131, 137, 138, 142).

[261] N. Samkharadze, G. Zheng, N. Kalhor, D. Brousse, A. Sammak, U. C. Mendes, A. Blais, G. Scappucci, and L. M. K. Vandersypen. "Strong spin-photon coupling in silicon". *Science* (2018) (cited on p. 131).

[262] X. Mi, M. Benito, S. Putz, D. Zajac, J. Taylor, G. Burkard, and J. Petta. "A coherent spin–photon interface in silicon". *Nature* (2018) (cited on p. 131).

[263] L. DiCarlo, J. Chow, J. Gambetta, L. S. Bishop, B. Johnson, D. Schuster, J. Majer, A. Blais, L. Frunzio, S. Girvin, et al. "Demonstration of two-qubit algorithms with a superconducting quantum processor". *Nature* 460.7252 (2009), p. 240 (cited on p. 131).

[264] B. Casabone, K. Friebe, B. Brandstätter, K. Schüppert, R. Blatt, and T. Northup. "Enhanced quantum interface with collective ion-cavity coupling". *Phys. Rev. Lett.* 114.2 (2015), p. 023602 (cited on p. 131).

[265] R. Reimann, W. Alt, T. Kampschulte, T. Macha, L. Ratschbacher, N. Thau, S. Yoon, and D. Meschede. "Cavity-Modified Collective Rayleigh Scattering of Two Atoms". *Phys. Rev. Lett.* 114.2 (2015), p. 023601 (cited on p. 131).

[266] A. Neuzner, M. Körber, O. Morin, S. Ritter, and G. Rempe. "Interference and dynamics of light from a distance-controlled atom pair in an optical cavity". *Nat. Photon.* 10.5 (2016), pp. 303–306 (cited on p. 131).

[267] A. Laucht, J. Villas-Bôas, S. Stobbe, N. Hauke, F. Hofbauer, G. Böhm, P. Lodahl, M.-C. Amann, M. Kaniber, and J. Finley. "Mutual coupling of two semiconductor quantum dots via an optical nanocavity". *Physical Review B* 82.7 (2010), p. 075305 (cited on p. 131).

[268] H. Kim, D. Sridharan, T. C. Shen, G. S. Solomon, and E. Waks. "Strong coupling between two quantum dots and a photonic crystal cavity using magnetic field tuning". *Optics express* 19.3 (2011), pp. 2589–2598 (cited on pp. 131, 138).

[269] A. Sipahigil, R. Evans, D. Sukachev, M. Burek, J. Borregaard, M. Bhaskar, C. Nguyen, J. Pacheco, H. Atikian, C. Meuwly, et al. "An integrated diamond nanophotonics platform for quantum-optical networks". *Science* 354.6314 (2016), pp. 847–850 (cited on pp. 131, 132, 134, 238, 249, 251, 252, 254, 264).

[270] S.-B. Zheng and G.-C. Guo. "Efficient scheme for two-atom entanglement and quantum information processing in cavity QED". *Physical Review Letters* 85.11 (2000), p. 2392 (cited on pp. 137, 142, 147).

[271] B. Pingault, D.-D. Jarausch, C. Hepp, L. Klintberg, J. N. Becker, M. Markham, C. Becher, and M. Atatüre. "Coherent control of the silicon-vacancy spin in diamond". *Nature Communications* 8 (2017) (cited on pp. 144, 147).

[272] J. Borregaard, P. Kómár, E. Kessler, A. S. Sørensen, and M. Lukin. "Heralded Quantum Gates with Integrated Error Detection in Optical Cavities". *Phys. Rev. Lett.* 114.11 (2015), p. 110502 (cited on p. 144).

[273] S. E. Economou, N. Lindner, and T. Rudolph. "Optically Generated 2-Dimensional Photonic Cluster State from Coupled Quantum Dots". *Phys. Rev. Lett.* 105 (9 2010), p. 093601 (cited on pp. 144, 147).

[274] D. Sridharan and E. Waks. "Generating entanglement between quantum dots with different resonant frequencies based on dipole-induced transparency". *Physical Review A* 78.5 (2008), p. 052321 (cited on p. 147).

[275] S. Fernández-Vidal, S. Zippilli, and G. Morigi. "Nonlinear optics with two trapped atoms". *Physical Review A* 76.5 (2007), p. 053829 (cited on p. 147).

[276] N. Friis, D. Orsucci, M. Skotiniotis, P. Sekatski, V. Dunjko, H. J. Briegel, and W. Dür. "Flexible resources for quantum metrology". *New Journal of Physics* 19.6 (2017), p. 063044 (cited on p. 147).

[277] B. Green, S. Mottishaw, B. Breeze, A. Edmonds, U. D'Haenens-Johansson, M. Doherty, S. Williams, D. Twitchen, and M. Newton. "Neutral Silicon-Vacancy Center in Diamond: Spin Polarization and Lifetimes". *Physical review letters* 119.9 (2017), p. 096402 (cited on p. 148).

[278] B. L. Green, M. W. Doherty, E. Nako, N. B. Manson, U. F. S. D'Haenens-Johansson, S. D. Williams, D. J. Twitchen, and M. E. Newton. "Electronic structure of the neutral silicon-vacancy center in diamond". *ArXiv e-prints* (2018) (cited on p. 148).

[279] J. Goss, P. Briddon, M. Rayson, S. Sque, and R. Jones. "Vacancy-impurity complexes and limitations for implantation doping of diamond". *Physical Review B* 72.3 (2005), p. 035214 (cited on p. 148).

[280] Y.-I. Sohn, S. Meesala, B. Pingault, H. A. Atikian, J. Holzgrafe, M. Gundogan, C. Stavrakas, M. J. Stanley, A. Sipahigil, J. Choi, et al. "Engineering a diamond spin-qubit with a nano-electro-mechanical system". *arXiv preprint arXiv:1706.03881* (2017) (cited on p. 149).

[281] P. Rabl, S. J. Kolkowitz, F. Koppens, J. Harris, P. Zoller, and M. D. Lukin. "A quantum spin transducer based on nanoelectromechanical resonator arrays". *Nature Physics* 6.8 (2010), p. 602 (cited on p. 149).

[282] O. Arcizet, V. Jacques, A. Siria, P. Poncharal, P. Vincent, and S. Seidelin. “A single nitrogen-vacancy defect coupled to a nanomechanical oscillator”. *Nature Physics* 7.11 (2011), p. 879 (cited on p. 149).

[283] M.-A. Lemonde, S. Meesala, A. Sipahigil, M. J. A. Schuetz, M. D. Lukin, M. Loncar, and P. Rabl. “Phonon networks with SiV centers in diamond waveguides”. *ArXiv e-prints* (2018) (cited on p. 149).

[284] W. Voigt. “Über das Gesetz der Intensitätsverteilung innerhalb der Linien eines Gasspektrums”. *Sitzungsberichte Königliche Bayerische Akademie der Wissenschaften* 42 (1912), pp. 603–620 (cited on p. 155).

[285] C. L. Perkins, S.-H. Lee, X. Li, S. E. Asher, and T. J. Coutts. “Identification of nitrogen chemical states in N-doped ZnO via x-ray photoelectron spectroscopy”. *J. Appl. Phys.* 97.3 (2005), p. 034907 (cited on p. 155).

[286] K. Kobayashi, M. Yabashi, Y. Takata, T. Tokushima, S. Shin, K. Tamasaku, D. Miwa, T. Ishikawa, H. Nohira, T. Hattori, et al. “High resolution-high energy x-ray photoelectron spectroscopy using third-generation synchrotron radiation source, and its application to Si-high k insulator systems”. *Appl. Phys. Lett.* 83.5 (2003), pp. 1005–1007 (cited on p. 155).

[287] J. F. Kielkopf. “New approximation to the Voigt function with applications to spectral-line profile analysis”. *JOSA* 63.8 (1973), pp. 987–995 (cited on p. 155).

[288] E. E. Whiting. “An empirical approximation to the Voigt profile”. *Journal of Quantitative Spectroscopy and Radiative Transfer* 8.6 (1968), pp. 1379–1384 (cited on p. 155).

[289] R. Wells. “Rapid approximation to the Voigt/Faddeeva function and its derivatives”. *Journal of Quantitative Spectroscopy and Radiative Transfer* 62.1 (1999), pp. 29–48 (cited on p. 155).

[290] J. Végh. “The Shirley-equivalent electron inelastic scattering cross-section function”. *Surface science* 563.1 (2004), pp. 183–190 (cited on p. 156).

[291] J. Végh. "On analyzing the intrinsic processes through the Shirley background correction procedure". *Surface science* 577.2 (2005), pp. 220–228 (cited on p. 156).

[292] J. Végh. "The Shirley background revised". *Journal of electron spectroscopy and related phenomena* 151.3 (2006), pp. 159–164 (cited on p. 156).

[293] S. Tougaard. "In-depth concentration profile information through analysis of the entire XPS peak shape". *Applied surface science* 32.3 (1988), pp. 332–337 (cited on p. 156).

[294] S. Tougaard. "Practical algorithm for background subtraction". *Surface Science* 216.3 (1989), pp. 343–360 (cited on p. 156).

[295] M. Seah. "Background subtraction: I. General behaviour of Tougaard-style backgrounds in AES and XPS". *Surface science* 420.2 (1999), pp. 285–294 (cited on p. 156).

[296] M. Seah, I. Gilmore, and S. Spencer. "Background subtraction: II. General behaviour of REELS and the Tougaard universal cross section in the removal of backgrounds in AES and XPS". *Surface science* 461.1 (2000), pp. 1–15 (cited on p. 156).

[297] M. Seah. "Background subtraction III: The application of REELS data to background removal in AES and XPS". *Surface science* 471.1 (2001), pp. 185–202 (cited on p. 156).

[298] M. Biesinger. *X-ray Photoelectron Spectroscopy (XPS) Reference Pages*. 2005. URL: http://www.xpsfitting.com (visited on 04/17/2018) (cited on p. 156).

[299] Casa Software Ltd. *Casa XPS Software Manual: Peak Fitting in XPS*. 2006. URL: http://www.casaxps.com/help_manual/manual_updates/peak_fitting_in_xps.pdf (visited on 04/17/2018) (cited on p. 156).

[300] K. Artyushkova. *ART OF CURVE-FITTING… OR BLACK MAGIC OF CURVE-FITTING XPS SPECTRA*. 2012. URL: https://kartyush.wordpress.com/2012/05/22/art-of-curve-fitting-or-black-magic-

of-curve-fitting-xps-spectra/ (visited on 04/17/2018) (cited on p. 156).

[301] R. E. Evans. *SpectraFitting package*. 2014. URL: https://github.com/ruffinevans/SpectraFitting (visited on 04/17/2018) (cited on p. 157).

[302] M. Chesters, S. Parker, and R. Raval. "Cyclohexane adsorption on Cu (111) studied by infrared and electron energy loss spectroscopy". *Studies in Surface Science and Catalysis* 26 (1986), pp. 155–162 (cited on p. 164).

[303] D. F. Edwards and E. Ochoa. "Infrared refractive index of diamond". *JOSA* 71.5 (1981), pp. 607–608 (cited on p. 164).

[304] Y. Xue, Z. Wang, J. Wang, C. Hu, F. Xie, D. Chen, and Z. He. "Evidence of Carboxyl Modification of Hydrogen-Free Diamond-Like Carbon Films Assisted by Radio Frequency Plasma in Vacuum". *ISRN Spectroscopy* 2012 (2012) (cited on p. 166).

[305] L. V. Zhigilei, D. Srivastava, and B. J. Garrison. "Vibrational dynamics of the CH stretching mode of H-terminated diamond surfaces". *Surface science* 374.1 (1997), pp. 333–344 (cited on pp. 166, 168).

[306] S. Lowry. "Analysis of Diamonds by FT-IR Spectroscopy" (2007) (cited on p. 166).

[307] S. Osswald, G. Yushin, V. Mochalin, S. O. Kucheyev, and Y. Gogotsi. "Control of sp2/sp3 carbon ratio and surface chemistry of nanodiamond powders by selective oxidation in air". *Journal of the American Chemical Society* 128.35 (2006), pp. 11635–11642 (cited on pp. 166, 168).

[308] A. Dementjev, K. Maslakov, I. Kulakova, V. Korolkov, and V. Dolmatov. "State of C-atoms on the modified nanodiamond surface". *Diamond and Related Materials* 16.12 (2007), pp. 2083–2086 (cited on p. 166).

[309] B. Mantel, M. Stammler, J. Ristein, and L. Ley. "The correlation between surface conductivity and adsorbate coverage on diamond as studied by infrared spectroscopy". *Diamond Relat. Mater.* 10.3 (2001), pp. 429–433 (cited on p. 166).

[310] W. K. Wootters. “Entanglement of Formation of an Arbitrary State of Two Qubits”. *Phys. Rev. Lett.* 80 (10 1998), pp. 2245–2248 (cited on p. 221).

[311] C. W. Chou, H. de Riedmatten, D. Felinto, S. V. Polyakov, S. J. van Enk, and H. J. Kimble. “Measurement-induced entanglement for excitation stored in remote atomic ensembles”. *Nature* 438.7069 (2005), pp. 828–832 (cited on pp. 221–223).

[312] M. Tavis and F. W. Cummings. “Exact solution for an N-molecule—radiation-field Hamiltonian”. *Physical Review* 170.2 (1968), p. 379 (cited on p. 244).

[313] C. W. Gardiner and M. J. Collett. “Input and output in damped quantum systems: Quantum stochastic differential equations and the master equation”. *Phys. Rev. A* 31 (6 1985), pp. 3761–3774 (cited on p. 245).